



The  
University  
Of  
Sheffield.

**INSIGNEO**  
Institute for *in silico* Medicine



**Prediction of the risk of vertebral fracture in patients with  
metastatic bone lesions as a tool for more effective patients'  
management**

A thesis submitted in fulfilment of the requirements for the degree of  
Doctor of Philosophy

By:

Maria Cristiana Costa

Supervisors

Dr. Enrico Dall'Ara

Prof. Marco Viceconti

The University of Sheffield  
Faculty of Medicine, Dentistry & Health  
Department of Oncology and Metabolism

November 2018



## Acknowledgements

I would like to thank to all the people who contributed directly and indirectly to the development of this thesis.

First I would like to thank to Dr Enrico Dall'Ara, my first supervisor, for giving me the opportunity to work in such a challenging project. Enrico, I admire you as a researcher and as a person. I learned a lot from you from the past 3 years and something. It was a pleasure to work with you! Thank you also to Prof Marco Viceconti, my second supervisor, for the insightful discussions and guidance along the project, and who was another inspiring person to me.

I would also like to thank to all the colleagues whose contributions were, in different ways, essential for the development of the sub-studies of this thesis. In particular to Dr Gianluca Tozzi, Dr Valentina Danesi, and Prof Luca Cristofolini for the sample preparation of the porcine bones and the development of the *in situ* mechanical testing, to Dr John Rochester for the collection and help with the sample preparation of the cadaveric human samples, to Dr Melissa Ryan for the help with the scanning, to Dr Áron Lazáry and especially to Dr Peter Eltes for all the effort made for the collection of the clinical data, in such a limited range of time, and for being always available for clarifications and discussion. Thank you also to Dr Yuan Chen, Dr Mario Giorgi, Dr Qasim Mohammed, Dr Zainab Altai, and (the almost Dr) Sara Oliviero by the most diverse technical helps provided along this project. Moreover, a big thank you to all my colleagues and friends at Insigneo. It has been a pleasure to be part of a great team of people and researchers as you guys. And as not all of this learning period was about research a special thank you to Dr Melissa Ryan and Dr Barbara Kalkman for helping me to achieve another goal this year, the half marathon, which I hope reflected in the best way possible in this thesis.☺

I would also like to thank to my parents Fernanda and Manuel without whom it would have been harder, or even unthinkable, to complete this work. Thank you for all the support and words of affection. You are an example to me of resilience and motivation. Another person which was of great importance for the emotional balance of this journey was my love, Nuno. Thank you for all your support, love, friendship, and also for clearing my mind in the cloudy moments of this journey. You were my strength!

Lastly, I would like to acknowledge my funding from the Sheffield Hospital Charity (grant nr. 141515-1) and from the EPSRC MultiSim project (grant nr. EP/K038771X/1).

## **Publications in scientific journals**

Costa MC, Tozzi G, Cristofolini L, Danesi V, Viceconti M, Dall'Ara E (2017) Micro Finite Element models of the vertebral body: Validation of local displacement predictions. PLoS ONE 12(7):e0180151. <https://doi.org/10.1371/journal.pone.0180151>

Costa MC, Eltes P, Lazary A, Viceconti M, Dall'Ara E Effect of lytic metastases on the vertebral strength estimated with subject-specific finite element models, *Submitted* to the Journal of Orthopaedic Research on November 2018.

## **Presentations in international and local conferences**

Costa MC, Tozzi G, Cristofolini L, Chen Y, Viceconti M, Dall'Ara E. Validation of local displacements in vertebral body predicted by microCT-based finite element models, Insigneo showcase, 5<sup>th</sup> May, 2016, Sheffield, UK. *Poster Presentation*.

Costa MC, Tozzi G, Cristofolini L, Chen Y, Danesi V, Viceconti M, Dall'Ara E. Validation of local displacements in vertebral body predicted with microCT-based finite element models, 22<sup>rd</sup> Congress of the European Society of Biomechanics, 10-13<sup>th</sup> July, 2016, Lyon, France. *Oral presentation*.

Costa MC, Tozzi G, Viceconti M, Dall'Ara E. Micro finite element models of vertebral bodies: comparison of local and structural properties, Insigneo showcase, 11<sup>th</sup> May, 2017, Sheffield, UK. *Poster presentation*.

Costa MC, Tozzi G, Viceconti M, Dall'Ara E. Micro finite element models of vertebral bodies: validation of local and structural properties, 23<sup>rd</sup> Congress of the European Society of Biomechanics, 2-5<sup>th</sup> July, 2017, Seville, Spain. *Oral presentation*.

Costa MC, Eltes P, Lazary A, Viceconti M, Dall'Ara E. Patient-specific QCT-based FE models of metastatic lytic vertebrae, Insigneo showcase, 3<sup>rd</sup> May, 2018, Sheffield, UK. *Poster presentation*.

Costa MC, Eltes P, Lazary A, Viceconti M, Dall'Ara E. Patient-specific QCT-based FE models of metastatic lytic vertebrae, Multi-scale hard and soft tissue modelling workshop - SoftMech conference, 18-20<sup>th</sup> June, 2018, Sheffield, UK. *Poster presentation*.

## **Abstract**

Lytic spinal metastases are a big burden for cancer patients. These lesions are described as focal regions of very low bone mineral density (BMD), which cause a decrease in bone strength and an increase in the risk of fracture. The assessment of vertebral fracture risk in patients with spinal metastases is based on the Spinal Instability Neoplastic Score (SINS), which in many cases, is not able to provide a clear guidance. This problem is mainly due to the qualitative nature of the SINS, which therefore leads to a lack of objectivity in the assessment of patients with spinal metastases.

Finite element (FE) models have been extensively used to study the mechanical properties of healthy human vertebrae at different dimensional scales. FE models based on subject-specific micro Computed Tomography (microCT) images have been validated and used to estimate how the local properties of bone tissues affect bone structure. Such models can be applied to better understand the effect of lytic lesions on the local and structural properties of human vertebrae. This was the aim of the first two studies presented in this thesis. In the first study, microFE models predictions of local and structural properties of vertebral bodies were validated. The validated microFE modelling method was then applied to study the effect of lytic lesions with different properties (size and location) on the local and structural properties of human vertebrae, from a feasibility study performed only for a small parametric sample. On the other hand, subject-specific Quantitative Computed Tomography (QCT) based FE models have been validated and used to predict the fracture risk of osteoporotic human vertebrae. Moreover, it has been shown that lytic lesions can be approximated to low BMD bone tissues. Therefore, these models can also be used to estimate the strength of vertebrae with lytic lesions. Thus, a third study included the development of a methodology to generate subject-specific QCT-based FE models of vertebrae with lytic lesions, and to assess their stability based on the physiological loads estimated from a spinal model. Such methodology was then applied to a cohort of 8 patients with lytic spinal metastases to provide a biomechanical analysis of vertebrae with lytic lesions to help in the assessment of the fracture risk.

To conclude, in this thesis two approaches were developed using subject-specific FE models of different dimensional scales, to provide biomechanical analyses of the effect of lytic lesions on human vertebrae. Both approaches can be used with the SINS to provide a more objective assessment of the risk of fracture of patients with lytic spinal metastases. Future work on the improvement of these approaches is important to make them more robust and helpful in clinics.

## **Abbreviations**

BMC- Bone mineral content

BMD- Bone mineral density

CT- Computed Tomography

DIC: Digital Image correlation

DOF- Degrees of freedom

DVC Digital volume correlation

DXA- Dual X-ray absorptiometry

FE- Finite Element

hFE: Homogenised Finite Element

HR-pQCT- High Resolution peripheral Quantitative Computed Tomography

IVD: inter-vertebral disc

microCT- micro Computed Tomography

microFE- micro Finite Element

NS- Nodal Spacing

QCT- Quantitative Computed Tomography

SINS- Spinal Instability Neoplastic Score

Tb.Sp- Trabecular spacing

Tb.Th- Trabecular thickness

# Contents

<b>Chapter I. Background</b>	<b>9</b>
1.1. Bone anatomy	9
1.1.1. <i>The human vertebrae</i>	10
1.2. Bone physiology	11
1.2.1. <i>Metastatic bone lesions</i>	12
1.3. Bone Imaging	16
1.3.1. <i>Micro Computed Tomography (microCT)</i>	16
1.3.2. <i>Quantitative Computed Tomography (QCT)</i>	18
1.4. Bone mechanics	21
1.4.1. <i>Biomechanics of human vertebrae</i>	23
1.5. Finite Element (FE) modelling	26
1.5.1. <i>MicroFE models</i>	31
1.5.2. <i>Homogenised FE (hFE) models</i>	33
1.5.3. <i>FE models validation</i>	34
1.6. References	39
<b>Chapter II. Motivation and Literature review</b>	<b>47</b>
2.1. Motivation	47
2.2. Vertebral mechanical properties	48
2.2.1. <i>Validation and application of Finite Element models</i>	50
2.3. Effect of lytic metastases on bone mechanics	54
2.3.1. <i>Use of FE models to study the effect of vertebral metastasis</i>	57
2.4. Objectives	60
2.5. References	61
<b>Chapter III. MicroFE models of vertebral bodies: Validation of local displacement predictions and analysis of structural properties</b>	<b>66</b>
3.1 Introduction	68
3.2 Materials and methods	71
3.2.1. <i>Specimen's preparation</i>	73
3.2.2. <i>Scanning and in situ mechanical testing</i>	73
3.2.3. <i>Properties of the specimens</i>	74
3.2.4. <i>Experimental displacement field</i>	76

3.2.5 <i>MicroFE modelling</i> .....	76
3.2.6 <i>Statistics</i> .....	79
3.3 Results .....	80
3.4 Discussion .....	87
3.5 References .....	92
Supplementary materials .....	96
<b>Chapter IV. Effect of the size and location of simulated lytic lesions on the structural properties of human vertebral bodies: A feasibility study</b> .....	<b>99</b>
4.1 Introduction .....	101
4.2 Materials and methods .....	103
4.3 Results .....	107
4.4 Discussion .....	115
4.5 References .....	119
Supplementary material .....	122
<b>Chapter V. Development of a methodology for generating CT-based subject-specific finite element models to evaluate the effect of lytic lesions on vertebral mechanical properties</b> .....	<b>129</b>
Introduction .....	131
5.1 Definition of densitometry calibrations .....	134
5.1.1 <i>Materials and methods</i> .....	134
5.1.2 <i>Results</i> .....	135
5.1.3 <i>Discussion</i> .....	139
5.2 Choice of the size of the mesh in the FE models .....	141
5.2.1 <i>Materials and methods</i> .....	141
5.2.2 <i>Results</i> .....	147
5.2.3 <i>Discussion</i> .....	151
5.3 Definition of boundary conditions and failure criterion .....	153
5.3.1 <i>Materials and methods</i> .....	153
5.3.2 <i>Results</i> .....	156
5.3.3 <i>Discussion</i> .....	160
5.4 Estimation of physiological vertebral loads .....	164
5.4.1 <i>Materials and methods</i> .....	165
5.4.2 <i>Results</i> .....	173
5.4.3 <i>Discussion</i> .....	175

5.5.References.....	179
Supplementary materials.....	183
<b>Chapter VI. Clinical subject-specific finite element models for prediction of the effect of lytic lesions on vertebral mechanical properties</b> .....	<b>190</b>
6.1.Introduction.....	192
6.2.Materials and methods .....	194
6.3.Results.....	198
6.4.Discussion.....	210
6.5.References.....	216
Supplementary materials.....	219
<b>Chapter VII.Conclusions</b> .....	<b>226</b>
7.1.Original contributions .....	226
7.2.Limitations .....	228
7.3.Future work.....	229
7.4.References.....	230



## Chapter I. Background

The aim of this chapter is to provide background information that will be relevant to understand the approach used in the following chapters. To start, the fundamentals of bone anatomy and physiology with a specific focus on human vertebrae will be discussed. Next, the clinical problem tackled in this work, i.e. vertebral metastatic bone lesions, and the current clinical methods used to identify patients with spinal instability and thus higher risk of fracture will be described. A section dedicated to bone imaging will aim to describe the techniques used to characterize bone geometry, microarchitecture, and density. The last section of this chapter will review bone and vertebral biomechanics obtained experimentally and numerically through different types of subject-specific imaging-based finite element models.

### 1.1. Bone anatomy

Bone is the main component of the skeletal system which together with cartilage, tendons and ligaments provide support, protection, and organic equilibrium to the body (Cowin, 2001). Bone is a composite material composed of over 60-70% of hydroxyapatite micro-crystals ( $\text{Ca}_{10}(\text{PO}_4)_6(\text{OH})_2$ ), an organic matrix of which 85 to 90% is made of type I collagen fibres, and 5 to 6% water (Currey, 2002). Bone tissue can be classified according to its microstructure as cortical or trabecular bone depending on how its substructures (osteons and trabeculae) are arranged (Fig 1.1). Cortical bone (compact bone or cortex) is formed by solid microstructures called “osteons”, of approximately 200  $\mu\text{m}$  in diameter (Cowin, 2001). On the other hand, trabecular bone (or spongy bone), is a highly porous material (up to 50% of porosity) composed of substructures called “trabeculae”. The mean thickness of the trabeculae can vary between 100  $\mu\text{m}$  and 640  $\mu\text{m}$  (Cowin, 2001). The trabecular substructures are organized in a network of connected plate- and beam-like structures which are well-aligned (i.e. anisotropic) near the loading surfaces (Fig 1.1) (Adams et al., 2002; Currey, 2002). Cortical bone forms 80% of the skeletal mass of an adult human and is found in the outer wall of all bones, whereas the remaining 20% of bone mass is trabecular bone that can be found in the inner regions of bones (Fig 1.1) (Currey, 2002). Both cortical and trabecular bone microstructures can be well discriminated and observed using high resolution Computed Tomography (CT) imaging

techniques (i.e. High Resolution peripheral Quantitative Computed Tomography, HR-pQCT, and micro Computed Tomography, microCT) (see section 1.3.1).

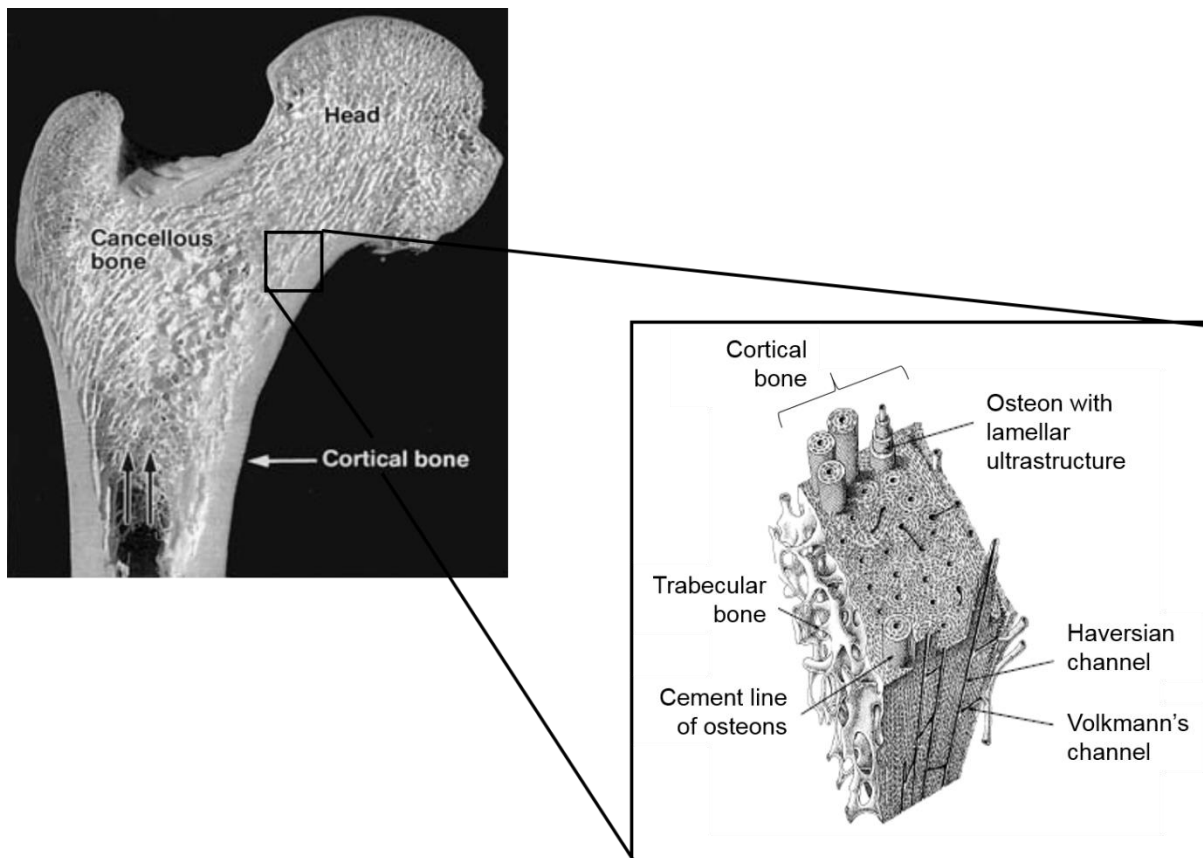


*Figure 1.1- Structure of a femoral bone from the organ level to the tissue level. Zoom in over a portion of cortical and trabecular bone extracted from the femoral neck where there is a high densification of trabecular bone organized along the principal lines of stress. Image adapted from Weiss (1988) and Kristic (1991).*

### **1.1.1. The human vertebrae**

The human spine can be divided in three regions known as: cervical (C1-C7), thoracic (T1-T12), and lumbar (L1-L5). Each region is composed by a number of vertebral units inter-connected by intervertebral discs and facet joints, present at the posterior part of each vertebrae. Each vertebra is formed by a vertebral body, composed by a centre of trabecular bone (mean trabecular thickness: 100  $\mu\text{m}$  to 400  $\mu\text{m}$ ) (Bevill & Keaveny, 2009; Fields et al., 2009a), surrounded by a thin cortical shell (mean cortical thickness: 380 $\pm$ 60  $\mu\text{m}$ ) (Eswaran et al., 2006), and two biconcave cortical endplates located at the superior and inferior faces of the vertebral body (Fig 1.2). Vertebral bodies are composed by 61%-79% of trabecular bone mass and 21-39% of cortical bone mass (excluding the endplates)

(Eswaran et al., 2006). Attached to the vertebral body there are a number of posterior elements as the pedicle, spinous process, and the articular processes, which provide the link and mobility among vertebrae (Fig. 1.2) (Adams et al., 2002). In between the posterior elements lies the vertebral foramen, which serves as a running canal for spinal nerves (e.g. spinal cord) and vessels.

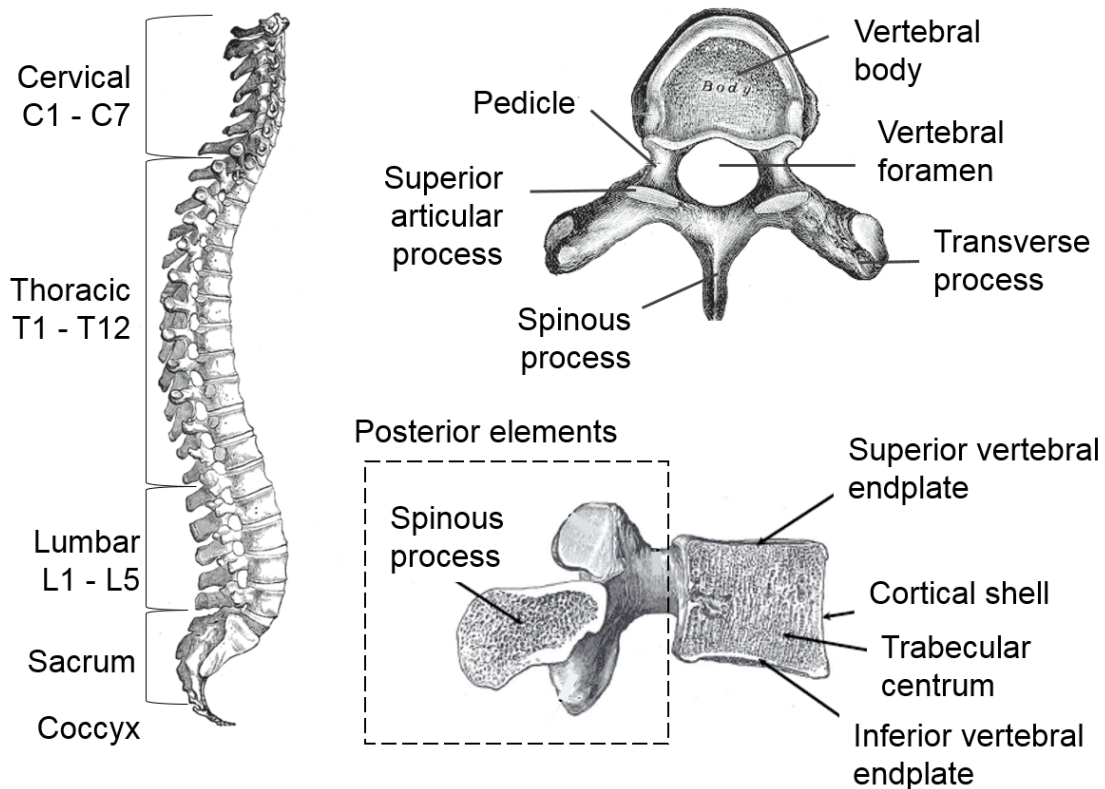
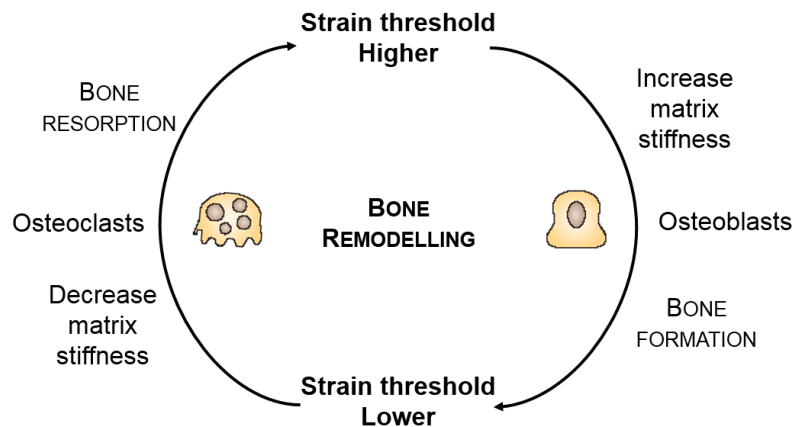


Figure 1.2- Vertebral body anatomy . Image adapted from Gray & Lewis (1918).

## 1.2. Bone physiology

Bone is a self-repairing and complex material of which mass, shape and mechanical properties can change with time, loading conditions, and many other factors, where some of these changes are of stochastic nature (Cole & Van Der Meulen, 2011; Cowin, 2001). Such changes happen continuously through remodelling processes driven by three cell types: osteocytes, osteoclasts, and osteoblasts. It has been suggested that osteocytes can sense mechanical stimuli and respond to changes in magnitude and distribution of strain by activating osteoclasts and osteoblasts to respectively reabsorb or deposit bone as needed (Fig 1.3) (Cowin, 2001). Through this remodelling processes bone is able to adapt its mass, shape, and properties

to changes in the mechanical environment (Cowin, 2001). A disruption in the activity of osteoclasts or osteoblasts can lead to an imbalance in bone reabsorption and deposition which can then lead to bone pathologies such as osteoporosis or metastatic bone lesions. In this thesis, the focus will be on metastatic bone lesions.



*Figure 1.3- Feedback mechanism of bone remodelling triggered by changes in magnitude and distribution of strains generated by the loads applied to a bone which mediate bone deposition or resorption through bone cells as osteoblasts and osteocytes respectively.*

### **1.2.1. Metastatic bone lesions**

Metastatic bone lesions develop from a secondary stage of cancer with the spine being the most common site of bone metastases (Vialle et al., 2015). Over 30% to 70% of cancer patients have spinal metastases (Vialle et al., 2015; Sutcliffe et al., 2013). Common cancer types that could lead to spinal metastases are breast-, lung-, prostate-, thyroid- and colorectal cancers, as well as multiple myeloma (Vialle et al., 2015; Mundy, 2002). Due to metastatic bone lesions bone strength is decreased, which leads to an increased risk of fracture (Hardisty et al., 2012; Ebihara et al., 2004). In many cases, patients eventually die from complications derived from the metastases rather than from the primary cancer (Vialle et al., 2015; Sutcliffe et al., 2013).

There are three types of metastatic lesions: blastic, lytic, and mixed lesions, which are developed from disruptions in bone remodelling (Maccauro et al., 2011; Mundy, 2002). Blastic lesions are generated by an increase in osteoblast activity, which leads to an increase in the deposition of calcified tissues with impaired properties (Lenherr et al., 2018; Nazarian et al., 2008; Mundy, 2002) (Fig 1.4- (b)). Lytic lesions, on the other hand, are due to an increase in the levels of bone reabsorption mediated by the osteoclasts. This leads to the formation of large

porosities in the extracellular matrix of bone and bone marrow, which are then filled with tumour tissue composed by cells similar to the primary tumour cells (Fig 1.4- (a)) (Maccauro et al., 2011; Mundy, 2002). In some cases, a mixture of both blastic and lytic lesions can occur in the same bone (Fig 1.4– (c)). Over 95% of the spinal metastases are lytic (Vialle et al., 2015).

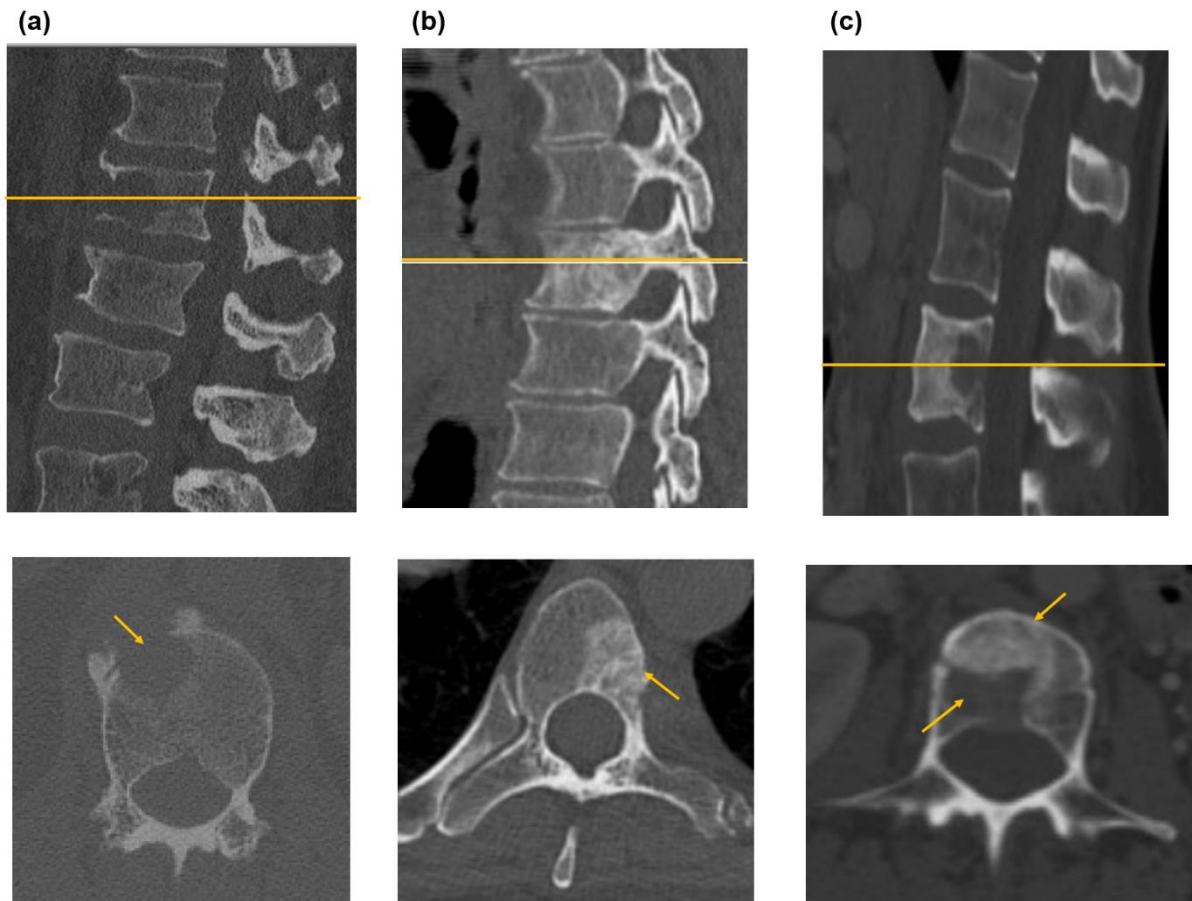


*Figure 1.4- Axial and transverse cross-section CT images of human vertebrae with (a) a lytic lesion, (b) a blastic lesion, and (c) a mixed lesion (c) (adapted from Vialle et al. (2015)).*

Spinal metastases are mostly located at the thoracic level (70%), while the lumbar and cervical levels are affected in 20% and 10% of the cases respectively (Vialle et al., 2015; Sutcliffe et al., 2013). In 80% of the cases, spinal metastases are located in the vertebral body, while the remaining 20% affects the posterior elements (Vialle et al., 2015; Sutcliffe et al., 2013; Maccauro et al., 2011). Spinal metastases can cause pain, instability and neurologic injuries, which can happen when metastatic lesions cause spinal cord compression (present in 5-10% of the patients) (Vialle et al., 2015). Patients with bone metastases have a short life expectancy, therefore, their condition has to be carefully managed in order to optimise their

quality of life, by pain relief and/or restoring mobility and neurologic function (Vialle et al., 2015). There are some treatment options to manage pain (e.g. medication), reduce the development of bone metastases (e.g. radiotherapy), or avoid further neurologic or orthopaedic complications (i.e. surgical interventions as cement augmentation or spinal stabilization) (Vialle et al., 2015; Maccauro et al., 2011). The clinical decision making for each patient is based on a multidisciplinary approach, involving specialists in oncology, radiology, pain, and orthopaedics, and takes into account some key aspects as the clinical status and life expectancy of the patient (Vialle et al., 2015). Clinical guidelines based on the assessment of pain and radiographic parameters such as Mirels' scoring system for metastases in long bones and the Spinal Instability Neoplastic Score (SINS), for spinal metastases have been used to help identify patients who may benefit from a certain clinical treatment (Benca et al., 2016; Vialle et al., 2015).

### *Clinical scoring system: Spinal Instability Neoplastic Score (SINS)*

The SINS has been proposed by the Spinal Oncology Study Group in 2010 as a clinical guideline to assess and categorize tumour related spinal instabilities, which are defined as “*losses of spinal integrity as a result of a neoplastic process that is associated with movement-related pain, symptomatic or progressive deformity and/or neural compromise under physiological loading*” (Versteeg et al., 2016; Fisher et al., 2010). The assessment of spinal instability is a critical factor and an essential component in the surgical decision making process of spinal metastases. However, before the development of the SINS, the diagnosis and treatment of spinal metastasis was variable and inaccurate, due to the lack of a systematic method to assess spinal metastases (Versteeg et al., 2016). In current clinical practice, the SINS is the standard framework to evaluate spinal instability through the scoring of six parameters, namely: the pain relief, type and location of the lesion, spinal alignment, vertebral body collapse, and postero-lateral involvement (Table 1.1) (Fisher et al., 2010). In the SINS, a score between 0 and 4 is given to each of the aforementioned parameters (Fisher et al., 2010) (Table 1.1). Based on the total score, spinal metastases are classified as stable, for SINS values between 0-6, indeterminate (possibly impending) instable, for SINS values between 7-12, or instable for SINS values between 13-18 (Fisher et al., 2010). Patients with instable vertebrae are strongly recommended to proceed with a surgical intervention (i.e. cement augmentation or spinal stabilizations). However, cases of indeterminate spinal instability are more

complicated and specialist consultation is especially important to help guide the surgical decision-making process (Vialle et al., 2015; Fisher et al., 2014; Fournay et al., 2011).

*Table 1.1- The SINS assessment and classification system of spinal instability in patients with metastatic lesions.*

SINS parameters	Score	Interpretation of the SINS scores
<b>Location</b>		<ul style="list-style-type: none"> <li>• Sum score 0-6: stable</li> <li>• Sum score 7-12: indeterminate (possibly impending) instability</li> <li>• Sum score 13-18: instability</li> <li>• SINS scores of 7-18 warrant surgical consultation</li> </ul>
Junctional (occiput-C2, C7-T2, T11-L1, L5-S1)	3	
Mobile spine (C3-C6, L2-L4)	2	
Semi-rigid (T3-T10)	1	
Rigid (S2-S5)	0	
<b>Pain<sup>1</sup></b>		
Yes	3	
Occasional pain but not mechanical	1	
Pain-free lesion	0	
<b>Bone lesion</b>		
Lytic	2	
Mixed (lytic/blastic)	1	
Blastic	0	
<b>Radiographic spinal alignment</b>		
Subluxation/translation present	4	
De novo deformity (kyphosis/scoliosis)	2	
Normal alignment	0	
<b>Vertebral body collapse</b>		
>50% collapse	3	
<50% collapse	2	
No collapse with >50% body involved	1	
None of the above	0	
<b>Posterolateral involvement of spinal elements<sup>2</sup></b>		
Bilateral	3	
Unilateral	1	
None of the above	0	

<sup>1</sup> Pain relief with recumbency and/or pain with movement/loading of the spine  
<sup>2</sup> Facet, pedicles, or CV joint fracture or replacement with tumor

The validity of the SINS has been tested (not prospectively) showing a sensitivity and specificity of 95.7% and 79.5% (Fisher et al., 2014; Fournay et al., 2011). Moreover, excellent inter- and intra-observer reliability (intraclass correlation coefficients (ICC) of 0.85 and 0.89 for inter and intra-observer reproducibility respectively) has been demonstrated for the assessment of the three clinical categories of spinal instability (Fisher et al., 2014; Fournay et al., 2011). The SINS is, however, a qualitative method that mostly depends on the visual assessment of radiological data and often relies on clinical experience to identify spinal instability (Vialle et al., 2015; Fisher et al., 2010). In addition, the inclusion of parameters which assess both the degree (e.g. pain and vertebral body collapse) and the risk (e.g. lesion type and location) of spinal instability limits the predictive power of true negative cases which

causes patients' overtreatment (Versteeg et al., 2016). Potentially, biomechanical analyses of metastatic lesions could provide an objective and quantitative method to evaluate mechanical stability, which could help in the surgical decision-making and improve treatment outcomes.

### **1.3. Bone Imaging**

Bone imaging techniques have been widely used to study bone geometries, microstructure, and density at different spatial resolutions. High resolution imaging techniques such as micro Computed Tomography (microCT) and High Resolution peripheral Quantitative Computed Tomography (HR-pQCT) can be used *ex vivo* to resolve and study the 3D microstructure of vertebrae (Schwiedrzik et al., 2016; Dall'Ara et al., 2012; Pahr et al., 2011; Wolfram et al., 2010a; Ladd et al., 1998). At the macroscopic level *in vivo* techniques as Dual X-ray absorptiometry (DXA), and Quantitative Computed Tomography (QCT) are mostly used to provide apparent measurements of bone mineral density through the conversion of the X-rays intensity values into a hydroxyapatite-equivalent density by the use of calibration phantoms (Griffith & Genant, 2008). This section will only address the two imaging techniques used in this thesis, namely microCT and QCT.

#### **1.3.1. Micro Computed Tomography (microCT)**

A microCT system is an X-ray imaging technique which allows to obtain a 3D image of a sample created through the reconstruction of multiple 2D projection images acquired at different viewing angles (i.e. rotational steps) of the sample. Each 2D projection of the sample is generated through the emission of an X-ray beam, from the radiation source, which by passing through the sample will be attenuated and recorded by a charge-coupled device detector that acquires the 2D projection image (Fig 1.5). In *ex vivo* systems the sample, placed on a rotation plate, rotates by 360° (or 180° for symmetric samples) in small rotational steps (usually 0.5° or less) to generate a multiple stack of 2D projection images (Fig 1.5). In *in vivo* systems the subject (patient, animal or object) lays on a bed and the detector and the X-rays source rotates around it. The projections are then reconstructed to a 3D image using back-projection algorithms (Bouxsein et al., 2010; Griffith & Genant, 2008; Cowin, 2001). When the X-ray beam is transmitted through the sample it will be attenuated, meaning that some X-rays will be absorbed and others transmitted depending on the density of the materials within the sample (e.g. dense materials as bone will absorb more X-rays than soft tissues as muscles and

ligaments), therefore causing a reduction in the intensity levels of the X-ray beam exiting the sample. The grey level of each voxel of the final 3D image is derived from the different levels of attenuation of the X-rays, which is associated to the local density of the materials that constitute the sample.

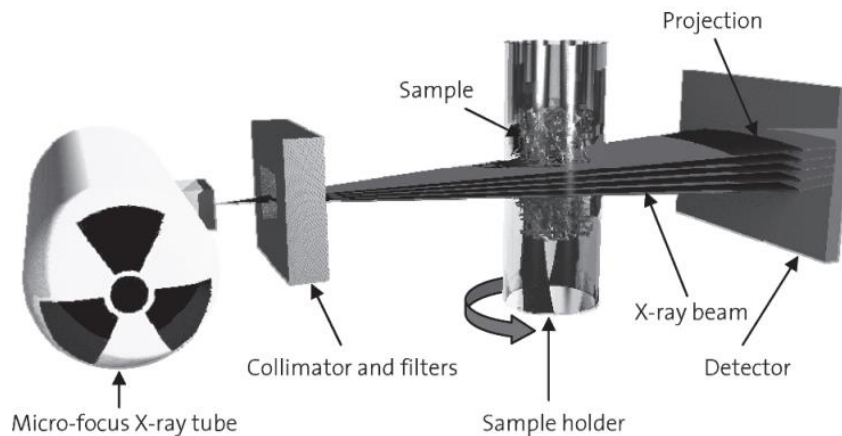


*Figure 1.5- Representation of the working principle of a microCT scanner. In order to avoid beam hardening artifacts generated from an increase in the mean energy of the X-ray beams that exit the sample (which is generated by an high attenuation of low energy photons), collimators and filters are used to avoid the the low energy photons of the beam. Image reproduced from Stauber & Muller (2008) with permission of Springer Nature.*

MicroCT scanners have been used to acquire images with resolutions between approximately 10  $\mu\text{m}$  to 40  $\mu\text{m}$  for specimens with diameters of a few millimetres to a maximum of 80-100mm (Hussein et al., 2012; Cowin, 2001). Bone microstructure can be assessed through morphological analysis of 3D microCT images (Müller et al., 1998). Typically, the characterization of trabecular bone microstructure is based on the assessment of the following morphological parameters: bone volume fraction (BV/TV) (Fig 1.6) computed as the amount of bone volume (BV) divided by the total volume of the regions of interest (TV), trabecular thickness (Tb.Th) (Fig 1.6), trabecular separation (Tb.Sp) (Fig 1.6), trabecular number (Tb.N), and bone anisotropy based on the Mean Intercept Length (MIL) method (Fields et al., 2009a; Nazarian et al., 2006; Odgaard, 1997). There are specific metrics for the assessment of the morphology of cortical bone, which will not be described here as they were not used in this thesis.

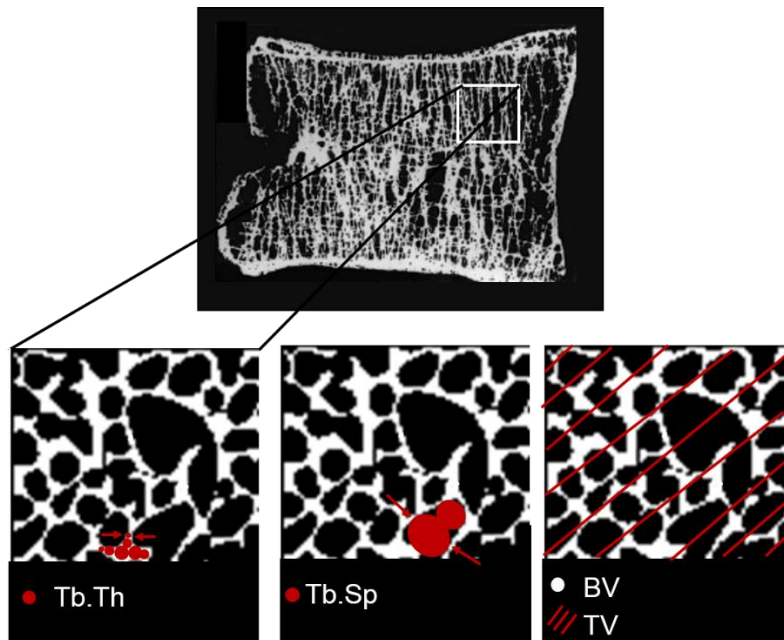


Figure 1.6- Cross section view of a human vertebra scanned in a microCT, following a representation of some of the morphometric measurements obtained from imaging analysis of a region of interest, including the mean trabecular thickness (Tb.Th), trabecular separation (Tb.Sp), and bone volume fraction (BV/TV) obtained from a frontal section of the cubic trabecular sample. Image adapted from Weiss (1988).

### 1.3.2. Quantitative Computed Tomography (QCT)

Quantitative Computed Tomography (QCT) images are obtained from a standard CT machine equipped with a hydroxyapatite-equivalent calibration phantom, which can be scanned simultaneously with the patient (i.e. in-line calibration phantoms) or off-line to calibrate the image grey levels into equivalent bone mineral density (BMD). Both DXA and QCT are densitometric techniques currently used in clinical practice to measure BMD in the assessment and diagnosis of osteoporosis and osteopenia (Griffith & Genant, 2008). The QCT has an advantage over DXA because it provides a volumetric measurements of BMD, contrary to the typical DXA areal (projected) measurements, and it can be used to measure bone properties separately in both cortical and trabecular compartments. Nonetheless, DXA is still the clinical gold standard due the low radiation dose (typically  $7\mu\text{Sv}$  by DXA vs.  $60\mu\text{Sv}$  by QCT for human vertebrae, depending on the scanning protocol) and costs (Griffith & Genant, 2008).

Three-dimensional grey scale QCT images are obtained based on the basic principles similar to those described above for *ex vivo* microCT images. In both cases 3D images are obtained through the reconstruction of multiple 2D projections obtained at different angles (Nishiyama

et al., 2019; Goldman, 2007) (Fig 1.7), while the subject translates axially with respect to the X-ray source-detector assembly (Fig 1.7). The X-ray attenuation coefficients obtained from a QCT image are calibrated to the attenuation coefficient of water and air and therefore are provided in Hounsfield Units (HU) (Goldman, 2007).

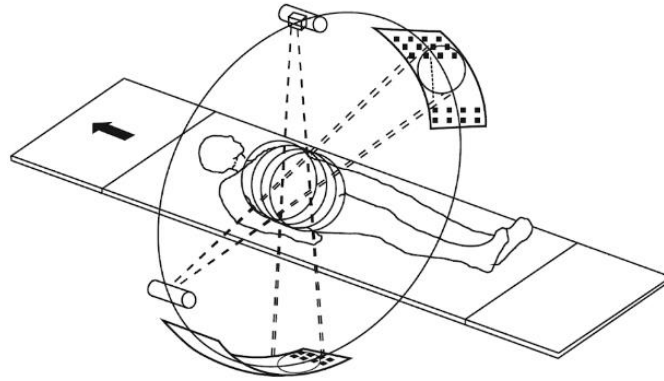


*Figure 1.7- Representation of the reconstruction system used in the current helical CT scanners which imply the continuous rotation of the X-ray source-detector assembly around the patient while he translates through. Image reproduced from Cierniak (2011).*

The density measurements provided by a QCT image are obtained with a densitometric calibration law, derived from a calibration phantom typically used during the scanning (Fig 1.8). A calibration phantom is composed by a series of insertion rods of water-equivalent and hydroxyapatite-equivalent materials (e.g. in-line dipotassium hydrogen phosphate phantoms  $K_2HPO_4$  are composed by 5 insertion rods with  $0 \text{ mg/cm}^3$ ,  $50 \text{ mg/cm}^3$ ,  $100 \text{ mg/cm}^3$ ,  $150 \text{ mg/cm}^3$ , and  $200 \text{ mg/cm}^3$ ) (Fig 1.8) (Griffith & Genant, 2008). To obtain a densitometric calibration equation regions of interest are defined within each insertion rod of the calibration phantom and a linear regression analysis is used to determine the relationship between the mean HU values and the known values of the equivalent BMD.

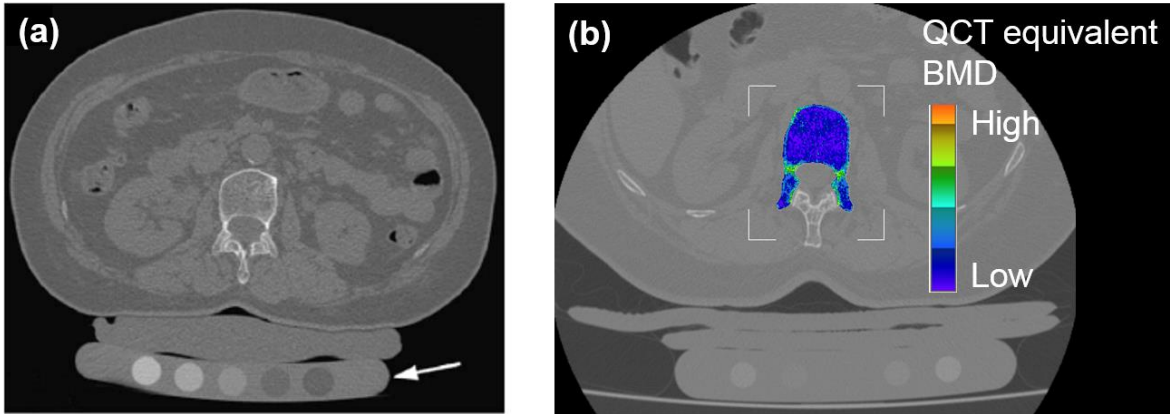


Figure 1.8- (a) QCT image of a human vertebra L2 scanned together with a calibration phantom composed by 5 insertion rods with equivalent densities of 0, 50, 100, 150, and 200 mg/cm<sup>3</sup> used to calibrate the image grey levels in equivalent BMD. Image reproduced from (Griffith & Genant, 2008) with permission of Elsevier. (b) Example of the distribution of the QCT equivalent BMD of a L2 vertebra.

The resolution of QCT images (i.e. 0.8 mm to 1.0 mm of in plane pixel spacing, 0.5 mm to 10.0 mm of slice thickness) does not provide enough detail to describe the trabecular bone microstructures or the thin cortical shell present, for instance, in human vertebrae. Such low resolution affects the partial volume effects of QCT images, which cause an underestimation of the BMD of cortical structures. Changes in patient's shapes and sizes can also affect the QCT measurements of BMD due to changes in the X-ray attenuation levels that can cause beam hardening artifacts (i.e. artificial lower grey level regions generated in deep and thick regions of the scanned object by a high attenuation of the X-ray energy) (Goldman, 2007). Apart from densitometric measurements, QCT images are also used to assess macrostructure of bones including bone sizes and shapes (Engelke et al., 2013). Therefore, by accounting for bone geometries and density, QCT images provide important means of information that can also be used to generate specimen-specific homogenized Finite Element (FE) models to assess bone strength (see section 1.5.2).

## 1.4. Bone mechanics

Bone is a heterogeneous, anisotropic, elastic material that undergoes plastic deformation and damage after yield (Wolfram & Schwiedrzik, 2016; Cowin, 2001). The mechanical behaviour of bones can be characterised by a linear elastic domain, a nonlinear post-yield behaviour, and fracture (Fig 1.9 – (b) zones I, II, and III respectively). In the elastic domain bone deforms in a reversible way following the Hooke's law (i.e. the change in length,  $\Delta l$ , is proportional to the applied force,  $F$ ) until it reaches the yield strength which is commonly estimated experimentally from the normalized force-displacement curve by a 0.2% strain-offset method (i.e. yield strength as the intersection point between the stress-strain curve and the line drawn from the 0.2% offset strain with slope equal to the normalized stiffness) (Boresi & Schmidt, 2003) (Fig. 1.9- (b) zone I). In the elastic domain, bone stiffness is computed as the slope of the linear portion of the force-displacement curve whereas normalized stiffness (i.e. the Young's modulus or the modulus of elasticity) can be obtained in the same way from the stress-strain curve (Fig 1.9- (a) and (b)). As a ductile material, after yield, vertebral bones undergo plastic deformation also known as plasticity (Dall'Ara et al., 2010) (Fig 1.9- (b) zone II). Different yield surface models have been proposed to describe the yield behaviour of bone tissue for example the Drucker-Prager and quadric yield criterion (Schwiedrzik, 2014). At the structural level it has been shown that these models approximate well to an isotropic criterion for uniaxial loading conditions (Levrero-Florencio et al., 2016). After yield, bone is known to show asymmetric strength values for tension and compression (Bayraktar et al., 2004; Niebur et al., 2000; Zysset, 1994). In particular, for trabecular bone, tension-compression yield strength ratio equals 0.46 according to Bayraktar et al. (2004) and 0.6 according to Zysset (1994). Plasticity develops until the ultimate point, after this the damaging processes that will lead to fracture start (Fig 1.9- (b) zone III). The amount of work and energy required to cause bone fracture can be estimated as the area under the force-displacement curve and stress-strain curve, respectively (Fig 1.9- (a) and (b)).

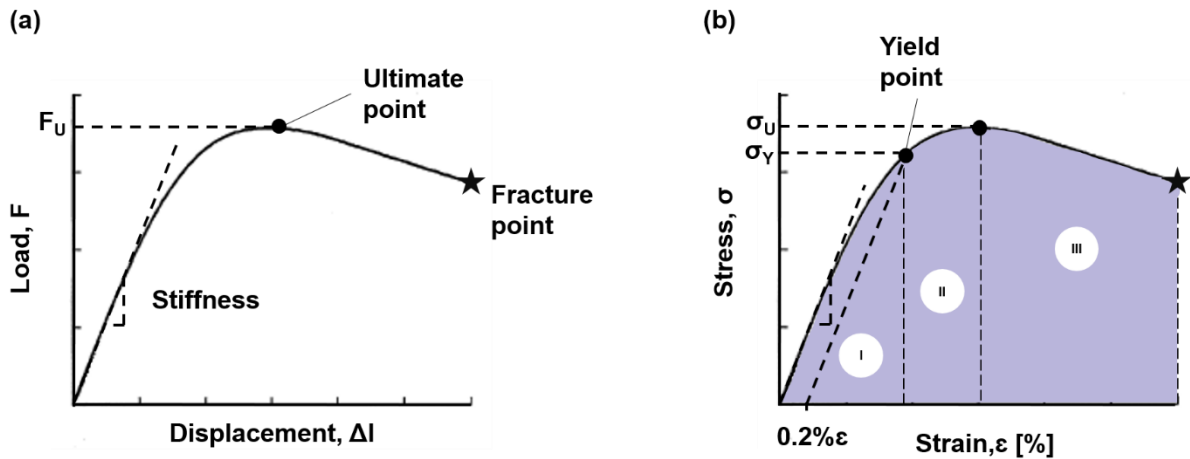


Figure 1.9- (a) Typical load-displacement curve and (b) normalised stress-strain curve obtained from quasi-static monotonic tests performed on bone samples highlighting the three domains of the mechanical behaviour of bones: I as the elastic domain, II as the post-yield zone, and III as the fracture zone (adapted from Wolfram & Schwiedrzik (2016)).

Variations in bone density and microstructure of both cortical and trabecular bone are expressed by different material properties which are affected, among other factors, by age, anatomical site, and subject's gender (Cowin, 2001; Morgan & Keaveny, 2001; Ebbesen et al., 1999). At the microscopic level it has been shown that such differences do not affect the mechanical behaviour of cortical and trabecular bone, which show similar material and mechanical behaviours (Pahr et al., 2011; Rho et al., 1998). However, there is still some controversy about the correspondence of mechanical properties between trabecular and cortical bone (Cowin, 2001). On the other hand, at the macroscopic level such tissue level differences are known to affect the mechanical behaviour of bone under loading (Pahr & Zysset, 2009). Accordingly, bone strength is known to be a function of bone geometry, density, microstructure, tissue properties, and loading conditions (Cole & Van Der Meulen, 2011).

Tissue properties, such as the elastic tissue modulus can be measured *ex vivo* with depth-sensing micro- or nano-indentation techniques. In a typical micro-indentation test, a diamond tip (usually Berkovich), with known geometry, is pressed against a flat sample surface while recording its force and displacements (Wolfram & Schwiedrzik, 2016; Zysset, 2009). Elastic tissue properties and hardness are then measured through the indentation load-displacement curve obtained during the loading and unloading of the indentation tip using the Oliver & Pharr (2004) method. Bone has a preferential orientation along the main loading direction, showing an higher elastic tissue modulus along the longitudinal direction for bone tissues collected from human vertebrae (Mirzaali et al., 2016; Wolfram et al., 2010b; Roy et al., 1999). Such

evidences suggest bone is a transverse isotropic material. Specifically, 3D morphological analysis of high resolution images has characterized the three planes of orthotropic symmetry of bone through the Mean Intercept Length (MIL) method (Zysset, 2003; Odgaard, 1997). Additionally bone also shows a time-dependent (Xie et al., 2017; Manda, Wallace, et al., 2016; Manda, Xie, et al., 2016) and rate-dependent mechanical behaviours under loading. Nonetheless, the studies developed in this thesis do not take into account the viscoelastic or the dynamic phenomena of bone.

Bone mass and density are the most studied determinants that describe the structural behaviour of bone (Morgan et al., 2003; Kopperdahl et al., 2002; Ebbesen et al., 1999). Density measurements of bone can be obtained in the form of apparent density ( $\rho_{app}$ ) [ $\text{g}/\text{cm}^3$ ], defined as the wet bone mass per unit of volume (Morgan et al., 2003); ash density ( $\rho_{ash}$ ) [ $\text{g}/\text{cm}^3$ ], as the ash weight per unit of volume (Schileo, Dall'Ara, et al., 2008); Tissue Mineral Density (TMD) [ $\text{g}/\text{cm}^3$ ], as the weight of mineral content per unit of volume (Tassani et al., 2011); or Bone Volume Fraction, BV/TV [%], as the amount of bone within a specific volume. In particular the BV/TV is obtained by geometrical analyses after image segmentation, and it is typically used as a microstructural property. In addition, densitometric techniques as DXA and QCT can also provide, respectively, an areal and volumetric apparent measurement of bone mineral density (including both bone and marrow) through the conversion of the X-rays intensity values into equivalent bone mineral density by the use of calibration phantoms (Griffith & Genant, 2008). The microstructure of bone can be assessed in 2D by histomorphometric analysis or in 3D by morphometric analysis of microCT images (see section 1.3.1). Due to its non-destructive nature, efficiency, accuracy, and the 3D space of measurement, microCT images have been most widely used and applied to morphological studies of bone (Müller et al., 1998).

#### **1.4.1. Biomechanics of human vertebrae**

Vertebral fractures occur when the applied load exceeds vertebral strength. The applied spinal loading is mainly a function of the subject's body weight and height, spinal curvature (i.e. sagittal thoracic kyphosis, TK, and lumbar lordosis, LL, angles), physical activity, muscle forces, and external forces (Alexander et al., 2017; Han et al., 2013; Rohlmann et al., 2008). However, other factors such as intervertebral disk deterioration, spinal balance, and frontal plane deformities resultant from degenerative spinal disease as scoliosis, are also known to affect vertebral loading (Alexander et al., 2012; Han et al., 2012). Vertebral strength is

determined by bone geometry, density, microstructure, tissue properties, and loading conditions (Jackman et al., 2015; Chevalier et al., 2008; Cowin, 2001). Vertebral bodies and intervertebral discs are the main pillars for the support of spinal loads (holding between 76% to 89% of the total load applied to the vertebrae), with the cortical shell (excluding the endplates) holding between 38% to 54% of the load applied to vertebral bodies in pure axial compression cases (Eswaran et al., 2006). The posterior elements are known to provide spinal stability, together with the spinal muscles and ligaments, and loading transfer between adjacent vertebrae (Bergmark, 1989). These structures can carry over 25% of the compressive loads applied to the vertebrae during flexion postures. However it has been observed that for neutral standing postures only a minor portion of compressive loads is transferred by the articular processes (Asano et al., 1992; Bergmark, 1989). Therefore, the effect of the posterior elements on the mechanical properties of human vertebrae will not be considered in this thesis.

Compression and bending are the vertebral loading conditions which lead to the most common types of vertebral fractures known as biconcave fractures and wedge shape fractures (Fig 1.10) (Jackman et al., 2015; Brinckmann et al., 1989). The compressive strength of vertebral bodies grows from the cranial to the caudal direction due to an increase in geometric dimensions of the endplates (Brinckmann et al., 1989; Miller & Schultz, 1988). Typically, the load due to axial compression in the thoracic and lumbar vertebrae from T7 to L4 equals  $6.4 \pm 2.4$  kN (Wang et al., 2012). Similar ultimate load values ( $6.6 \pm 2.2$  kN) were obtained for thoracolumbar levels, T12-L5, tested under eccentric compression (Dall'Ara et al., 2012). Clinically, the vertebral fracture assessment (VFA) system uses the gold standard semi-quantitative method developed by Genant et al. (1996). to evaluate vertebral fracture as deformations higher or equal than 20% in height of the vertebral bodies (Fig 1.10) (Schousboes et al., 2011; Genant & Jergas, 2003). This semi-quantitative method relies on the use of X-ray images to determine the degree of vertebral height reduction and changes in morphology among the neighbouring vertebrae (Genant & Jergas, 2003).

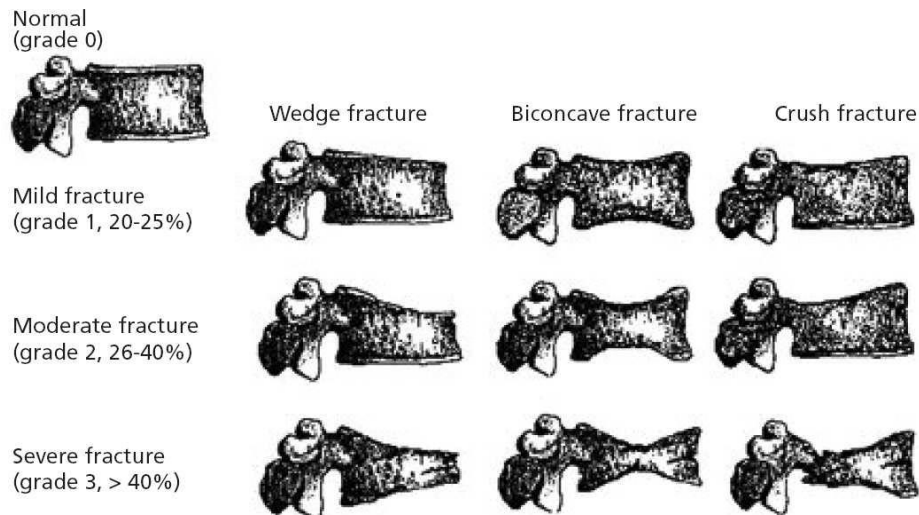


*Figure 1.10- Genant criteria of vertebral fractures. Image reproduced from Genant et al. (1996) with permission of John Wiley and Sons.*

The mechanisms of vertebral fracture, observed for axial compression and compression with anterior bending loading modes, are mostly associated with a large deflection of the superior endplates and adjacent trabecular bone which progress along the superior third and the mid-transverse plane of the vertebrae (Hussein et al., 2018; Jackman et al., 2015; Brinckmann et al., 1989). It has been shown that variations in the microstructure of the trabecular bone underlying the superior endplate affect the initiation and progression of vertebral failure (Hussein et al., 2018; Jackman et al., 2015). For combined loading conditions of compression with anterior bending, vertebral deflections are mostly located in the anterior half of the endplates involving an outward bulge of the anterior cortex, resulting in most cases into wedge shape fractures and a mixture of wedge and biconcave fractures (Jackman et al., 2015). For axial compression loading, the initiation and progression of vertebral fracture occurs more often over the central part of the endplates involving the cortical rim, typically leading to the development of biconcave fractures (Fig 1.10) (Hussein et al., 2018; Jackman et al., 2015; Brinckmann et al., 1989).

## 1.5. Finite Element (FE) modelling

Finite element (FE) models have been used in the field of orthopaedic biomechanics since the 1990s to study the mechanical properties of bones at different dimensional scales (Zysset et al., 2013).

Briefly, the FE method is a numerical technique, which provides an approximated solution to problems which are difficult to solve analytically due to the presence of complex geometries, material properties, and/or boundary conditions (Baguley & Hose, 1994). The FE method relies on the discretization of the problem domain (i.e. complex structures) into small structural components of known geometry, called elements. Each element is composed of a number of nodes, which are associated to a finite number of degrees of freedom (DOF, usually the three Cartesian components of the displacements for three-dimensional problems) used to model the mechanical behaviour of each element. The geometry of each element is assumed to follow a linear, quadratic, or higher order polynomial shape function based on the element type used in the FE model. For structural analysis, after discretization, a global stiffness matrix [Eq 1.10], which results from assembling the stiffness matrix of each individual element of the model [Eq 1.9], is calculated. After the definition of the material properties and boundary conditions of the model, described in terms of displacement or force, the equilibrium equations are solved for each DOF.

The displacements in each point of the element are related to the nodal displacements through the shape functions as:

$$\{u^{(e)}\} = [N^{(e)}]\{U^{(e)}\} \quad [\text{Eq 1.1}]$$

Where  $\{u^{(e)}\}$  represents the vector of the displacements of each element ( $e$ ) in function of the matrix of the shape function of the element type used in the model,  $[N^{(e)}]$ , and the unknown nodal displacement vector  $\{U^{(e)}\}$ .

The strain vector in each element,  $\{\varepsilon^e\}$ , can then be obtained through differentiation of the nodal displacement vector as:

$$\{\varepsilon^e\} = [B^{(e)}]\{U^{(e)}\} \quad [\text{Eq 1.2}]$$

$$[B^{(e)}] = [L] [N^{(e)}] \quad [\text{Eq 1.3}]$$

Where the strain vector  $\{\varepsilon^e\}$  of the element ( $e$ ) is estimated in function of the derivative of the element shape function,  $[B^{(e)}]$ , and the nodal displacements  $\{U^{(e)}\}$  of the element ( $e$ ). The derivative of the element shape function is obtained by the product between a differentiation operator  $[L]$  and the element shape function  $[N^{(e)}]$ .

In the linear elastic range, the element stresses,  $\{\sigma^e\}$ , are then related to the strains based on the Hook's law as follows:

$$\{\sigma^e\} = [D^{(e)}]\{\varepsilon^e\} \quad [\text{Eq 1.4}]$$

For models with isotropic materials (i.e. materials with symmetrical properties in all directions), the elasticity matrix,  $[D^{(e)}]$ , is defined based on the elastic modulus ( $E$ ) and the Poisson's ratio ( $\nu$ ) as follows:

$$[D^{(e)}] = \frac{E}{(1+\nu)(1-2\nu)} \begin{bmatrix} 1-\nu & \nu & \nu & 0 & 0 & 0 \\ \nu & 1-\nu & \nu & 0 & 0 & 0 \\ \nu & \nu & 1-\nu & 0 & 0 & 0 \\ 0 & 0 & 0 & \frac{1-2\nu}{2} & 0 & 0 \\ 0 & 0 & 0 & 0 & \frac{1-2\nu}{2} & 0 \\ 0 & 0 & 0 & 0 & 0 & \frac{1-2\nu}{2} \end{bmatrix} \quad [\text{Eq 1.5}]$$

The Poisson's ratio,  $\nu$ , describes the ratio between transverse ( $\varepsilon_x$ ) and axial deformations ( $\varepsilon_z$ ) of 3D models.

The stiffness matrix of each element,  $[K^{(e)}]$ , is then derived from:

$$[K^{(e)}] = \int_V [B^{(e)}]^T [D^{(e)}] [B^{(e)}] dV \quad [\text{Eq 1.6}]$$

The FE method then uses the minimization principle of potential energy ( $\Pi$ ), [Eq 1.7] to get the equilibrium equations of the system [Eq 1.9].

$$\frac{\partial \Pi}{\partial U} = 0 \quad [\text{Eq 1.7}]$$

$$\Pi = \sum_{e=1}^e \pi^{(e)} = \sum_{e=1}^e \Lambda^{(e)} - \sum_{e=1}^e W^{(e)} = \sum_{e=1}^e \frac{1}{2} \{U^{(e)}\}^T [K^{(e)}] \{U^{(e)}\} - \sum_{e=1}^e \{U^{(e)}\}^T \{F^{(e)}\} \quad [\text{Eq 1.8}]$$

Where  $\Pi$  represents the potential energy of the whole system as the sum of the potential energies,  $\pi^{(e)}$ , of each element in function of the strain energy,  $\Lambda^{(e)}$ , and the work done by the external load,  $W^{(e)}$  of each element ( $e$ ).

$$\sum_{e=1}^e ([K^{(e)}] \{U^{(e)}\} - \{F^{(e)}\}) = 0 \quad [\text{Eq 1.9}]$$

Where  $\{U^{(e)}\}$  represents the vector of unknown nodal displacements in the element ( $e$ ),  $\{F^{(e)}\}$  the vector of the nodal forces, and  $[K^{(e)}]$  the stiffness matrix of each element, which depends on the material properties assigned to each element ( $e$ ).

The equilibrium equations or element stiffness matrices of every element of the model are then assembled together in a global system of algebraic equations called global stiffness matrix [Eq 1.10], which will describe the behaviour of the whole structure in function of the selected unknowns.

$$[K] \{U\} = \{F\} \quad [\text{Eq 1.10}]$$

Where  $[K]$  represents the global stiffness matrix,  $\{U\}$  is the vector of unknown nodal displacements, and  $\{F\}$  the vector of the nodal forces applied to the model.

Under a certain loading condition, a 3D structure is subjected to a strain state composed by three normal and three shear strain components aligned to a global reference coordinate system. Principal strains are the normal strains that act along principal planes, in which the shear strain equals zero. Principal strains are the eigenvalues of the strain tensor [Eq 1.11] (Boresi & Schmidt, 2003) which are denoted as  $\varepsilon_{P1}$ ,  $\varepsilon_{P2}$ , and  $\varepsilon_{P3}$ , where  $\varepsilon_{P1} > \varepsilon_{P2} > \varepsilon_{P3}$ , meaning that

$\varepsilon_{p1}$  is the maximum principal strain (most positive component in tension), and  $\varepsilon_{p3}$  the minimum principal strains (most negative component in compression) in normal uniaxial loading conditions.

$$\begin{vmatrix} \varepsilon_x - \varepsilon_0 & 2\varepsilon_{xy} & 2\varepsilon_{xz} \\ 2\varepsilon_{xy} & \varepsilon_y - \varepsilon_0 & 2\varepsilon_{yz} \\ 2\varepsilon_{xz} & 2\varepsilon_{yz} & \varepsilon_z - \varepsilon_0 \end{vmatrix} = 0 \quad [\text{Eq 1.11}]$$

Contrary to what happens in a linear analysis, in nonlinear FE models the stiffness matrix will change at each time step of the analysis either due to geometrical effects (large deformations) or the use of nonlinear constitutive laws. The Newton-Raphson method is one of the most common methods used to solve nonlinear models (Fung & Tong, 2001). This method solves an iterative series of linear approximation found at each step,  $n$ , of the analysis, which is generated by small load increments  $\Delta F_n$  (Fig 1.11). Based on this method, and assuming that the solution of  $\{U\}_n$  at  $\{F\} = \{F\}_n$  is known, one seeks to compute the solution  $\{U\}_{n+1}$  at the applied load  $\{F\}_{n+1} = \{F\}_n + \{\Delta F\}_n$ . For each iteration  $i$ th of the load step  $n+1$ , a new approximation of the displacement vector,  $\{U\}_{n+1}^i$ , is obtained from the increment in displacements,  $\{\Delta U\}^i$ , computed from [Eq 1.14]. Iterations over the displacement will continue until the residual forces,  $\{\Delta R\}_{n+1}^{i-1}$  [Eq 1.13], of the incremental solution of the tangent stiffness matrix [Eq 1.12], are acceptably small so that the solution is converged and is in equilibrium within an acceptable tolerance (Fig 1.11).

$$[K_T]_{n+1}^{i-1} \{\Delta U\}^i = \{F^{ext}\}_{n+1} - \{F^{int}\}_{n+1}^{i-1} \quad [\text{Eq 1.12}]$$

$$\{\Delta R\}_{n+1}^{i-1} = \{F^{ext}\}_{n+1} - \{F^{int}\}_{n+1}^{i-1} = 0 \quad [\text{Eq 1.13}]$$

$$\{U\}_{n+1}^i = \{U\}_{n+1}^{i-1} + \{\Delta U\}^i \quad [\text{Eq 1.14}]$$

Where  $\{U\}_{n+1}^0 = U_n$  and  $\{F^{int}\}_{n+1}^0 = F_n$ . In addition,  $[K_T]_{n+1}^{i-1}$  represents the tangent stiffness matrix updated to the geometric and material properties at the  $i$ th iteration of the load-step  $n+1$ . The incremental nodal displacements,  $\{\Delta U\}^i$ , computed from [Eq 1.12] are then used to obtain the next approximation of the nodal displacements  $\{U\}_{n+1}^i$ . Each iteration of [Eq 1.12] and [Eq 1.14] are solved until the residual forces,  $\{\Delta R\}_{n+1}^{i-1}$ , which means the difference between the

externally applied forces  $\{F^{ext}\}_{n+1}$  and the internal element nodal forces,  $\{F^{int}\}_{n+1}^{i-1}$ , reach equilibrium at each load step  $n+1$  (Fig 1.11).

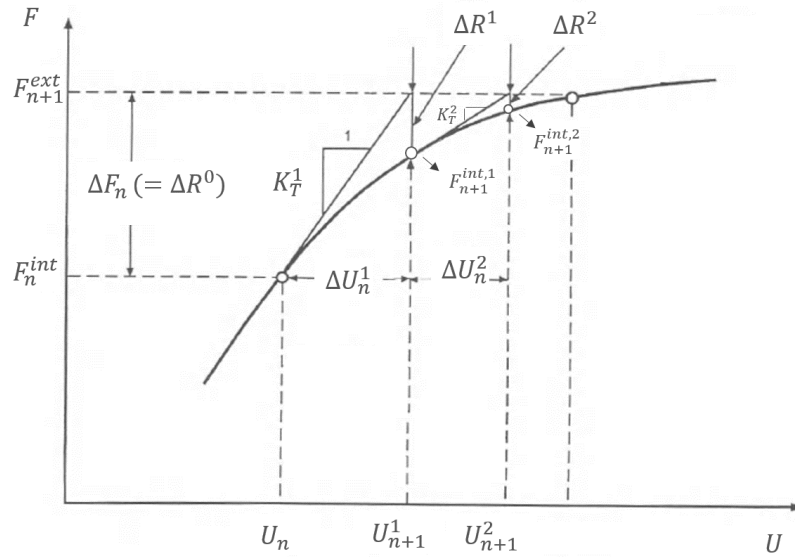


Figure 1.11- Scheme of the Newton-Raphson method showing the iterative process of the applied load step  $n+1$ . Image adapted from Fung & Tong (2001) with permission of World Scientific.

In this thesis, the mechanical properties of human vertebrae will be studied using FE models from two different dimensional scales namely: microFE models and homogenised FE (hFE) models. In particular, microFE models are generated based on high-resolution images, which allow a good reconstruction of the heterogeneous microstructure of specimen-specific bone tissues. Conversely, in hFE models bone microstructures cannot be resolved as low resolution scans are used for reconstruction of the specimen-specific bone samples which are modelled assuming a continuum between bone and marrow tissues. Below, further detail is provided about these different FE modelling approaches.

### 1.5.1. MicroFE models

*Ex vivo* microFE models have been used to improve our understanding of the mechanical behaviour of bone as a function of its microstructure. It has been demonstrated that bone microstructure and density, explain 60-85% of the changes in bone stiffness and strength (Cole & Van Der Meulen, 2011; Fields et al., 2009). MicroFE models are generated from high-resolution images (e.g. HR-pQCT or microCT) to define the geometry, including the detailed bone microstructure (Fig 1.12). Generally, these models are generated through the segmentation (i.e. binarization) of the “bone voxels” of the 3D images, which are then directly converted into linear 8-noded hexahedral elements (i.e. Cartesian voxel-based mesh) (van Rietbergen et al., 1995; Fields et al., 2009; Eswaran et al., 2006; Homminga et al., 2004). For organ level bones (e.g. human vertebrae), this approach can result in models having several millions of DOF (typically around 100million). Therefore, it is necessary to use specialized FE solvers and high-performance parallel computing. Due to such computational demands these models are often restricted to run within the linear elastic regime. Recent approaches that use nonlinear analysis to model bone plasticity and damage, have been applied to models generated from small portions of trabecular bone tissues (Levrero-Florencio & Pankaj, 2018; Hambli, 2013; Bevill & Tony M Keaveny, 2009; Verhulp et al., 2008). However, the computational demand is still a limiting factor when these nonlinear approaches are applied to whole bones, such as vertebrae. In addition to the linear elasticity, the gold standard of microFE modelling assumes the bone tissue to be isotropic and homogeneous (Pahr et al., 2011; Wolfram et al., 2010a; Ladd et al., 1998), with the Poisson’s ratio typically equal to 0.3 and the elastic tissue modulus (Young’s modulus) with different values calculated from micro-indentation measurements (Wolfram et al., 2010a; Chevalier et al., 2007) or back-calculation procedures (Pahr et al., 2011; Niebur et al., 2000; Ladd et al., 1998; van Rietbergen et al., 1995). The heterogeneity in the tissue seems to have a minor effect on the predictions of structural properties with the microFE models for samples of trabecular bone scanned with a resolution of 10  $\mu\text{m}$  (Gross et al., 2012) or for vertebral body specimens scanned at 82  $\mu\text{m}$  (Pahr et al., 2011). The assumption of isotropy and homogeneity has been supported by good agreement between the outputs of the models and experimental results for trabecular bone specimens (Chen, Dall’Ara, et al., 2017; Schwiedrzik et al., 2016; Wolfram et al., 2010a).

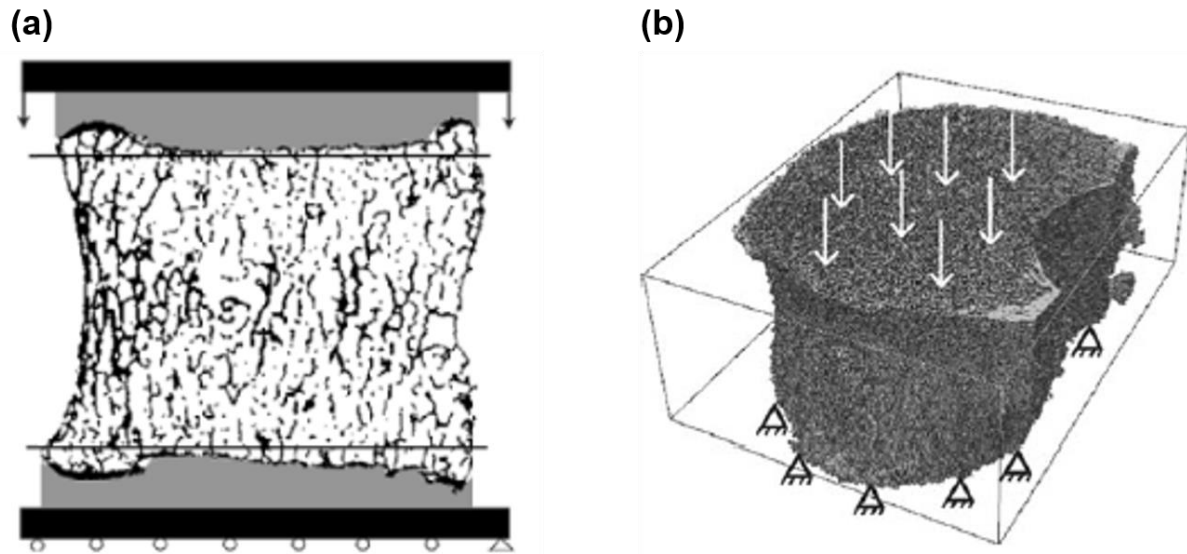


Figure 1.12- High-resolution FE models of human vertebrae simulating axial compression applied through displacement-based boundary conditions (a) mid axial section of the FE model generated from microCT images reconstructed to isotropic voxels of 60  $\mu\text{m}$ . Boundary conditions applied over the flat surfaces of the layers of embedding material added to the endplates (Eswaran et al., 2006). (b) MicroFE model generated from HR-pQCT images with 82  $\mu\text{m}$  of isotropic voxel size. Boundary conditions applied to flat sections of the vertebral body (Dall'Ara et al., 2012).

The accuracy of microFE models is highly dependent on the imaging and the segmentation procedure used to reconstruct bone tissues (Bevill & Tony M Keaveny, 2009; Chevalier et al., 2007). Back-calculation procedures are often applied to fit experimental and computational data by tuning the elastic tissue properties of the bone tissues (Pahr et al., 2011; Hou et al., 1998; Ladd et al., 1998; van Rietbergen et al., 1995). Due to its dependence on the specific set of specimens, images, and models the back-calculation of the elastic tissue properties of the microFE models has a reduced applicability and generalization.

So far microFE models of the human vertebrae are only appropriate to use for research purposes as the clinical CT does not reach the required resolution to resolve the bone microstructure.

## 1.5.2. Homogenised FE (hFE) models

For central sites of the human skeleton (e.g. spine or femur) QCT-based hFE models can be used for clinical applications. In this approach, bones are modelled as continuum structures with heterogeneous material properties assigned in function of the local BMD values obtained from calibrated QCT images (Fig 1.13- (a)) (Jenni M. Buckley et al., 2007; Crawford, Cann, et al., 2003; Kopperdahl et al., 2002). Homogenised FE models are generated based on the segmentation of 3D bone geometries acquired from QCT images or HR-pQCT images, followed by meshing and mapping of heterogeneous material properties. Typically, hFE models are discretized either using a voxel-based Cartesian mesh (Keaveny et al., 2014; Kopperdahl et al., 2014; Dall'Ara et al., 2012; Jenni M. Buckley et al., 2007; Crawford, Cann, et al., 2003) or a smooth mesh (Pahr et al., 2011, 2014; Imai et al., 2006)(Fig 1.13). Cartesian meshes, composed by 8-nodes hexahedral elements cannot, as opposed to smooth meshes, made of 10-nodes tetrahedron elements, provide a reliable representation of the curved surface geometries of bones, present for instance in the vertebrae (Fig 1.13- (a) against (b)). Despite the increase in the pre-processing time required to generate hFE with smooth meshes, which after segmentation require an additional step of surface reconstruction, these models are known to contain less partial volume errors and provide a better recovery of bone surfaces, which result in more reliable results when compared to Cartesian based hFE (Ulrich et al., 1998; Viceconti et al., 1998).

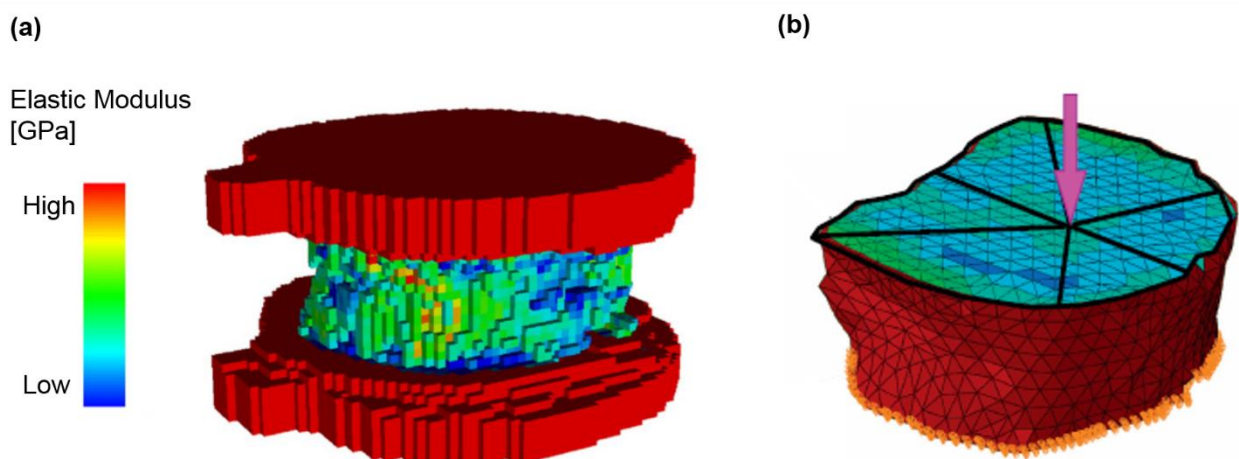


Figure 1.13 –Homogenised FE models of human vertebrae discretized based on voxel meshes (Jenni M. Buckley et al., 2007) (a) and smooth tetrahedral meshes (Pahr et al., 2014) (b). Colour map represents the distribution of elastic modulus obtained from the calibration of QCT images.

Due to the low image resolution, QCT-based hFE models, are not able to resolve the heterogeneity in structure and density of both the trabecular bone and the thin cortical shell observed in human vertebrae. However, some hFE models account for the difference in density between cortical and trabecular bone present in the human vertebrae through the generation of a layer of constant thickness representing the cortical shell at the boundary of the low density trabecular centrum (Fig 1.13- (b)) (Pahr et al., 2011; Imai et al., 2006). As information about the orientation of trabeculae cannot be obtained from QCT images, commonly isotropic (Imai et al., 2006) or constant geometry-dependent transverse isotropic models (assuming higher mechanical properties along the cranial to caudal direction compared to the transverse ones) are used to define the material properties of QCT-based hFE models (Wang et al., 2012; Pahr et al., 2011; Dall'Ara et al., 2010; Chevalier et al., 2008; Jenni M. Buckley et al., 2007; Crawford, Cann, et al., 2003). Recently, different methods have been developed to include information about bone anisotropy into hFE models (Taghizadeh et al., 2016; Larsson et al., 2014) but their potential has not been explored for the vertebrae yet. The relatively low number of DOF (typically between  $10^5$  and  $10^6$ ) in QCT-based hFE models, make them ideal for the study of the post-yield mechanical properties of bone.

### **1.5.3. FE models validation**

When a physical problem is analysed using the FE method, it involves approximations in geometry and in solution. Verification and validation processes are fundamental steps to test the accuracy and reliability of the FE models predictions (Anderson et al., 2007). The error of the approximated solution obtained from the FE model can be estimated through verification processes. The verification process often relates to discretization errors which are evaluated through mesh refinement methods that aim to evaluate the convergence of the FE solutions to an acceptable value (i.e. which error falls below a specified value). In the validation processes the FE models predictions are compared to experimental measurements obtained under similar conditions. Monotonic mechanical testing is the most used method to validate the predictions of structural (i.e. stiffness and failure load) properties computed from numerical models of vertebral bodies (Dall'Ara et al., 2010; Fields et al., 2009) (Fig 1.14) (revision of the method in Chapter II section 2.2).

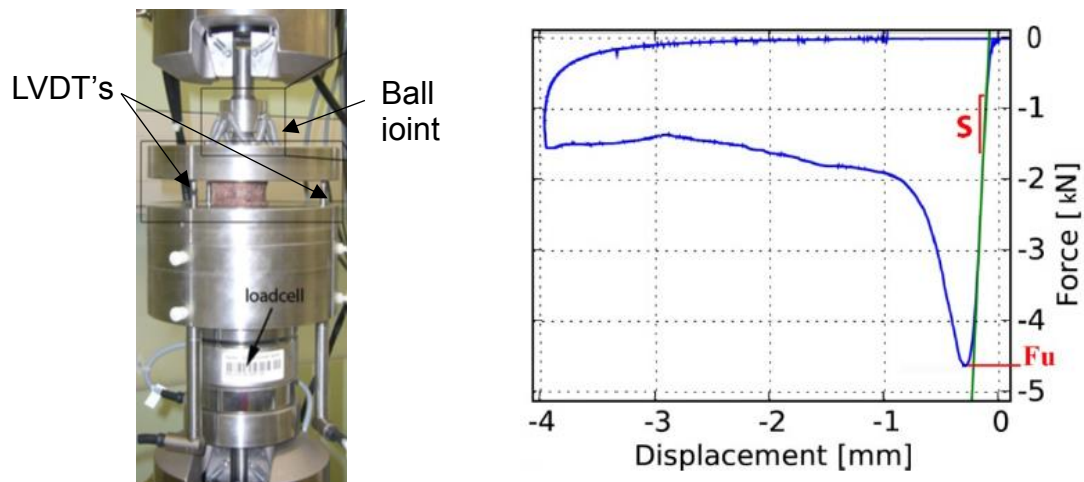


Figure 1.14- Monotonic mechanical testing of a human vertebral body under a combined loading of compression and anterior bending (left), and typical force-displacement curve ( $S$ : stiffness and  $F_u$ : ultimate force) (right) (from Dall'Ara et al., 2010).

Nevertheless, in order to better understand the failure behaviour of bones it is also important to understand the accuracy of the local predictions of the FE models (e.g. local displacements and strains). Recently, time-lapsed experiments (also called *in situ* experiments as they are performed inside a scanning machine) that combine both stepwise loading and high resolution imaging techniques, have been developed and applied to obtain more information about bone yield and failure behaviour (Fig 1.15). Combined with Digital Volume Correlation (DVC) algorithms, such *in situ* experiments can be used to validate a 3D-field of displacements and strains obtained at the tissue level from microFE models of bones (Chen, Dall'Ara, et al., 2017; Hosseini et al., 2014; Hussein et al., 2012). The DVC is an extension of an optical technique called Digital Image Correlation (DIC), which has been used to compute 2D-fields of displacements and strains at the surface of bone samples. The DIC method has also been used to validate the predictions of FE models for human vertebral bodies (Gustafson et al., 2017) and to measure the strain distribution within porcine spinal units that include full vertebrae, intervertebral discs and ligaments (Ruspi et al., 2017). Nevertheless, the DIC measurements can only be obtained at the surface of the bone, thus limiting the 3D validation of the FE models. Therefore, part of this thesis will aim to validate the 3D field of local displacements and strains of microFE models. More detailed information about the DVC method is reported below.

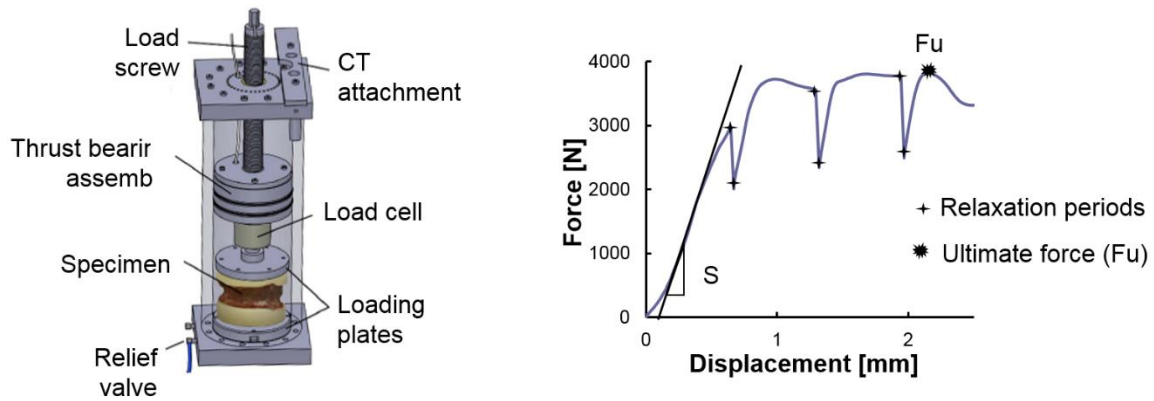


Figure 1.15- In situ jig used for time-lapsed experiment performed on human vertebra (on the left) (Hosseini et al., 2014), and typical force-displacement curve obtained from in situ experiments.

### Digital Volume Correlation (DVC)

The DVC approach is based on the analyses of high-resolution images obtained from a bone sample in its undeformed and deformed conditions during an *in situ* experiment (Roberts et al., 2014). The DVC combines a deformable image registration method, which calculates a 3D field of displacements, and a differentiation algorithm to calculate the local strains. By providing volumetric measurements obtained at the tissue level of bone samples, this technique is the gold standard for validation of microFE models predictions of local properties (Oliviero et al., 2018; Chen, Dall'Ara, et al., 2017; Costa et al., 2017; Zauel et al., 2006).

The DVC method aims to find the best transformation function to convert the image of the undeformed specimen into that acquired in its deformed configuration (Roberts et al., 2014). In this process a number of different strategies using a local (Gillard et al., 2014) or global (Dall'Ara et al., 2014) approach can be adopted. In this thesis a global DVC approach will be used because it was found more accurate and precise than the local approaches in measuring the full-field of local displacements in similar applications (Palanca et al., 2015, 2016; Dall'Ara et al., 2014). The global DVC mapping method superimposes a homogeneous cubic grid, with a specific subvolume size, Nodal Spacing (NS), to both undeformed and deformed images (Fig 1.16) (Palanca et al., 2015). Then, the software computes the displacements at the nodes of the DVC grid by mapping each point of the undeformed image into the points of the deformed image, using trilinear functions to interpolate the displacements between the nodes (Palanca et al., 2015). The approach consists in finding the displacement functions  $u(x, y, z)$ ,  $v(x, y, z)$

and  $w(x, y, z)$  that better correlate the grey levels in the undeformed image  $f(x, y, z)$  with the subsets of the deformed image  $m(x', y', z')$  (Fig 1.16) (Palanca et al., 2015; Roberts et al., 2014), such that:

$$m(x + u, y + v, z + w) = f(x, y, z) \quad [\text{Eq 1.15}]$$

The DVC approach used in this study accounts for potential changes in the grey levels of the two images by including an intensity displacement function  $h(x, y, z)$  such that the final form of the registering equation can be written as  $m(x + u, y + v, z + w, s + h) = f(x, y, z, s)$  (Fig 1.16) (Palanca et al., 2015). Mutual information metric is used to compare the two images during the optimization algorithm. Estimations of local strains can also be obtained through the differentiation of the displacement field using an external FE software package (Fig 1.16).

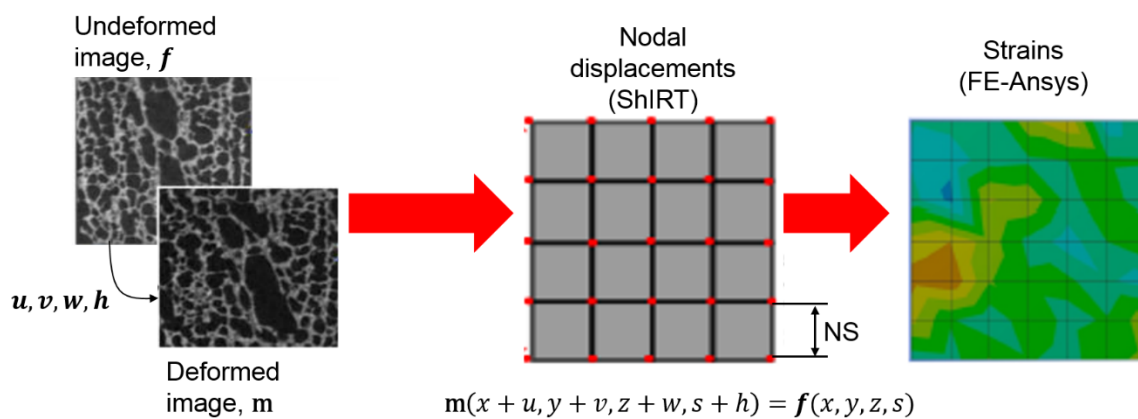


Figure 1.16- Overview over the global DVC method ShIRT-FE used to map the subvolumes of an undeformed image to the deformed image. The subvolumes of the undeformed image  $f(x, y, z)$  are mapped to the deformed image  $m(x', y', z')$  by finding the deformation  $(u, v, w)$  that better correlate the images based on the recognition of structural features. To account for changes in the grey-levels, the algorithm includes an extra intensity displacement function  $h(x, y, z)$ . The displacements are computed at the nodes of each subvolume (spatial distance between nodes is specified as the Nodal Spacing,  $NS$ ) assuming continuity among subvolumes (neighboring dependent), and tri-linear interpolation to find the displacements between nodes. The strains are computed through differentiation of the displacement field using the FE solver of Ansys. Image adapted from Palanca et al. (2015) and Madi et al. (2013).

Reports of the accuracy and precision of this method agree on the importance of the  $NS$ , which refers to the spatial resolution of the displacement field provided by the DVC method (Dall'Ara et al., 2017). The errors associated with the DVC methods are usually assessed with

“zero-strain studies”. These tests are based on the registration of repeated scans for which the strain should be zero in all locations. The DVC method shows to be accurate in measuring displacements (i.e. errors in the order of a fraction of voxel size) even for small NS, using ShIRT-FE errors of  $0.0013 \mu\text{m}$  for  $\text{NS}=5$  voxels corresponding to  $50 \mu\text{m}$  (Palanca et al., 2015). It has been shown that such errors are mainly due to “imaging inaccuracies” (e.g. noise) that depend on the scanning hardware and protocol (Palanca et al., 2015; Dall’Ara et al., 2014; Hussein et al., 2012; Liu & Morgan, 2007). Nevertheless, strain errors can be much higher due to the differentiation step. Accuracy and precision uncertainties of the DVC method for estimations of strains decrease with increases in NS (spatial resolution in displacement measurements) following a power law (Palanca et al., 2015; Dall’Ara et al., 2014). Errors can be below a few hundred microstrain for a reasonably large NS. Using the ShIRT-FE algorithm, errors of  $534 \mu\epsilon$  have been found for sub-volumes of trabecular bone specimens (i.e. NS) of 45 voxels, the equivalent to  $448 \mu\text{m}$  (Palanca et al., 2015). Moreover, the choice of the NS that provides the best performance of the method, depends on the morphology and density of the bone structure under analysis (Dall’Ara et al., 2017).

## 1.6. References

- Adams, M. A., Bogduk, N., Burton, K. & Dolan, P. (2002). *The Biomechanics of Back Pain*. Churchill Livingstone.
- Alexander, B. G., Anderson, D. E., Agostino, J. D. & Bouxsein, M. L. (2012). The Effect of Thoracic Kyphosis and Sagittal Plane Alignment on Vertebral Compressive Loading. *Journal of Bone and Mineral Research*, 27(10), 2144–2151.
- Alexander, B. G., Burkhart, A. K., Allaire, A. B., Anderson, D. E. & Bouxsein, M. L. (2017). Spinal Loading Patterns From Biomechanical Modeling Explain the High Incidence of Vertebral Fractures in the Thoracolumbar Region. *Journal of Bone and Mineral Research*, 32(6), 1–9.
- Anderson, A. E., Ellis, B. J., Weiss, J. A. (2007). Verification , Validation and Sensitivity Studies in Computational Biomechanics. *Computer Methods in Biomechanics and Biomedical Engineering*, 10(3), 171–184.
- Asano, S., Kaneda, K., Umehara, S. & Tadano, S. (1992). The Mechanical Properties of the Human L4-5 Functional Spinal Unit during Cyclic Loading: The Structural Effects of the Posterior Elements. *Spine*, 17(11), 1343–1352.
- Baguley, R. & Hose, D. R. (1994). *How to Plan a Finite Element Analysis*. Hamilton, Scotland: NAFEMS.
- Bayraktar, H. H., Morgan, E. F., Niebur, G. L., Morris, G. E., Wong, E. K. & Keaveny, T. M. (2004). Comparison of the Elastic and Yield Properties of Human Femoral Trabecular and Cortical Bone Tissue. *Journal of Biomechanics*, 37, 27–35.
- Benca, E., Patsch, J. M., Mayr, W., Pahr, D. H. & Windhager, R. (2016). The Insufficiencies of Risk Analysis of Impending Pathological Fractures in Patients with Femoral Metastases: A Literature Review. *Bone Reports*, 5, 51–56.
- Bergmark, A. (1989). Stability of the Lumbar Spine: A Study in Mechanical Engineering. *Acta Orthopaedica*, 60(S230), 1–54.
- Bevill, G. & Keaveny, T. M. (2009). Trabecular Bone Strength Predictions Using Finite Element Analysis of Micro-Scale Images at Limited Spatial Resolution. *Bone*, 44, 579–84.
- Boresi, A. P. & Schmidt, R. J. (2003). *Advanced Mechanics of Materials*. John Wiley & Sons, Inc.
- Bouxsein, M. L., Boyd, S. K., Christiansen, B. a., Guldborg, R. E., Jepsen, K. J. & Müller, R. (2010). Guidelines for Assessment of Bone Microstructure in Rodents Using Micro-Computed Tomography. *Journal of Bone and Mineral Research*, 25(7), 1468–1486.
- Brinckmann, P., Biggemann, M. & Hilweg, D. (1989). Prediction of the Compressive Strength of Human Lumbar Vertebrae. *Spine*, 14(6), 606–610.
- Buckley, J. M., Loo, K. & Motherway, J. (2007). Comparison of Quantitative Computed Tomography-Based Measures in Predicting Vertebral Compressive Strength. *Bone*, 40(3), 767–774.
- Chen, Y., Dall’Ara, E., Sales, E., Manda, K., Wallace, R. & Viceconti, M. (2017). Micro-CT Based Finite Element Models of Cancellous Bone Predict Accurately Displacement Once the Boundary Condition Is Well Relicated: A Validation Study. *Journal of the Mechanical Behavior of Biomedical Materials*, 65, 644–651.
- Chevalier, Y., Charlebois, M., Pahra, D., Varga, P., Heini, P., Schneider, E., et al. (2008). A Patient-Specific Finite Element Methodology to Predict Damage Accumulation in

- Vertebral Bodies under Axial Compression, Sagittal Flexion and Combined Loads. *Computer Methods in Biomechanics and Biomedical Engineering*, 11(5), 477–487.
- Chevalier, Y., Pahr, D., Allmer, H., Charlebois, M. & Zysset, P. (2007). Validation of a Voxel-Based FE Method for Prediction of the Uniaxial Apparent Modulus of Human Trabecular Bone Using Macroscopic Mechanical Tests and Nanoindentation. *Journal of Biomechanics*, 40, 3333–3340.
- Cierniak, R. (2011). Technical Concepts of X-Ray Computed Tomography Scanners, in: *X-ray Computed Tomography in Biomedical Engineering*, (pp. 21–33). Springer Science and Business Media.
- Cole, J. H. & Van Der Meulen, M. C. H. (2011). Whole Bone Mechanics and Bone Quality. *Clinical Orthopaedics and Related Research*, 469(8), 2139–2149.
- Costa, M. C., Tozzi, G., Cristofolini, L., Danesi, V., Viceconti, M. & Dall'Ara, E. (2017). Micro Finite Element Models of the Vertebral Body: Validation of Local Displacement Predictions. *PLoS ONE*, 12(7), 1–18.
- Cowin, S. C. (2001). *Bone Mechanics Handbook* (Stephen C. Cowin, Ed.). McGraw-Hill.
- Crawford, R. P., Cann, C. E. & Keaveny, T. M. (2003). Finite Element Models Predict in Vitro Vertebral Body Compressive Strength Better than Quantitative Computed Tomography. *Bone*, 33, 744–750.
- Currey, J. D. (2002). *Bones: Structure and Mechanics*. Princeton: Princeton University Press.
- Dall'Ara, E., Barber, D. & Viceconti, M. (2014). About the Inevitable Compromise between Spatial Resolution and Accuracy of Strain Measurement for Bone Tissue: A 3D Zero-Strain Study. *Journal of Biomechanics*, 47, 2956–2963.
- Dall'Ara, E., Pahr, D., Varga, P., Kainberger, F. & Zysset, P. (2012). QCT-Based Finite Element Models Predict Human Vertebral Strength in Vitro Significantly Better than Simulated DEXA. *Osteoporosis International*, 23, 563–572.
- Dall'Ara, E., Peña-Fernández, M., Palanca, M., Giorgi, M., Cristofolini, L. & Tozzi, G. (2017). Precision of Digital Volume Correlation Approaches for Strain Analysis in Bone Imaged with Micro-Computed Tomography at Different Dimensional Levels. *Frontiers in Materials*, 4, 1-13.
- Dall'Ara, E., Schmidt, R., Pahr, D., Varga, P., Chevalier, Y., Patsch, J., et al. (2010). A Nonlinear Finite Element Model Validation Study Based on a Novel Experimental Technique for Inducing Anterior Wedge-Shape Fractures in Human Vertebral Bodies in Vitro. *Journal of Biomechanics*, 43, 2374–2380.
- Ebbesen, E. N., Thomsen, J. S., Beck-nielsen, H., Nepper-rasmussen, H. J. & Mosekilde, L. I. S. (1999). Age- and Gender-Related Differences in Vertebral Bone Mass, Density, and Strength. *Journal of Bone and Mineral Research*, 14(8), 1394–1403.
- Ebihara, H., Ito, M., Abumi, K., Taneichi, H., Kotani, Y., Minami, A., et al. (2004). A Biomechanical Analysis of Metastatic Vertebral Collapse of the Thoracic Spine: A Sheep Model Study. *Spine*, 29(9), 994–999.
- Engelke, K., Likanati, C., Fuerst, T., Zysset, P. & Genant, H. K. (2013). Advanced CT Based In Vivo Methods for the Assessment of Bone Density, Structure, and Strength. *Current Osteoporosis Reports*, 11, 246–255.
- Eswaran, S., Gupta, A., Adams, M. & Keaveny, T. (2006). Cortical and Trabecular Load Sharing in the Human Vertebral Body. *Journal of Bone and Mineral Research*, 21, 307–314.
- Fields, A. J., Eswaran, S. K., Jekir, M. G. & Keaveny, T. M. (2009a). Role of Trabecular Microarchitecture in Whole-Vertebral Body Biomechanical Behavior. *Journal of Bone*

- and *Mineral Research*, 24(9), 1523–1530.
- Fields, A. J., Eswaran, S. K., Jekir, M. G. & Keaveny, T. M. (2009b). Role of Trabecular Microarchitecture in Whole-Vertebral Body Biomechanical Behavior. *Journal of Bone and Mineral Research*, 24(9), 1523–1530.
- Fisher, C. G., DiPaola, C. P., Ryken, T. C., Bilsky, M. H., Shaffrey, C. I., Berven, S. H., et al. (2010). A Novel Classification System for Spinal Instability in Neoplastic Disease. An Evidence-Based Approach and Expert Consensus from the Spine Oncology Study Group. *Spine*, 35(22), E1221–E1229.
- Fisher, C. G., Schouten, R., Versteeg, A. L., Boriani, S., Varga, P. P., Rhines, L. D., et al. (2014). Reliability of the Spinal Instability Neoplastic Score ( SINS ) among Radiation Oncologists : An Assessment of Instability Secondary to Spinal Metastases. *Radiation Oncology*, 9(1), 1–7.
- Fourney, D. R., Frangou, E. M., Ryken, T. C., Dipaola, C. P., Shaffrey, C. I., Berven, S. H., et al. (2011). Spinal Instability Neoplastic Score : An Analysis of Reliability and Validity From the Spine Oncology Study Group. *Journal of Clinical Oncology*, 29(22), 3072–3077.
- Fung, Y. C. & Tong, P. (2001). *Classical and Computational Solid Mechanics. Advances Series in Engineering Science - Volume 1*. World Scientific Publishing Co. Pte. Ltd.
- Genant, H., Jergas, M., Palermo, L., Nevitt, M., Valentin, R., Black, D., et al. (1996). Comparison of Semiquantitative Visual and Quantitative Morphometric Assessment of Prevalent and Incident Vertebral Fractures in Osteoporosis The Study of Osteoporotic Fractures Research Group. *Journal of Bone and Mineral Research*, 11(7), 984–96.
- Genant, H. K. & Jergas, M. (2003). Assessment of Prevalent and Incident Vertebral Fractures in Osteoporosis Research. *Osteoporosis International*, 14(3), S43–S55.
- Gillard, F., Boardman, R., Mavrogordato, M., Hollis, D., Sinclair, I., Pierron, F., et al. (2014). The Application of Digital Volume Correlation (DVC) to Study the Microstructural Behaviour of Trabecular Bone during Compression. *Journal of the Mechanical Behavior of Biomedical Materials*, 29, 480–499.
- Goldman, L. W. (2007). Principles of CT and CT Technology. *Journal of Nuclear Medicine Technology*, 35(3), 115–128.
- Gray, H. & Lewis, H. (1918). *Anatomy of the Human Body (Gray's Anatomy)*. Lea & Febiger.
- Griffith, J. F. & Genant, H. K. (2008). Bone Mass and Architecture Determination: State of the Art. *Best Practice & Research Clinical Endocrinology & Metabolism*, 22(5), 737–64.
- Gross, T., Pahr, D. H., Peyrin, F., Zysset, P. K., Gross, T., Pahr, D. H., et al. (2012). Mineral Heterogeneity Has a Minor Influence on the Apparent Elastic Properties of Human Cancellous Bone : A SR MCT-Based Finite Element Study. *Computer Methos in Biomechanics and Biomedical Engineering*, 15, 1137–1144.
- Gustafson, H. M., Cripton, P. A., Ferguson, S. J. & Helgason, B. (2017). Comparison of Specimen-Specific Vertebral Body Finite Element Models with Experimental Digital Image Correlation Measurements. *Journal of the Mechanical Behavior of Biomedical Materials*, 65, 801–807.
- Hambli, R. (2013). Micro-CT Finite Element Model and Experimental Validation of Trabecular Bone Damage and Fracture. *Bone*, 56, 363–374.
- Han, K., Rohlmann, A., Zander, T. & Taylor, W. R. (2013). Lumbar Spinal Loads Vary with Body Height and Weight. *Medical Engineering and Physics*, 35(7), 969–977.
- Han, K., Zander, T., Taylor, W. R. & Rohlmann, A. (2012). An Enhanced and Validated Generic Thoraco-Lumbar Spine Model for Prediction of Muscle Forces. *Medical*

- Engineering & Physics*, 34, 709–716.
- Hardisty, M. R., Akens, M. K., Hojjat, S. P., Yee, A. & Whyne, C. M. (2012). Quantification of the Effect of Osteolytic Metastases on Bone Strain within Whole Vertebrae Using Image Registration. *Journal of Orthopaedic Research*, 30, 1032–1039.
- Homminga, J., Van-Rietbergen, B., Lochmüller, E. M., Weinans, H., Eckstein, F. & Huiskes, R. (2004). The Osteoporotic Vertebral Structure Is Well Adapted to the Loads of Daily Life, but Not to Infrequent “Error” Loads. *Bone*, 34, 510–516.
- Hosseini, H. S., Clouthier, A. L. & Zysset, P. K. (2014). Experimental Validation of Finite Element Analysis of Human Vertebral Collapse under Large Compressive Strains. *Journal of Biomechanical Engineering*, 136, 1–10.
- Hou, F. J., Lang, S. M., Hoshaw, S. J., Reimann, D. a. & Fyhrie, D. P. (1998). Human Vertebral Body Apparent and Hard Tissue Stiffness. *Journal of Biomechanics*, 31, 1009–1015.
- Hussein, A., Barbone, P. E. & Morgan, E. F. (2012). Digital Volume Correlation for Study of the Mechanism of Whole Bones. *Procedia IUTAM*, 4, 116–125.
- Hussein, A. I., Louzeiro, D. T. & Morgan, E. F. (2018). Differences in Trabecular Microarchitecture and Simplified Boundary Conditions Limit the Accuracy of Quantitative Computed Tomography-Based Finite Element Models of Vertebral Failure. *Journal of Biomechanical Engineering*, 140, 1–11.
- Imai, K., Ohnishi, I. & Bessho, M. (2006). Nonlinear Finite Element Model Predicts Vertebral Bone Strength and Fracture Site. *Spine*, 31(16), 1789–1794.
- Jackman, T. M., Hussein, A. I., Curtiss, C., Fein, P. M., Camp, A., De, L., et al. (2015). Quantitative, 3-D Visualization of the Initiation and Progression of Vertebral Fractures under Compression and Anterior Flexion. *Journal of Bone and Mineral Research*, 1–37.
- Keaveny, T. M., Mcclung, M. R., Genant, H. K., Zanchetta, J. R., Kendler, D., Brown, J. P., et al. (2014). Femoral and Vertebral Strength Improvements in Postmenopausal Women With Osteoporosis Treated With Denosumab. *Journal of Bone and Mineral Research*, 29(1), 158–165.
- Kopperdahl, D. L., Aspelund, T., Hoffmann, P. F., Sigurdsson, S., Siggeirsdottir, K., Harris, T. B., et al. (2014). Assessment of Incident Spine and Hip Fractures in Women and Men Using Finite Element Analysis of CT Scans. *Journal of Bone and Mine*, 29(3), 570–580.
- Kopperdahl, D. L., Morgan, E. F. & Keaveny, T. M. (2002). Quantitative Computed Tomography Estimates of the Mechanical Properties of Human Vertebral Trabecular Bone. *Journal of Orthopaedic Research*, 20, 801–805.
- Kristic, R. (1991). *Human Microscopic Anatomy. An Atlas for Students of Medicine and Biology*. Heidelberg, Berlin: Springer.
- Ladd, A. J. C., Kinney, J. H., Haupt, D. L. & Goldstein, S. A. (1998). Finite-Element Modeling of Trabecular Bone : Comparison with Mechanical Testing and Determination of Tissue Modulus. *Journal of Orthopaedic Research*, 16, 622–628.
- Larsson, D., Luisier, B., Kersh, M. E., Dall’Ara, E., Zysset, P. K., Pandy, M. G., et al. (2014). Assessment of Transverse Isotropy in Clinical-Level CT Images of Trabecular Bone Using the Gradient Structure Tensor. *Annals of Biomedical Engineering*, 42(5), 950–959.
- Lenherr, C., Voumard, B., Stadelmann, M., Buck, F., Haschtmann, D., Hoppe, S., et al. (2018). *Indentation Properties of Metastatic Vertebral Trabecular Bone*. 8<sup>th</sup> World Congress of Biomechanics, Dublin, Ireland, 8-12<sup>th</sup> July 2018.
- Levrero-Florencio, F., Margetts, L., Sales, E., Xie, S., Manda, K. & Pankaj, P. (2016). Evaluating the Macroscopic Yield Behaviour of Trabecular Bone Using a Nonlinear Homogenisation Approach. *Journal of the Mechanical Behavior of Biomedical Materials*,

61, 384–396.

- Lavrero-Florencio, F. & Pankaj, P. (2018). Using Non-Linear Homogenization to Improve the Performance of Macroscopic Damage Models of Trabecular Bone. *Frontiers in Physiology*, 9, 1–15.
- Liu, L. & Morgan, E. F. (2007). Accuracy and Precision of Digital Volume Correlation in Quantifying Displacements and Strains in Trabecular Bone. *Journal of Biomechanics*, 40(15), 3516–3520.
- Maccauro, G., Spinelli, M. S., Mauro, S., Perisano, C., Graci, C. & Rosa, M. A. (2011). Physiopathology of Spine Metastasis. *International Journal of Surgical Oncology*, 2011, 1–8.
- Madi, K., Tozzi, G., Zhang, Q. H., Tong, J., Cossey, A., Au, A., et al. (2013). Computation of Full-Field Displacements in a Scaffold Implant Using Digital Volume Correlation and Finite Element Analysis. *Medical Engineering and Physics*, 35(9), 1298–1312.
- Manda, K., Wallace, R. J., Xie, S. & Pankaj, F. L. P. (2016). Nonlinear Viscoelastic Characterization of Bovine Trabecular Bone. *Biomechanics and Modeling in Mechanobiology*, 16, 173–189.
- Manda, K., Xie, S., Wallace, R. J., Lavrero-Florencio, F. & Pankaj, P. (2016). Linear Viscoelasticity - Bone Volume Fraction Relationships of Bovine Trabecular Bone. *Biomechanics and Modeling in Mechanobiology*, 15(6), 1631–1640.
- Miller, J. A. & Schultz, A. B. (1988). Biomechanics of the Human Spine and Trunk. *Exercise and Sport Sciences Reviews*, 16, 169–204.
- Mirzaali, M. J., Schwiedrzik, J. J., Thaiwichai, S., Best, J. P., Michler, J., Zysset, P. K., et al. (2016). Mechanical Properties of Cortical Bone and Their Relationships with Age, Gender, Composition and Microindentation Properties in the Elderly. *Bone*, 93, 196–211.
- Morgan, E. F., Bayraktar, H. H. & Keaveny, T. M. (2003). Trabecular Bone Modulus-Density Relationships Depend on Anatomic Site. *Journal of Biomechanics*, 36(7), 897–904.
- Morgan, E. F. & Keaveny, T. M. (2001). Dependence of Yield Strain of Human Trabecular Bone on Anatomic Site. *Journal of Biomechanics*, 34(5), 569–577.
- Müller, R., Van Campenhout, H., Van Damme, B., Van Der Perre, G., Dequeker, J., Hildebrand, T., et al. (1998). Morphometric Analysis of Human Bone Biopsies: A Quantitative Structural Comparison of Histological Sections and Micro-Computed Tomography. *Bone*, 23(1), 59–66.
- Mundy, G. R. (2002). Metastasis to Bone: Causes, Consequences and Therapeutic Opportunities. *Nature Reviews Cancer*, 2(8), 584–593.
- Nazarian, A., Stauber, M., Zurakowski, D., Snyder, B. D. & Müller, R. (2006). The Interaction of Microstructure and Volume Fraction in Predicting Failure in Cancellous Bone. *Bone*, 39(6), 1196–202.
- Nazarian, A., Von Stechow, D., Zurakowski, D., Müller, R. & Snyder, B. D. (2008). Bone Volume Fraction Explains the Variation in Strength and Stiffness of Cancellous Bone Affected by Metastatic Cancer and Osteoporosis. *Calcified Tissue International*, 83, 368–379.
- Niebur, G. L., Feldstein, M. J., Yuen, J. C., Chen, T. J. & Keaveny, T. M. (2000). High-Resolution Finite Element Models with Tissue Strength Asymmetry Accurately Predict Failure of Trabecular Bone. *Journal of Biomechanics*, 33, 1575–1583.
- Nishiyama, K., Dall’Ara, E. & Engelke, K. (2019). Advanced Techniques of Bone Mass Measurements and Strength in Adults, in: Bilezikian, J. P. (Ed.), *Metabolic Bone Diseases and Disorders of Mineral Metabolism*, (pp. 260–271). John Wiley & Sons, Inc.

- Odgaard, a. (1997). Three-Dimensional Methods for Quantification of Cancellous Bone Architecture. *Bone*, 20(4), 315–328.
- Oliver, W. C. & Pharr, G. M. (2004). Measurement of Hardness and Elastic Modulus by Instrumented Indentation: Advances in Understanding and Refinements to Methodology. *Journal of Materials Research*, 19(01), 3–20.
- Oliviero, S., Giorgi, M. & Dall’Ara, E. (2018). Validation of Finite Element Models of the Mouse Tibia Using Digital Volume Correlation. *Journal of the Mechanical Behavior of Biomedical Materials*, 86, 172–184.
- Pahr, D. H., Dall’Ara, E., Varga, P. & Zysset, P. K. (2011). HR-PQCT-Based Homogenised Finite Element Models Provide Quantitative Predictions of Experimental Vertebral Body Stiffness and Strength with the Same Accuracy as MFE Models. *Computer Methods in Biomechanics and Biomedical Engineering*, 15, 711–20.
- Pahr, D. H., Schwiedrzik, J., Dall, E. & Zysset, P. K. (2014). Clinical versus Pre-Clinical FE Models for Vertebral Body Strength Predictions. *Journal of the Mechanical Behavior of Biomedical Materials*, 33, 76–83.
- Pahr, D. H. & Zysset, P. K. (2009). A Comparison of Enhanced Continuum FE with Micro FE Models of Human Vertebral Bodies. *Journal of Biomechanics*, 42(4), 455–462.
- Palanca, M., Cristofolini, L., Dall’Ara, E., Curto, M., Innocente, F., Danesi, V., et al. (2016). Digital Volume Correlation Can Be Used to Estimate Local Strains in Natural and Augmented Vertebrae: An Organ-Level Study. *Journal of Biomechanics*, 49, 3882–3890.
- Palanca, M., Tozzi, G., Cristofolini, L., Viceconti, M. & Dall’Ara, E. (2015). Three-Dimensional Local Measurements of Bone Strain and Displacement: Comparison of Three Digital Volume Correlation Approaches. *Journal of Biomechanical Engineering*, 137(7), 071006.
- Rho, J. Y., Tsui, T. Y. & Pharr, G. M. (1998). Elastic Properties of Osteon and Trabecular Bone Measured by Nanoindentation. *Journal of Biomechanics*, 31(20), 21.
- van Rietbergen, B., Weinans, H., Huiskes, R. & Odgaard, A. (1995). A New Method to Determine Trabecular Bone Elastic Properties and Loading Using Micromechanical Finite-Element Models. *Journal of Biomechanics*, 28, 69–81.
- Roberts, B. C., Perilli, E. & Reynolds, K. J. (2014). Application of the Digital Volume Correlation Technique for the Measurement of Displacement and Strain Fields in Bone: A Literature Review. *Journal of Biomechanics*, 47, 923–934.
- Rohlmann, A., Graichen, F., Kayser, R., Bender, A., Nat, R. & Bergmann, G. (2008). Loads on a Telemeterized Vertebral Body Replacement Measured in Two Patients. *Spine*, 33(11), 1170–1179.
- Roy, M. E., Rho, J., Tsui, T. Y., Evans, N. D., Pharr, G. M. & Al, R. O. Y. E. T. (1999). Mechanical and Morphological Variation of the Human Lumbar Vertebral Cortical and Trabecular Bone. *Journal of Biomedical Materials Research*, 44(2), 191–7.
- Ruspi, M. L., Palanca, M., Faldini, C. & Cristofolini, L. (2017). Full-Field in Vitro Investigation of Hard and Soft Tissue Strain in the Spine by Means of Digital Image Correlation. *Muscles, Ligaments and Tendons Journal*, 7(4), 538–545.
- Schileo, E., Dall’Ara, E., Taddei, F., Malandrino, A., Schotkamp, T., Æ, M. B., et al. (2008). An Accurate Estimation of Bone Density Improves the Accuracy of Subject-Specific Finite Element Models. *Journal of Biomechanics*, 41, 2483–2491.
- Schousboes, J. T., Vokes, T., Binkley, N. & Genant, H. K. (2011). *Vertebral Fracture Initiative Part III Densitometric Vertebral Fracture Assessment (VFA)*. International Osteoporosis Foundation.

- Schwiedrzik, J., Gross, T., Bina, M., Pretterklieber, M., Zysset, P. & Pahr, D. (2016). Experimental Validation of a Nonlinear• MicroFE Model Based on Cohesive-Frictional Plasticity for Trabecular Bone. *International Journal for Numerical Methods in Biomedical Engineering*, 32, e02739.
- Schwiedrzik, J. J. (2014). Experimental, Theoretical and Numerical Investigation of the Nonlinear Micromechanical Properties of Bone. *PhD Thesis*. University of Bern, Graduate School for Cellular and Biomedical Sciences.
- Stauber, M. & Muller, R. (2008). Micro-Computed Tomography: A Method for Non-Destructive Evaluation of the Three-Dimensional Structure of Biological Specimens. *Methods in Molecular Biology*, 455, 273–292.
- Sutcliffe, P., Connock, M., Shyangdan, D., Court, R., Kandala, N. B. & Clarke, A. (2013). A Systematic Review of Evidence on Malignant Spinal Metastases: Natural History and Technologies for Identifying Patients at High Risk of Vertebral Fracture and Spinal Cord Compression. *Health technology assessment (Winchester, England)*, 17, 1–274.
- Taghizadeh, E., Reyes, M., Zysset, P., Latypova, A., Terrier, A. & Büchler, P. (2016). Biomechanical Role of Bone Anisotropy Estimated on Clinical CT Scans by Image Registration. *Annals of Biomedical Engineering*, 44(8), 2505–2517.
- Tassani, S., Öhman, C., Baruffaldi, F., Baleani, M. & Viceconti, M. (2011). Volume to Density Relation in Adult Human Bone Tissue. *Journal of Biomechanics*, 44(1), 103–108.
- Ulrich, D., Van Rietbergen, B., Weinans, H. & Rüeegsegger, P. (1998). Finite Element Analysis of Trabecular Bone Structure: A Comparison of Image-Based Meshing Techniques. *Journal of Biomechanics*, 31(12), 1187–1192.
- Verhulp, E., Rietbergen, B. Van, Mu, R. & Huiskes, R. (2008). Indirect Determination of Trabecular Bone Effective Tissue Failure Properties Using Micro-Finite Element Simulations. *Journal of Biomechanics*, 41, 1479–1485.
- Versteeg, A. L., Verlaan, J. J., Sahgal, A., Mendel, E., Quraishi, N. A., Fourney, D. R., et al. (2016). The Spinal Instability Neoplastic Score: Impact on Oncologic Decision-Making. *Spine*, 41(20), S231–S237.
- Vialle, L. R., Gokaslan, Z. L., Fisher, C. G. & Boriani, S. (2015). *AOSpine Master Series. Volume 1. Metastatic S* (L. R. Vialle, Ed.). New York, NY: Thieme Medical Publishers, Inc.
- Viceconti, M., Bellingeri, L., Cristofolini, L. & Toni, A. (1998). A Comparative Study on Different Methods of Automatic Mesh Generation of Human Femurs. *Medical Engineering & Physics*, 20(1), 1–10.
- Wang, X., Sanyal, A., Cawthon, P. M., Palermo, L., Jekir, M., Christensen, J., et al. (2012). Prediction of New Clinical Vertebral Fractures in Elderly Men Using Finite Element Analysis of CT Scans. *Journal of Bone and Mineral Research*, 27(4), 808–816.
- Weiss, L. (1988). *Cell and Tissue Biology, A Textbook of Histology*. Baltimore: Urban and Schwarzenberg.
- Wolfram, U. & Schwiedrzik, J. (2016). Post-Yield and Failure Properties of Cortical Bone. *BoneKEy Reports*, 5, 1–10.
- Wolfram, U., Wilke, H. & Zysset, P. K. (2010a). Valid Micro Finite Element Models of Vertebral Trabecular Bone Can Be Obtained Using Tissue Properties Measured with Nanoindentation under Wet Conditions. *Journal of Biomechanics*, 43, 1731–1737.
- Wolfram, U., Wilke, H. & Zysset, P. K. (2010b). Rehydration of Vertebral Trabecular Bone : Influences on Its Anisotropy, Its Stiffness and the Indentation Work with a View to Age, Gender and Vertebral Level. *Bone*, 46, 348–354.

- Xie, S., Manda, K., Wallace, R. J., Levrero-Florencio, F., Simpson, A. H. R. W. & Pankaj, P. (2017). Time Dependent Behaviour of Trabecular Bone at Multiple Load Levels. *Annals of Biomedical Engineering*, 45(5), 1219–1226.
- Zauel, R., Yeni, Y. N., Bay, B. K., Dong, X. N. & Fyhrie, D. P. (2006). Comparison of the Linear Finite Element Prediction of Deformation and Strain of Human Cancellous Bone to 3D Digital Volume Correlation Measurements. *Journal of Biomechanical Engineering*, 128, 1–6.
- Zysset, P. (1994). A Constitutive Law for Trabecular Bone. *PhD Thesis*. Ecole Polytechnique Federale De Lausanne.
- Zysset, P. K. (2003). A Review of Morphology-Elasticity Relationships in Human Trabecular Bone: Theories and Experiments. *Journal of Biomechanics*, 36(10), 1469–1485.
- Zysset, P. K. (2009). Indentation of Bone Tissue : A Short Review. *Osteoporosis International*, 20, 1049–1055.
- Zysset, P. K., Dall'Ara, E., Varga, P. & Pahr, D. H. (2013). Finite Element Analysis for Prediction of Bone Strength. *BoneKEy Reports*, 2, 1–9.

## Chapter II. Motivation and Literature review

### 2.1. Motivation

The general motivation of the present thesis is to better understand the effect of lytic metastatic lesion on the mechanical properties of vertebrae through the use of specimen-specific Finite Element (FE) models aiming at a better assessment of vertebral stability.

Lytic lesions are one of the most severe types of metastatic bone lesions and affect the spine of cancer patients in up to 70% of the cases (details in Chapter I section 1.2.1). These lesions are described as focal regions with low bone mineral density which can cause pain, neurological injuries, and mechanical instability, as bone becomes more fragile and susceptible to fracture. Such complications decrease the quality of life of patients with already severely reduced life expectancy. Therefore, the correct assessment of spinal instability, and related fracture risk, is fundamental to guide the clinical decision making to avoid further skeletal complications.

The assessment of spinal instability and consequent risk of fracture of patients with metastases is based on the Spinal Instability Neoplastic Score (SINS) framework, which relies on the qualitative assessment of pain and of radiographic images (more details in Chapter I, section 1.2.1). To date, this is the clinical standard used to identify patients with spinal metastases who may benefit from surgical intervention. However, this scoring system fails in providing an objective guidance for the cases of indeterminate (possibly impending) spinal instability where treatment decision making relies only on clinical experience.

FE models have been extensively used to study the mechanical properties of healthy human vertebrae at different dimensional scales. Such models have also the potential of being applied to the study of vertebrae with lytic lesions. Two approaches can be used. FE models based on micro Computed Tomography (microCT) images (microFE) have been validated and applied to study the local deformation of bone tissues and the mechanics of initiation and progression of vertebral fracture. MicroFE models can be used to estimate how local bone microstructure affects vertebral mechanics. Thus, these models could be used to study the effect of lytic lesions on the mechanical behaviour of vertebrae.

Another approach is to measure the structural stability of vertebrae with lesions with subject-specific FE models generated from clinical Quantitative Computed Tomography

(QCT) images. QCT-based FE models account for the subject-specific bone geometries and heterogeneous distribution of material properties.

The following literature review aims to describe the state of the art of the relevant experimental and numerical studies performed on vertebral bone tissues with and without (i.e. healthy) lytic lesions. In the end of the chapter a summary of the objectives of the thesis is presented.

## 2.2. Vertebral mechanical properties

The mechanical properties of human vertebrae have been extensively studied through monotonic *ex vivo* experimental tests performed for the most common spinal loading conditions, namely axial compression and eccentric compression towards the anterior side of the vertebrae. The biomechanics of the human spine was investigated *ex vivo* using either vertebral segments (i.e. composed by two or more vertebrae including adjacent intervertebral discs), or single vertebral specimens (i.e. whole vertebrae or isolated vertebral body with or without endplates) (Brandolini et al., 2014). However, most of the *ex vivo* experiments focused on the testing of the structural properties of the vertebral bone by using single vertebral body specimens whose top and bottom endplates were either embedded in layers of poly-methyl-methacrylate (PMMA), or sectioned to ensure that the loading surfaces were flat and parallel (Fig 2.1-(a)) (Kopperdahl et al., 2014; Wang et al., 2012; Chevalier et al., 2009; Jenni M. Buckley et al., 2007; Crawford, Rosenberg, et al., 2003). Experimental stiffness and strength of healthy human vertebral bodies are usually estimated from the force-displacement curve as the slope of the linear range and the peak force, respectively (see Chapter I, section 1.4). For axial compression experiments, stiffness values equal to  $7.99 \pm 2.39$  kN/mm (range 5.38-12.72 kN/mm) and ultimate force values equal to  $5.53 \pm 2.12$  kN (range 3.06-9.76 kN) were found for lumbar vertebrae (L1-L5, n=12) with an average bone volume density of  $0.18 \pm 0.041$  g/cm<sup>3</sup> (Fig 1.2- (a)) (Chevalier et al., 2009). For eccentric compression (Fig 1.2-(b)), vertebral stiffness and strength values equal to  $35.0 \pm 9.7$  kN/mm (range 17.1-55.0 kN/mm) and  $5.30 \pm 1.67$  kN (range 2.31-9.19 kN) were found for thoracolumbar vertebrae (T12 to L5, n=37) with a mean volumetric BMD of  $0.17 \pm 0.064$  g/cm<sup>3</sup> (range 0.059-0.29 g/cm<sup>3</sup>) (Dall'Ara et al., 2010). The large differences in stiffness values were driven by the different boundary conditions used in the test (axial compression with embedded plate versus eccentric compression applied on vertebral body sections). Vertebral strength has been shown to vary

with gender (Jenni M. Buckley et al., 2007; Ebbesen et al., 1999), age (Ebbesen et al., 1999), and vertebral level (Singer et al., 1995) due to differences in geometry and material properties. Moreover, the compressive structural strength of the vertebrae was shown to correlate with areal bone mineral density (aBMD,  $0.37 \leq R^2 \leq 0.70$ ) (Perilli et al., 2012), volumetric BMD ( $R^2 = 0.63$ ) (Buckley et al., 2007), bone mineral content (BMC,  $0.49 \leq R^2 \leq 0.76$ ) (Perilli et al., 2012; Fields et al., 2009b), and trabecular bone volume fraction (BV/TV,  $0.52 \leq R^2 \leq 0.66$ ) (Fields et al., 2009b). However, such determinants of bone strength are just surrogate measures of vertebral strength and cannot directly estimate the structural mechanical properties of vertebrae, which can be directly estimated with FE models.

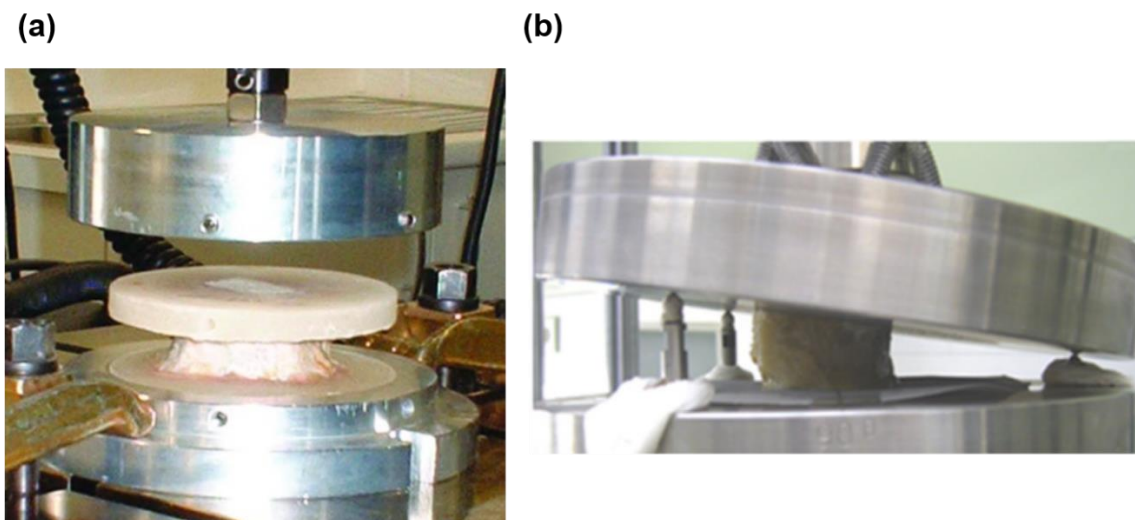


Figure 2.1- Typical experimental set-ups used to test vertebral bodies under (a) compression (Chevalier et al., 2009) and (b) compression with anterior bending (Dall'Ara et al., 2010).

Detailed analysis of the local deformation of bone tissues requires *in situ* time-lapsed experiments performed along with high-resolution microCT imaging and Digital Volume Correlation (DVC) methods. Such experiments have been used to study the mechanisms of bone deformation and fracture at the local level of trabecular bone tissues (Gillard et al., 2014) and human vertebrae (Hussein et al., 2012, 2018; Jackman et al., 2015; Hosseini et al., 2014). *In situ* experiments on human vertebrae are typically performed on spine segments where the central vertebra is loaded through the adjacent intervertebral discs (IVD) to account for a more physiological loading scenario (Fig 2.2). Vertebral deformation under axial compression or eccentric compression have been studied *in situ*. For instance, Jackman et al. (2016) showed that for combined loading cases, some vertebrae were still able to support compression even

after showing a drop in the flexion moment, or a marked endplate deflection and anterior bulging. Conversely, for axial compression the endplate deflection was always followed by a decrease in the load bearing capacity of the vertebral body (Jackman et al., 2016). Moreover, the deformation and fracture of vertebral bodies under axial compression was shown to be associated to the microstructure of the trabecular bone underlying the top endplate (BV/TV, Tb.Sp, connectivity, and others.  $0.006 \leq p \leq 0.008$ ) (Hussein et al., 2018; Jackman et al., 2016).

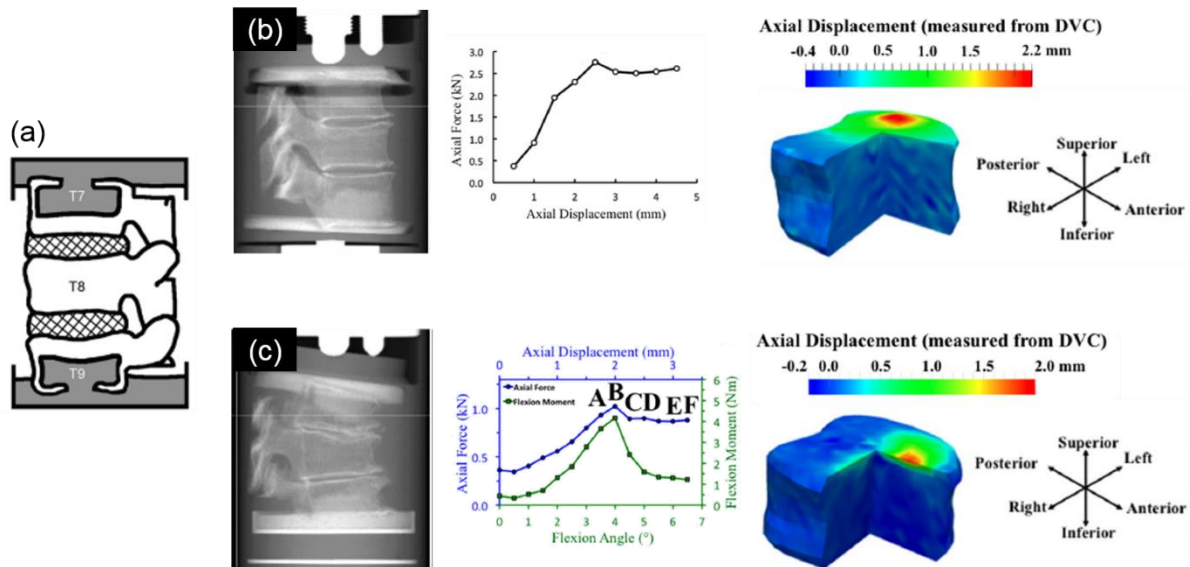


Figure 2.2- (a) Schematic of a typical vertebral segment composed by three vertebrae with the top and bottom ones embedded in PMMA and the middle one loaded via the intervertebral discs. (b) and (c) Sagittal views of the vertebral segment tested in axial compression and compression with anterior bending, respectively, next to the corresponding force-displacement curves and measured 3D field of displacements obtained from DVC. Image adapted from Jackman et al. (2015).

### 2.2.1. Validation and application of Finite Element models

FE models have been used to analyse the mechanical behaviour of vertebral bone tissues under loading at different dimensional scales.

MicroFE models have been used to predict the local deformation of trabecular bone tissue. The predicted local displacements under compressive load by these models were validated by comparison with DVC measurements for specimens of trabecular bone scanned at  $10 \mu\text{m}$  (Chen et al., 2017) and  $35 \mu\text{m}$  (Zrael et al., 2006) of isotropic voxel size (Fig 2.3). Good correlations were found between microFE models predictions and experimental measurements ( $R^2=0.99$  with slopes close to 1 and intercepts between  $-5 \mu\text{m}$  and approximately  $0 \mu\text{m}$  for axial

displacements; and  $0.97 \leq R^2 \leq 0.99$  with slopes close to 1 and intercepts ranging -6 to 6  $\mu\text{m}$  for transverse displacements) (Chen et al., 2017). As expected, the match between experimental and numerical boundary conditions was shown to be fundamental to correct for the experimental artifacts of the *in situ* testing (e.g. misalignment between loading axial and the specimen axis, micro-rotations of the loading plate, etc.) (Hussein et al., 2018; Chen et al., 2017). Nevertheless, the DVC method applied to microCT images (i.e. voxel size ranging from 10  $\mu\text{m}$  to 40  $\mu\text{m}$ ) showed uncertainties in the order of 200  $\mu\epsilon$  for strain measurement in both cortical and trabecular bone only for sub-volume sizes of approximately 600-700  $\mu\text{m}$  (Fig 2.3) (Dall'Ara et al., 2017; Palanca et al., 2015; Zael et al., 2006). Therefore, considering that the dimension of trabecular is smaller than this sub-volume size, microFE models predictions of local strains can be only evaluated qualitatively over large sub-regions of the vertebra. Recent advances in the DVC approach using Synchrotron (SR)-microCT imaging revealed the ability of the method to measure strains at the tissue level with uncertainties, obtained from zero-strain conditions, lower than 200  $\mu\epsilon$  for sub-volumes of up to 160  $\mu\text{m}$  (Palanca et al., 2017). These improvements are a result of the increase in the spatial resolution and in the signal-to-noise ratio of the input images used in the DVC method (Palanca et al., 2017). Nevertheless, X-rays irradiation from the SR-microCT imaging procedure induces bone damage and, therefore, this approach cannot be used for *in situ* mechanical testing of large specimens. Therefore, validation of local predictions of FE models is limited to the displacement field.

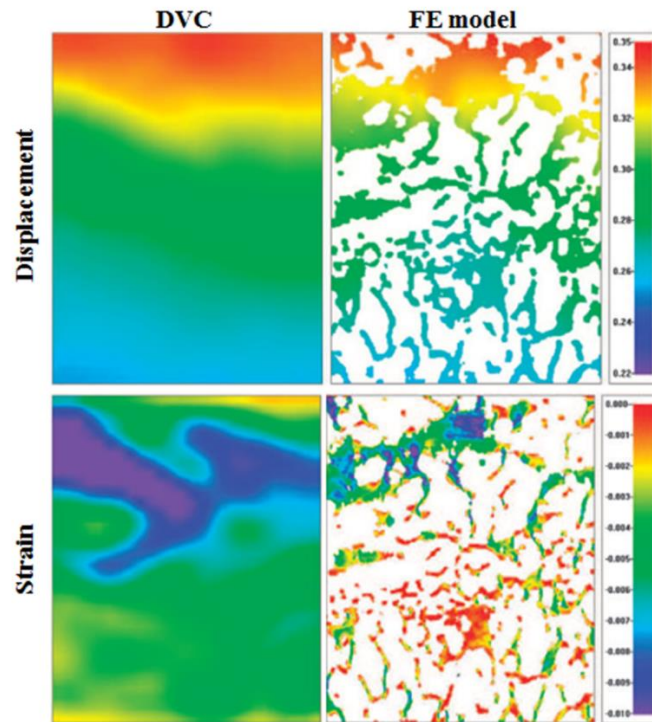


Figure 2.3 - Section view of the field of axial displacements and strains obtained from DVC and linear microFE models (ZaueI et al., 2006).

The DVC method has been also used to measure the local deflection and deformation of human vertebral bones scanned in a microCT (Hussein et al., 2012, 2018; Jackman et al., 2015; Hosseini et al., 2014). This approach was already used in the attempt of validating predictions of vertebral deformation and fracture obtained by QCT-based homogenised FE (hFE) models (Jackman et al., 2016). However, hFE models predictions of local displacements showed median errors larger than 50% and a wide range of correlation values with experimental measurements obtained for both axial and eccentric compression (Pearson correlation coefficients between 0.40 and 0.95, derived from plot) (Jackman et al., 2016).

Structural properties of vertebral bones have been predicted by both microFE models based on HR-pQCT images (Dall'Ara, 2012; Pahr et al., 2011) and hFE models based on clinical QCT images (Zysset, Pahr, et al., 2015; Keaveny et al., 2014; Kopperdahl et al., 2014; Pahr et al., 2014; Dall'Ara, 2012; Wang et al., 2012; Jenni M. Buckley et al., 2007; Imai et al., 2006; Crawford, Cann, et al., 2003). Linear elastic and isotropic microFE models generated from specimen-specific HR-pQCT images showed to predict between 78% and 84% of the variability in vertebral stiffness and between 88% and 92% of the variability in vertebral strength obtained from experimental tests of compression with eccentric compression

(Dall'Ara, 2012; Pahr et al., 2011). However, the quantitative agreement between microFE models predictions and experimental measurements of structural properties was dependent on the tuning (i.e. back-calculation) of the elastic modulus of the bone tissue. On the other hand, hFE models revealed to be able to predict mechanical properties of vertebral bodies with similar accuracy ( $0.68 \leq R^2 \leq 0.71$  for stiffness and  $0.77 \leq R^2 \leq 0.79$  for strength) without requiring any tuning of the input parameters (Pahr et al., 2014; Dall'Ara, 2012). Both modelling approaches showed to predict vertebral strength better than the aBMD obtained from simulated DXA (Dall'Ara, 2012). QCT-based hFE models with simple nonlinear elastic-perfectly-plastic and bilinear elastic-plastic constitutive laws, defined based on symmetric yield strain properties for tension and compression, showed to be accurate in predicting vertebral ultimate forces in compression ( $0.80 \leq R^2 \leq 0.95$ ) (Wang et al., 2012; Jenni M. Buckley et al., 2007; Imai et al., 2006). More sophisticated models including both plasticity and damage were also introduced with similar performance for eccentric compression loading ( $0.77 \leq R^2 \leq 0.79$ ) (Pahr et al., 2014; Dall'Ara et al., 2010; Chevalier et al., 2008). Furthermore, a few studies combined predictions of vertebral strength obtained from subject-specific hFE models with estimations of vertebral loads obtained for specific physiological conditions, in order to estimate the vertebral fracture risk (Wang et al., 2012; Melton et al., 2007; Boussein et al., 2006). In particular, predictions of compressive vertebral strength, volumetric BMD, and load-to-strength ratios obtained from the nonlinear hFE model used by Wang et al. (2012) showed to improve the assessment of fracture risk compared to the measurements of areal BMD used in clinics to assess patients with osteoporosis (area under the curve, AUC, between 0.82 and 0.83 versus AUC equal to 0.76 for areal BMD).

The boundary conditions of hFE models are typically applied either through embedded endplates or vertebral body sections. Both approaches were found to be equivalent for predictions of ultimate force and damage distributions (Maquer et al., 2012). Nevertheless, the modelling of a single vertebral body is not representative of the physiological loading conditions which happen along the spine where vertebrae are loaded through the intervertebral disks (Hussein et al., 2013, 2018; Danesi et al., 2016; Jackman et al., 2015). Nonetheless, the inclusion of hyperplastic intervertebral disks did not improve the prediction of vertebral strength compared to typical hFE models loaded in axial compression through the embedded endplates (Lu et al., 2014). Therefore, in most applications it is considered acceptable to homogeneously distribute the applied load on the endplate (thus simulating the loading condition that the vertebra would undergo if embedded in resin).

### 2.3. Effect of lytic metastases on bone mechanics

Metastatic lytic lesions are focal regions with low bone density (Burke et al., 2018; Borggrefe et al., 2015) and affected microstructure (reduced trabecular bone volume content and thickness) (Burke et al., 2018; Nazarian et al., 2008). Despite the microstructural changes promoted by lytic lesions on bone tissues, it was observed that there is no significant difference between the material properties of normal and lytic trabecular bone tissues extracted from human vertebrae and measured with micro-indentation ( $p > 0.05$  and  $n = 14$ ) (Lenherr et al., 2018). Moreover, Nazarian et al. (2008) observed similar relationships between the mechanical properties and the volumetric BMD of healthy and metastatic trabecular bone tissues ( $0.76 \leq R^2 \leq 0.87$  for metastatic bone tissues versus  $0.77 \leq R^2 \leq 0.81$  for control bone tissues). These observations suggest that modelling bone tissue affected by metastases as low BMD tissue would be acceptable.

Considering the challenge of collecting human vertebrae with metastatic lesions for experimental characterization, in order to study the effect of bone lesions on the mechanical properties of the vertebrae one used approach is to mechanically induce lesions (holes) in healthy tissue. Vertebrae with lytic lesions induced by drilling holes in the thoracic vertebral levels from T3 to T12 were experimentally tested in order to study the effect of size and location of the lesions on the vertebral strength (Fig 2.4) (Ebihara et al., 2004; Windhagen et al., 1997; McGowan et al., 1993; Silva et al., 1993).

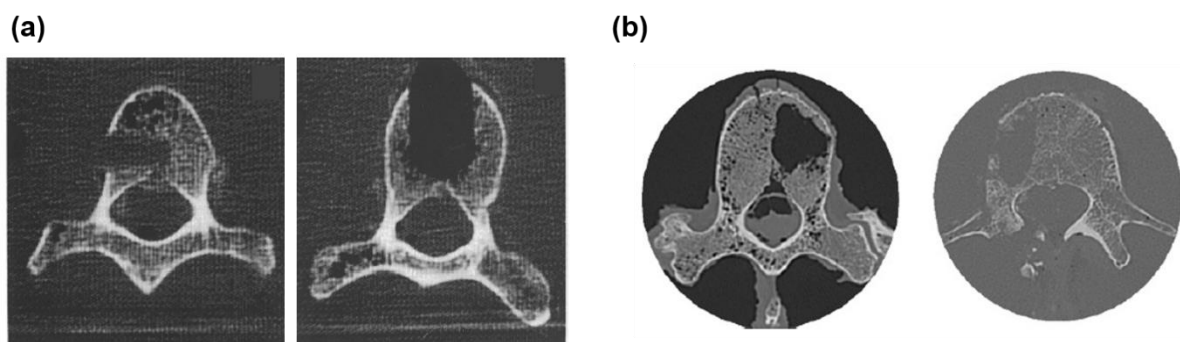


*Figure 2.4- Induced lytic lesions experimentally generated by drilling holes of different sizes in different positions of the vertebral body. (a) Lesions generated in the middle transverse plane from the cortical shell into the centrum of trabecular bone of the vertebral body (Silva et al., 1993) ; and (b) lesions generated from a small access hole opened in the cortical shell used to get access to create cavities in the trabecular bone of the vertebral body (Alkalay et al., 2018).*

However, the effect of the size and location of induced lytic lesions on vertebral strength is still controversial. For instance, moderate to strong correlation were found between the size of the lesion and the vertebral failure load in the studies where induced lytic defects were generated affecting mainly the trabecular centrum of thoracic vertebral bodies (Fig 2.4 (b)) ( $R^2=0.51$  for human vertebral bodies by McGowan et al. (1993); and  $R^2=0.78$  for sheep vertebral segments by Ebihara et al. (2004)) (Table 2.1). Moreover, lesions causing a disruption of the trabecular centrum and the costovertebral joints showed to cause a significantly higher reduction in failure loads compared to the lesions affecting the pedicles and facet joints (Ebihara et al., 2004). For lesions involving the cortical shell of the vertebral body (i.e. transcortical lesions), only a weak correlation was found between the size of the lesions and the relative failure load of thoracic human vertebrae ( $R^2=0.26$ ) (Fig 2.4 (a)) (Table 2.1) (Silva et al., 1993). Lesions affecting the cortical shell also showed a significant decrease in the relative failure loads compared to lesions occupying the trabecular centrum ( $p=0.002$ ) (McGowan et al., 1993; Silva et al., 1993). Conversely, other studies showed no correlation between the size and predicted failure loads of vertebrae with induced lesions affecting between 5% to 41% of the middle cross-section area and tested under axial compression (Alkalay et al., 2018) or eccentric compression (Windhagen et al., 1997) (Table 2.1). Similarly, no relationship was found between the location of the induced lesions and the vertebral mechanical properties (Table 2.1) (Windhagen et al., 1997; Silva et al., 1993). By using Digital Image Correlation (DIC) on vertebrae with induced lytic defects of different sizes created from the pedicles up to the anterior wall, it was shown that lesions greater than 30% of the vertebral body volume start generating critical strains (i.e. close to the yield strains of vertebral bone tissues) over the anterior wall of the vertebral bodies loaded in eccentric compression (Palanca et al., 2018).

*Table 2.1-Overview of the experimental studies developed on vertebrae with mechanically induced lytic lesions and respective correlations between the properties of the induced lytic lesions (i.e. size and location) and the measured vertebral failure loads.*

Reference	Specie (sample size)	Vertebral level	Loading condition	Predictor property (ranges)	Estimated mechanical property	Correlation (R <sup>2</sup> )
<b>McGowan et al. (1993)</b>	Human (n=27)	T2-T12	Eccentric compression (isolated vertebrae)	Size of the lesion <sup>1</sup> (10%-80%)	Relative failure load <sup>3</sup>	0.51
<b>Silva et al. (1993)</b>	Human (n=45)	T3-T12	Eccentric compression (isolated vertebrae)	Size of the lesion <sup>1</sup> (20%-55%) Location of the lesion <sup>2</sup> (TC at A, P, L)	Relative failure load <sup>3</sup>	0.26 No correlation (p=0.76)
<b>Windhagen et al. (1997)</b>	Human (n=19)	T5 and T11	Eccentric compression (vertebral segments)	Size of the lesion <sup>1</sup> (4%-35%) Location of the lesion <sup>2</sup> (P, C, L)	Failure load	No correlation (p=0.53) No correlation
<b>Ebihara et al. (2004)</b>	Sheep (n=87)	T8 and T11	Eccentric compression (vertebral segments)	Size of the lesion <sup>1</sup> (24%-75%)	Failure load	0.78
<b>Alkalay et al. (2018)</b>	Human (n=32)	T7, T10, and L1	Axial compression (vertebral segment)	Size of the lesion <sup>1</sup> (28%-41%)	Failure load	0.27

<sup>1</sup>Size of the lesions computed as the ratio between the mid cross-sectional area of the lesion and the total mid cross-sectional area of the vertebral body;

<sup>2</sup>Location of the lesion mechanically induced in the vertebral body. A: anterior, P: posterior, L: lateral; C: central. TC: for transcortical lesions which involve a major disruption of the cortex. If not specified the induced lesions majorly affect the trabecular bone centrum

<sup>3</sup>Relative failure load computed as the ratio between the failure load of the vertebrae with lesion and the control vertebrae

Experimental tests have been also used to study the effect of lytic lesions on the mechanisms of deformation and fracture of the vertebrae. Vertebrae loaded under eccentric compression with mechanically induced lesions disrupting the lateral side of the cortical shell, showed

higher principal strains in both cortical and trabecular bone adjacent to the lesion. In those cases, failure occurred as bulging and buckling of the vertebral cortex surrounding the lesion site (Alkalay & Harrigan, 2016; Ron N Alkalay, 2015). Moreover, Alkalay & Harrigan (2016) revealed differences between strain distribution for the vertebrae with lytic lesions and an adjacent control.

Furthermore, vertebral fractures in patients with multiple myeloma, which show a widespread distribution of lytic lesions, showed to be well discriminated from volumetric measurements of trabecular bone BMD obtained from routine QCT images (Odds Ratios, ORs=1.6 for n=104 pooled data) (Borggreffe et al., 2015).

The experimental approaches described above are not suitable for estimating the effect of different lesions on the vertebral strength. Moreover, they are limited to the generation of lytic lesions that disrupt the cortical shell and do not account for the intrinsic microstructure and BMD distribution of the bone tissue. Conversely, biomechanical subject-specific computational models can be used to test the effect of lytic lesion properties on vertebral strength in a more systematic way, account for bone microstructure (i.e. microFE models) and provide a more detailed analysis of the local and structural effect of lytic lesions.

### **2.3.1. Use of FE models to study the effect of vertebral metastasis**

The application of FE models to study the effect of lytic lesions over the structural properties and stability of human vertebrae has been evolving from the use of idealized geometries of human vertebral bodies with virtually simulated lytic defects (Tschirhart et al., 2004, 2007, Whyne et al., 2001, 2003; Mizrahi et al., 1992), to the use of subject-specific vertebrae with simulated (Galbusera et al., 2018; Groenen et al., 2018; Matsuura et al., 2014) or real lytic lesions (Campbell et al., 2017).

Poro-elastic FE models of generalised geometries of human vertebral bodies were used to study the effect of the size and location of virtually induced lesions, vertebral bone quality, loading rate, among other parameters, on the risk of burst fracture initiation (Fig 2.5 (a)) (Tschirhart et al., 2004, 2007, Whyne et al., 2001, 2003). Burst fractures were described to occur due to internal pressurization followed by expansion of the vertebral body and endplate failure (Holdsworth, 1970). Both the size of the lesions and the bone quality of the vertebral body showed to increase the vertebral bulge of 14-fold and up to 2.6-fold, respectively (Whyne et al., 2003). A less critical effect was observed for the location and shape of the lesions on the

risk of initiation of burst fracture (increase in vertebral bulge of up to 40%) (Tschirhart et al. , 2004). The same group showed that transcortical lesions simulated in the anterior, posterior or lateral compartments of the vertebral body, decrease of 30% the risk of burst fracture in comparison to centrally located metastases (Tschirhart et al., 2007). Mizrahi et al. (1992) showed by using linear elastic FE models of idealized vertebral bodies that transcortical lesions occupying 40% of the vertebral body increased by 2.2-fold the peak principal compressive stresses of the cortical shell compared to lesions of the same size located within the trabecular bone. Lesions smaller than 40% of the volume of the vertebral body caused only a minor effect on the peak stresses (up to 1.25-fold) (Mizrahi et al., 1992).

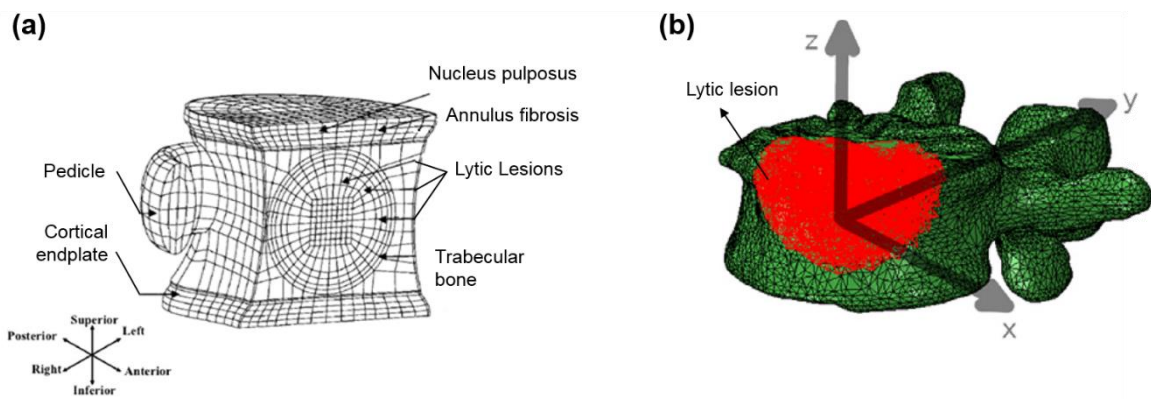


Figure 2.5- Parametrical FE models of the human vertebra used to virtually simulate lytic lesions within (a) idealized geometries of the vertebrae body (Whyne et al., 2003); and (b) subject-specific QCT-based geometries of human vertebrae (Galbusera et al., 2018).

Recently, Galbusera et al. (2018) performed similar parametric analysis to linear hFE models with subject-specific vertebral geometries and heterogeneous material properties by including simulated focal lesions of low compressibility and stiffness (Fig 2.5 (b)). In line with previous literature, this study confirmed the critical effect of the lesion size over the bone quality, position of the lesion, and vertebral level on the risk of burst fracture initiation (Galbusera et al., 2018; Tschirhart et al., 2007; Whyne et al., 2003).

A few other studies focused on the validation of the predictions of structural properties of human vertebrae with lytic lesion by subject-specific FE models (Stadelmann et al., 2018; Matsuura et al., 2014). In particular, Matsuura et al. (2014) showed that subject-specific QCT-based hFE models were able to predict 76% of the variability in ultimate forces obtained from compression experiments of vertebrae with simulated hole-like lytic lesions. In this study,

plasticity was modelled using a bilinear elastic-plastic constitutive model with isotropic hardening elasticity of 0.05 (Matsuura et al., 2014). On the contrary, hFE models of vertebral segments with lytic lesions simulated on the middle vertebra were unable to predict the ultimate loads measured from compression experiments ( $0.22 \leq R^2 \leq 0.25$ ), even though predictions of stiffness were good ( $0.64 \leq R^2 \leq 0.69$ ) (Groenen et al., 2018). Similarly, Alkalay & Harrigan (2016) showed that while QCT-based hFE models of vertebrae with simulated lytic lesions were able to predict the general deformation at the surface of the vertebral segments tested in compression ( $0.66 \leq R^2 \leq 0.91$ ), they were limited in predicting structural failure.

Recently, Stadelmann et al. (2018) showed that subject-specific hFE models of vertebral bodies predict the ultimate force in compression of human vertebral bodies with real lytic lesions ( $R^2=0.73$ ) with a similar accuracy as that obtained for predictions of strength of vertebrae without lesions ( $R^2=0.77$ ) (Pahr et al., 2014). In that study, hFE models were generated from resampled microCT images (i.e. from 0.025 mm to 1 mm voxel size). The hFE models showed similar ability in predicting the vertebral mechanical properties compared to microCT based microFE models of the same specimens (Stadelmann et al., 2018).

Simple elastic-perfectly-plastic QCT-based hFE models also showed to predict vertebral fracture better than other surrogate measurements of density and microstructure for patients with multiple myeloma (i.e. Odds Ratios,  $1.7 \leq ORs \leq 2.3$  found for predicted stiffness, yield force, and work-to-yield, against  $1.4 \leq ORs \leq 1.7$  for trabecular and cortical volumetric BMD and BV/TV) (Campbell et al., 2017).

So far the FE models used to study the effect of the properties of lytic lesions on the mechanical properties of the vertebrae do not account for the microstructure of the bone tissue. In addition, an approach to evaluate the effect of lytic lesions on the vertebral strength from clinical images of patients with spinal metastases is still missing. These approaches may help the clinical decision for the treatment of patients with spinal metastases and were therefore the main objectives of this study.

## 2.4. Objectives

The aim of this project is to study the effect of lytic metastatic on the mechanical properties of the human vertebrae by using two types of computation models: microCT based microFE models to account for the microstructure of the vertebrae; and QCT based hFE models for subject-specific evaluation of the stability of vertebrae with lytic lesions.

This aim could be achieved by addressing the following four objectives:

- 1) To generate a procedure to create and validate the mechanical behaviour of microCT based microFE models of the whole vertebral body. Validation of the predictions of local and structural properties by the microFE models were performed for four porcine vertebrae by means of *in situ* mechanical testing (performed by collaborators at the University of Portsmouth) and DVC measurements (Chapter III).
- 2) To apply the subject-specific microFE models previously validated to study the effect of simulated lytic lesions with different sizes and locations on the mechanical properties of human vertebral bodies. This step involved the development of a computational framework to parametrize the generation of simulated lytic lesions with different properties (sizes and location) from subject-specific microFE models of a vertebral body. Local and structural properties of models with lesions were analysed with respect to the corresponding control model without lesions (Chapter IV).
- 3) To develop a method to generate subject-specific QCT-based hFE models to evaluate the structural stability of vertebrae with lytic lesions compared to adjacent vertebrae without lesions (Chapter V). The parameters of the models (e.g. mesh size, failure load, etc.) were optimised and a subject-specific simplified 2D model of the sagittal alignment of the spine was developed in order to estimate the applied loads for two different loading conditions.
- 4) To apply the aforementioned method to the QCT images retrospectively collected from a small number of patients with clinically identified vertebral lytic lesions (Chapter VI). The effect of lytic lesions on vertebral strength and stability was evaluated per patient only for cases where the SINS did not provide a clear guideline for the clinical decision making. Furthermore, a report template was developed to present and facilitate the interpretation of the computational analyses to clinicians.

## 2.5. References

- Alkalay, R., Adamson, R., Miropolsky, A. & Hackney, D. (2018). Female Human Spines with Simulated Osteolytic Defects: CT-Based Structural Analysis of Vertebral Body Strength. *Radiology*, 288(2), 436–444.
- Alkalay, R. N. (2015). Effect of the Metastatic Defect on the Structural Response and Failure Process of Human Vertebrae : An Experimental Study. *Clinical Biomechanics*, 30(2), 121–128.
- Alkalay, R. N. & Harrigan, T. P. (2016). Mechanical Assessment of the Effects of Metastatic Lytic Defect on the Structural Response of Human Thoracolumbar Spine. *Journal of Orthopaedic Research*, 34(10), 1808–1819.
- Borggreffe, J., Giravent, S., Thomsen, F., Peña, J., Campbell, G., Wulff, A., et al. (2015). Association of QCT Bone Mineral Density and Bone Structure With Vertebral Fractures in Patients With Multiple Myeloma. *Journal of Bone and Mineral Research*, 30(7), 1329–1337.
- Bouxsein, M. L., Melton, L. J., Riggs, B. L., Muller, J., Atkinson, E. J., Oberg, A. L., et al. (2006). Age- and Sex-Specific Differences in the Factor of Risk for Vertebral Fracture: A Population-Based Study Using QCT. *Journal of Bone and Mineral Research*, 21(9), 1475–1482.
- Brandolini, N., Cristofolini, L. & Viceconti, M. (2014). Experimental Methods for the Biomechanical Investigation of the Human Spine: A Review. *Journal of Mechanics in Medicine and Biology*, 14(01), 1430002.
- Buckley, J. M., Loo, K. & Motherway, J. (2007). Comparison of Quantitative Computed Tomography-Based Measures in Predicting Vertebral Compressive Strength. *Bone*, 40(3), 767–774.
- Burke, M., Akens, M., Kiss, A., Willett, T. & Whyne, C. (2018). Mechanical Behavior of Metastatic Vertebrae Are Influenced by Tissue Architecture, Mineral Content, and Organic Feature Alterations. *Journal of Orthopaedic Research*, 1–10.
- Campbell, G. M., Peña, J. A., Giravent, S., Thomsen, F., Damm, T., Glüer, C. C., et al. (2017). Assessment of Bone Fragility in Patients With Multiple Myeloma Using QCT-Based Finite Element Modeling. *Journal of Bone and Mineral Research*, 32(1), 151–156.
- Chen, Y., Dall’Ara, E., Sales, E., Manda, K., Wallace, R., Panjak, P., et al. (2017). Micro-CT Based Finite Element Models of Cancellous Bone Predict Accurately Displacement Computed by Elastic Registration: A Validation Study. *Journal of Mechanical Behavior of Biomedical Materials*, 65, 644–651.
- Chevalier, Y., Charlebois, M., Pahr, D., Varga, P., Heini, P., Schneider, E., et al. (2008). A Patient-Specific Finite Element Methodology to Predict Damage Accumulation in Vertebral Bodies under Axial Compression, Sagittal Flexion and Combined Loads. *Computer Methods in Biomechanics and Biomedical Engineering*, 11(5), 477–487.
- Chevalier, Y., Pahr, D. & Zysset, P. K. (2009). The Role of Cortical Shell and Trabecular Fabric in Finite Element Analysis of the Human Vertebral Body. *Journal of Biomechanical Engineering*, 131(11), 1110031–12.
- Crawford, R. P., Cann, C. E. & Keaveny, T. M. (2003). Finite Element Models Predict in Vitro Vertebral Body Compressive Strength Better than Quantitative Computed Tomography. *Bone*, 33, 744–750.
- Crawford, R. P., Rosenberg, W. S. & Keaveny, T. M. (2003). Quantitative Computed

- Tomography-Based Finite Element Models of the Human Lumbar Vertebral Body : Effect of Element Size on Stiffness , Damage , and Fracture Strength. *Journal of Biomechanical Engineering*, 125, 434–438.
- Dall'Ara, E., Pahr, D., Varga, P., Kainberger, F. & Zysset, P. (2012). QCT-Based Finite Element Models Predict Human Vertebral Strength in Vitro Significantly Better than Simulated DEXA. *Osteoporosis International*, 23, 563–572.
- Dall'Ara, E., Peña-Fernández, M., Palanca, M., Giorgi, M., Cristofolini, L. & Tozzi, G. (2017). Precision of Digital Volume Correlation Approaches for Strain Analysis in Bone Imaged with Micro-Computed Tomography at Different Dimensional Levels. *Frontiers in Materials*, 4, 1-13.
- Dall'Ara, E., Schmidt, R., Pahr, D., Varga, P., Chevalier, Y., Patsch, J., et al. (2010). A Nonlinear Finite Element Model Validation Study Based on a Novel Experimental Technique for Inducing Anterior Wedge-Shape Fractures in Human Vertebral Bodies in Vitro. *Journal of Biomechanics*, 43, 2374–2380.
- Danesi, V., Erani, P., Brandolini, N., Juszczak, M. M. & Cristofolini, L. (2016). Effect of the In Vitro Boundary Conditions on the Surface Strain Experienced by the Vertebral Body in the Elastic Regime. *Journal of Biomechanical Engineering*, 138(10), 104503.
- Ebbesen, E. N., Thomsen, J. S., Beck-nielsen, H., Nepper-rasmussen, H. J. & Mosekilde, L. I. S. (1999). Age- and Gender-Related Differences in Vertebral Bone Mass, Density, and Strength. *Journal of Bone and Mineral Research*, 14(8), 1394–1403.
- Ebihara, H., Ito, M., Abumi, K., Taneichi, H., Kotani, Y., Minami, A., et al. (2004). A Biomechanical Analysis of Metastatic Vertebral Collapse of the Thoracic Spine: A Sheep Model Study. *Spine*, 29(9), 994–999.
- Fields, A. J., Eswaran, S. K., Jekir, M. G. & Keaveny, T. M. (2009). Role of Trabecular Microarchitecture in Whole-Vertebral Body Biomechanical Behavior. *Journal of Bone and Mineral Research*, 24(9), 1523–1530.
- Galbusera, F., Qian, Z., Casaroli, G., Bassani, T., Costa, F., Schlager, B., et al. (2018). The Role of the Size and Location of the Tumors and of the Vertebral Anatomy in Determining the Structural Stability of the Metastatically Involved Spine: A Finite Element Study. *Translational Oncology*, 11(3), 639–646.
- Gillard, F., Boardman, R., Mavrogordato, M., Hollis, D., Sinclair, I., Pierron, F., et al. (2014). The Application of Digital Volume Correlation (DVC) to Study the Microstructural Behaviour of Trabecular Bone during Compression. *Journal of the Mechanical Behavior of Biomedical Materials*, 29, 480–499.
- Groenen, K. H. J., Bitter, T., van Veluwen, T. C. G., van der Linden, Y. M., Verdonschot, N., Tanck, E., et al. (2018). Case-Specific Non-Linear Finite Element Models to Predict Failure Behavior in Two Functional Spinal Units. *Journal of Orthopaedic Research*, 1–11.
- Holdsworth, F. (1970). Fractures, Dislocations, and Fracture-Dislocations of the Spine. *Journal of Bone and Joint Surgery*, 52(8), 1534–1551.
- Hosseini, H. S., Clouthier, A. L. & Zysset, P. K. (2014). Experimental Validation of Finite Element Analysis of Human Vertebral Collapse under Large Compressive Strains. *Journal of Biomechanical Engineering*, 136, 1–10.
- Hussein, A., Barbone, P. E. & Morgan, E. F. (2012). Digital Volume Correlation for Study of the Mechanism of Whole Bones. *Procedia IUTAM*, 4, 116–125.
- Hussein, A. I., Louzeiro, D. T. & Morgan, E. F. (2018). Differences in Trabecular Microarchitecture and Simplified Boundary Conditions Limit the Accuracy of

- Quantitative Computed Tomography-Based Finite Element Models of Vertebral Failure. *Journal of Biomechanical Engineering*, 140, 1–11.
- Hussein, A. I., Mason, Z. D. & Morgan, E. F. (2013). Presence of Intervertebral Discs Alters Observed Stiffness and Failure Mechanisms in the Vertebra. *Journal of Biomechanics*, 46(10), 1683–1688.
- Imai, K., Ohnishi, I. & Bessho, M. (2006). Nonlinear Finite Element Model Predicts Vertebral Bone Strength and Fracture Site. *Spine*, 31(16), 1789–1794.
- Jackman, T. M., Delmonaco, A. M. & Morgan, E. F. (2016). Accuracy of Finite Element Analyses of CT Scans in Predictions of Vertebral Failure Patterns under Axial Compression and Anterior Flexion. *Journal of Biomechanics*, 49, 267–275.
- Jackman, T. M., Hussein, A. I., Curtiss, C., Fein, P. M., Camp, A., De, L., et al. (2015). Quantitative, 3-D Visualization of the Initiation and Progression of Vertebral Fractures under Compression and Anterior Flexion. *Journal of Bone and Mineral Research*, 31(4), 1–37.
- Keaveny, T. M., Mcclung, M. R., Genant, H. K., Zanchetta, J. R., Kendler, D., Brown, J. P., et al. (2014). Femoral and Vertebral Strength Improvements in Postmenopausal Women With Osteoporosis Treated With Denosumab. *Journal of Bone and Mineral Research*, 29(1), 158–165.
- Kopperdahl, D. L., Aspelund, T., Hoffmann, P. F., Sigurdsson, S., Siggeirsdottir, K., Harris, T. B., et al. (2014). Assessment of Incident Spine and Hip Fractures in Women and Men Using Finite Element Analysis of CT Scans. *Journal of Bone and Mine*, 29(3), 570–580.
- Lenherr, C., Voumard, B., Stadelmann, M., Buck, F., Haschtmann, D., Hoppe, S., et al. (2018). *Indentation Properties of Metastatic Vertebral Trabecular Bone*. 8<sup>th</sup> World Congress of Biomechanics, Dublin, Ireland, 8-12<sup>th</sup> July 2018.
- Lu, Y., Maquer, G., Museyko, O., Püschel, K., Engelke, K., Zysset, P., et al. (2014). Finite Element Analyses of Human Vertebral Bodies Embedded in Polymethylmethacrylate or Loaded via the Hyperelastic Intervertebral Disc Models Provide Equivalent Predictions of Experimental Strength. *Journal of Biomechanics*, 47(10), 2512–2516.
- Maquer, G., Dall'Ara, E. & Zysset, P. K. (2012). Removal of the Cortical Endplates Has Little Effect on Ultimate Load and Damage Distribution in QCT-Based Voxel Models of Human Lumbar Vertebrae under Axial Compression. *Journal of Biomechanics*, 45(9), 1733–1738.
- Matsuura, Y., Giambini, H., Ogawa, Y., Fang, Z., Thoreson, A. R., Yaszemski, M. J., et al. (2014). Specimen-Specific Nonlinear Finite Element Modelling to Predict Vertebrae Fracture Loads after Vertebroplasty. *Spine*, 39(22), E1291–E1296.
- McGowan, D. P., Hipp, J. A., Takeuchi, T., White, A. A. & Hayes, W. C. (1993). Strength Reductions from Trabecular Destruction within Thoracic Vertebrae. *Journal of Spinal Disorders*, 6(2), 130–6.
- Melton, L. J., Riggs, B. L., Keaveny, T. M., Achenbach, S. J., Hoffmann, P. F., Camp, J. J., et al. (2007). Structural Determinants of Vertebral Fracture Risk. *Journal of Bone and Mineral Research*, 22(12), 1885–1892.
- Mizrahi, J., Silva, M. J. & Hayes, W. C. (1992). Finite Element Stress Analysis of Simulated Metastatic Lesions in the Lumbar Vertebral Body. *Journal of Biomedical Engineering*, 14(6), 467–475.
- Nazarian, A., Von Stechow, D., Zurakowski, D., Müller, R. & Snyder, B. D. (2008). Bone Volume Fraction Explains the Variation in Strength and Stiffness of Cancellous Bone Affected by Metastatic Cancer and Osteoporosis. *Calcified Tissue International*, 83, 368–

- Pahr, D. H., Dall'Ara, E., Varga, P. & Zysset, P. K. (2011). HR-PQCT-Based Homogenised Finite Element Models Provide Quantitative Predictions of Experimental Vertebral Body Stiffness and Strength with the Same Accuracy as MFE Models. *Computer Methods in Biomechanics and Biomedical Engineering*, 15, 711–20.
- Pahr, D. H., Schwiedrzik, J., Dall, E. & Zysset, P. K. (2014). Clinical versus Pre-Clinical FE Models for Vertebral Body Strength Predictions. *Journal of the Mechanical Behavior of Biomedical Materials*, 33, 76–83.
- Palanca, M., Barbanti Brodano, G. & Cristofolini, L. (2018). The Size of Simulated Lytic Metastases Affects the Strain Distribution on the Anterior Surface of the Vertebra. *J Biomechanical Engineering (ASME)*, 140, 1–9.
- Palanca, M., Bodey, A. J., Giorgi, M., Viceconti, M., Lacroix, D., Cristofolini, L., et al. (2017). Local Displacement and Strain Uncertainties in Different Bone Types by Digital Volume Correlation of Synchrotron Microtomograms. *Journal of Biomechanics*, 58, 27–36.
- Palanca, M., Tozzi, G., Cristofolini, L., Viceconti, M. & Dall'Ara, E. (2015). Three-Dimensional Local Measurements of Bone Strain and Displacement: Comparison of Three Digital Volume Correlation Approaches. *Journal of Biomechanical Engineering*, 137(7), 071006.
- Perilli, E., Briggs, A. M., Kantor, S., Codrington, J., Wark, J. D., Parkinson, I. H., et al. (2012). Failure Strength of Human Vertebrae: Prediction Using Bone Mineral Density Measured by DXA and Bone Volume by Micro-CT. *Bone*, 50(6), 1416–1425.
- Silva, M. J., Hipp, J. A., McGowan, D. P., Takeuchi, T. & Hayes, W. C. (1993). Strength Reductions of Thoracic Vertebrae in the Presence of Transcortical Osseous Defects: Effects of Defect Location, Pedicle Disruption, and Defect Size. *European Spine Journal*, 2(3), 118–125.
- Singer, K., Day, R., Breidahl, P. & Price, R. (1995). Prediction of Thoracic and Lumbar Vertebral Body Compressive Strength: Correlations with Bone Mineral Density and Vertebral Region. *Bone*, 17(2), 167–174.
- Stadelmann, M., Alkalay, R., Maquer, G., Buck, F., Hoppe, S., Theumann, N., et al. (2018). *Can Micro and Homogenized Finite Element Analysis Estimate the Strength of Human Metastatic Vertebrae?* 8<sup>th</sup> World Congress of Biomechanics, Dublin, Ireland, 8-12<sup>th</sup> July 2018.
- Tschirhart, C. E., Finkelstein, J. a. & Whyne, C. M. (2007). Biomechanics of Vertebral Level, Geometry, and Transcortical Tumors in the Metastatic Spine. *Journal of Biomechanics*, 40(1), 46–54.
- Tschirhart, C. E., Nagpurkar, A. & Whyne, C. M. (2004). Effects of Tumor Location, Shape and Surface Serration on Burst Fracture Risk in the Metastatic Spine. *Journal of Biomechanics*, 37(5), 653–660.
- Wang, X., Sanyal, A., Cawthon, P. M., Palermo, L., Jekir, M., Christensen, J., et al. (2012). Prediction of New Clinical Vertebral Fractures in Elderly Men Using Finite Element Analysis of CT Scans. *Journal of Bone and Mineral Research*, 27(4), 808–816.
- Whyne, C. M., Hu, S. S. & Lotz, J. C. (2001). Parametric Finite Element Analysis of Vertebral Bodies Affected by Tumors. *Journal of Biomechanics*, 34(10), 1317–1324.
- Whyne, C. M., Hu, S. S. & Lotz, J. C. (2003). Burst Fracture in the Metastatically Involved Spine: Development, Validation, and Parametric Analysis of a Three-Dimensional Poroelastic Finite-Element Model. *Spine*, 28(7), 652–660.
- Windhagen, H. J., Hipp, J. A., Silva, M. J., Lipson, S. J. & Hayes, W. C. (1997). Predicting

Failure of Thoracic Vertebrae With Simulated and Actual Metastatic Defects. *Clinical Orthopaedics and Related Research*, 344, 313–319.

Zauel, R., Yeni, Y. N., Bay, B. K., Dong, X. N. & Fyhrie, D. P. (2006). Comparison of the Linear Finite Element Prediction of Deformation and Strain of Human Cancellous Bone to 3D Digital Volume Correlation Measurements. *Journal of Biomechanical Engineering*, 128, 1–6.

Zysset, P., Pahr, D., Engelke, K., Genant, H. K., McClung, M. R., Kendler, D. L., et al. (2015). Comparison of Proximal Femur and Vertebral Body Strength Improvements in the FREEDOM Trial Using an Alternative Finite Element Methodology. *Bone*, 81, 122–130.



## **Chapter III. MicroFE models of vertebral bodies: Validation of local displacement predictions and analysis of structural properties**

Based on the published manuscript:

Costa MC, Tozzi G, Cristofolini L, Danesi V, Viceconti M, Dall'Ara E (2017) Micro Finite Element models of the vertebral body: Validation of local displacement predictions. PLoS ONE 12(7):e0180151. <https://doi.org/10.1371/journal.pone.0180151>

### **Acknowledgments**

This study was performed in partnership with the Universities of Bologna and Portsmouth where the experimental methods and testing essential for this validation study were developed. This included the sample's preparation and the *in situ* time lapsed experiments with acquisition of high-resolution images. The author of this thesis did not contribute to the mechanical tests performed in this study.

## Abstract

The estimation of local and structural mechanical properties of bones with micro Finite Element (microFE) models based on Micro Computed Tomography images depends on the quality bone geometry is captured, reconstructed and modelled, the bone microstructure and the local material properties. The aim of this study was to validate microFE models predictions of local displacements for vertebral bodies, analyse models' predictions of axial forces, and to evaluate the effect of the elastic tissue modulus on models' predictions.

Four porcine thoracic vertebrae were axially compressed *in situ*, in a step-wise fashion and scanned at approximately 39  $\mu\text{m}$  resolution in preloaded and loaded conditions. A global digital volume correlation (DVC) approach was used to compute the full-field displacements. Homogeneous, isotropic and linear elastic microFE models were generated with boundary conditions assigned from the interpolated displacement field measured from the DVC. Measured and predicted local displacements were compared for the cortical and trabecular compartments in the middle of the specimens. Models were run with two different tissue moduli defined from microindentation data (12.0 GPa) and a back-calculation procedure (4.6 GPa). The predicted sum of axial reaction forces was compared to the experimental values for each specimen.

MicroFE models predicted more than 87% of the variation in the displacement measurements ( $R^2=0.87-0.99$ ). However, the estimated axial forces were largely overestimated (80-369%) for a tissue modulus of 12.0 GPa, whereas differences in the range of 10-80% were found for a back-calculated tissue modulus. The specimen with the lowest density showed a large number of elements strained beyond yield and the highest predictive errors. This study shows that the simplest microFE models can accurately predict quantitatively the local displacements and qualitatively the strain distributions of vertebral bodies, independently from the considered bone microstructures.

### 3.1 Introduction

Throughout life the structural stability of bones is compromised by a reduction in bone mineral density (BMD) due to the changes driven by bone diseases. Vertebral fractures are common and related to different pathologies such as osteoporosis and bone metastases (Sutcliffe et al., 2013; Johnell & Kanis, 2006). The current clinical methods used to evaluate pathological risk of fracture are mainly based on areal measurements of BMD and qualitative assessments of radiological data which per se are not enough to provide an objective and accurate prediction of bone strength (Unnanuntana, 2010). On the other hand, the relationship between bone morphology and mechanics has been driving the development of more accurate and reliable micro Finite Element (microFE) models to predict non-invasively the local and structural properties of bone under loading. MicroFE models based on high-resolution imaging (i.e. High Resolution peripheral Quantitative Computed Tomography, HR-pQCT, and micro Computed Tomography, microCT) can resolve bone structural heterogeneities and are used to better understand bone deformation under complex loading. Such models are typically generated by segmentation of the images, and conversion of bone voxels into linear hexahedral elements (Homminga et al., 2004; Ulrich et al., 1998; van Rietbergen et al., 1995). Due to the long computation time required to run non-linear models with several millions of degrees of freedom (DOF), typically microFE models at the organ level are run within the elastic regime. Furthermore, the bone tissue is usually considered as isotropic and homogeneous (Chen, Dall'Ara, et al., 2017; Gross et al., 2012; Pahr et al., 2011; Dall'Ara et al., 2010; Verhulp et al., 2008; Chevalier et al., 2007), with the Poisson's ratio equal to 0.3 and the Young's modulus estimated from microindentation measurements (Wolfram et al., 2010a; Chevalier et al., 2007), or through back-calculation procedures (Pahr et al., 2011; Niebur et al., 2000; Ladd et al., 1998; van Rietbergen et al., 1995). Specifically, the local elastic properties of vertebral bone reported in the literature showed a wide range of values: mean values ( $\pm$ standard deviations) from  $5.7\pm 1.6$  GPa ((Hou et al., 1998) from back-calculation procedures) to  $12.3\pm 1.0$  GPa ((Wolfram et al., 2010a) from microindentation tests performed on wet bone structural units, BSU) (Table 3.1).

Table 3.1- Overview of the elastic modulus of human vertebral bone tissue reported in the literature from wet microindentation tests performed at the BSU level, or from back-calculation procedures in combination with microFE models.

Reference	Method	Sample Size	Bone Type	E <sub>tissue</sub> [GPa] (range)	Dimensional level of $\mu$ FE models	Imaging technique (voxel size)	$\mu$ FE models (element size)
Wolfram et al. (2010)	Wet microindentation <sup>a</sup>	N=104	Trab	12.0±1.0 (N/A) <sup>b</sup>	N/A	N/A	N/A
Wolfram et al. (2010) <sup>c</sup>	Wet microindentation <sup>a</sup>	N=30	Trab	12.3±1.0 (N/A) <sup>b</sup>	Biopsy	$\mu$ CT (12 $\mu$ m)	Linear(36 $\mu$ m)
Hou et al. (1998)	Back-calculation	N=28	Trab	5.7±1.6 (2.7 – 9.1)	Biopsy	$\mu$ CT (50 $\mu$ m)	Linear(50 $\mu$ m )
Ladd et al. (1998)	Back-calculation	N=5	Trab	6.6± 1.1 (5.4 – 7.7)	Biopsy	SR- $\mu$ CT (23 $\mu$ m)	Linear(23 $\mu$ m )
Pahr et al. (2011)	Back-calculation	N=37	Trab/ Cort	8.8±N/A (N/A)	Vertebral body	HR-pQCT (82 $\mu$ m)	Linear(82 $\mu$ m )

<sup>a</sup> Penetration Depth equal to 2.5  $\mu$ m, loading rate=120 mN/min, holding time 30s

<sup>b</sup> Values of elastic tissue modulus computed from indentations performed along the axial direction

<sup>c</sup> In this study predictions of microFE models of trabecular bone set with an average tissue modulus measured from wet microindentation tests provided excellent quantitative predictions of structural stiffness measured in compression (concordance correlation coefficient of 0.97)

N/A Information not available.

MicroFE models predictions of structural properties depend on the defined tissue properties (Bayraktar et al., 2004; Niebur et al., 2000; Rietbergen, 2000). The specificity of the back-calculated tissue's elastic modulus to the imaging procedure, anatomical site, and modelling approach (Pahr et al., 2011; van Rietbergen et al., 1995), reduces its applicability and generalization. However, microFE models defined with an elastic tissue modulus based on the average value measured through wet microindentation tests have been shown to provide accurate estimations of apparent stiffness for trabecular bone biopsies scanned with 12  $\mu$ m voxel size and extracted from human vertebrae tested in compression (concordance correlation coefficient equal to 0.97) (Wolfram et al., 2010a). Nevertheless, from the literature it is not clear if this value can be used also for whole vertebral bodies. MicroFE models generated from HR-pQCT images with 82  $\mu$ m voxel size were found to predict up to 84% of the variability in bone stiffness and up to 92% in variability of bone strength when compared to *ex vivo* compression tests of human vertebral bodies (Dall'Ara et al., 2012; Pahr et al., 2011). However,

a good quantitative agreement of structural stiffness (Slope=0.88, Intercept=0.07 GPa) was obtained only once a back-calculated tissue modulus was used (Pahr et al., 2011).

Digital Volume Correlation (DVC) can provide an accurate measurement of the 3D displacement field in bone tissue given two microCT images of the undeformed and deformed specimens (Grassi & Isaksson, 2015; Roberts et al., 2014), and has been used to validate displacement predictions of microFE models for trabecular bone specimens scanned with voxel size equal to 10  $\mu\text{m}$  and 35  $\mu\text{m}$  (Chen, Dall'Ara, et al., 2017; Zael et al., 2006). In particular, it has been demonstrated that in order to obtain proper correlations between the displacement values measured with DVC and predicted with microFE, the boundary conditions in the models need to be interpolated from the DVC displacement field in order to correct for potential experimental artifacts in the *in situ* time lapsed mechanical testing. The DVC approach has been also used to study the failure behaviour of vertebral bodies (Tozzi et al., 2016; Jackman et al., 2015; Hussein et al., 2012) and trabecular bone tissues (Gillard et al., 2014). Jackman et al. used DVC to compare the predicted local axial displacements of QCT-based FE models of vertebral bodies tested up to failure, showing a wide range of predictive ability of the best models (Pearson correlation coefficients between 0.40 and 0.95, derived from the plots) and large median errors (45-50%, estimated from the plot) (Jackman et al., 2016).

The accuracy of homogeneous microFE models in predicting bone mechanical properties is mostly affected by their ability of modelling bone geometry, microstructure and material properties (Bevill & Tony M. Keaveny, 2009; Chevalier et al., 2007). Therefore, inaccuracies depend on the type of bone (i.e. differences in bone architecture and volume fraction) (Bevill & Tony M. Keaveny, 2009; Ladd et al., 1998), the used imaging protocols (Rietbergen et al., 1998), which should minimize discretization errors such as partial volume effect (Chen et al., 2014; Niebur et al., 1999), and the assigned tissue modulus. To the authors' knowledge there is no evidence in the literature about quantitative comparison of specimen-specific microFE models predictions of local displacements at the organ level, where the accuracy of microFE models relies also on the ability of the imaging procedure to capture both cortical and trabecular bone microarchitectures. Moreover, linear microFE models predictions of structural properties have been only validated for input images with 82  $\mu\text{m}$  voxel size, leaving unknown their predictive ability if based on images with higher resolution. In particular, considering the ability of this method to account for bone microarchitecture and its potential to analyse the effect of musculoskeletal pathologies and related interventions (Hardisty et al., 2012; Hojjat et al., 2012; Nazarian et al., 2008), it is very important to understand if the models can accurately

predict the local displacements in the elastic regime and provide reasonable estimations of structural properties.

Therefore, the aim of this study was to evaluate the ability of specimen-specific microFE models to predict the local displacements across the whole vertebral body, and in particular on cortical and trabecular compartments, measured with *in situ* compressive tests and DVC analyses. Furthermore, in order to evaluate the effect of the tissue modulus on the structural properties of vertebral bodies, the axial forces predicted by the microFE models were compared to those experimentally measured.

## **3.2 Materials and methods**

*In situ* compressive tests were performed within a microCT system that was used to acquire the geometry and microstructure of preloaded and loaded specimens as described in (Tozzi et al., 2016). A DVC algorithm was applied to preloaded and loaded images to obtain the displacement fields. MicroFE models were generated from the preloaded images and displacements were imposed according to the DVC output at the boundaries. The predicted local displacements were compared to those experimentally measured with DVC in the middle of the specimen. Predicted and measured axial forces corresponding to the deformed state were compared as well.

Data from mechanical testing and imaging of the porcine vertebrae was shared by collaborators at the University of Portsmouth. The specimen preparation, imaging and testing are briefly described in sections 3.2.1 and 3.2.2.

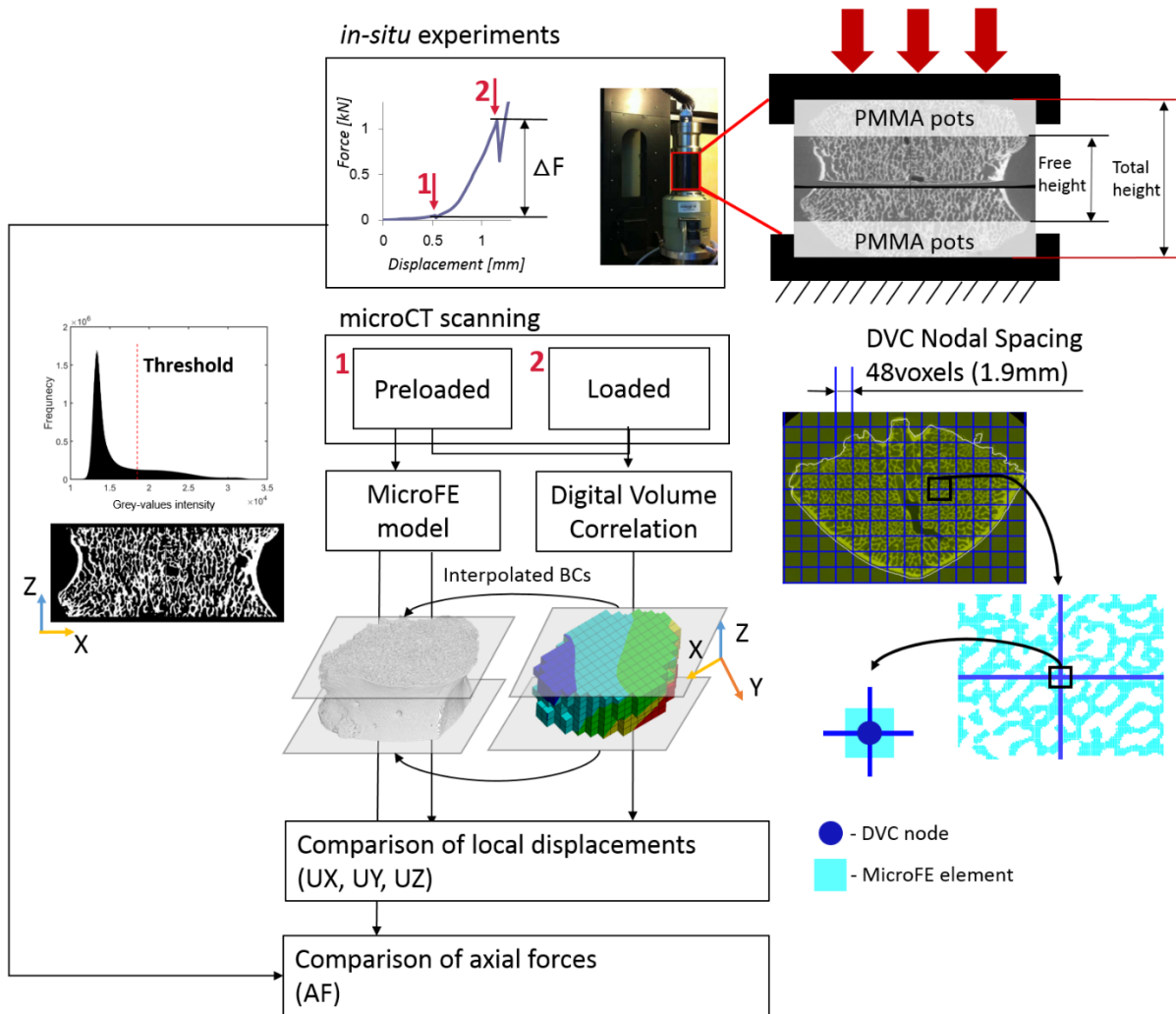


Figure 3.1- Workflow used to compare predicted and experimental local displacements and axial force. An example of the step-wise load displacement curve is reported on the top highlighting the Preloaded (1) and Loaded (5% apparent strain, 2) conditions. A picture of the loading jig and a scheme of the sample fixation are reported on the top-right corner. The Digital Volume Correlation (DVC) algorithm was applied to the Preloaded and Loaded images to calculate the map of displacement in the whole vertebral body. MicroFE models of the vertebral body between the PMMA pots were generated from the preloaded image after the application of a single level threshold chosen from the analyses of the frequency plot of the grey-values and visual inspection. The displacement values at the top and bottom layer of the microFE models were assigned by interpolation of the DVC measurements in those planes. Displacements along the axial (Z) and transverse (X, Y) directions were compared between microFE predictions and DVC measurements at the nodes of the DVC grid that lay within microFE elements. Predicted axial forces were compared to those measured from the experimental load-displacement curves ( $\Delta F$ ).

### **3.2.1 Specimen's preparation**

Four thoracic porcine vertebrae (T1-T3) were harvested from young animals (all females from the same breed, approximately 9 months old, and approximately 100 kg in weight) that were destined to alimentary purposes. Endplates, adjacent growth plates and surrounding soft tissues were removed and approximately 20% of the most caudal and cranial remaining portions of vertebral bodies were embedded in poly-methyl-methacrylate (PMMA). The spinous processes were used as reference to centre and align the specimens along the transverse plane using a protocol adapted from Danesi et al. (2014). Afterwards, the posterior arches were also removed.

### **3.2.2 Scanning and in situ mechanical testing**

An *in situ* mechanical loading device (CT5000, Deben Ltd, UK; nominal precision of axial displacement and force measurements were 10  $\mu\text{m}$  and 50 N, respectively) was used to axially compress the specimens inside the microCT scanner. The two flat parallel external surfaces of the embedding material were positioned between the loading plates of the jig. A sandpaper disk was applied between the embedding material and the bottom loading platen to avoid relative rotations of the loading plate. The free height of each specimen (i.e. distance between the internal surfaces of the embedding material, see Fig 3.1) was measured with a calliper. The specimens were compressed in displacement control at a loading rate of 0.1 mm/s while immersed in a physiological saline solution. The vertebral bodies were scanned with a microCT system (XTH225, Nikon Metrology, UK) in a preloaded condition (50 N in compression, in order to avoid moving artifacts during the microCT scanning) and after a 5% nominal global strain was applied considering as initial height the free height of specimens (loaded condition, Fig 3.1). The scanning was started approximately 15min after each compression step in order to reduce the effect of relaxation. Each image was acquired with an isotropic voxel size of approximately 39  $\mu\text{m}$ , and reconstructed after applying a median filter (kernel 3x3) on the projections (CTPro, Nikon Metrology, UK). The scanning parameters were: voltage of 88 kV, current of 110  $\mu\text{A}$ , exposure time of 2 s, and rotational step of 0.23° over 360° total rotation. The scanning time was approximately 90 min for each step. For more details about the experimental procedure please refer to Danesi et al. (2016).

### 3.2.3 Properties of the specimens

The free height of each specimen was computed as the mean distance between the top and bottom embedded pots measured with a calliper in three different positions (lateral left, lateral right, anterior and posterior. Fig 3.1). The total height of each vertebra was determined from the reconstructed microCT images. The preloaded and loaded images were cropped in order to remove image artifacts detected on the top and bottom slices (3-12% of the total height of the images) and therefore minimise the errors related to the elastic image registration procedure. From each cropped preloaded image a specimen-specific mask was created by defining an initial contour of the entire bone structure applying a low threshold value and by using dilation and filling morphological functions (MATLAB 8.5, MathWorks, Inc., USA). To avoid modelling the portion of the bone within the embedding material, which had attenuation similar to the surrounding saline solution, the middle 50% (with respect to the total height) portion of the image acquired during the preload for each specimen was cropped together with the masks in order to compute the total bone volume fraction (Tot.BV/TV), calculated by dividing the volume of bone voxels (BV) by the total volume within the mask (TV). A single threshold value was chosen visually for each portion of the preloaded image by comparing cross-sections of binary and grey scale images (Fig 3.2). An automatic threshold value used in other applications (Oliviero et al., 2017) and based on the middle point between the two peaks (bone and background) of the frequency plots was not possible in this study as no distinct peaks were recognizable (Fig 3.2- (c)). After the threshold, a connectivity filter was applied to remove the voxels without face connectivity (Chen et al., 2017) and to obtain the binary images required for the computation of the morphometric parameters and for the generation of the microFE models.

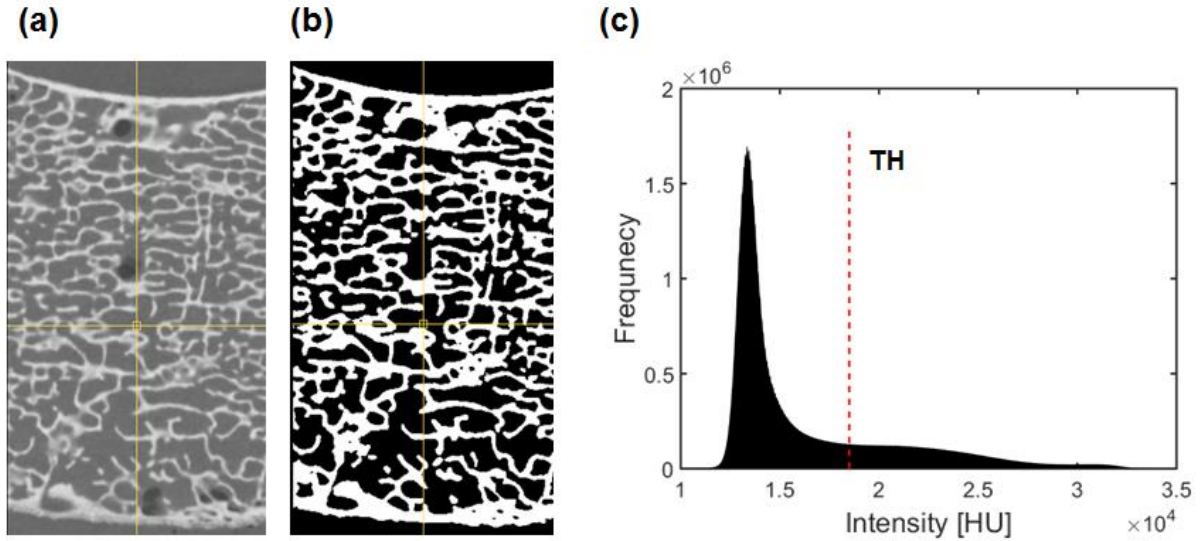


Figure 3.2- (a)  $\mu$ CT image of a cross-section (YZ) of the middle region of S#2, (b) correspondent binary image, and (c) typical global threshold value (TH).

To estimate the morphology of the trabecular bone for each specimen, four regions ( $5 \times 5 \times 10 \text{ mm}^3$ ) centred with respect to the mid cross-sectional plane were cropped in the lateral left, lateral right, anterior and posterior locations. For each region trabecular bone volume fraction (Tb.BV/TV), thickness (Tb.Th), separation (Tb.Sp), and degree of anisotropy (DA) were computed using the BoneJ 1.4.1 plug-in (Doube et al., 2010) on ImageJ 1.50e software (Schneider et al., 2012).

Table 3.2- Properties of the specimens.

Specimen ID	Level	Free Height [mm]	Voxel size [ $\mu\text{m}$ ]	Tot.BV/TV [%]	Tb.BV/TV <sup>a</sup> [%]	Tb.Th <sup>a</sup> [ $\mu\text{m}$ ]	Tb.Sp <sup>a</sup> [ $\mu\text{m}$ ]	DA <sup>a</sup>
S#1	T3	12.9	39.0	41.3	41.5 $\pm$ 2.4	217 $\pm$ 39	419 $\pm$ 138	0.65 $\pm$ 0.03
S#2	T2	12.6	38.6	40.3	41.4 $\pm$ 1.6	241 $\pm$ 42	465 $\pm$ 136	0.67 $\pm$ 0.04
S#3	T1	10.8	38.6	32.7	32.9 $\pm$ 3.6	198 $\pm$ 37	503 $\pm$ 154	0.53 $\pm$ 0.05
S#4	T3	13.3	38.6	48.6	48.4 $\pm$ 4.6	239 $\pm$ 53	396 $\pm$ 122	0.65 $\pm$ 0.10

<sup>a</sup> measurements performed on four sub-volumes in the lateral left, lateral right, anterior and posterior locations of the vertebral body. Data reported as mean  $\pm$  standard deviation.

### 3.2.4 Experimental displacement field

The elastic image registration toolkit ShIRT (Sheffield Image Registration Toolkit, University of Sheffield, UK) was used to find the full-field displacements over the entire specimen during the mechanical testing. The registration was applied to the cropped preloaded and loaded images using only the information within the mask, in order to reduce the effect of image noise outside the border of the specimens (Palanca et al., 2016). Details of the DVC algorithm can be found in (Dall'Ara et al., 2014). Briefly, ShIRT overlaps to the 3D images a grid with nodes spaced by a selected “Nodal Spacing” (NS). The software computes the nodal displacements to minimise the differences between the undeformed image to which the displacement map is applied and the deformed image. Tri-linear interpolation of the nodal displacements was used to compute the displacements within each sub-volume (hexahedral cell of the grid). The DVC grid is then converted into an 8-noded hexahedral mesh, the displacement field measured from DVC is imposed to the mesh as boundary conditions and is then imported to an FE software package (ANSYS® Academic Research, Release 15.0) to compute the strain field. A NS equal to 48 voxels (approximately 1872 $\mu\text{m}$ ) was chosen as the best compromise between precision and spatial resolution of the DVC approach (precision errors below 3.7  $\mu\text{m}$  for displacements (Tozzi et al., 2017) and approximately 100  $\mu\text{e}$  for strains (Palanca et al., 2016)).

### 3.2.5 MicroFE modelling

Each microFE model was generated by converting every bone voxel within the middle 50% of the total height of each specimen (computed from the preloaded images, Fig 3.1) into an 8-noded linear hexahedral element. MicroFE models and DVC displacement maps were referred to the same reference system by matching the axial position between the cropped images used in the DVC and the images used to build the microFE model of each specimen to allow *a posteriori* the comparison of correspondent bone regions between experimental and numerical methods. The boundary conditions (BCs) of the microFE models were assigned by trilinear interpolation of the DVC displacement field (Fig 3.3) (Chen, Dall'Ara, et al., 2017; Zauel et al., 2006). Homogeneous and isotropic material properties were assigned to every bone element considering a tissue elastic modulus ( $E_t$ ) of 12.0 GPa (Wolfram et al., 2010b) and a Poisson's ratio equal to 0.3. Moreover, a back-calculated tissue modulus was also determined as the best least square fit between predicted and experimental axial forces for the four specimens. The

experimental axial force ( $\Delta F$ ) was determined as the difference between the peak force measured at the loaded step (i.e. 5% apparent strain) and the force measured at the end of the relaxation period of the preload step (see Fig 3.1). From the microFE models, the total axial force (AF) was computed as the sum of the axial reaction forces obtained from the bottom surface nodes (i.e. closer to the fixed loading platen). Experimental and numerical results of local displacements were compared in all nodes of the DVC grid which lay at the centroid of a micro finite element (number of comparison points for the specimens were between 130 and 226). In order to reduce the effect of the boundary conditions the comparison was performed within the middle 70% (in height) of the microFE models. For all analyses the Z direction is representative of the axial axis of the vertebral body. X and Y axis refer to transverse directions without a precise anatomical reference. MicroFE models and DVC analyses were based on the original microCT images without applying any rotation, in order to avoid potential errors induced by image interpolation.

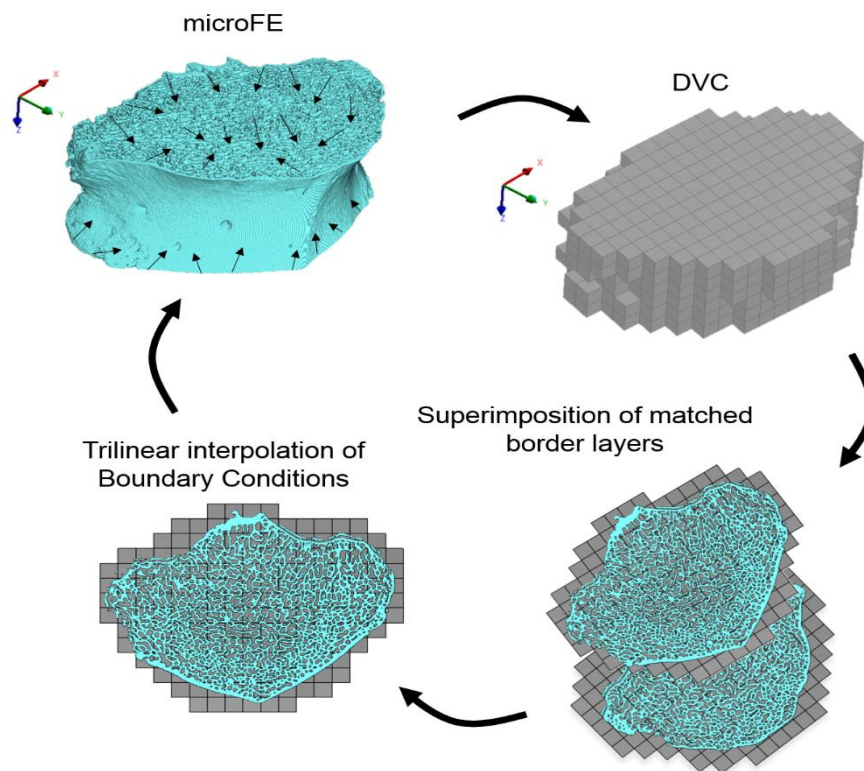


*Figure 3.3- Scheme of the assignment of microFE models boundary conditions obtained from trilinear interpolation of the displacement field measured from the DVC at the border layers of the microFE models.*

In order to investigate the results for trabecular and cortical sub-structures separately a mask of the cortical shell was generated (CTAnalyzer software version 1.16.4.1, SkyScan product provided by Bruker) for each specimen. A polygonal 2D region of interest (ROI) along the internal surfaces of the cortical shell was drawn and inverted approximately every ten sections for each 3D preloaded image were used to generate the microFE models (Fig 3.4). A dynamic interpolation was applied in between ROIs. The mask was used to identify the points of comparison between DVC and microFE models that laid within the cortical shell (the number of points in the cortical shell ranged from 9 to 31 for the different specimens) and those elements with strain beyond yield within the cortical shell.

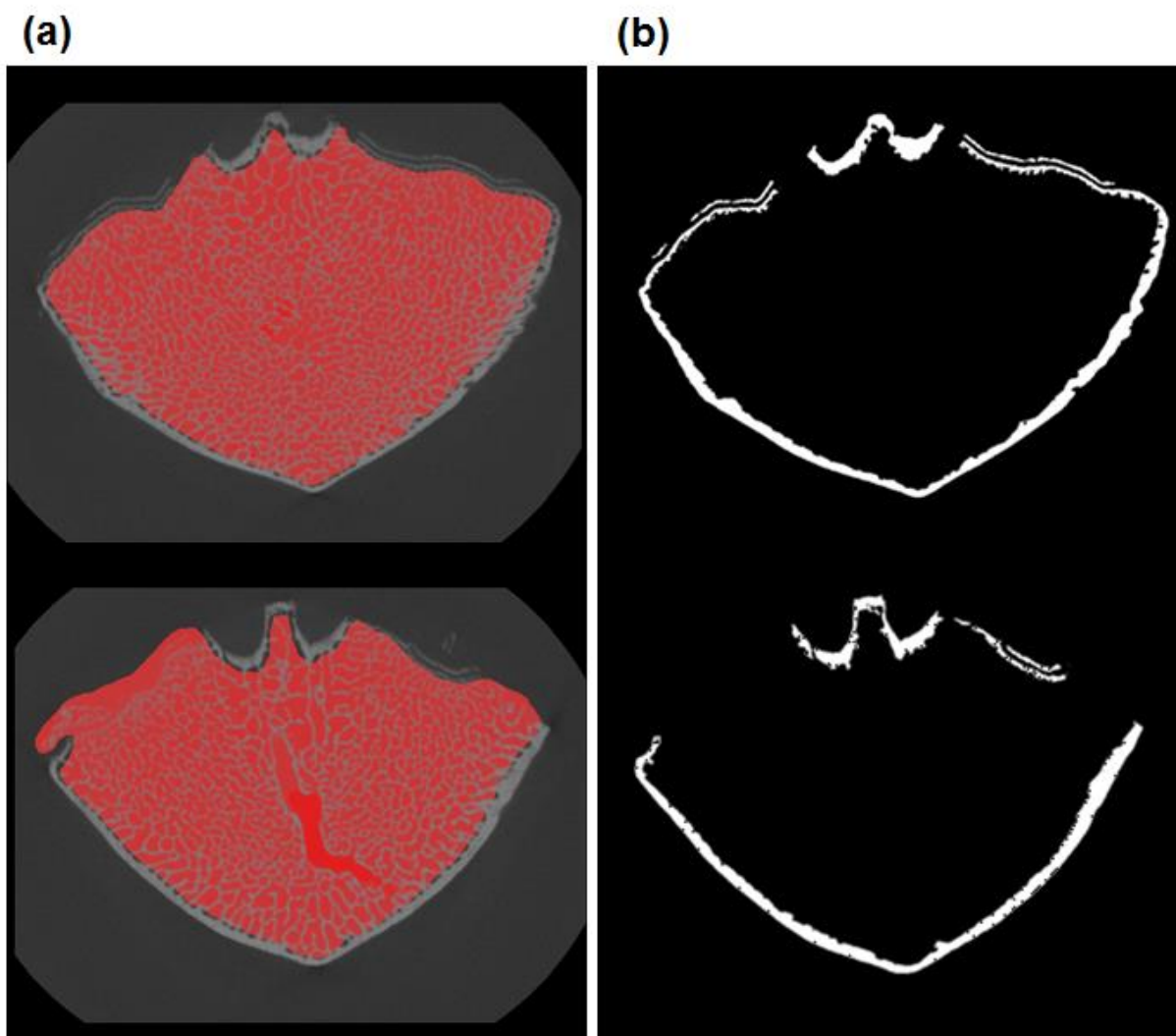


Figure 3.4- (a) Definition of the cortical mask through the manual setting of polygon regions of interest (ROI) accross the border between trabeculae and cortex bone of sample S#1. ROI interpolated along a border slice (to images) and a mid-section slice (bottom images). (b) correspondent binary images of the masked cortex contours. The specimens were all still in the growth age making the cortical shell very porous mostly over the postero-lateral regions of the vertebrae (i.e. link to the posterior elements), limiting thus the recognition of the cortical contours in those regions.

The largest microFE model contained over 962 million DOF and on average the analysis required approximately 120 minutes to solve in the finite element software Mechanical APDL (*ANSYS® Academic Research, Release 15.0*) using parallel distributed memory (use of a maximum of 64 CPUs and maximum memory of 311Gb).

### **3.2.6 Statistics**

To remove outliers, the Cook's distance method was applied to delete any data point with Cook's distance equal or higher than five times the Cook's distance mean value for each specimen in each displacement direction (Fox & Long, 1990). Linear regressions were used to correlate the numerical and experimental values of local displacements and the slope, intercept, and the coefficient of determination ( $R^2$ ) were reported. The accuracy of numerical models predictions of local displacements was evaluated through the computation of the root mean square error (RMSE), the RMSE divided by the absolute maximum experimental value (RMSE%), the absolute maximum value of the difference between the predicted and the experimental values (MaxError), and the concordance correlation coefficient (CC (Lin, 1989)).

The absolute percentage difference (%diff\_AF) between numerical and experimental values of axial reaction forces was calculated for each specimen for the models solved with an elastic tissue modulus obtained from the literature ( $E_t=12.0$  GPa) and from a back-calculation procedure ( $E_t=4.6$  GPa).

### 3.3 Results

MicroFE models predictions of local displacements are reported for models generated with  $E_t=12.0$  GPa, but as expected similar results were obtained for the back-calculated tissue modulus which was found to be  $E_t=4.6$  GPa (differences of RMSE% smaller than 0.007% for all the specimens along X, Y and Z directions) (Table S3.1 in Supporting materials). From the analysis of local displacements, less than 3.3% of the total number of points was excluded from each specimen by applying the Cook's distance criterion (Table 3.3). MicroFE models predictions of local displacements were highly correlated and in agreement with the experimental measurements ( $R^2$  and CC both ranged between 0.87 and  $>0.99$ ) (Table 3.3, Fig 3.5). In addition, slopes and intercepts of the linear regression analysis were close to the 1:1 relationship for all the directions and for all the specimens (Slope: 0.71 to 1.09, Intercept: -22.10  $\mu\text{m}$  to 4.56  $\mu\text{m}$ ) (Table 3.3, Fig 3.5).

For S#1, S#2, and S#4, predictions of local displacements along the axial direction (Z) were more accurate (RMSE% close to 1%) than the predictions computed along the transverse directions (X, Y) (RMSE% in the range 1-5%) (Table 3.3). For S#3 higher errors were observed along the axial direction, Z, (RMSE%=3%-5%) and worse correlations were found compared to the other three specimens ( $0.87 < R^2 < 0.91$  for S#3 and  $0.97 < R^2 < 1.00$  for all the others) (Table 3.3). Maximum differences between numerical and experimental local displacements were lower than or equal to 13  $\mu\text{m}$  for S#1, S#2, and S#4 (Table 3). For those specimens the distribution of residuals was homogenous and with an average value close to zero. For S#3 the residuals were more scattered and associated with a systematic overestimation of the predictions of axial local displacements (along Z) up to a maximum of 46  $\mu\text{m}$  (Fig 3.5, Table 3.3).

Table 3.3- Linear regression analysis between experimental and predicted local displacements for a tissue modulus  $E_t=12.0$  GPa. Data are reported for predictions along the three Cartesian directions (X and Y in a transverse plane, Z in the axial direction) for the individual specimens and for pooled data.

Specimen ID	Direction	Nr. Comparison points (%)	Slope	Intercept [ $\mu\text{m}$ ]	$R^2$	RMSE [ $\mu\text{m}$ ]	RMSE%	MaxError [ $\mu\text{m}$ ]	CC <sup>1</sup>
<b>S#1</b>	UX	213 (98.6%)	1.05	0.33	0.99	1.35	3.99	6.36	0.99
	UY	215 (99.5%)	0.98	1.12	0.97	1.64	5.25	7.42	0.98
	UZ	215 (99.5%)	0.99	3.25	0.99	2.78	0.70	9.20	0.99
<b>S#2</b>	UX	205 (96.7%)	1.02	0.35	0.97	2.31	2.47	12.56	0.98
	UY	209 (98.6%)	1.00	-1.96	0.99	2.31	1.25	9.48	0.99
	UZ	207 (97.6%)	0.99	1.30	>0.99	2.93	1.11	10.79	1.00
<b>S#3</b>	UX	130 (99.2%)	0.71	-8.00	0.87	3.11	5.20	12.23	0.87
	UY	130 (99.2%)	0.95	3.85	0.96	3.26	2.72	9.92	0.98
	UZ	131 (100%)	1.05	-22.10	0.91	11.88	5.08	45.86	0.90
<b>S#4</b>	UX	226 (98.7%)	1.05	-1.06	0.98	1.25	3.19	4.50	0.99
	UY	226 (98.7%)	1.09	-1.12	0.99	0.97	2.05	5.05	0.98
	UZ	225 (98.3%)	0.99	4.56	0.99	1.69	0.57	9.33	0.99
<b>Pooled</b>	UX	774 (98.2%)	0.99	1.04	0.99	2.55	2.74	12.56	1.00
	UY	780 (99.0%)	0.98	1.46	>0.99	2.18	1.18	9.92	1.00
	UZ	778 (98.7%)	1.04	-10.21	0.99	6.96	1.74	45.86	0.99

<sup>1</sup>Concordance Correlation Coefficient according to (Lin, 1989).

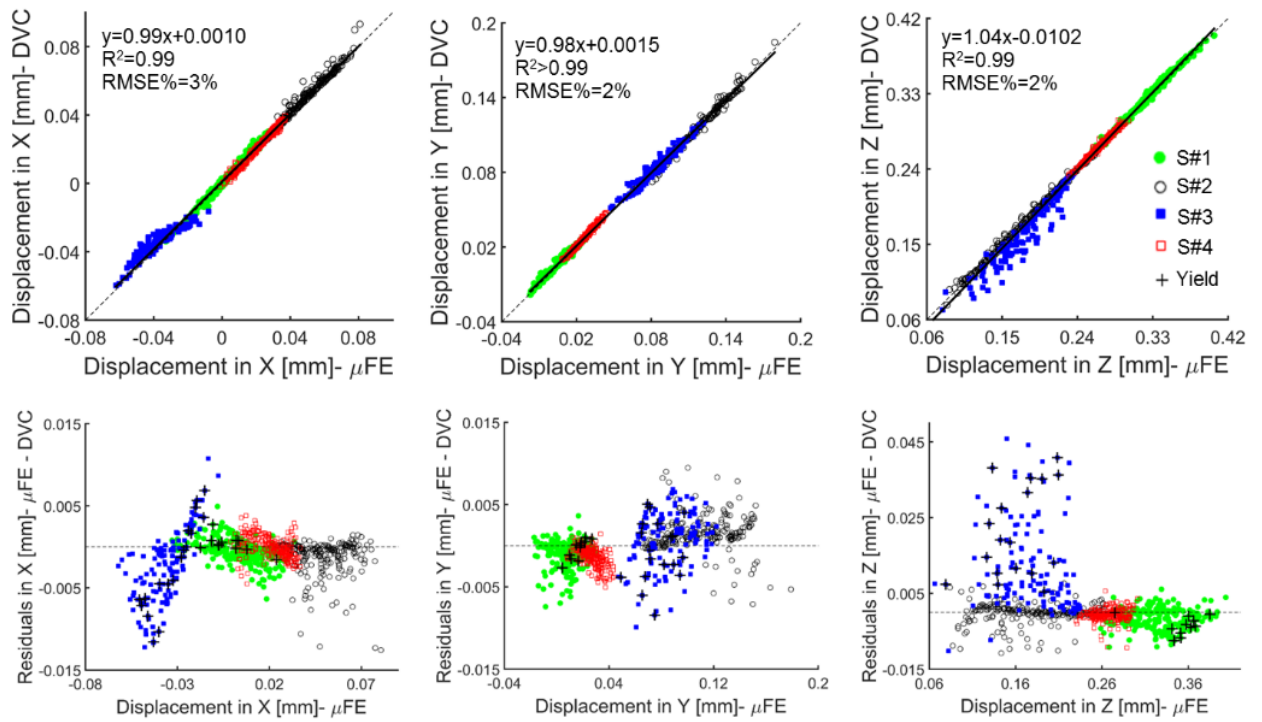


Figure 3.5- Linear regression and residual analysis estimated between predicted and experimental local displacements for pooled data. Top: correlation between the displacements along the transverse (X, Y) and axial (Z) directions computed by the microFE models and measured experimentally by the DVC approach for the pooled data. Bottom: plots of the residuals estimated as the difference between predicted and experimental local displacements. The elements with tensile or compressive strains beyond the yield limits ( $\epsilon_{p1Y}=7200 \mu\epsilon$  and  $\epsilon_{p3Y}=-8000 \mu\epsilon$  for vertebral trabecular bone (Morgan et al., 2001)) are reported with black crosses.

Similar trends were found for microFE predictions of local displacements in the cortical and trabecular bone regions (i.e. RMSE% between 1% and 5% in the cortical and trabecular bone along transverse directions and RMSE% approximately of 1% for points in the cortical and trabecular regions along the axial direction for all specimens but S#3) (Fig 3.6 and Table 3.3). Considering all directions and all specimens, similar correlations were found for microFE predictions performed in the cortical region ( $0.90 \leq R^2 < 1.00$ ,  $0.83 \leq \text{Slopes} \leq 1.09$ , and  $-7.89 \mu\text{m} \leq \text{Intercepts} \leq 15.26 \mu\text{m}$ ) compared to those obtained in the trabecular region ( $0.86 \leq R^2 < 1.00$ ,  $0.70 \leq \text{Slopes} \leq 1.10$  and  $-20.92 \mu\text{m} \leq \text{Intercepts} \leq 3.96 \mu\text{m}$ ) (Fig 3.6 and Table S3.2 in Supporting materials). In particular, the largest difference between predictions of the cortical and trabecular regions was observed for the axial displacement in S#3 ( $R^2 > 0.99$  and RMSE%=1%, compared to  $R^2=0.91$  and RMSE%=5% for the trabecular region).

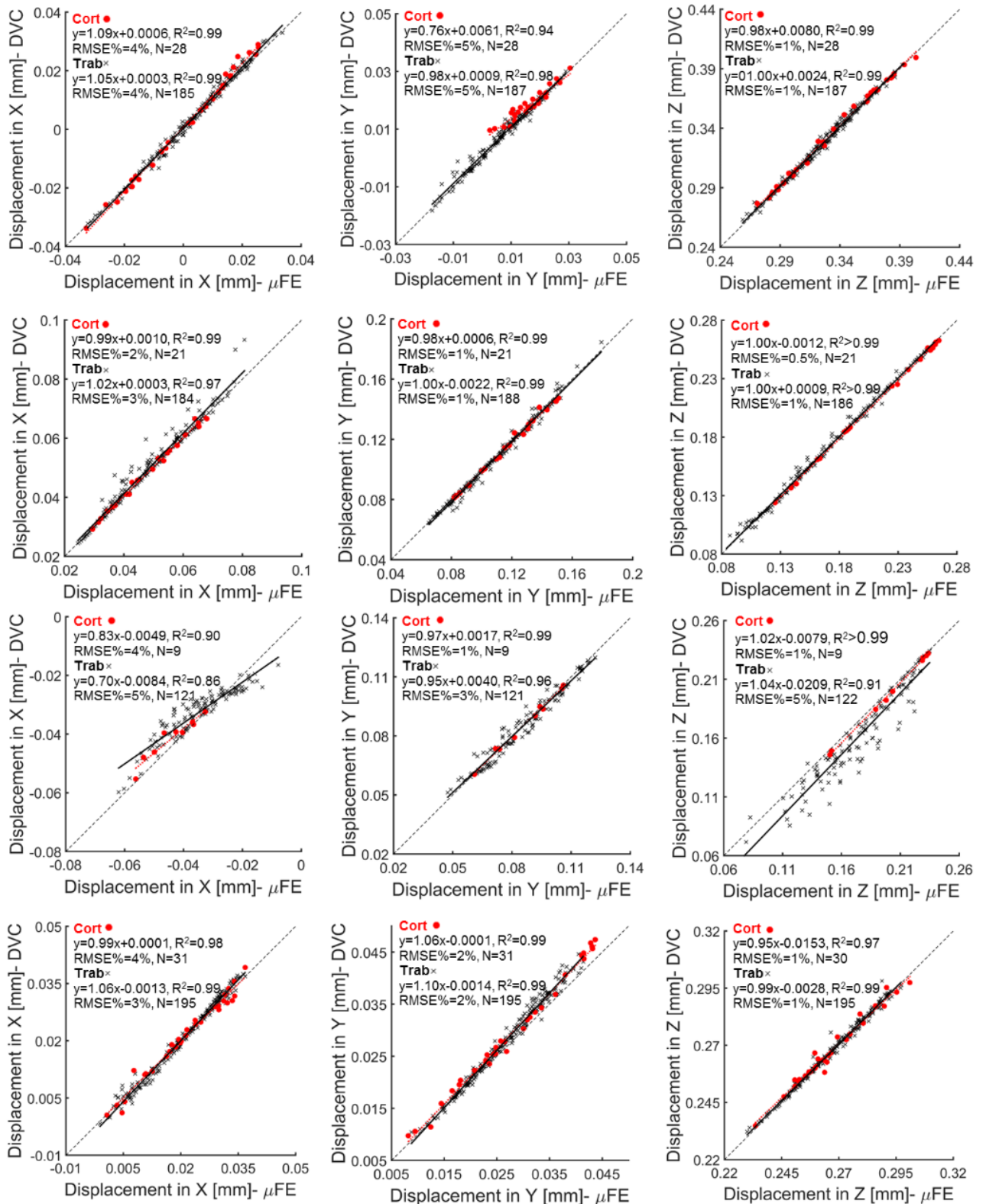


Figure 3.6- Regression analysis of microFE models predictions of local displacements per specimen and bone type. MicroFE models predictions and DVC measurements computed along the transverse (X, Y) and axial (Z) directions for each specimen within cortical (red circles) and trabecular (black crosses) bone regions.

The distribution of the microFE predicted principal strains revealed a predominance of compressive strains for all the specimens. The number of elements with third principal strain ( $\epsilon_{p3}$ ) exceeding the yield value in compression ( $\epsilon_{p3Y}$ ) was always larger (range: 0.3%-13% for  $\epsilon_{p3Y} = -8000 \mu\epsilon$ ) than the number of nodes with first principal strain ( $\epsilon_{p1}$ ) exceeding the yield value in tension ( $\epsilon_{p1Y}$ ; range: 0.01%-0.3% for  $\epsilon_{p1Y} = 7200 \mu\epsilon$ ) (Fig 3.7). S#3 showed the highest percentage of nodes with strain exceeding the compressive yield limit (13%) followed by S#1 (5%), S#4 (2%) and S#2 (0.3%) (Fig 3.7). In S#3 the high strains were located at the bottom portion of the microFE model, which correspond to the region closer to the experimental platen where the load was applied (Fig 3.7). In spite of the difference between the dimensions of the cells used for computing the strain with the DVC (cell size approximately 1872  $\mu\text{m}$ ) and microFE analysis (element size approximately 39 $\mu\text{m}$ ), similar principal strain distributions were observed between both methods for all the specimens (Fig 3.7).

A higher percentage of cortical elements were found to be deformed beyond compressive yield in S#1 and S#4 (proportion of cortical elements with respect to the total number of elements beyond yield in compression: 2.70% for S#1, 0.00% for S#2, 0.04% for S#3, and 0.55% for S#4). No or a very low number of elements were strained above yield in tension in the cortical shell (proportion of cortical elements with respect to the total number of elements beyond yield in tension: 0.00% for S#1, S#2, and S#3, and 0.01% for S#4). To achieve a good agreement between predicted and measured axial forces the tissue modulus had to be decreased from 12.0 GPa to 4.6 GPa through a back-calculation procedure (Fig 3.8).

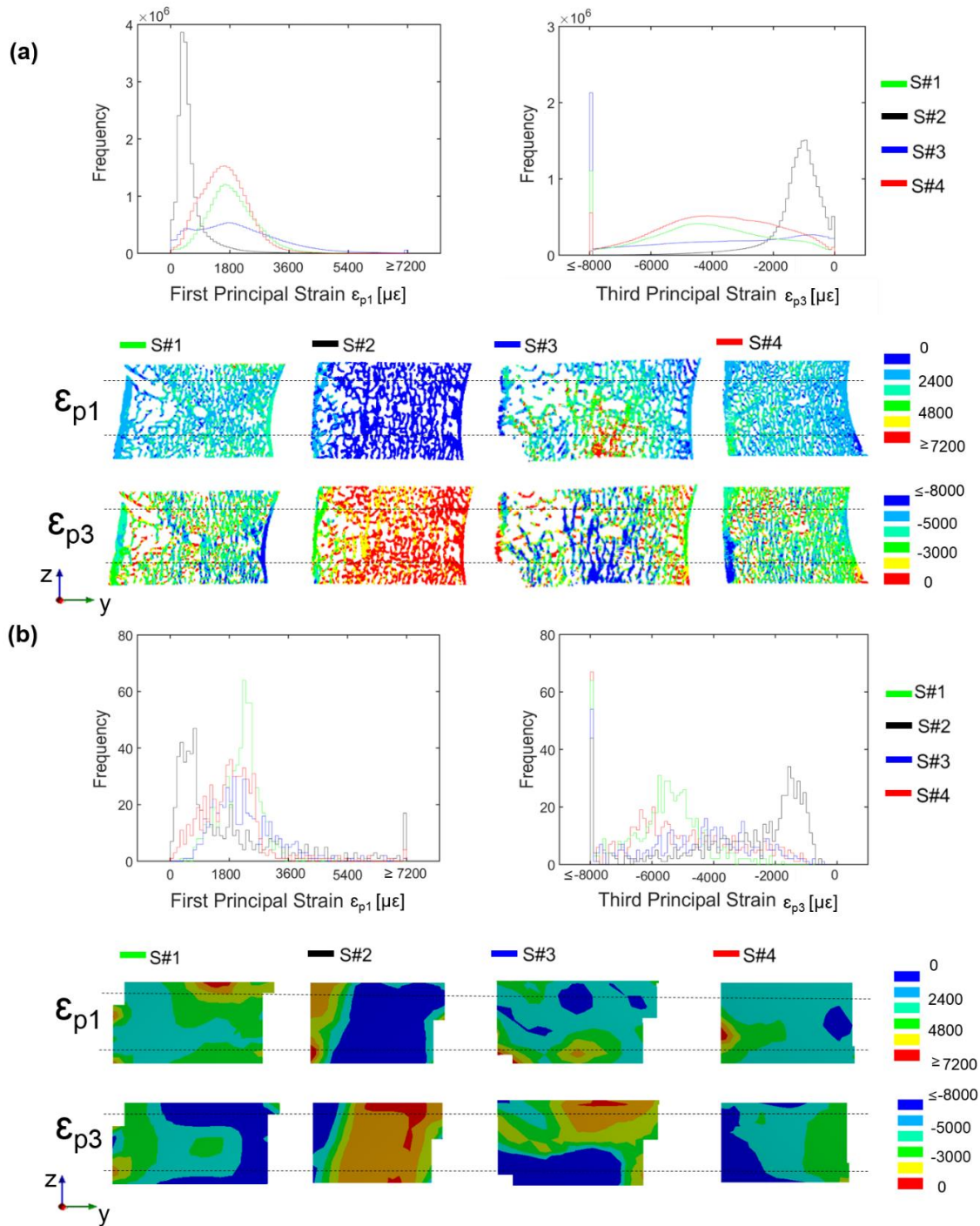


Figure 3.7- Distribution of first and third principal strains from microFE models (a) and DVC measurements (b) for each specimen (Green line S#1, black S#2, blue S#3 and red S#4). For both sub-graphs in the top the frequency plots of the first (tension,  $\epsilon_{p1}$ ) and third (compression,  $\epsilon_{p3}$ ) principal strains are reported for the middle portion of each microFE model (a) and for the corresponding region from the DVC analysis (b). The highest and lowest bins represent the number of elements beyond the yield. For both sub-graphs in the bottom the rendering of strain distribution calculated from the microFE models (a) and DVC analysis (b) are reported for a sagittal mid-section (posterior on the left, anterior on the right) for each specimen. Black dashed lines represent the portion of the microFE models and DVC analysis included in the calculation of the frequency plots.

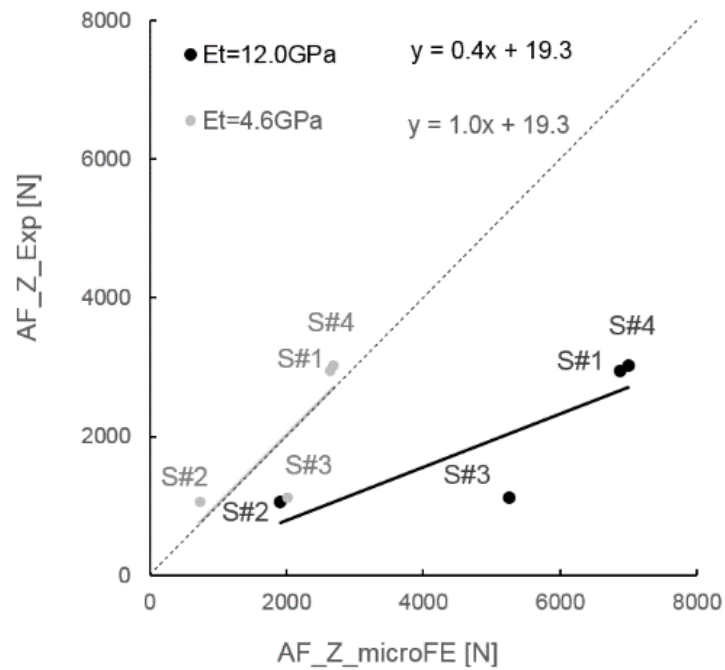


Figure 3.8- Relationship between numerical ( $AF\_Z\_microFE$ ) and experimental ( $AF\_Z\_Exp$ ) measurements of axial force for each specimen. Predictive results obtained from models generated with a tissue modulus ( $E_t$ ) equal to 12.0 GPa (black) or 4.6 GPa (grey).

The axial forces predicted by microFE models with an elastic tissue modulus of 12.0 GPa largely overestimated the experimental values (%diff\_AF between 80% and 369%, Table 3.4). For simulations using the back-calculated tissue modulus of 4.6 GPa, the percentage differences were smaller, between 10% and 80% (Table 3.4). For both  $E_t=12.0$  GPa and  $E_t=4.6$  GPa, S#3 showed the larger residuals.

Table 3.4- Values of axial forces predicted by the microFE models for  $E_t=12.0$  GPa and  $E_t=4.6$  GPa and experimentally measured, for all specimens. The absolute percentage differences (%diff\_AF) between numerical and experimental values are reported.

Specimen ID	AF_Exp [N]	$E_t=12.0$ GPa		$E_t=4.6$ GPa	
		AF_microFE [N]	%diff_AF	AF_microFE [N]	%diff_AF
S#1	2953	6881	133%	2643	10%
S#2	1060	1910	80%	734	31%
S#3	1122	5256	369%	2019	80%
S#4	3028	6999	131%	2689	11%

### 3.4 Discussion

The aim of this study was to validate microFE models predictions of local displacements against an accurate experimental dataset collected from step-wise *in situ* tests performed on four porcine vertebral bodies. For the first time this analyses was also performed in the trabecular and cortical compartments, separately. Furthermore, due to the uncertainty about the elastic tissue modulus to use in the microFE models based on microCT images with resolution of approximately 39  $\mu\text{m}$ , analyses between predicted and measured axial forces for two different tissue moduli were performed.

The results showed that microFE models could predict more than 87% of the variation of local displacements in vertebral bodies in any of the three Cartesian directions (Table 3.3), in line with previous investigations performed on trabecular bone specimens by Chen et al. (2017). The predictive error of the microFE models was lower than 13  $\mu\text{m}$  (1/3 of the voxel size) for three out of four specimens (Table 3.3, Fig 3.5). Smaller errors were observed along the axial direction, which are probably driven by the larger experimental displacements along the direction of compression, Z (RMSE% ranged from 3-5% for UX, and 1-5% for UY and UZ). For three specimens most of the residuals computed for the local displacements were homogeneously distributed and fell within the range of the experimental precision error of the DVC approach (i.e. 3.7  $\mu\text{m}$ , as previously reported by Palanca et al. (2016) using similar specimens) (Fig 3.5). However, for one specimen (S#3) larger differences were found, especially along the axial direction. For that specimen the axial displacements were systematically overestimated by up to 46  $\mu\text{m}$ . This overestimation was probably due to the fact that for S#3, more than 10% of the elements were in the plastic regime (over 13% of the elements were compressed beyond the yield strain of  $-8000 \mu\epsilon$  (Morgan et al., 2001), while for the other specimens only up to 5% of the elements were over the yield strain). Thus, the linear microFE modelling approach used in this study, supported by the linear elastic deformation imposed experimentally to each one of the specimens (typical experimental force-displacement curve represented on the top of Fig 3.1), could not describe the local plastic behaviour of the yielded region. Even though, predictions of local displacements obtained from S#3 were well correlated with the experimental measurements ( $0.86 \leq R^2 \leq 0.91$ ). The good correlation between displacements may have resulted from the reliable reproduction of the experimental displacement-control boundary conditions used in the models, which were obtained through trilinear interpolation of the experimental displacement field obtained from DVC. On the other hand, the fragile internal microstructure of S#3 (low Tot.BV/TV 32.7% vs 40.3-48.6% for the

other specimens, and Tb.Th 198  $\mu\text{m}$  vs 217-241  $\mu\text{m}$  for the other specimens) (Table 3.2) may have affected the distribution of high compressive yield strains in the surroundings of a localised yield region (Fig 3.7). The error of representing a non-linear behaviour using a linear model, especially for S#3, was then evident in predictions of axial forces. Further analysis were performed in order to investigate differences between microFE model predictions for cortical and trabecular bone separately. It was observed that microFE models prediction of local displacements performed equally well for both cortical and trabecular bone (RMSE% for cortical and trabecular bone varied from 1% to 5% for transverse directions and were approximately 1% in the axial direction for all specimens but S#3). The absolute maximum errors of microFE models predictions of local displacements ranged between 3  $\mu\text{m}$  to 7  $\mu\text{m}$  in cortical regions (i.e. 18% the voxel size) while in the trabecular bone it was between 4  $\mu\text{m}$  and 46  $\mu\text{m}$  with S#3, the specimen which seems to be strained beyond the yield, showing the highest errors (see S3.2 Table). In fact, in S#3 most of the yielded elements are in the trabecular regions, which is in agreement with the strain distribution observed along the sagittal cross-section of the specimen's model reported by the DVC (Fig 3.7). While for three out of four specimens most of the elements strained beyond compressive yield were localized in the trabecular region (range: 70% to 100%), for S#1 the yielded elements were evenly distributed in cortical and trabecular regions (48% in trabecular bone, 52% in the cortical shell), highlighting the variability in strain distributions for the different specimens.

This validation study has focused on the comparison of predicted and measured local displacement, due to the fact that reasonable precision of the DVC approach for strain measurements can be obtained only if large nodal spacing (approximately 50 times higher than the element size of the microFE elements) is used, limiting the spatial resolution of the experimental strain measurement. Nevertheless, a qualitative agreement between the strain distributions measured with DVC and predicted by the microFE models is found for all the specimens (Fig 3.7). However, direct quantitative comparison between predicted and DVC measured local strains could be only performed by increasing the resolution of the original input images (for example with Synchrotron radiation microCT images (Palanca et al., 2017)).

A reasonable quantitative agreement between the total axial forces predicted by the microFE models and that measured experimentally was achieved only when a back-calculated elastic tissue modulus of 4.6 GPa was assigned. This value is much lower than that experimentally measured by wet microindentation tests on adult human bone (mean values around 12.0 GPa, Table 3.1) and lower than that back-calculated in other studies performed on adult human

vertebrae (mean values between 5.7 GPa and 8.8 GPa, Table 3.1). It is known that the back-calculation compensates not only for actual material properties, but also for potential limitations in the scanning and modelling approaches: partial volume errors, segmentation errors, the use of a Cartesian mesh, and the assumptions of homogenous, isotropic and linear elastic material properties. The quality of the microCT images used for the reconstruction of bone geometry and microstructures is an important factor for the reliability of microFE models. In previous studies the predictions of microFE models of trabecular bone biopsies were found to be sensitive to the segmentation procedure (Chevalier et al., 2007; Hara et al., 2002) and a small changes in the global threshold (e.g. 6% change to the considered optimum value) were associated to large differences (approximately 50% changes) in predictions of global stiffness, with larger effects for specimens with low bone volume fraction. In this study we have investigated the sensitivity of the microFE models in function of the applied global threshold value for predictions of axial forces. Differences of 3% in the threshold value lead to differences in the predicted axial force between 9% and 29% for microFE run with a back-calculated tissue modulus (i.e. 1%  $\Delta$ AF < 20% excluding S#3 for a decrease of 3% in the threshold value; S1 Supporting Information). Contrary to what has been reported in similar studies (Chevalier et al., 2007; Hara et al., 2002), a worse prediction of axial forces by microFE models generated from higher bone volume fraction specimen was observed (i.e. Tot.BV/TV of S#4 equal to 48% and between 33% and 42% for the other three specimens; S1 Supporting Information). This difference can be due to differences in scanning resolution (15  $\mu$ m and 22  $\mu$ m voxel size in those studies) and bone microarchitecture.

The discretization of bone structures through a tetrahedral mesh could provide better local strain estimations compared to standard Cartesian meshes when applied to trabecular bone (Viceconti, 2016), and may therefore improve the predictions of structural forces. The assumption of local tissue homogeneity seems to have a minor effect on the predictions of microFE models as shown for trabecular bone specimens scanned at a voxel size of 10  $\mu$ m (Gross et al., 2012) or for vertebral bodies scanned with HR-pQCT with 82  $\mu$ m voxel size (Pahr et al., 2011). However, it is not clear yet if for microCT scans with approximately 40  $\mu$ m voxel size this approach would be beneficial. Post-yield (Schwiedrzik et al., 2016; Bevill & Tony M Keaveny, 2009; Verhulp et al., 2008; Bayraktar et al., 2004; Niebur et al., 2000), damage (Levrero-Florencio & Pankaj, 2018; Hambli, 2013; Harrison et al., 2013), and viscoelastic (Sandino et al., 2015; Schwiedrzik, 2014) behaviours have been modelled for trabecular bone specimens, but nonlinear microFE models of whole bones have been limited due to its high

computational demand (Christen et al., 2014; MacNeil & Boyd, 2008). Recently Levrero-Florencio & Pankaj (2018) proposed the use of nonlinear micro FE models with isotropic and anisotropic combined damage formulations to improve the macroscopic damage behaviour of whole bone models in different loading scenarios based on a homogenization scheme applied to microFE models of trabecular samples (i.e. averaging of stresses and strains over a representative volume element of the material). Nevertheless, the computational demand of such models is still a limiting factor (Levrero-Florencio & Pankaj, 2018; Christen et al., 2014; MacNeil & Boyd, 2008). Interestingly, by using creep-recovery experiments, Manda et al. (2016) showed that even at lower stress levels trabecular bone experiences both recoverable and irrecoverable local deformations. Such deformations had a faster trend in specimens with a low bone volume fraction, thus underlining the impact of inter-specimen heterogeneity. The specificity of the back-calculated modulus to a set of specimens, images, and models makes the comparison among similar studies difficult. The differences with respect to the study performed by (Pahr et al., 2011) ( $E_t=8.78$  GPa) may be due to the different age and species (young porcine vs adult human) and the different resolution of the images used (82  $\mu\text{m}$  voxel size in that study vs 39  $\mu\text{m}$  voxel size in this study). For a lower scanning resolution (23  $\mu\text{m}$  voxel size) Ladd et al. found a back-calculated tissue modulus for trabecular bone samples of human vertebra higher than that found in this study ( $6.6\pm 1.1$  GPa, range: 5.4-7.7 GPa, N=5) (Ladd et al., 1998). However, with similar image resolution (50  $\mu\text{m}$  voxel size) Hou et al. found a tissue modulus for human vertebral trabecular bone samples closer to that determined in this study ( $5.7\pm 1.6$  GPa; range: 2.7-9.1 GPa, N=28) (Hou et al., 1998).

The main limitation of this study is the low sample size and the animal origin of the specimens. It remains to be investigated if the different microarchitecture of the human vertebral bodies (i.e. thinner cortical shell and lower density) would affect the predictive ability of microFE models. This detailed validation study limits its applicability to a large sample size and the results obtained from the four specimens confirms the feasibility of this approach. Regarding the effect of using young porcine tissue the assessment is more complicated. In fact, while it is more ethical to perform validation studies on animal tissues, the lack of experimental data reporting the tissue modulus of vertebral bone tissue from young (nine months old) porcine may be an issue. However, the local elastic modulus measured with depth-sensing microindentation in wet conditions from the mid-diaphysis of femurs collected from young pigs at 6-12 months of age (range for osteonal bone: 13.8-19.4 GPa; range for interstitial bone: 17.5-20.0 GPa; computed from the graphs reported by (Feng et al., 2012)) and from adult

human subjects (mean for osteonal bone: 16.2 GPa; mean for interstitial bone: 18.0 GPa; computed from the tables reported by (Mirzaali et al., 2016)) are similar. Therefore, in this study the average elastic tissue modulus reported by (Wolfram et al., 2010a), who performed measurements on human vertebral tissue is used, assuming small differences between young porcine and adult human local elastic properties. A further limitation is the use of simple (but efficient) microFE models (i.e. Cartesian, homogeneous, linear elastic, and isotropic). Nevertheless, the goal of this study was not to optimize the modelling approach but to show the predictive ability of local displacements and of axial forces for the simplest and most commonly used microFE modelling approach.

In conclusion, the results of this study show that homogeneous linear elastic microFE models can be used to accurately predict the local displacements within both cortical and trabecular bone tissue of vertebral bodies, but at the structural level reasonable predictions of axial forces can be achieved only with properly tuned tissue modulus. The good predictions of local mechanical properties found in this validation study provides a fundamental insight for developing reliable models that link local bone deformation with mechano-regulated cell activity, essential for predicting bone remodelling over time.

### 3.5 References

- Bayraktar, H. H., Morgan, E. F., Niebur, G. L., Morris, G. E., Wong, E. K. & Keaveny, T. M. (2004). Comparison of the Elastic and Yield Properties of Human Femoral Trabecular and Cortical Bone Tissue. *Journal of Biomechanics*, 37, 27–35.
- Bevill, G. & Keaveny, T. M. (2009). Trabecular Bone Strength Predictions Using Finite Element Analysis of Micro-Scale Images at Limited Spatial Resolution. *Bone*, 44, 579–584.
- Bevill, G. & Keaveny, T. M. (2009). Trabecular Bone Strength Predictions Using Finite Element Analysis of Micro-Scale Images at Limited Spatial Resolution. *Bone*, 44, 579–84.
- Chen, Y., Dall’Ara, E., Sales, E., Manda, K., Wallace, R. & Viceconti, M. (2017). Micro-CT Based Finite Element Models of Cancellous Bone Predict Accurately Displacement Once the Boundary Condition Is Well Relicated: A Validation Study. *Journal of the Mechanical Behavior of Biomedical Materials*, 65, 644–651.
- Chen, Y., Pani, M., Taddei, F., Mazz, C. & Viceconti, M. (2014). Large-Scale Finite Element Analysis of Human Cancellous Bone Tissue Micro Computer Tomography Data : A Convergence Study. *Journal of Biomechanical Engineering*, 136, 1010131–7.
- Chevalier, Y., Pahr, D., Allmer, H., Charlebois, M. & Zysset, P. (2007). Validation of a Voxel-Based FE Method for Prediction of the Uniaxial Apparent Modulus of Human Trabecular Bone Using Macroscopic Mechanical Tests and Nanoindentation. *Journal of Biomechanics*, 40, 3333–3340.
- Christen, D., Zwahlen, A. & Mu, R. (2014). Reproducibility for Linear and Nonlinear Micro-Finite Element Simulations with Density Derived Material Properties of the Human Radius. *Journal of the Mechanical Behavior of Biomedical Materials*, 29, 500–507.
- Dall’Ara, E., Barber, D. & Viceconti, M. (2014). About the Inevitable Compromise between Spatial Resolution and Accuracy of Strain Measurement for Bone Tissue: A 3D Zero-Strain Study. *Journal of Biomechanics*, 47, 2956–2963.
- Dall’Ara, E., Pahr, D., Varga, P., Kainberger, F. & Zysset, P. (2012). QCT-Based Finite Element Models Predict Human Vertebral Strength in Vitro Significantly Better than Simulated DEXA. *Osteoporosis International*, 23, 563–572.
- Dall’Ara, E., Schmidt, R., Pahr, D., Varga, P., Chevalier, Y., Patsch, J., et al. (2010). A Nonlinear Finite Element Model Validation Study Based on a Novel Experimental Technique for Inducing Anterior Wedge-Shape Fractures in Human Vertebral Bodies in Vitro. *Journal of Biomechanics*, 43, 2374–2380.
- Danesi, V., Tozzi, G. & Cristofolini, L. (2016). Application of Digital Volume Correlation to Study the Efficacy of Prophylactic Vertebral Augmentation. *Clinical Biomechanics*, 39, 14–24.
- Danesi, V., Zani, L., Scheele, A., Berra, F. & Cristofolini, L. (2014). Reproducible Reference Frame for in Vitro Testing of the Human Vertebrae. *Journal of Biomechanics*, 47, 313–318.
- Doube, M., K, M., Arganda-carreras, I., Cordelières, F. P., Dougherty, R. P., Jackson, J. S., et al. (2010). BoneJ : Free and Extensible Bone Image Analysis in ImageJ. *Bone*, 47, 1076–1079.
- Feng, L., Chittenden, M., Schirer, J., Dickinson, M. & Jasiuk, I. (2012). Mechanical Properties of Porcine Femoral Cortical Bone Measured by Nanoindentation. *Journal of Biomechanics*, 45, 1775–1782.

- Fox, J. & Long, S. (1990). *Modern Methods of Data Analysis* (S. Publications, Ed.). Newbury Park, Calif.
- Gillard, F., Boardman, R., Mavrogordato, M., Hollis, D., Sinclair, I., Pierron, F., et al. (2014). The Application of Digital Volume Correlation (DVC) to Study the Microstructural Behaviour of Trabecular Bone during Compression. *Journal of the Mechanical Behavior of Biomedical Materials*, 29, 480–499.
- Grassi, L. & Isaksson, H. (2015). Extracting Accurate Strain Measurements in Bone Mechanics: A Critical Review of Current Methods. *Journal of the Mechanical Behavior of Biomedical Materials*, 50, 43–54.
- Gross, T., Pahr, D. H., Peyrin, F., Zysset, P. K., Gross, T., Pahr, D. H., et al. (2012). Mineral Heterogeneity Has a Minor Influence on the Apparent Elastic Properties of Human Cancellous Bone: A SR MCT-Based Finite Element Study. *Computer Methods in Biomechanics and Biomedical Engineering*, 15, 1137–1144.
- Hambli, R. (2013). Micro-CT Finite Element Model and Experimental Validation of Trabecular Bone Damage and Fracture. *Bone*, 56, 363–374.
- Hara, T., Tanck, E., Homminga, J. & Huiskes, R. (2002). The Influence of Microcomputed Tomography Threshold Variations on the Assessment of Structural and Mechanical Trabecular Bone Properties. *Bone*, 31(1), 107–109.
- Hardisty, M. R., Akens, M. K., Hojjat, S. P., Yee, A. & Whyne, C. M. (2012). Quantification of the Effect of Osteolytic Metastases on Bone Strain within Whole Vertebrae Using Image Registration. *Journal of Orthopaedic Research*, 30, 1032–1039.
- Harrison, N. M., McDonnell, P., Mullins, L., Wilson, N., Mahoney, D. O. & Mchugh, P. E. (2013). Failure Modelling of Trabecular Bone Using a Non-Linear Combined Damage and Fracture Voxel Finite Element Approach. *Biomechanics and Modeling in Mechanobiology*, 12, 225–241.
- Hojjat, S., Beek, M., Akens, M. K. & Whyne, C. M. (2012). Can Micro-Imaging Based Analysis Methods Quantify Structural Integrity of Rat Vertebrae with and without Metastatic Involvement? *Journal of Biomechanics*, 45, 2342–2348.
- Homminga, J., Van-Rietbergen, B., Lochmüller, E. M., Weinans, H., Eckstein, F. & Huiskes, R. (2004). The Osteoporotic Vertebral Structure Is Well Adapted to the Loads of Daily Life, but Not to Infrequent “Error” Loads. *Bone*, 34, 510–516.
- Hou, F. J., Lang, S. M., Hoshaw, S. J., Reimann, D. a. & Fyhrie, D. P. (1998). Human Vertebral Body Apparent and Hard Tissue Stiffness. *Journal of Biomechanics*, 31, 1009–1015.
- Hussein, A., Barbone, P. E. & Morgan, E. F. (2012). Digital Volume Correlation for Study of the Mechanism of Whole Bones. *Procedia IUTAM*, 4, 116–125.
- Jackman, T. M., Delmonaco, A. M. & Morgan, E. F. (2016). Accuracy of Finite Element Analyses of CT Scans in Predictions of Vertebral Failure Patterns under Axial Compression and Anterior Flexion. *Journal of Biomechanics*, 49, 267–275.
- Jackman, T. M., Hussein, A. I., Curtiss, C., Fein, P. M., Camp, A., De, L., et al. (2015). Quantitative, 3-D Visualization of the Initiation and Progression of Vertebral Fractures under Compression and Anterior Flexion. *Journal of Bone and Mineral Research*, 1–37.
- Johnell, O. & Kanis, J. (2006). An Estimate of Worldwide Prevalence and Disability Associated with Osteoporotic Fractures. *Osteoporosis International*, 17, 1726–1733.
- Ladd, A. J. C., Kinney, J. H., Haupt, D. L. & Goldstein, S. A. (1998). Finite-Element Modeling of Trabecular Bone: Comparison with Mechanical Testing and Determination of Tissue Modulus. *Journal of Orthopaedic Research*, 16, 622–628.
- Levrero-Florencio, F. & Pankaj, P. (2018). Using Non-Linear Homogenization to Improve the

- Performance of Macroscopic Damage Models of Trabecular Bone. *Frontiers in Physiology*, 9, 1–15.
- Lin, L. I. (1989). A Concordance Correlation Coefficient to Evaluate Reproducibility. *Biometrics*, 45, 255–268.
- MacNeil, J. a. & Boyd, S. K. (2008). Bone Strength at the Distal Radius Can Be Estimated from High-Resolution Peripheral Quantitative Computed Tomography and the Finite Element Method. *Bone*, 42, 1203–1213.
- Manda, K., Wallace, R. J., Xie, S. & Pankaj, F. L. P. (2016). Nonlinear Viscoelastic Characterization of Bovine Trabecular Bone. *Biomechanics and Modeling in Mechanobiology*, 16, 173–189.
- Mirzaali, M. J., Schwiedrzik, J. J., Thaiwichai, S., Best, J. P., Michler, J., Zysset, P. K., et al. (2016). Mechanical Properties of Cortical Bone and Their Relationships with Age, Gender, Composition and Microindentation Properties in the Elderly. *Bone*, 93, 196–211.
- Morgan, E. F., Yeh, O. C., Chang, W. C. & Keaveny, T. M. (2001). Nonlinear Behavior of Trabecular Bone at Small Strains. *Journal of Biomechanical Engineering*, 123, 1–9.
- Nazarian, A., Von Stechow, D., Zurakowski, D., Müller, R. & Snyder, B. D. (2008). Bone Volume Fraction Explains the Variation in Strength and Stiffness of Cancellous Bone Affected by Metastatic Cancer and Osteoporosis. *Calcified Tissue International*, 83, 368–379.
- Niebur, G. L., Feldstein, M. J., Yuen, J. C., Chen, T. J. & Keaveny, T. M. (2000). High-Resolution Finite Element Models with Tissue Strength Asymmetry Accurately Predict Failure of Trabecular Bone. *Journal of Biomechanics*, 33, 1575–1583.
- Niebur, G. L., Yuen, J. C., Hsia, A. C. & Keaveny, T. M. (1999). Convergence Behavior of High-Resolution Finite Element Models of Trabecular Bone. *Journal of Biomechanical Engineering*, 121, 629–635.
- Oliviero, S., Lu, Y., Viceconti, M. & Dall’Ara, E. (2017). Effect of Integration Time on the Morphometric, Densitometric and Mechanical Properties of the Mouse Tibia. *Journal of Biomechanics*, 65, 203–211.
- Pahr, D. H., Dall’Ara, E., Varga, P. & Zysset, P. K. (2011). HR-PQCT-Based Homogenised Finite Element Models Provide Quantitative Predictions of Experimental Vertebral Body Stiffness and Strength with the Same Accuracy as MFE Models. *Computer Methods in Biomechanics and Biomedical Engineering*, 15, 711–20.
- Palanca, M., Bodey, A. J., Giorgi, M., Viceconti, M., Lacroix, D., Cristofolini, L., et al. (2017). Local Displacement and Strain Uncertainties in Different Bone Types by Digital Volume Correlation of Synchrotron Microtomograms. *Journal of Biomechanics*, in Press.
- Palanca, M., Cristofolini, L., Dall’Ara, E., Curto, M., Innocente, F., Danesi, V., et al. (2016). Digital Volume Correlation Can Be Used to Estimate Local Strains in Natural and Augmented Vertebrae: An Organ-Level Study. *Journal of Biomechanics*, 49, 3882–3890.
- Rietbergen, B. Van, Majumdar, S., Pistoia, W., Newitt, D. C. & Kothari, M. (1998). Assessment of Cancellous Bone Mechanical Properties from Micro-FE Models Based on Micro-CT, PQCT and MR Images. *Technology and Health Care*, 6, 413–420.
- van Rietbergen, B., Weinans, H., Huiskes, R. & Odgaard, A. (1995). A New Method to Determine Trabecular Bone Elastic Properties and Loading Using Micromechanical Finite-Element Models. *Journal of Biomechanics*, 28, 69–81.
- Rietbergen, V. (2000). Prediction of Trabecular Bone Failure Parameters Using a Tissue Failure Criterion and MFE Analysis. *Computer Simulation & Modelling in Medicine*, 1(2), 98–101.

- Roberts, B. C., Perilli, E. & Reynolds, K. J. (2014). Application of the Digital Volume Correlation Technique for the Measurement of Displacement and Strain Fields in Bone: A Literature Review. *Journal of Biomechanics*, 47, 923–934.
- Sandino, C., Mcerlain, D. D., Schipilow, J. & Boyd, S. K. (2015). The Poro-Viscoelastic Properties of Trabecular Bone: A Micro Computed Tomography-Based Finite Element Study. *Journal of the Mechanical Behavior of Biomedical Materials*, 44, 1–9.
- Schwiedrzik, J., Gross, T., Bina, M., Pretterklieber, M., Zysset, P. & Pahr, D. (2016). Experimental Validation of a Nonlinear MicroFE Model Based on Cohesive-Frictional Plasticity for Trabecular Bone. *International Journal for Numerical Methods in Biomedical Engineering*, 32, e02739.
- Schwiedrzik, J. J. (2014). Experimental, Theoretical and Numerical Investigation of the Nonlinear Micromechanical Properties of Bone. *PhD Thesis*. University of Bern, Graduate School for Cellular and Biomedical Sciences.
- Sutcliffe, P., Connock, M., Shyangdan, D., Court, R., Kandala, N. B. & Clarke, A. (2013). A Systematic Review of Evidence on Malignant Spinal Metastases: Natural History and Technologies for Identifying Patients at High Risk of Vertebral Fracture and Spinal Cord Compression. *Health technology assessment (Winchester, England)*, 17, 1–274.
- Tozzi, G., Dall, E., Palanca, M., Curto, M., Innocente, F. & Cristofolini, L. (2017). Strain Uncertainties from Two Digital Volume Correlation Approaches in Prophylactically Augmented Vertebrae: Local Analysis on Bone and Cement- Bone Microstructures. *Journal of the Mechanical Behavior of Biomedical Materials*, 67, 117–126.
- Tozzi, G., Danesi, V., Palanca, M. & Cristofolini, L. (2016). Elastic Full-Field Strain Analysis and Microdamage Progression in the Vertebral Body from Digital Volume Correlation. *Strain*, 52, 446–455.
- Ulrich, D., Van Rietbergen, B., Weinans, H. & Rügsegger, P. (1998). Finite Element Analysis of Trabecular Bone Structure: A Comparison of Image-Based Meshing Techniques. *Journal of Biomechanics*, 31(12), 1187–1192.
- Unnanuntana, A. (2010). The Assessment of Fracture Risk. *The Journal of Bone and Joint Surgery*, 92, 743–753.
- Verhulp, E., Rietbergen, B. Van, Mu, R. & Huiskes, R. (2008). Indirect Determination of Trabecular Bone Effective Tissue Failure Properties Using Micro-Finite Element Simulations. *Journal of Biomechanics*, 41, 1479–1485.
- Viceconti, M. (2016). Can We Trust Micro-FE Models of Bone Tissue? Verification and Validation of Multiple Tissue-Scale Modelling Techniques, 22<sup>rd</sup> Congress of the European Society of Biomechanics, Lyon, France, 10-13<sup>th</sup> July, 2016.
- Wolfram, U., Wilke, H. & Zysset, P. K. (2010a). Valid Micro Finite Element Models of Vertebral Trabecular Bone Can Be Obtained Using Tissue Properties Measured with Nanoindentation under Wet Conditions. *Journal of Biomechanics*, 43, 1731–1737.
- Wolfram, U., Wilke, H. & Zysset, P. K. (2010b). Rehydration of Vertebral Trabecular Bone: Influences on Its Anisotropy, Its Stiffness and the Indentation Work with a View to Age, Gender and Vertebral Level. *Bone*, 46, 348–354.
- Zael, R., Yeni, Y. N., Bay, B. K., Dong, X. N. & Fyhrie, D. P. (2006). Comparison of the Linear Finite Element Prediction of Deformation and Strain of Human Cancellous Bone to 3D Digital Volume Correlation Measurements. *Journal of Biomechanical Engineering*, 128, 1–6.

## Supplementary materials

*S3.1 Table. Statistical analysis for the linear regressions between experimentally measured displacements and those predicted by microFE models generated with the back-calculated elastic tissue modulus  $E_t=4.6$  GPa. Data is reported for predictions along the three Cartesian directions (X and Y in a transverse plane, Z in the axial direction) for all the specimens separately and for pooled data.*

<b>Specimen ID</b>	<b>Direction</b>	<b>Nr. Comparison points (%)</b>	<b>Slope</b>	<b>Intercept [<math>\mu\text{m}</math>]</b>	<b>R<sup>2</sup></b>	<b>RMSE [<math>\mu\text{m}</math>]</b>	<b>RMSE%</b>	<b>MaxError [<math>\mu\text{m}</math>]</b>	<b>CC<sup>1</sup></b>
<b>S#1</b>	UX	213 (98.6%)	1.05	0.33	0.99	1.35	3.99	6.36	0.99
	UY	215 (99.5%)	0.98	1.12	0.97	1.64	5.25	7.42	0.98
	UZ	215 (99.5%)	0.99	3.25	0.99	2.78	0.70	9.20	0.99
<b>S#2</b>	UX	205 (96.7%)	1.01	0.54	0.97	2.31	2.47	12.28	0.98
	UY	209 (98.6%)	1.00	-1.91	0.99	2.33	1.26	10.05	0.99
	UZ	207 (97.6%)	1.00	0.57	1.00	2.91	1.11	10.49	1.00
<b>S#3</b>	UX	130 (99.2%)	0.71	-8.00	0.87	3.11	5.20	12.23	0.87
	UY	130 (99.2%)	0.95	3.85	0.96	3.26	2.72	9.92	0.98
	UZ	131 (100%)	1.05	-22.10	0.91	11.88	5.08	45.86	0.90
<b>S#4</b>	UX	226 (98.7%)	1.05	-1.06	0.98	1.25	3.19	4.50	0.99
	UY	226 (98.7%)	1.09	-1.12	0.99	0.97	2.05	5.05	0.98
	UZ	225 (98.3%)	0.99	4.56	0.99	1.69	0.57	9.33	0.99
<b>Pooled</b>	UX	774 (98.2%)	0.99	1.03	0.99	2.54	2.72	12.28	1.00
	UY	780 (99.0%)	0.98	1.47	1.00	2.18	1.18	10.05	1.00
	UZ	778 (98.7%)	1.04	-10.75	0.99	6.89	1.72	45.86	0.99

S3.2 Table. Additional linear regression analysis between experimental and predicted local displacements for a tissue modulus  $E_t=12.0$  GPa performed for the different bone types (i.e. cortical, Cort, and trabecular, Trab, bones). Data are reported for predictions along the three Cartesian directions (X and Y in a transverse plane, Z in the axial direction) for the individual specimens.

Specimen ID	Direction	Nr. Comparison points (%)	Bone sites	Nr. Comparison points	Slope	Intercept [ $\mu\text{m}$ ]	$R^2$	RMSE%	MaxError [ $\mu\text{m}$ ]
<b>S#1</b>	UX	213 (98.6%)	Cort	28	1.09	0.63	0.99	4.27	6.36
			Trab	185	1.05	0.31	0.99	3.93	4.93
	UY	215 (99.5%)	Cort	28	0.76	6.10	0.91	4.86	6.98
			Trab	187	0.98	0.94	0.98	4.83	7.42
	UZ	215 (99.5%)	Cort	28	0.98	7.96	0.99	0.69	7.47
			Trab	187	1.00	2.38	0.99	0.70	9.20
<b>S#2</b>	UX	205 (96.7%)	Cort	21	0.99	0.99	0.99	1.52	2.67
			Trab	184	1.02	0.32	0.97	2.55	12.56
	UY	209 (98.6%)	Cort	21	0.98	0.57	0.99	1.25	4.37
			Trab	188	1.01	-2.20	0.99	1.28	9.48
	UZ	207 (97.6%)	Cort	21	1.00	-1.17	1.00	0.47	4.36
			Trab	186	1.00	0.89	1.00	1.15	10.79
<b>S#3</b>	UX	130 (99.2%)	Cort	9	0.83	-4.94	0.90	3.64	7.03
			Trab	121	0.70	-8.39	0.86	5.18	12.23
	UY	130 (99.2%)	Cort	9	0.97	1.67	0.99	1.10	2.11
			Trab	121	0.95	3.96	0.96	2.81	9.92
	UZ	131 (100%)	Cort	9	1.02	-7.89	1.00	0.56	5.76
			Trab	122	1.04	-20.92	0.91	5.16	45.86
<b>S#4</b>	UX	226 (98.7%)	Cort	31	0.99	0.12	0.98	4.02	4.50
			Trab	195	1.06	-1.28	0.99	3.09	3.79
	UY	226 (98.7%)	Cort	31	1.06	-0.09	0.99	2.05	3.91
			Trab	195	1.10	-1.40	0.99	2.14	5.05
	UZ	225 (98.3%)	Cort	30	0.95	15.26	0.97	0.83	7.29
			Trab	195	0.99	2.85	0.99	0.51	9.33

## S1. Effect of threshold value on the predictions of the microFE models

In order to analyze the sensitivity of the microFE models predictions in function of the global threshold value, used for image segmentation, a further investigation was performed for models generated with the back-calculated elastic tissue modulus ( $E_t = 4.6$  GPa).

Variations of  $\pm 3\%$  from the optimal threshold values of each specimen were considered as the maximum range that would still allow reasonable reconstructions of bone tissue microstructures for all specimens, based on visual inspection of binary and original grey scale images.

For each specimen three models were generated: one with the optimal threshold value, one with the optimal threshold value increased of 3% and one with the optimal threshold value decreased of 3%. Predictions of local displacements and axial forces against experimental values were performed as described in the manuscript. The accuracy of predicted and experimental local displacements were compared along X, Y, and Z (UX, UY, and UZ) by reporting the Root Mean Square Error percentage (RMSE%). Whereas predicted axial reaction forces were compared to the experimental values (percentage difference, %diff\_AF).

*Table S3.1. Effect of a 3% variation ( $\pm 3\%Th_{opt}$ ) in the optimal threshold values ( $Th_{opt}$ ) of each specimen on microFE models predictions of local (RMSE%\_Ui range for UX, UY, and UZ) and structural (%diff\_AF) properties using  $E_t = 4.6$  GPa.*

Specimen ID	%diff_AF			RMSE%_Ui		
	-3%Th_opt	Th_opt	+3%Th_opt	-3%Th_opt	Th_opt	+3%Th_opt
<b>S#1</b>	1%	10%	19%	1%-5%	1%-5%	1%-5%
<b>S#2</b>	1%	31%	52%	1%-2%	1%-2%	1%-2%
<b>S#3</b>	95%	80%	67%	3%-5%	3%-5%	3%-5%
<b>S#4</b>	20%	11%	36%	1%-3%	1%-3%	1%-4%

A variation of 3% in the threshold value did not affected the predictive power of microFE models predictions of local displacement (i.e. largest difference in RMSE% equal to 0.38%). On the other hand, the microFE models predictions of axial force were very sensitive to small changes in the threshold value. Relative changes of 3% in the threshold lead to differences in microFE models predictions of axial forces ranging from 9% to 29%.



## **Chapter IV. Effect of the size and location of simulated lytic lesions on the structural properties of human vertebral bodies: A feasibility study**

### **Acknowledgments**

This study was performed in collaboration with Mr. John Rochester (Medical teaching unit of the University of Sheffield), who provided and helped to prepare the bone specimens, and Dr. Melissa Ryan, who helped with the scanning and reconstruction of the microCT images used in this chapter.

## Abstract

The lack of an objective method to assess the structural stability of patients with spinal metastasis can mislead the treatment decision making, that in the worst case scenario, can lead to orthopaedic complications that could be avoided. The clinical standard used to evaluate spinal structural instability caused by lytic lesions is the Spinal Instability Neoplastic Score (SINS) system. This system does not account for the effect of the lesion size and location on structural instability. In this study we aim to use an approach validated in the previous Chapter III, which used Finite Element (FE) models based on micro Computed Tomography (microCT) images, to analyse the effect of lytic lesions with different sizes and locations on the vertebral mechanical properties.

A microFE model of a vertebral body obtained from a cadaver donor was generated from a microCT image. Lytic lesions were simulated as local spherical regions of bone loss with 4 different sizes (4%-12%-24%-35% of the vertebral body volume, VBvol) placed in 5 anatomical compartments (centre, lateral right, lateral left, posterior and anterior) of the mid-cross section of the vertebral body. Bone was assumed homogenous, isotropic and linear elastic. Each model with or without lytic lesions was loaded in axial compression. Local and structural properties were computed for each one of the models with simulated lytic lesions and reported with respect to the control model.

The results show a linear relationship between the size of simulated lytic lesions and the difference in structural properties (stiffness and ultimate force) with respect to the control model. Locally, there was a homogeneous redistribution of compressive and tensile principal strains among the models with simulated lytic lesions occupying 35% of the VBvol compared to the control model. Higher strains were observed in the cortical shell and in the regions surrounding the simulated lytic lesions.

This study shows that the size of the lytic lesions, which could be measured through the clinical CT data, is well correlated to the reduction in structural properties of vertebral bodies under compression. Thus, by providing a relationship between the size of lytic lesions and their effect over the structural properties of the vertebrae this approach can help to guide the clinical decision making in a more objective way. However, this is only a feasibility study and a greater sample size and number of parameters will be required to allow a meaningful statistical analysis. Considering the long time required to run the models and to address different loading scenarios, the definition of a larger database was not in the scope of this thesis.

## 4.1. Introduction

Lytic lesions are the most common type of metastases found in the spine (95% of spinal metastases) at advanced stages of a primary cancer (Vialle et al., 2015). These lesions are characterized by focal regions of bone loss, which cause an increase in bone fragility and risk of pathological fractures (Burke et al., 2018; Hardisty et al., 2012; Ebihara et al., 2004). Clinically, spinal instability, and consequently the risk of fracture of metastatic vertebrae is assessed through a scoring method named Spinal Instability Neoplastic Score (SINS) system, which takes into account the presence of pain, the type of lesion, spinal alignment, vertebral body collapse, and posterior involvement. This is a qualitative method which does not provide a clear guidance for patients who are classified as having undetermined spinal stability, for whom the treatment relies on clinical experience. Moreover, this method lacks of accuracy in predicting true negative cases (specificity equal to 79.5%) which increases the risks for the patients to develop further complications related to the invasive surgical procedure used for spinal stabilization (Vialle et al., 2015; Sutcliffe et al., 2013). Therefore, a more objective evaluation of spinal stability is required, to better identify the lesions which need treatment. The SINS system does not account for the properties of the lesion, as its size and location, in the estimation of vertebral stability. These parameters are already used for the assessment of stability of long bones affected by metastatic lesions (Mirels' scoring system). However, it remains to be investigated if the properties of the lesion play an important role in the vertebral mechanical properties.

Parametric finite element (FE) models have been used to better understand the importance of the size and location of lytic lesions on the risk of burst fracture initiation (Galbusera et al., 2018; Tschirhart et al., 2004; Whyne et al., 2001, 2003). The literature in this field evolved from the validation and use of idealised geometries of human vertebrae (L1) modelled with homogeneous material properties (Tschirhart et al., 2004; Whyne et al., 2001, 2003; Mizrahi et al., 1992), to the modelling of subject-specific geometries and material heterogeneities from medical images (Galbusera et al., 2018). Moreover, lytic lesions have been modelled as holes within bone (Mizrahi et al., 1992), or as regions within bone either with poro-elastic material properties (Tschirhart et al., 2004; Whyne et al., 2001, 2003) or homogeneous material properties with low stiffness and compressibility (Galbusera et al., 2018). These models showed that the effect of the size of the simulated lytic lesions on the risk of initiation of vertebral burst fractures (associated to measures of maximum radial and axial displacements and load-induced canal narrowing) was more critical than that of the location of the lytic lesions

within the vertebral body (Galbusera et al., 2018; Tschirhart et al., 2004). Specifically, the size of the lytic lesions caused for an increase of approximately 8-fold in axial displacements for lesions occupying 30% of the volume of the vertebral body, while the location of the lesions caused only an increase of up to 5% in axial displacements (Galbusera et al., 2018; Tschirhart et al., 2004). However, both types of models did not account for the intrinsic morphology of the bone tissue and the complex microarchitecture within the vertebral body.

Experimentally there has been some controversy about the effect of the size of mechanically induced lytic lesions (as drilled holes) on the strength of human vertebrae. For instance Windhagen et al. (1997) showed no correlation between failure load and the size of induced lytic lesions obtained from human vertebrae (n=19, from T5 and T11 levels) tested under eccentric compression. Silva et al. (1993) observed a weak relationship between the size of induced transcortical lytic lesions (i.e. involvement of the cortical shell) and the strength reduction of human thoracic vertebrae computed with respect to control vertebrae (without lesions) under eccentric compression ( $R^2=0.26$ , from T3 to T12 levels, n=62 for control vertebrae and n= 45 for vertebrae with simulated lesions). Transcortical lesions caused larger reductions in strength (Silva et al., 1993) compared to induced lesions disrupting mainly the trabecular bone (McGowan et al., 1993), as shown by similar studies. On the contrary, an experimental study performed on thoracic sheep vertebrae showed a good correlation between the cross-section size of induced lytic lesions and the failure load ( $R^2=0.78$ , n=12 for control vertebrae and n=87 for vertebrae with simulated lesions from T7 to T12) measured for motion segments tested under eccentric compression (Ebihara et al., 2004). Recent experiments, performed with a digital image correlation technique, showed a significant increase in the values of principal strains distributed along the anterior surface of the human vertebral body for artificial lesions larger than 30% of the vertebral body volume. Additionally, a relationship between the progression of the strain pattern and the failure location was shown (Palanca et al., 2018).

On the other hand, it is still unknown how lytic lesions affect the local behaviour of the vertebral bone tissues and how this translates to the structural level. Recently, FE models generated from high resolution images, named microFE models, have been validated for predictions of local properties, as displacements and strains, of vertebral bodies (Chapter III) (Costa et al., 2017). MicroFE models were also accurate in predicting structural properties ( $R^2 \geq 0.88$  for vertebral strength) (Dall'Ara, 2012; Pahr et al., 2011). By resolving bone microstructure, these models can provide a better and more detailed understanding about the

effect of musculoskeletal pathologies which affect bone structures, such as lytic bone lesions, on the local and structural properties of bones. Therefore, the aim of this study was to develop a computational framework based on microFE models to analyse the effect of the size and location of simulated lytic lesions on the local and structural behaviour of bone tissues.

## 4.2. Materials and methods

Four cadaveric spines fixed in formaldehyde which included vertebral segments from L5 to T7 were obtained from 2 females and 2 males donors ranging the 67-101 years old. The cadaveric spines were provided by the Medical Teaching Unit of the University of Sheffield, and the study was approved by the ethics committee of the University of Sheffield (reference number 012716). From each spine, vertebral motion segments from T12 to L2 were isolated and the posterior elements were removed. Each vertebral motion segment included 3 vertebral bodies, the upper and bottom intervertebral discs surrounding the mid-vertebra, and all the other soft-tissues. The specimens were submerged in a phosphate-buffered saline (PBS) solution (pH=7.4) overnight (for approximately 15h) before scanning.

Only the middle vertebra of each vertebral segment (i.e. L1) was scanned in a microCT scanner (Viva 80 of Scanco Medical, Bruttisellen, Switzerland) with a voltage of 70 kVp, an intensity of 114 mA, an integration time of 300 ms, and an isotropic voxel size of 39  $\mu\text{m}$  similar to Hussein et al. (2012). This protocol allowed the reconstruction of images similar to those used in Chapter III, which shows the validation of the methodology used in this study. The specimens were kept hydrated in saline solution during the scanning. Only one out of the four specimens scanned was adequate to model due to the presence of lytic lesions, large osteophytes, or very low trabecular bone density (which suggest osteopenia or osteoporosis) in the remaining 3 specimens. In order to reduce the dimension of the models and the computational time, 20% of the height of the chosen vertebral body (measured as the total height of the microCT images) was removed from the top and bottom endplates, and a vertebral body section of approximately 20 mm height was obtained from the original microCT images (Fig 4.1 left side). The 3D microCT images of the vertebral body section were smoothed, using a Gauss filter (kernel=3 and  $\sigma=1.2$ ) (Chen et al., 2017) in order to reduce high frequency noise. Due to the presence of partial volume effects, the images were then segmented using a single level threshold value. The choice for the single level threshold value that best captured the microarchitecture of bone, relied on the visual inspection performed between cross-sections of binary and grey scale images. After segmentation a connectivity filter was used to remove bone

voxels without face connectivity (Chen et al., 2017). The final segmented image was used to measure the volume of bone (BV) of the specimen and to generate the microFE model. To measure the total volume of the vertebral body section (VBvol) and its total bone volume fraction (Tot.BV/TV), a masked image of the vertebral body section was generated using the procedure described in a previous chapter (Chapter III section 2.2.3). Both morphological parameters were measured using the BoneJ 1.4.1 plug-in (Doubé et al., 2010) of ImageJ 1.50e software (Schneider et al., 2012). A reconstructed surface of the specimen was generated from the masked image using the marching cube algorithm (Amira v6.0.1, Thermo Fisher Scientific, Oregon, USA). This surface was used to align the vertebral body section along the anatomical transverse plane based on an *in silico* reference framework (Danesi et al., 2014). This procedure required the definition and alignment of a set of landmarks defined at the right and left edges of the posterior wall of the top endplate (BuilderM2O 1.0 Build 140) (more details in Chapter V, section 5.2.1).

From the segmented image a microFE model, called control model, was generated by converting every bone voxel of the vertebral body section into an 8-noded linear hexahedral element (see Chapter III section 2.2.5). The model was then aligned based on the rigid transformation obtained from the alignment step. Homogeneous, isotropic, and linear elastic material properties were assumed for bone with an elastic tissue modulus of 12GPa (Wolfram et al., 2010a) and a Poisson's ratio of 0.3. An axial compression of 1% apparent strain was applied to the nodes of the cranial section of the vertebral body, whereas the nodes of the caudal section were constrained in all directions.

From this control model 20 other parametric microFE models were generated with simulated lytic lesions of different sizes occupying different locations within the middle cross-section plane of the vertebral body (Fig 4.1). Simulated lytic lesions were modelled as focal spherical regions of bone loss (i.e. holes) which were designed to be placed within the vertebral body volume. The size of the lesion was defined as a function of the volume of the vertebral body section (VBvol). Lesions occupying 4%, 12%, 24%, and 35% of the VBvol were simulated. Each lesion was then placed in the central, lateral right, lateral left, anterior, and posterior compartments of the middle cross-section of the vertebral body. The location of the centre of each lesion was defined with respect to a local cylindrical coordinate system set within the geometric centre of the middle cross-section of the model (Fig 4.1- right side). The most lateral, and anterior-posterior points of the mid-section of the model were obtained and used together with the lesions size to define the radial position (R) of the centre of each lesion (Fig 4.1- right

side). The angular position ( $\theta$ ) of the centre of each lesion varied from  $0^\circ$  to  $270^\circ$  with increments of  $90^\circ$  (Fig 4.1 right side). In particular, the centre of the lesions occupying 4% VBvol matched the centre of the lesions occupying 12% VBvol as it was defined based on radius of the latter (Fig 4.1 yellow dashed lines). Lesions with 24% VBvol or 35% VBvol had their own centres varying based on their sizes (Fig 4.1- blue and green dashed lines). Thus, the three biggest lesions simulated in this study (i.e. 12%-24%-35% VBvol) were tangent to the cortical shell of the vertebral body (Fig 4.1). Each model was simulated under the same boundary conditions of the control model. In terms of computational demand, the number of DOF of the models with simulated lytic lesions varied from 278 million to 366 million. The corresponding running times (including solving and post-processing) varied from 5 hours to 28 hours in the FE software Mechanical APDL (ANSYS® Academic Research, Release 15.0) using parallel distributed memory over a maximum of 64 cores on the shared memory High-Performance Computing cluster of the Insigneo Institute named Beagle (2.70GHz, 104 cores, 1.7TB of RAM).

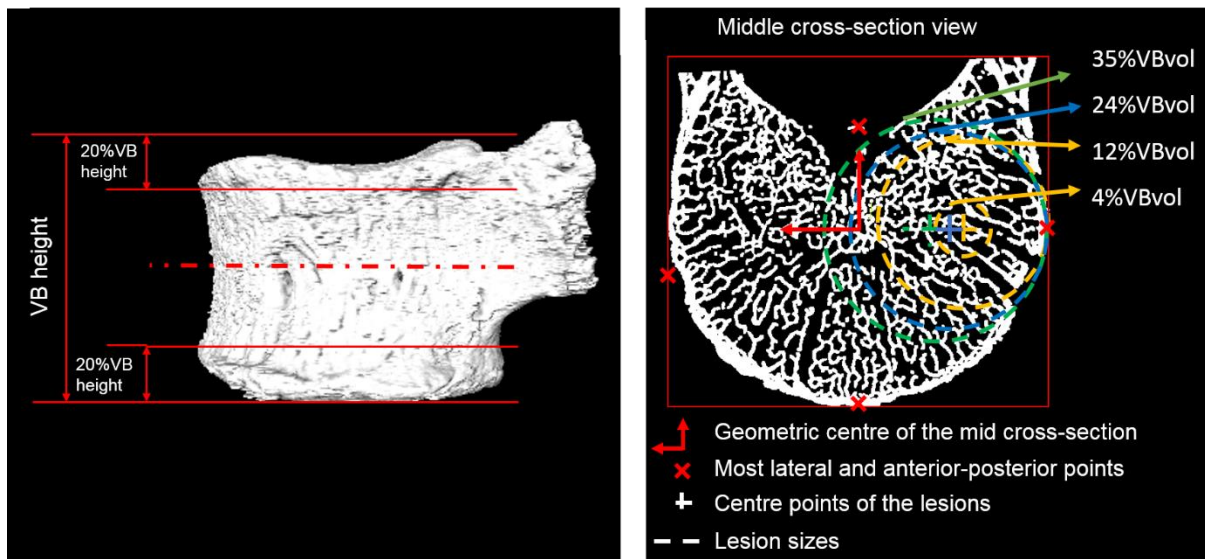


Figure 4. 1- Left: Representation of the pre-processing operations performed for the definition of the vertebral body section model (cropping of the endplates in 20% of the vertebral body height). Right: Middle cross-section of the vertebral model, used to set up the position of the simulated lytic lesions in function of the distance between the geometric centre of the mid-section and the most lateral and anterior-posterior points (red crosses), and the size of the lesions. Illustration of lesions occupying 4%, 12% (orange), 24% (blue), and 35% (green) of the VB vol, placed over the lateral left compartment of the mid-cross section of the vertebral model.

Spring stiffness ( $K$ ) was computed for each model as the ratio between the sum of the axial reaction forces estimated from the caudal section of each model and the applied displacement. The ultimate force ( $F_U$ ) was estimated as the force required to cause the yield, in compression ( $\epsilon_{p3Y} = -8000 \mu\epsilon$ ) or tension ( $\epsilon_{p1Y} = 7200 \mu\epsilon$ ), of 2% of the elements of the model. The percentage difference found between the structural properties ( $K$  and  $F_U$ ) estimated from the vertebral models with and without simulated lytic lesions was computed to analyse the effect of the simulated lesions. Moreover, the distribution of third and first principal strains of models with and without simulated lytic lesions was computed from the middle 70% in height of the vertebral body section. Local strain distributions were analysed by frequency plots and plots obtained from the mid-cross section of the models.

### 4.3. Results

The decrease in structural properties computed for the models with simulated lytic lesions with respect to the control model ranged from 3% to 30% (Table 4.1).

Strong linear relationships were found between the size of the simulated lytic lesions and the decrease in predicted structural properties ( $K$  and  $F_U$ ) ( $R^2 \geq 0.99$ , intercept between  $-0.004$  and  $-0.049$  %) (Fig 4.2).

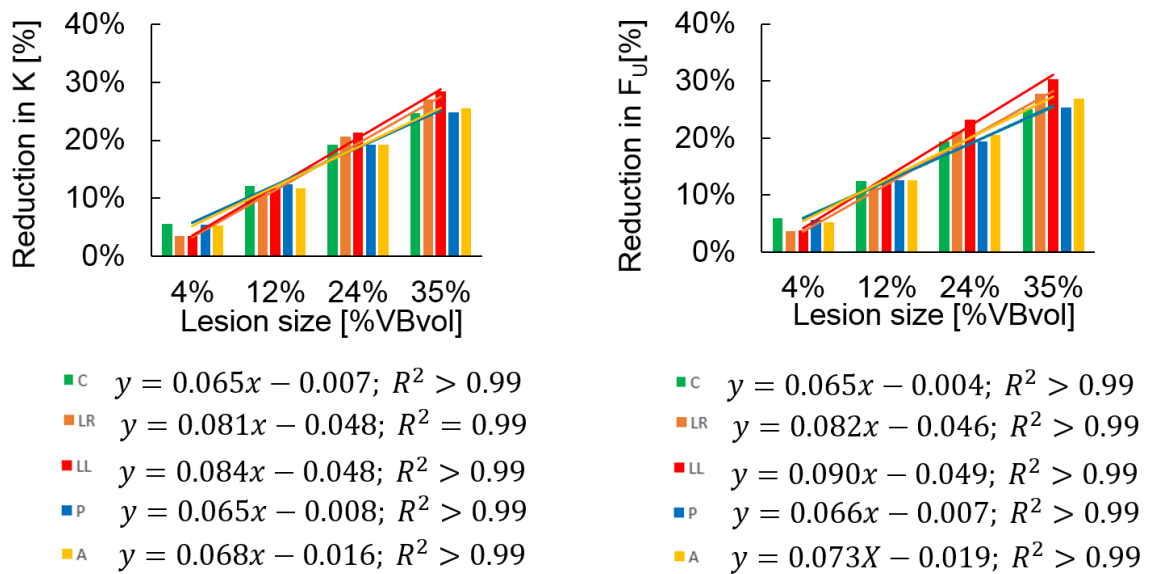


Figure 4.2- Percentage reduction of predicted structural properties (spring stiffness,  $K$ , and ultimate force,  $F_U$ ) caused by lytic lesions simulated with different sizes (4%, 12%, 24%, and 35% of the VBvol) and in different locations (C: centre, LR: lateral right, LL: lateral left, P: posterior, and A: anterior).

In particular, lesions occupying from 4% to 12% of the VBvol located in the central and in the most anterior-posterior compartments of the vertebral body caused a similar reduction in  $K$  and  $F_U$  as lesions of the same size located in the most lateral compartments (% reduction in  $K$  and  $F_U$  between 5%-13% for lesions located in the central, anterior, and posterior regions of the vertebral body against 3%-13% obtained for lateral lesions) (Table 4.1). Lesions occupying 24% and 35% of the VBvol located in the most lateral compartments of the vertebral body had a slightly higher impact over the predicted structural properties compared to lesions located in the central and anterior-posterior regions of the vertebral body (21%-30% reduction in  $K$  and  $F_U$  for lateral lesions against 19%-27% reduction for the other lesion location) (Table 4.1).

Table 4.1- Structural properties (spring stiffness,  $K$ , and ultimate forces,  $F_u$ ) predicted from the vertebral models with and without simulated lytic lesions. Simulated lytic lesions grouped based on their sizes, and location (C: centre, LR: lateral right, LL: lateral left, P: posterior, and A: anterior).

Model ID	Lesion size [%VBvol]	Lesion location	K [kN/mm]	%diff K [%]	Fu [kN]	%diff Fu [%]
<b>Control</b>	-	-	70.6	-	8.2	-
<b>L#1</b>		C	66.6	6%	7.7	6%
<b>L#2</b>		LR	68.2	3%	7.9	4%
<b>L#3</b>	4%	LL	68.1	4%	7.9	4%
<b>L#4</b>		P	66.8	5%	7.7	6%
<b>L#5</b>		A	66.9	5%	7.8	5%
<b>L#6</b>		C	62.0	12%	7.2	12%
<b>L#7</b>		LR	63.0	11%	7.3	11%
<b>L#8</b>	12%	LL	62.3	12%	7.1	13%
<b>L#9</b>		P	61.8	12%	7.2	13%
<b>L#10</b>		A	62.3	12%	7.2	13%
<b>L#11</b>		C	57.0	19%	6.6	19%
<b>L#12</b>		LR	56.1	21%	6.5	21%
<b>L#13</b>	24%	LL	55.6	21%	6.3	23%
<b>L#14</b>		P	57.0	19%	6.6	19%
<b>L#15</b>		A	57.0	19%	6.5	21%
<b>L#16</b>		C	53.1	25%	6.2	25%
<b>L#17</b>		LR	51.5	27%	5.9	28%
<b>L#18</b>	35%	LL	50.5	28%	5.7	30%
<b>L#19</b>		P	53.1	25%	6.1	25%
<b>L#20</b>		A	52.6	25%	6.0	27%

At the local level, there was a generally homogeneous distribution of axial strains within the bone tissues of the models with and without simulated lytic lesions (mean $\pm$ standard deviation of  $-5000\pm 3000 \mu\epsilon$  for the third principal strains,  $\epsilon_{P3}$ , and  $2000\pm 1000 \mu\epsilon$  for the first principal strains,  $\epsilon_{P1}$ ) (Fig 4.3 and 4.4).

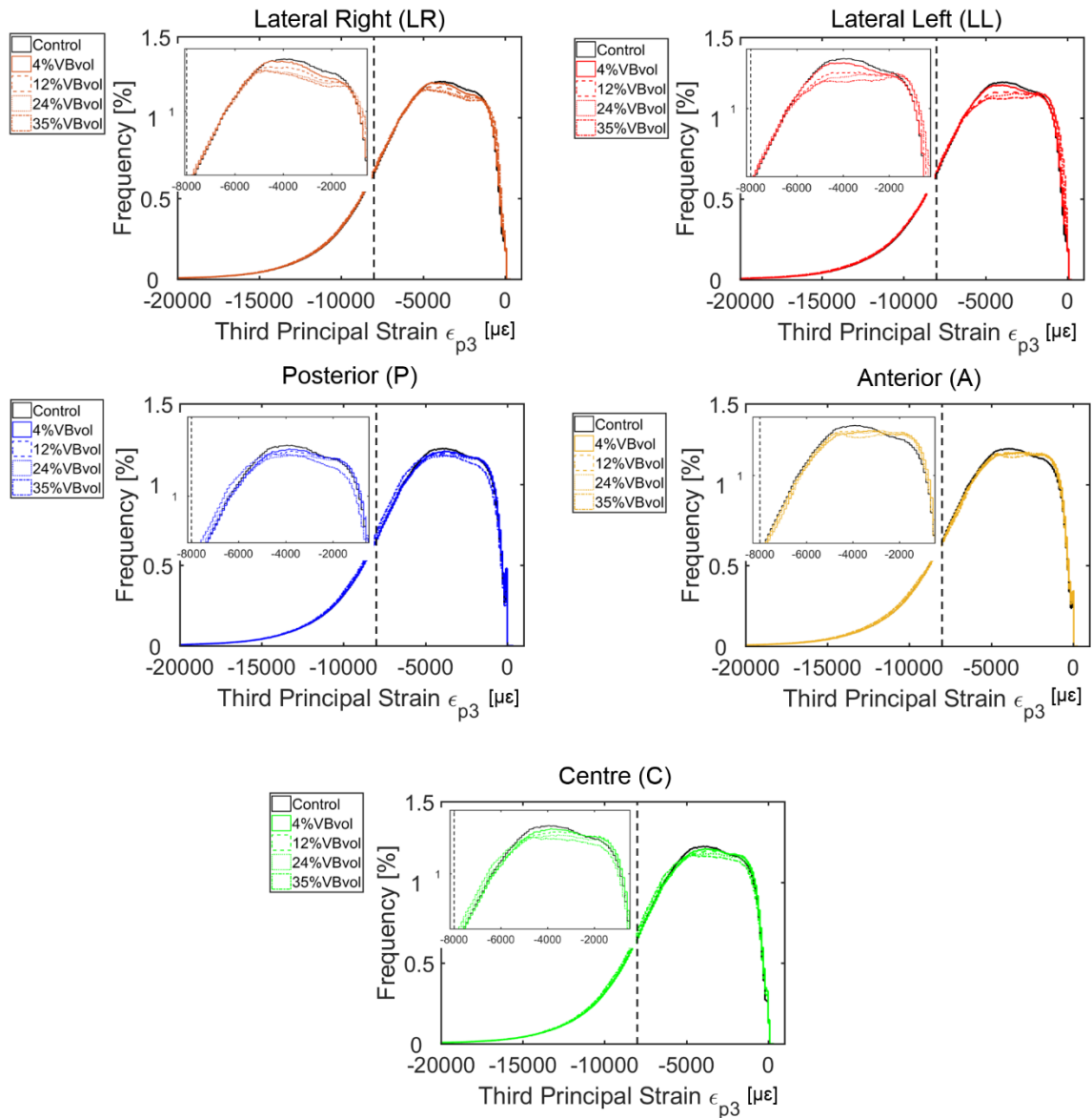


Figure 4.3- Distribution of the third principal strains obtained from the parametric models of simulated lytic lesions based on the location (centre, C; lateral right, LR; lateral left, LL; anterior, A; and posterior, P regions of the mid-cross section of the model) and size (4%, 12%, 24%, and 35% of the VBvol) of the lesions compared to the control model (solid black lines).

As expected, the predominant failure mode of the models with and without simulated lytic lesions was in compression (approximately 97% of the elements showed third principal strains over the compressive yield strain considered as  $\epsilon_{p3Y} = -8000 \mu\epsilon$ , whereas the remaining 3% of the elements showed tensile yield strains higher than  $\epsilon_{p1Y} = 7200 \mu\epsilon$  (Morgan et al., 2001)).

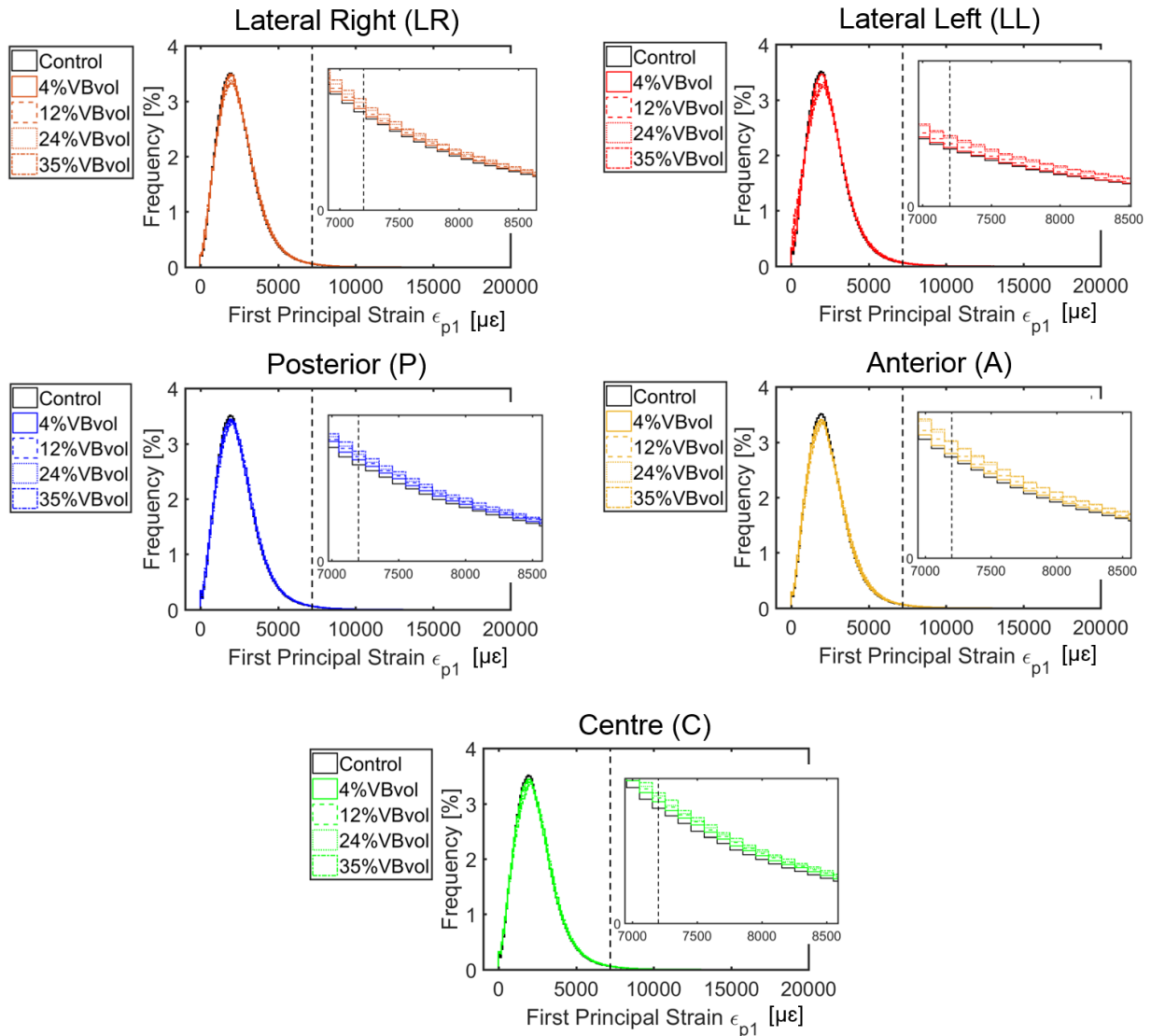


Figure 4.4- Distribution of the first principal strains obtained from the parametric models of simulated lytic lesions based on the location centre, C; lateral right, LR; lateral left, LL; anterior, A; and posterior, P regions of the mid-cross section of the model) and size (4%, 12%, 24%, and 35% of the VBvol) of the lesions compared to the control model (solid black lines).

Locally, a high concentration of compressive strains was observed in the cortical shell of the mid cross-section of the vertebrae for the models with and without simulated lytic lesions (Fig 4.5, 4.6 and Figs S4.1 and S4.2 of the supplementary material). Some concentration of compressive and tensile principal strains in the bone tissues surrounding the lesion was also observed for all the parametric models (Fig 4.5, 4.6 and Figs S4.1 and S4.2 of the supplementary material). Nevertheless, similar distributions of principal strains were observed in the other regions of the models with or without simulated lesions (control versus L#1 to L#20) (Fig 4.3-4.6 and Figs S4.1 and S4.2 of the supplementary material).

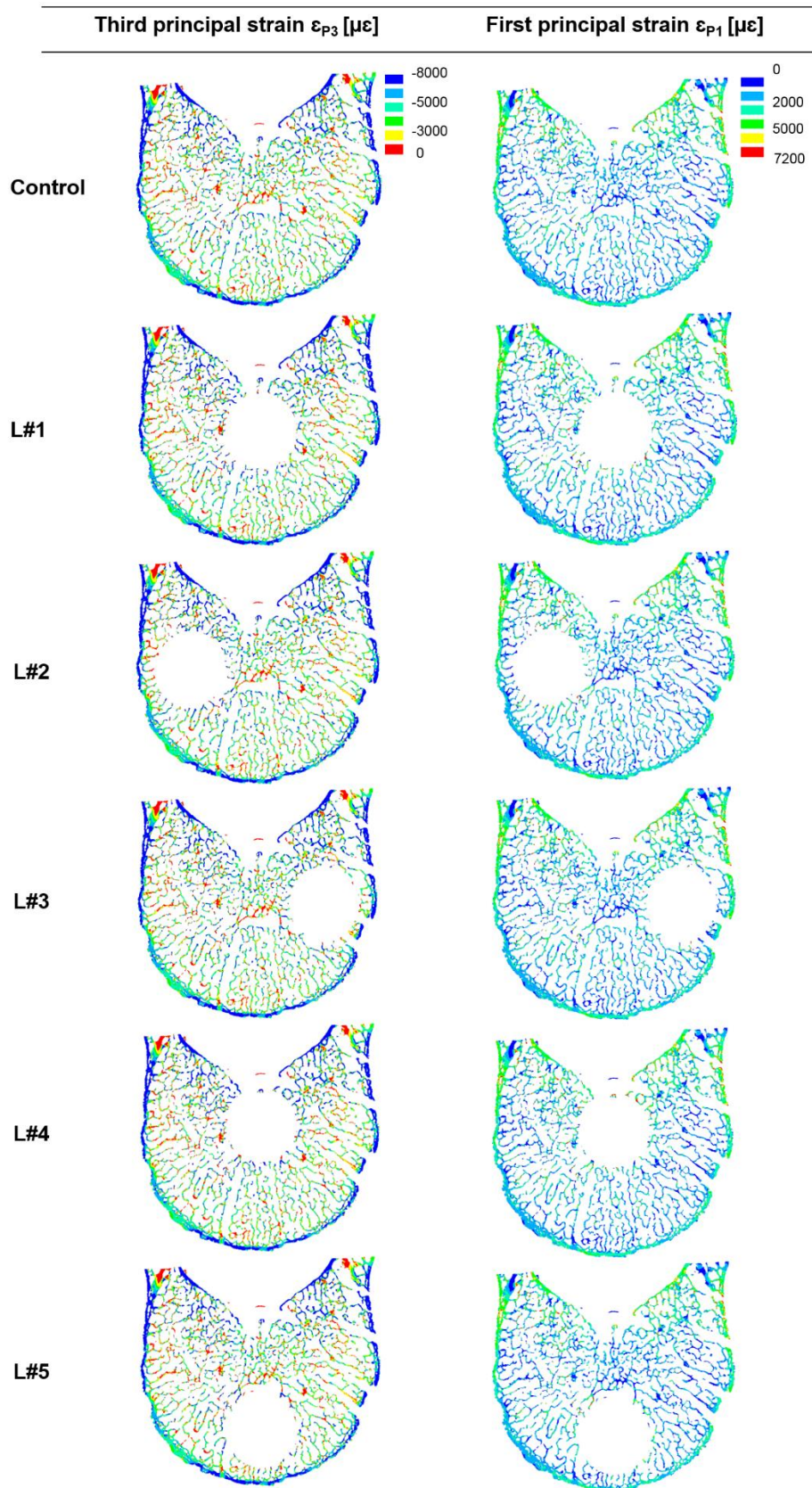


Figure 4.5- Distribution of third and first principal strain along the mid-cross section of the of the control model (top) against the models with simulated lesions of 4% of the VBvol placed in the central (L#1), lateral right (L#2), lateral left (L#3), posterior (L#4), and anterior (L#5) regions of the vertebral body.

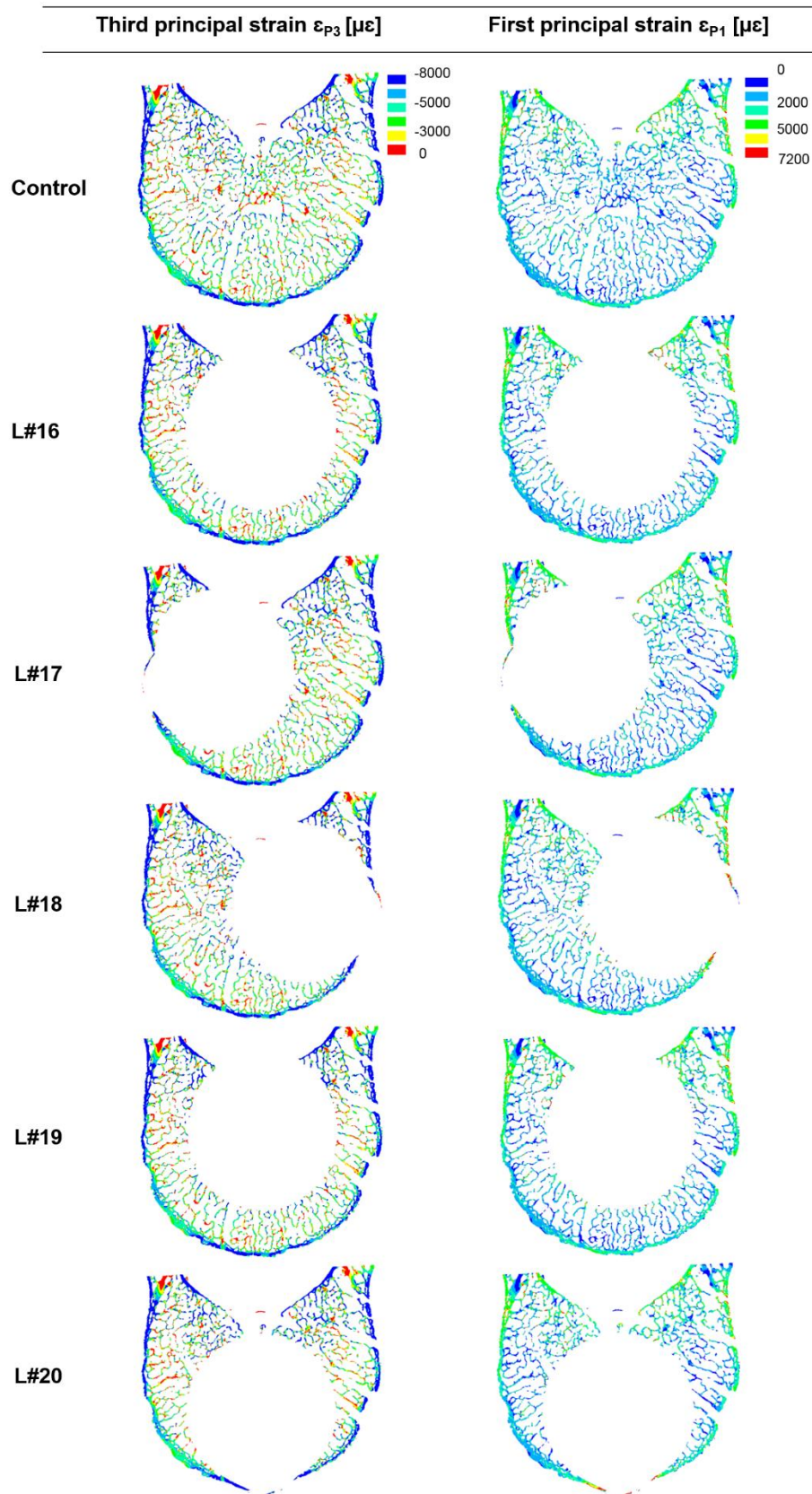


Figure 4.6- Distribution of third and first principal strain along the mid-cross section of the control model (top) against the models with simulated lesions of 35% VBvol placed in the central (L#16), lateral right (L#17), lateral left (L#18), posterior (L#19), and anterior (L#20) regions of the vertebral body.

Lesions involving the cortical shell (i.e. size between 12% and 35% of the VBvol) placed over the anterior (Fig 4.7) and most lateral regions (Fig S4.3 and S4.4 of the supplementary material) of the vertebral body showed a redistribution of the compressive and tensile strains observed along the frontal surface of the vertebral body in comparison to the control model. An increase in size of the simulated lesions adjacent to the anterior cortical shell caused a slight increase of the compressive and tensile principal strains surrounding the lesion (Fig 4.7 L#10 to L#20).

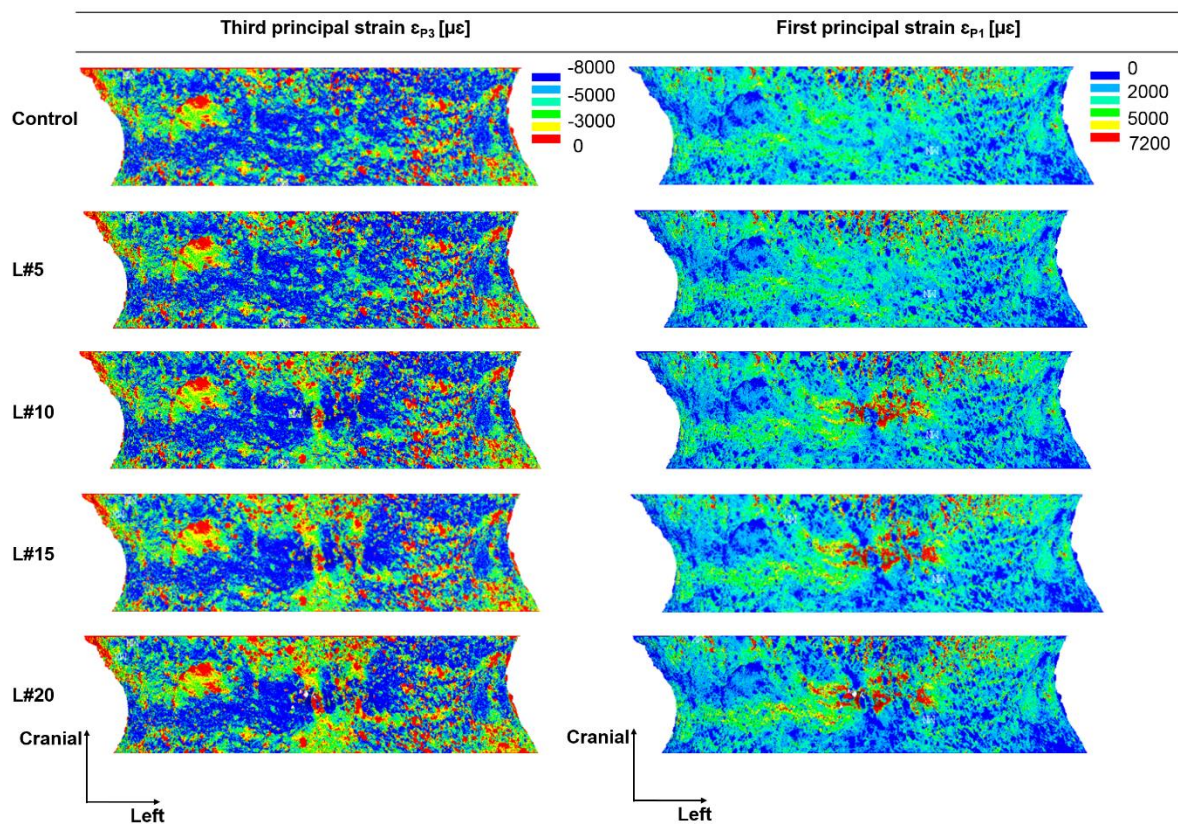


Figure 4.7- Distribution of third and first principal strains obtained from the middle 70% in height of the vertebral body. Plots show the frontal surface view of the control model (top) against the models with simulated lytic lesions of 4% VBvol (L#5), 12% VBvol (L#10), 24% VBvol (L#15), and 35% VBvol (L#20). Lesions located in the most anterior region of the vertebral body.

On the other hand, there was no difference in the strain distribution pattern observed along the frontal surface of all the models with simulated lesions placed over the central and posterior regions of the vertebral body (i.e. no damage of the frontal side cortical shell) compared to the control model (Fig 4.8).

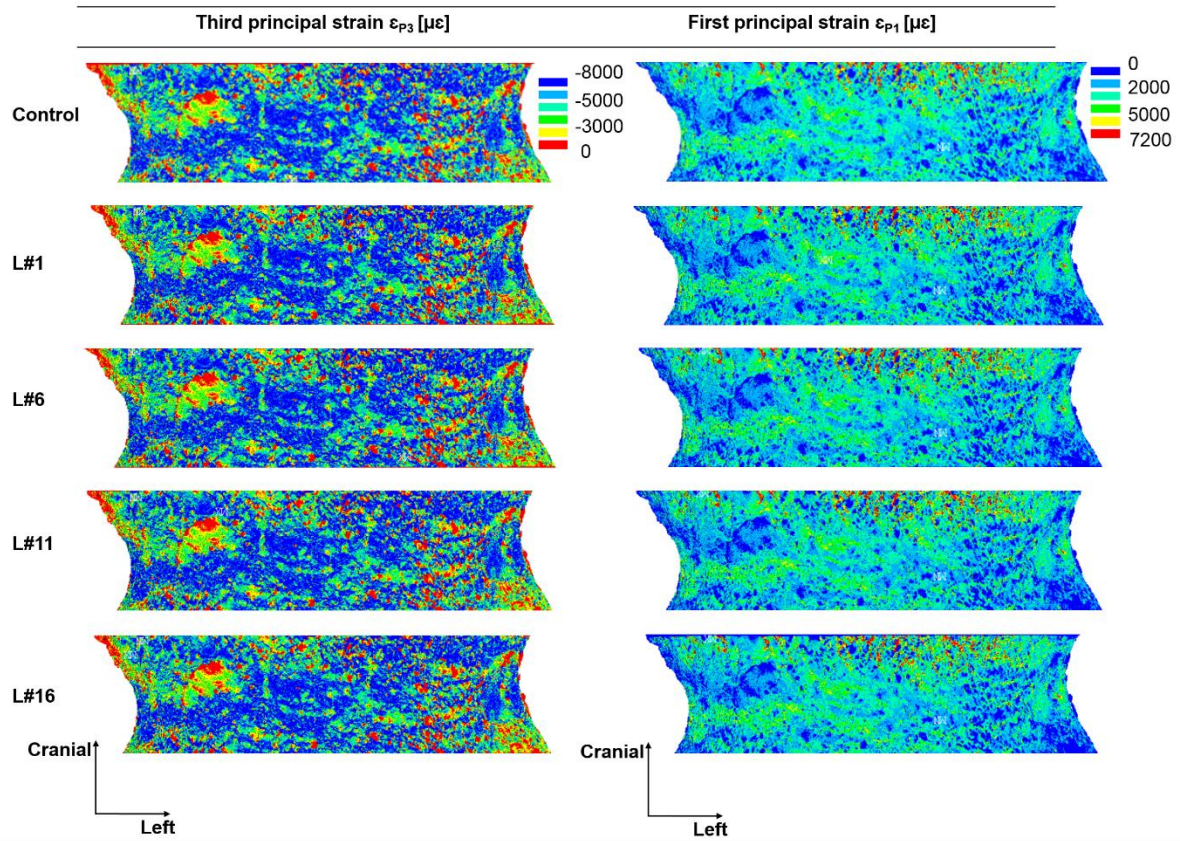


Figure 4.8- Distribution of third and first principal strains obtained from the middle 70% in height of the vertebral body. Plots show the frontal surface view of the control model (top) against the models with simulated lytic lesions of 4% VBvol (L#1), 12% VBvol (L#6), 24% VBvol (L#11), and 35% VBvol (L#16). Lesions located in the centre of the vertebral body.

## 4.4. Discussion

The aim of this study was to propose a method to evaluate the effect of the size and location of simulated lytic lesions on the local and structural properties of the human vertebral body using a previously validated microFE modelling method (see Chapter III).

In the previous chapter it was shown that microFE models are accurate in predicting local properties but limited in predicting structural properties for vertebral bones due to its specificity to the material properties of the bone tissues (Chapter III). Therefore, in this study these models were used to predict relative changes in structural properties induced by simulated lytic lesions with different properties (size and location). The size of the simulated lytic lesions was linearly related to the decrease in predicted structural properties. Experimentally, only weak to moderate linear correlations were found between the size of induced lytic lesions and the reductions in failure forces measured with respect to control human vertebrae (without lesions) (Windhagen et al., 1997; Silva et al., 1993). The strong linear correlations observed in this study resulted in part from the use of homogeneous displacement-control boundary conditions and of linear elastic models. Moreover, the majority of the lesions simulated in this study were placed at the border of the vertebral body implying a disruption of the cortical shell which is shown to hold most of the deformation applied to the vertebrae. There is only one case, in this study, where the induced lesions affect only the trabecular bone tissues, exhibiting thus an unbalanced analysis over the effect of the size of lytic lesions occupying the different bone structures which can be influencing the analysis too. Thus, it remains to be investigated whether the same linear relationship would hold for an increase of the range of parameters included in the parametric analysis and of the sample size. Due to limitations in the computational time required to run this models this was not the aim of the study.

The variability in predicted ultimate forces of the vertebrae with simulated lytic lesions was smaller than the values obtained from experimental studies where human vertebral bodies with induced lytic lesions, occupying 25% of the trabecular bone volume of the vertebral body, were compressed (Coefficient of variation, CV of 10% for the spring stiffness and ultimate force predicted in this study against CV of up to 49% for the spring stiffness and 54% for ultimate forces predicted by Matsuura et al. (2014)). The smaller variability found in this study may result from the use of a single vertebral sample for the parametric analysis performed in this study. On the other hand, the combined effects of the location and size of the lesions on the predicted structural properties did not show a clear trend. It was observed that lesions greater than 25% VBvol located over the most lateral compartments of the vertebral body caused a

slightly higher decrease in structural properties compared to lesions of the same size located over the central and anterior-posterior regions. However, the range of structural properties predicted in these groups was similar, and thus, for the sample size used in this study, it was not possible to evaluate what would be the most critical locations of the lytic lesions, for the considered loading conditions. Similar results were found in the literature, showing a higher effect of the size of simulated lytic lesions compared to its location, on the local properties of the vertebrae (e.g. radial and axial endplate displacements, and maximum principal strains) which are often associated to the risk of burst fracture initiation (Galbusera et al., 2018; Tschirhart et al., 2004; Whyne et al., 2001, 2003). These findings also agree with the experimental studies that showed no relationship between the location and failure force of vertebrae with simulated lytic lesions (Windhagen et al., 1997; Silva et al., 1993).

At the local level, the compressive and tensile principal strains were homogeneous among all the models with and without simulated lytic lesion (Figs 4.3 and 4.4). High compressive and tensile principal strains (Figs 4.5, 4.6 and Supplementary material Figs S4.1 and S4.2) and stresses (Supplementary material Fig S4.6), were mostly located in the cortical shell and in the bone tissues surrounding the lesions. The lytic lesions simulated in this study, which occupied up to 35% VBvol, involving in some cases both the trabecular and cortical bone microstructures, had a minor impact on the first and third principal strains. However, it was observed a reduction in the distribution of the local maximum and minimum principal stresses along the frontal mid-section of the vertebral models with lesions of 35% VBvol compared to the control model (Supplementary material Fig S4.7). Such observation explains the reduction in structural properties observed for the models with lytic lesions. The reduction in the local stresses was localized over the bone tissues surrounding the lesions (Supplementary material Fig S4.7). A great concentration of low principal stresses was observed along the rightmost and leftmost regions of the vertebral body for the models with lateral lesions, regions which were more affected by a loss of connectivity among the bone tissues induced by the simulated lesions.

In comparison with the control model, the distribution of compressive and tensile strains observed along the frontal surface of the vertebral body was only affected by lesions involving the cortical shell located in the anterior and lateral compartments of the vertebral body. In particular, lesions placed in the anterior compartment of the vertebra and involving the cortical shell (12% to 35% VBvol) caused a concentration of strains over the anterior wall of the vertebral body (Fig 4.7 and Fig S4.3 and S4.4 of the supplementary material). For these lesions,

it was observed a progression of high strains over the middle of the anterior surface of the vertebral body, which is in line with the results obtained for healthy vertebral bodies under compression (Hussein et al., 2018). In a recent study, significant differences in the strain distribution patterns measured in the anterior surface of vertebrae with mechanically induced lytic lesions were only observed for lesions larger than 30% of the VBvol (Palanca et al., 2018). This study also showed a significant increase in the average strains measured in the anterior surface of vertebrae with lesions greater than 30% of the VBvol. Similar results were obtained by Mizrahi et al. (1992) who observed an increase in the peak stresses caused by polyhedral-like virtually simulated lesions, which occupied 40% of the volume of the vertebral centrum including the cortical shell, using homogenized and homogeneous FE models of idealized shapes of the vertebral body loaded in eccentric anterior compression. Such increase in strains was not observed in this study. The different results observed in this study may be explained by the different loading condition and types of lesions. In particular, in this study we used axial compression while other studies used eccentric compression with anterior bending applied to single vertebral bodies (Mirzaali et al., 2016) or to spinal motion segments composed by 3 vertebrae with adjacent intervertebral discs (Palanca et al., 2018). Furthermore, in this study an ideal spherical lesion was simulated, while in Palanca et al. (2018) lesions were generated from two opened holes accessed from the pedicles up to the anterior wall of the vertebral body. Moreover, in the present study we did not model multiple lesions with increased sizes affecting mainly the trabecular structures of the vertebral body as in Palanca et al. (2018). In the present study the boundary conditions were approximated based on the experimental loading of individual vertebral bodies which is typically performed through embedded top and bottom endplates, in displacement-control axial compression. This assumption was required in order to have models that would run in a reasonable time and that could be used on the computational resources available. Nevertheless, it means that we did not account for the deformation of the endplates or other relevant structures, such as the intervertebral disks, which are important in the physiological loading distribution (Palanca et al., 2018; Ruspi et al., 2017).

In this study, lytic lesions were modelled as focal spherical regions of bone loss. This assumption seemed to be reasonable based on the inspection of some real lytic lesions from the clinical data shown in Chapter VI. However, it is clear from the analysis of the clinical images of Chapter VI that lesions are heterogeneous in geometry and distribution (i.e. focal versus widespread lesions), and thus some could be better approximated by other geometrical shapes (i.e. cylindrical or elliptic). Moreover, in this study lytic lesions were assumed as hole-like

structures. The same simplification has also been used in experimental studies due to the difficulty in reproducing the cancer-like tissues which compose the lesions (Palanca et al., 2018; Alkalay & Harrigan, 2016; Ron N. Alkalay, 2015; Silva et al., 1993). On the other hand, the present computational framework have the advantage of allowing the simulation of lytic lesions within the trabecular tissues of the vertebrae without causing any damage over the cortical shell, contrary to what happens for experimentally induced lesions.

This study uses a methodology, which was validated in the previous chapter III for porcine vertebral bodies. There are differences between the porcine and human vertebral bone tissues which are evident at the microstructural level. For instance, the mean trabecular thickness of healthy human vertebrae ranges between 100  $\mu\text{m}$  and 400  $\mu\text{m}$  (Bevill & Tony M Keaveny, 2009; Fields et al., 2009a), whereas for the porcine tissues studied in Chapter III the mean trabecular thickness was of approximately 200  $\mu\text{m}$ . To avoid inaccuracies coming from the Cartesian discretization of the models, the image voxel size should be less or equal to  $\frac{1}{4}$  of the mean trabecular thickness (Niebur et al., 1999; van Rietbergen et al., 1995). This means that the current method would be limited in capturing low density trabeculae tissues, with mean thickness inferior than 150  $\mu\text{m}$ . However, this was not a problem for the sample used in this study, in which the mean trabecular thickness was  $204\pm 59$   $\mu\text{m}$  (computed using a procedure similar to the one used in morphological analysis presented in Chapter III).

Despite the potential of the parametric analyses in exploring a wide range of properties of lytic lesions (size and location), this study was restricted to the parametrization of only 4 different sizes and 5 different locations due to the still high computational demand of the microFE models, which contained between 278 and 376 million DOF. Further studies should also consider an increase of the sample size to account for differences in microstructure, as in this study we only explored the feasibility of the parametric routine for a single sample. To conclude, if we increase the number of parameters of the analysis and the sample size, in order to have a sample that describes the typical population of patients affected by vertebral metastases, we could provide a meaningful analysis of the effect of lytic lesions on the vertebral mechanical properties. Such approach could be included in the SINS to help for a more objective classification of patients with lytic spinal metastases.

## 4.5. References

- Alkalay, R. N. (2015). Effect of the Metastatic Defect on the Structural Response and Failure Process of Human Vertebrae: An Experimental Study. *Clinical Biomechanics*, 30(2), 121–128.
- Alkalay, R. N. & Harrigan, T. P. (2016). Mechanical Assessment of the Effects of Metastatic Lytic Defect on the Structural Response of Human Thoracolumbar Spine. *Journal of Orthopaedic Research*, 34(10), 1808–1819.
- Bevill, G. & Keaveny, T. M. (2009). Trabecular Bone Strength Predictions Using Finite Element Analysis of Micro-Scale Images at Limited Spatial Resolution. *Bone*, 44, 579–84.
- Burke, M., Akens, M., Kiss, A., Willett, T. & Whyne, C. (2018). Mechanical Behavior of Metastatic Vertebrae Are Influenced by Tissue Architecture, Mineral Content, and Organic Feature Alterations. *Journal of Orthopaedic Research*, 1–10.
- Chen, Y., Dall'Ara, E., Sales, E., Manda, K., Wallace, R. & Viceconti, M. (2017). Micro-CT Based Finite Element Models of Cancellous Bone Predict Accurately Displacement Once the Boundary Condition Is Well Relicated: A Validation Study. *Journal of the Mechanical Behavior of Biomedical Materials*, 65, 644–651.
- Costa, M. C., Tozzi, G., Cristofolini, L., Danesi, V., Viceconti, M. & Dall'Ara, E. (2017). Micro Finite Element Models of the Vertebral Body: Validation of Local Displacement Predictions. *PLoS ONE*, 12(7), 1–18.
- Dall'Ara, E., Pahr, D., Varga, P., Kainberger, F. & Zysset, P. (2012). QCT-Based Finite Element Models Predict Human Vertebral Strength in Vitro Significantly Better than Simulated DEXA. *Osteoporosis International*, 23, 563–572.
- Doube, M., K, M., Arganda-carreras, I., Cordelières, F. P., Dougherty, R. P., Jackson, J. S., et al. (2010). BoneJ : Free and Extensible Bone Image Analysis in ImageJ. *Bone*, 47, 1076–1079.
- Ebihara, H., Ito, M., Abumi, K., Taneichi, H., Kotani, Y., Minami, A., et al. (2004). A Biomechanical Analysis of Metastatic Vertebral Collapse of the Thoracic Spine: A Sheep Model Study. *Spine*, 29(9), 994–999.
- Fields, A. J., Eswaran, S. K., Jekir, M. G. & Keaveny, T. M. (2009). Role of Trabecular Microarchitecture in Whole-Vertebral Body Biomechanical Behavior. *Journal of Bone and Mineral Research*, 24(9), 1523–1530.
- Galbusera, F., Qian, Z., Casaroli, G., Bassani, T., Costa, F., Schlager, B., et al. (2018). The Role of the Size and Location of the Tumors and of the Vertebral Anatomy in Determining the Structural Stability of the Metastatically Involved Spine: A Finite Element Study. *Translational Oncology*, 11(3), 639–646.
- Hardisty, M. R., Akens, M. K., Hojjat, S. P., Yee, A. & Whyne, C. M. (2012). Quantification of the Effect of Osteolytic Metastases on Bone Strain within Whole Vertebrae Using Image Registration. *Journal of Orthopaedic Research*, 30, 1032–1039.
- Hussein, A., Barbone, P. E. & Morgan, E. F. (2012). Digital Volume Correlation for Study of the Mechanism of Whole Bones. *Procedia IUTAM*, 4, 116–125.
- Hussein, A. I., Louzeiro, D. T. & Morgan, E. F. (2018). Differences in Trabecular Microarchitecture and Simplified Boundary Conditions Limit the Accuracy of Quantitative Computed Tomography-Based Finite Element Models of Vertebral Failure. *Journal of Biomechanical Engineering*, 140, 1–11.
- Matsuura, Y., Giambini, H., Ogawa, Y., Fang, Z., Thoreson, A. R., Yaszemski, M. J., et al.

- (2014). Specimen-Specific Nonlinear Finite Element Modelling to Predict Vertebrae Fracture Loads after Vertebroplasty. *Spine*, 39(22), E1291–E1296.
- McGowan, D. P., Hipp, J. A., Takeuchi, T., White, A. A. & Hayes, W. C. (1993). Strength Reductions from Trabecular Destruction within Thoracic Vertebrae. *Journal of Spinal Disorders*, 6(2), 130–6.
- Mirzaali, M. J., Schwiedrzik, J. J., Thaiwichai, S., Best, J. P., Michler, J., Zysset, P. K., et al. (2016). Mechanical Properties of Cortical Bone and Their Relationships with Age, Gender, Composition and Microindentation Properties in the Elderly. *Bone*, 93, 196–211.
- Mizrahi, J., Silva, M. J. & Hayes, W. C. (1992). Finite Element Stress Analysis of Simulated Metastatic Lesions in the Lumbar Vertebral Body. *Journal of Biomedical Engineering*, 14(6), 467–475.
- Morgan, E. F., Yeh, O. C., Chang, W. C. & Keaveny, T. M. (2001). Nonlinear Behavior of Trabecular Bone at Small Strains. *Journal of Biomechanical Engineering*, 123, 1–9.
- Niebur, G. L., Yuen, J. C., Hsia, A. C. & Keaveny, T. M. (1999). Convergence Behavior of High- Resolution Finite Element Models of Trabecular Bone. *Journal of Biomechanical Engineering*, 121, 629–635.
- Pahr, D. H., Dall’Ara, E., Varga, P. & Zysset, P. K. (2011). HR-PQCT-Based Homogenised Finite Element Models Provide Quantitative Predictions of Experimental Vertebral Body Stiffness and Strength with the Same Accuracy as MFE Models. *Computer Methods in Biomechanics and Biomedical Engineering*, 15, 711–20.
- Palanca, M., Barbanti Brodano, G. & Cristofolini, L. (2018). The Size of Simulated Lytic Metastases Affects the Strain Distribution on the Anterior Surface of the Vertebra. *Journal of Biomechanical Engineering*, 140, 1–9.
- van Rietbergen, B., Weinans, H., Huiskes, R. & Odgaard, A. (1995). A New Method to Determine Trabecular Bone Elastic Properties and Loading Using Micromechanical Finite-Element Models. *Journal of Biomechanics*, 28, 69–81.
- Ruspi, M. L., Palanca, M., Faldini, C. & Cristofolini, L. (2017). Full-Field in Vitro Investigation of Hard and Soft Tissue Strain in the Spine by Means of Digital Image Correlation. *Muscles, Ligaments and Tendons Journal*, 7(4), 538–545.
- Schneider, C. A., Rasband, W. S. & Eliceiri, K. W. (2012). NIH Image to ImageJ: 25 Years of Image Analysis. *Nature Methods*, 9(7), 671–5.
- Silva, M. J., Hipp, J. A., McGowan, D. P., Takeuchi, T. & Hayes, W. C. (1993). Strength Reductions of Thoracic Vertebrae in the Presence of Transcortical Osseous Defects: Effects of Defect Location, Pedicle Disruption, and Defect Size. *European Spine Journal*, 2(3), 118–125.
- Sutcliffe, P., Connock, M., Shyangdan, D., Court, R., Kandala, N. B. & Clarke, A. (2013). A Systematic Review of Evidence on Malignant Spinal Metastases: Natural History and Technologies for Identifying Patients at High Risk of Vertebral Fracture and Spinal Cord Compression. *Health technology assessment (Winchester, England)*, 17, 1–274.
- Tschirhart, C. E., Nagpurkar, A. & Whyne, C. M. (2004). Effects of Tumor Location, Shape and Surface Serration on Burst Fracture Risk in the Metastatic Spine. *Journal of Biomechanics*, 37(5), 653–660.
- Vialle, L. R., Gokaslan, Z. L., Fisher, C. G. & Boriani, S. (2015). *AOSpine Master Series. Volume 1. Metastatic S* (L. R. Vialle, Ed.). New York, NY: Thieme Medical Publishers, Inc.
- Whyne, C. M., Hu, S. S. & Lotz, J. C. (2001). Parametric Finite Element Analysis of Vertebral Bodies Affected by Tumors. *Journal of Biomechanics*, 34(10), 1317–1324.

- Whyne, C. M., Hu, S. S. & Lotz, J. C. (2003). Burst Fracture in the Metastatically Involved Spine: Development, Validation, and Parametric Analysis of a Three-Dimensional Poroelastic Finite-Element Model. *Spine*, 28(7), 652–660.
- Windhagen, H. J., Hipp, J. A., Silva, M. J., Lipson, S. J. & Hayes, W. C. (1997). Predicting Failure of Thoracic Vertebrae With Simulated and Actual Metastatic Defects. *Clinical Orthopaedics and Related Research*, 344, 313–319.
- Wolfram, U., Wilke, H. & Zysset, P. K. (2010). Valid Micro Finite Element Models of Vertebral Trabecular Bone Can Be Obtained Using Tissue Properties Measured with Nanoindentation under Wet Conditions. *Journal of Biomechanics*, 43, 1731–1737.

## Supplementary material

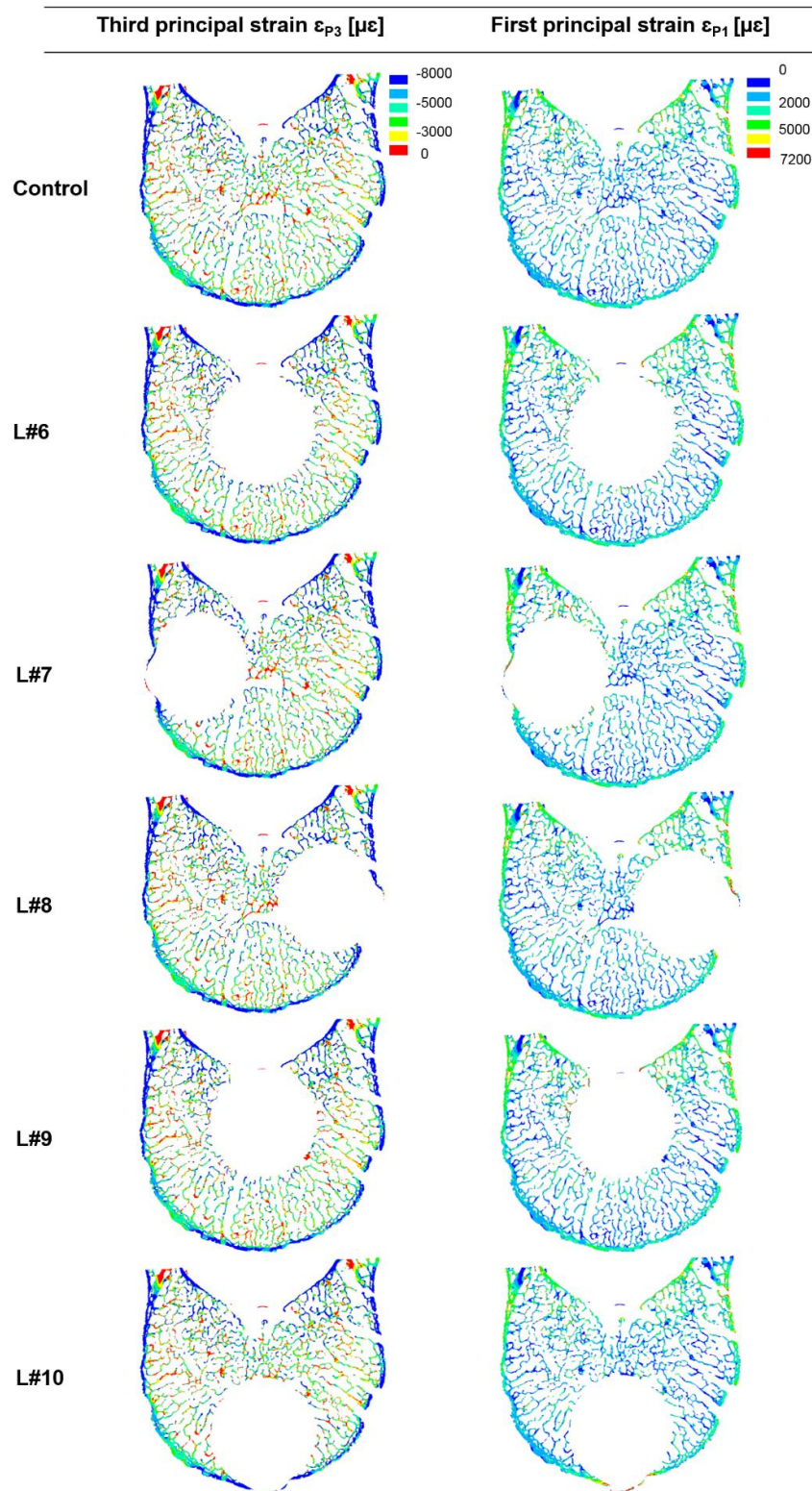


Figure S4.1- Distribution of third and first principal strain along the mid-cross section of the control model (top) against the models with simulated lesions of 12% VBvol placed in the central (L#6), lateral right (L#7), lateral left (L#8), posterior (L#9), and anterior (L#10) regions of the vertebral body.

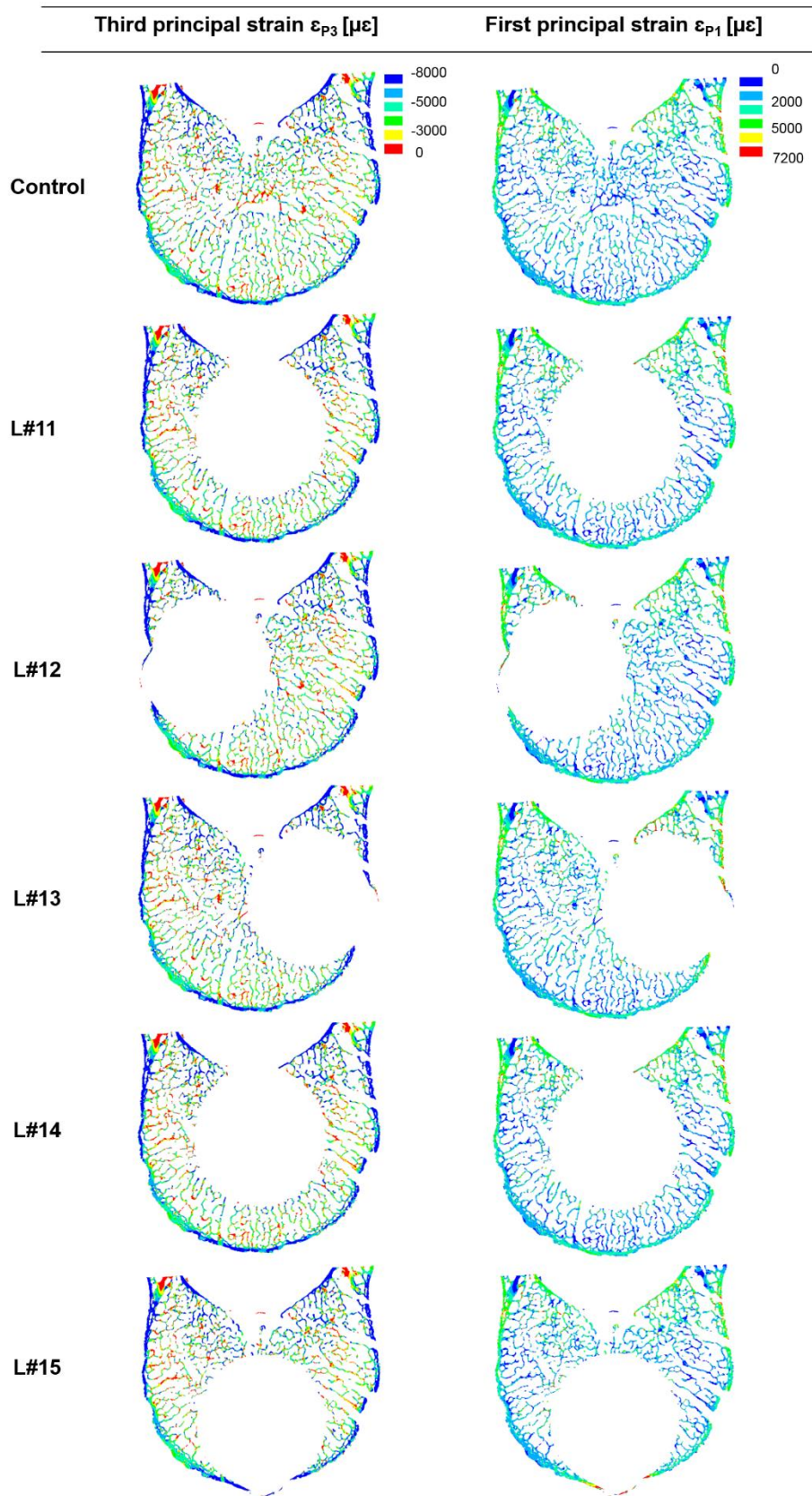


Figure S4.2- Distribution of third and first principal strain along the mid-cross section of the control model (top) against the models with simulated lesions of 24% VBvol placed in the central (L#11), lateral right (L#12), lateral left (L#13), posterior (L#14), and anterior (L#15) regions of the vertebral body.

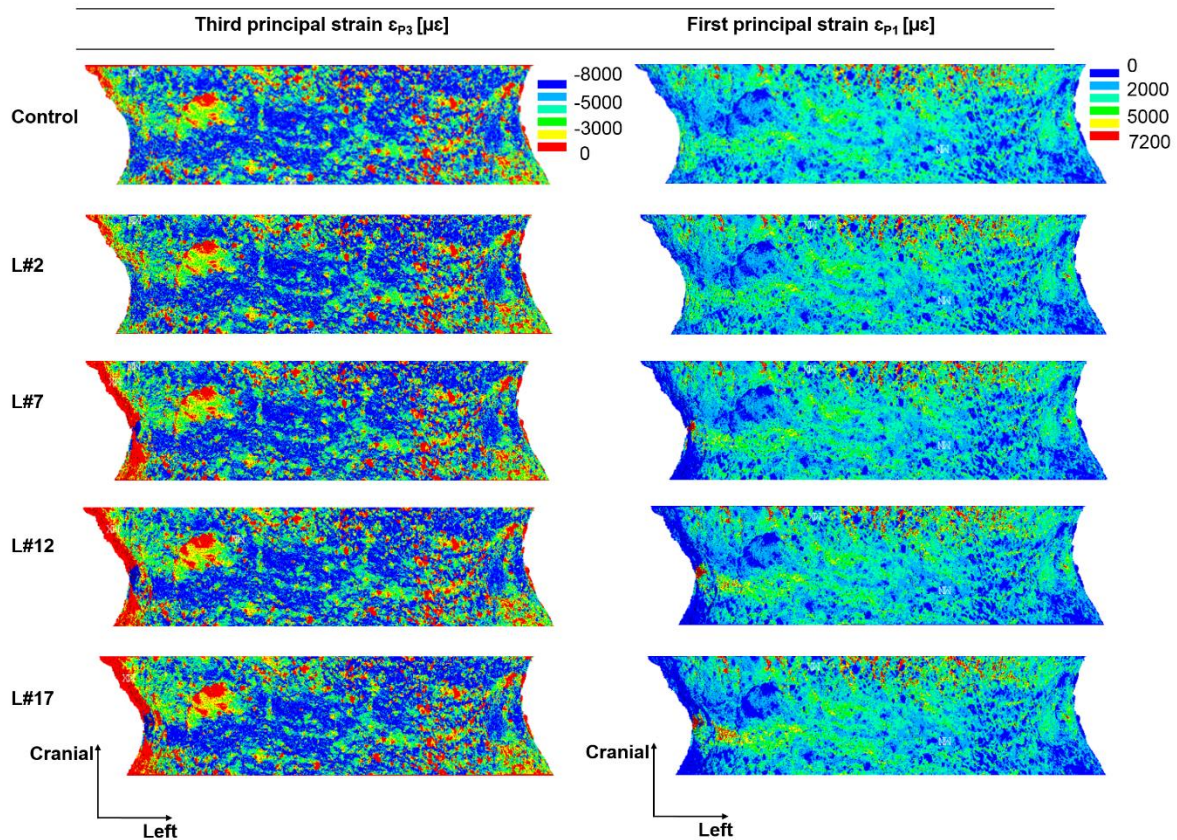


Figure S4.3- Distribution of third and first principal strains obtained from the middle 70% in height of the vertebral body. Plots show the frontal surface view of the control model (top) against the models simulated lytic lesions of 4%VBvol (L#2), 12%VBvol (L#7), 24%VBvol (L#12), and 35%VBvol (L#17). Lesions located in the lateral right region of the vertebral body.

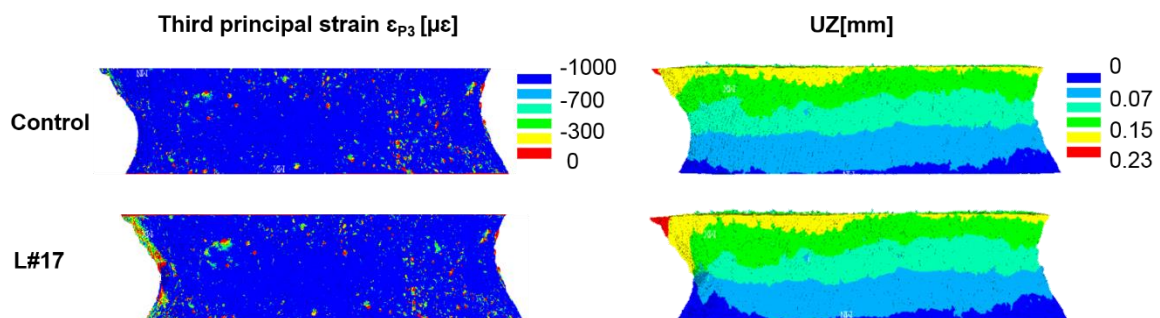


Figure S4.3- Distribution of third principal strains and axial displacements (UZ) obtained from the middle 70% in height of the vertebral body. Plots show the frontal surface view of the control model (top) against the model with a simulated lytic lesions of 35%VBvol (L#17) placed in the lateral right region of the vertebral body. The plot evidences that the regions of low strains observed along the side of lytic lesion are not due to rigid body motion. The same should apply for lesions greater or equal to 12% VBvol, and for lesions located in the lateral left side of the vertebral body.

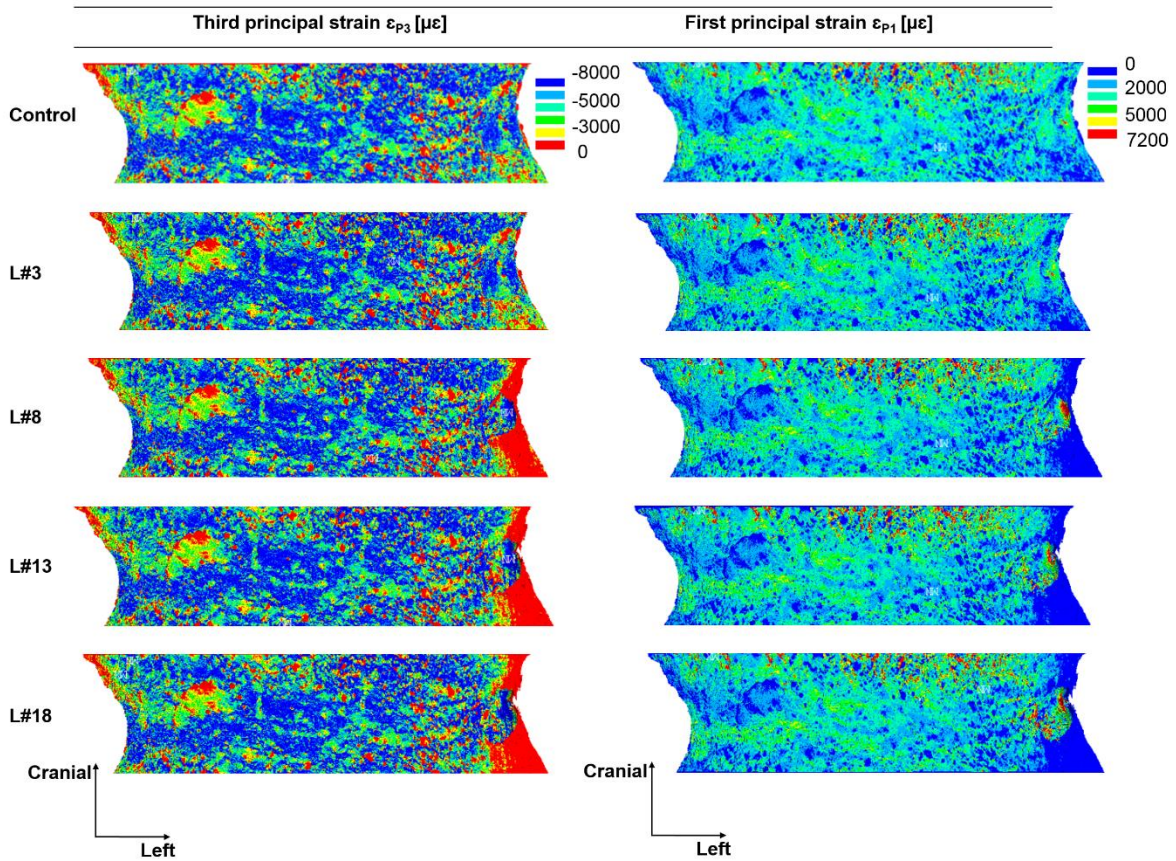


Figure S4.4- Distribution of third and first principal strains obtained from the middle 70% in height of the vertebral body. Plots show the frontal surface view of the control model (top) against the models with simulated lytic lesions occupying 4% VBvol (L#3), 12% VBvol (L#8), 24% VBvol (L#13), and 35% VBvol (L#18). Lesions located in the lateral left region of the vertebral body.

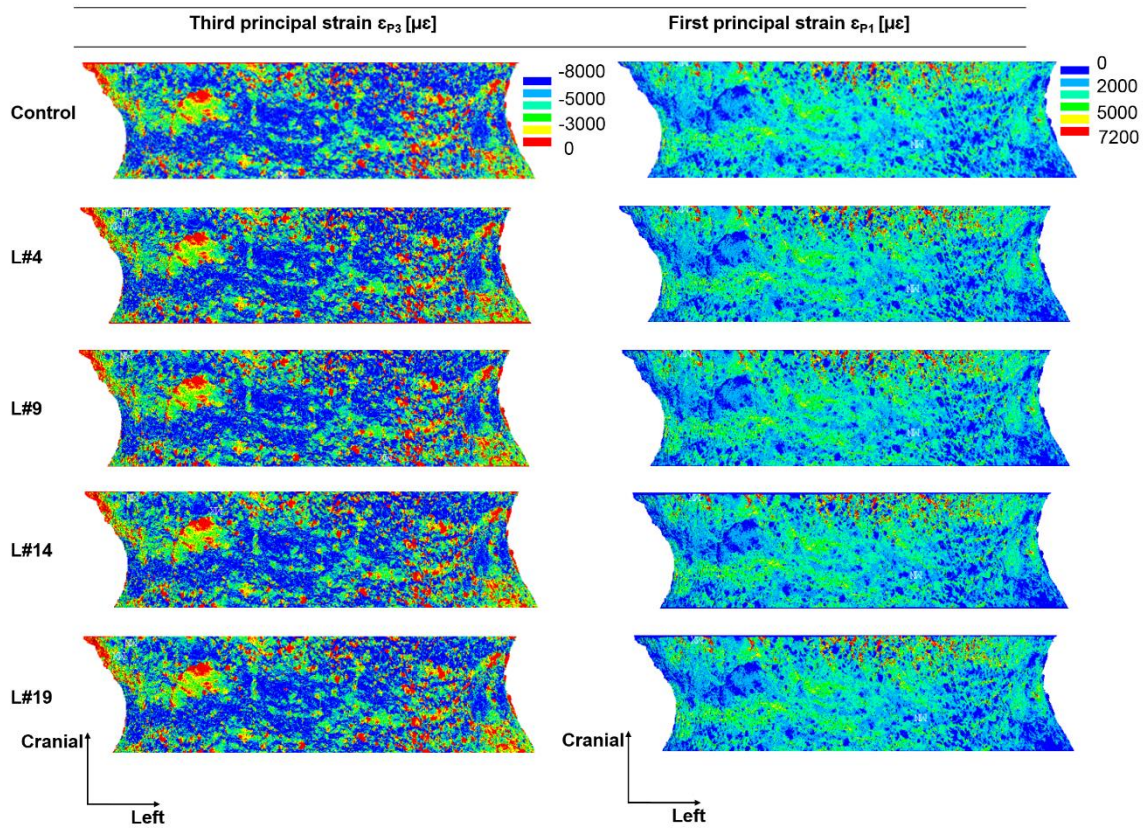


Figure S4.5- Distribution of third and first principal strains obtained from the middle 70% in height of the vertebral body. Plots show the frontal surface view of the control model (top) against the models with simulated lytic lesions of 4%VBvol (L#4), 12%VBvol (L#9), 24%VBvol (L#14), and 35%VBvol (L#19). Lesions located in the most posterior region of the vertebral body.

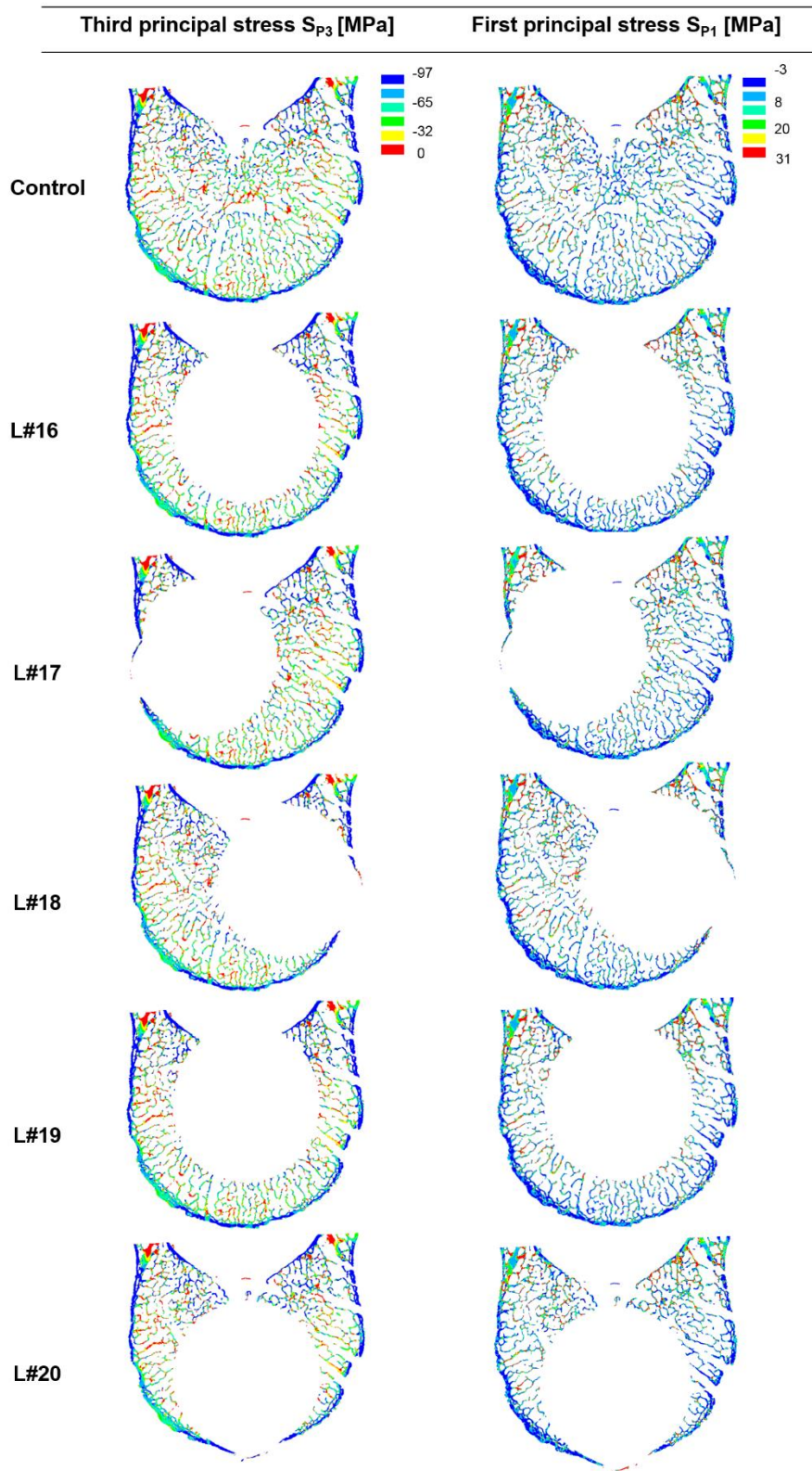


Figure S4.6- Distribution of third and first principal stresses along the mid-cross section of the control model (top) against the models with simulated lesions of 35% VBvol placed in the central (L#16), lateral right (L#17), lateral left (L#18), posterior (L#19), and anterior (L#20) regions of the vertebral body.

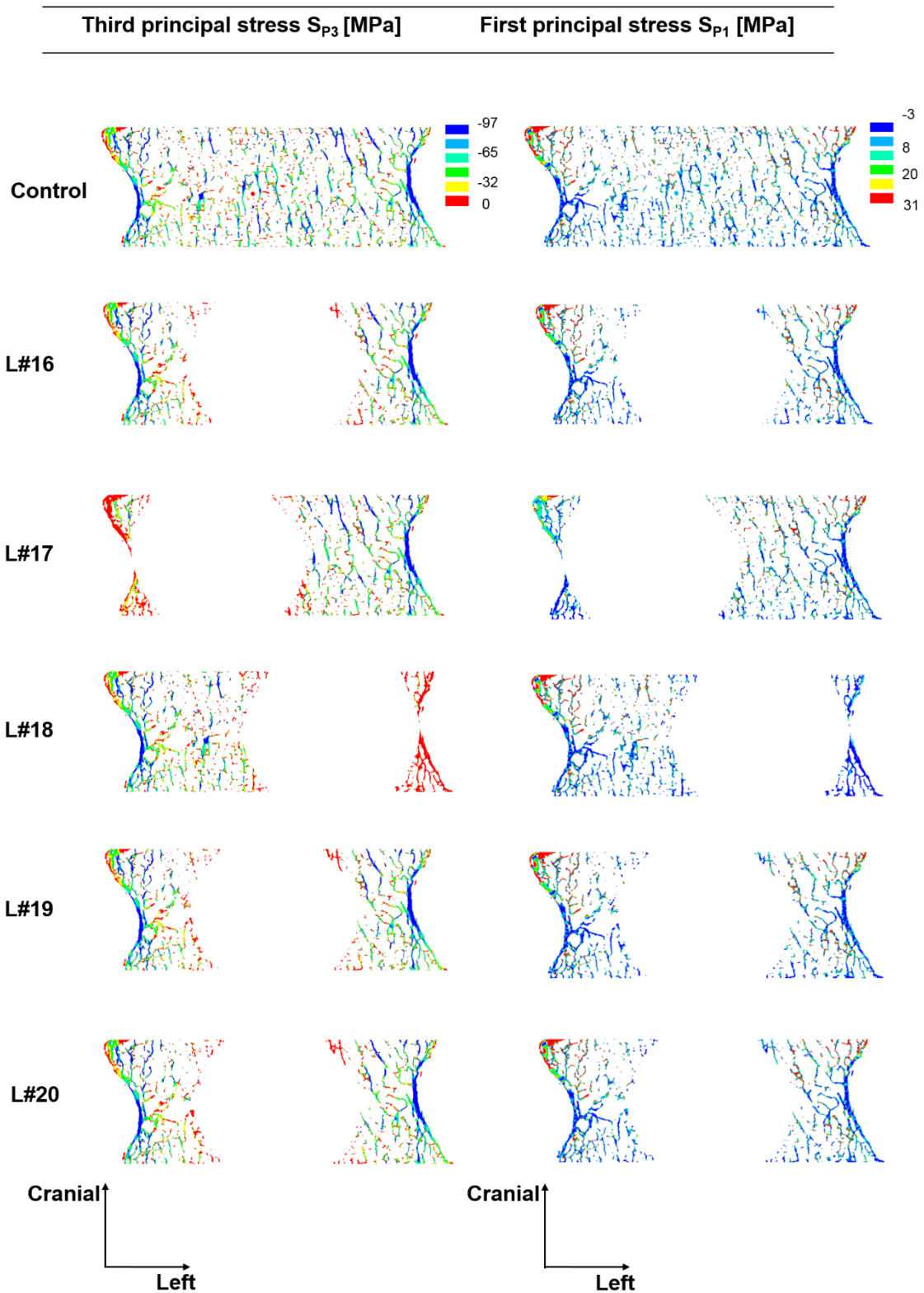


Figure S4.7- Distribution of third and first principal stresses along the frontal mid-cross section of the control model (top) against the models with simulated lesions of 35% VBvol placed in the central (L#16), lateral right (L#17), lateral left (L#18), posterior (L#19), and anterior (L#20) regions of the vertebral body.

## **Chapter V. Development of a methodology for generating CT-based subject-specific finite element models to evaluate the effect of lytic lesions on vertebral mechanical properties**

### **Acknowledgments**

This study was performed in collaboration with Dr Peter Endre Eltes and Dr Áron Lazáry from the National Centre for Spinal Disorders in Budapest, Hungary, who provided the anonymized QCT datasets of patients with lytic vertebrae.

## **Abstract**

Clinical methods used to evaluate the risk of fracture of spinal lytic metastases lack of specificity and do not account for patient-specific risk parameters. Finite Element (FE) models based on Quantitative Computed Tomography (QCT) images allow the estimation of bone strength considering patient-specific bone geometries, heterogeneous material properties, and physiological loading conditions. Such models have been validated for predictions of stiffness and strength for healthy vertebrae, and have the potential of being applied to model vertebrae with metastatic lesions. Therefore, the aim of this study was to develop a methodological workflow for the modelling of subject-specific QCT-based FE models of vertebrae with and without lytic lesions to evaluate differences in mechanical properties and structural stability.

The accuracy of vertebral models with lytic lesions mostly depends on the ability of the discretized model to offer a good representation of bone geometry and material properties. Moreover, the assessment of structural stability also depends on how the models account for the effect of physiological loading conditions on the strength of lytic vertebrae. In this direction a dual approach was adopted involving the FE modelling of subject-specific vertebrae with and without lytic lesions and a subject-specific geometric static model of the sagittal alignment of the spine.

The chapter will describe the process of definition of the models in terms of material properties, discretization, boundary conditions, failure criterion, and physiological loading, which will be then applied in Chapter VI.

## Introduction

Patients with metastatic lytic vertebrae are at risk of developing pathological fractures due to an increase in fragility and instability of the skeletal system. The risk of fracture of vertebrae with lytic lesions is clinically evaluated by using a standard qualitative scoring system named Spinal Instability Neoplastic Scoring (SINS) (see Chapter I, section 1.2.1). This method has limitations linked to its qualitative way of assessment of spinal stability. In fact, the method lacks of specificity and often leads to an overtreatment of patients, which are already weakened from a primary cancer condition (Fisher et al., 2014; Fourney et al., 2011). Moreover, for scores between 7 and 12 the SINS scoring system classifies the spine of patients with lytic lesions as having indeterminate instability. In these cases, surgical consultation is required as there is no clear guideline to decide if the patient should be referred to surgical treatment or not. For these reasons quantitative ways of estimating bone strength should be preferred.

From the biomechanical point of view, the risk of bone fracture depends on the load bearing capacity of bones, which in turn is function of bones geometry, structure, material properties, and loading conditions. FE models based on QCT images allow to perform an estimation of bone strength considering the aforementioned patient-specific structural and material parameters under loading. Such models were validated for predictions of stiffness and strength of healthy vertebral bodies (Pahr et al., 2014; Dall'Ara et al., 2010; Jenni M. Buckley et al., 2007; Crawford, Rosenberg, et al., 2003). So far this models were able to predict up to 66% (Pahr et al., 2014) of the variability in vertebral stiffness and up to 97% of variations in vertebral strength of healthy human specimens (Imai et al., 2006). The model predictions of vertebral strength performed better than the clinical method based on area BMD measurements provided by dual X-ray absorptiometry (DXA) (AUC=0.76 for area BMD and AUC=0.83 for predicted vertebral strength) used for the assessment of the fracture risk of osteoporotic vertebrae (Wang et al., 2012). These evidences show the potential of these models for applications in pathological conditions, such as vertebrae with lytic lesions. In fact, a very recent study showed that subject-specific models of cadaveric vertebrae with lytic lesions resampled at a clinical like CT resolution (i.e. 1 mm voxel size), can predict vertebral strength ( $R^2=0.73$ ) (Stadelmann et al., 2018) with an accuracy similar to the strength predicted by similar models for healthy vertebrae ( $R^2=0.77$ ) (Pahr et al., 2014). Nonlinear elastic-plastic clinical-based FE models of human vertebral bodies with and without simulated lytic lesions were also validated for predictions of vertebral strength ( $R^2=0.76$ ) (Matsuura et al., 2014).

Another recent study, showed that QCT-based FE models predictions of structural properties improved the assessment of vertebral fractures compared to volumetric BMD and morphologic parameters in patients with multiple myeloma, who show a widespread bone lytic lesions, (i.e.  $1.73 \leq ORs \leq 2.28$  for model's predictions of stiffness, yield-load, and work-to-yield against  $1.4 \leq ORs \leq 1.7$  for BMD and BV/TV) (Campbell et al., 2017). On the other hand, specimen-specific FE models of human femoral bones have been extensively used and validated for sample-specific simulated lytic defects, generated by drilling holes of varied sizes through the cortex in different locations (Derikx et al., 2012, 2015), and for subject-specific femurs with lytic lesions, which were validated against retrospective clinical data (Sternheim et al., 2018; Yosibash et al., 2014). Differences between femoral and vertebral bones with respect to structure, material properties, loading conditions, and mechanical behaviour under loading (i.e. failure criterion) limit the direct translation of methods. Thus, it is important that the methods used to model different types of bones are adapted to each specific case. For instance, due to its dense structure, mainly composed by cortical bone, human femurs are known to fail as brittle materials after reaching critical local strains (Schileo, Taddei, et al., 2008) contrary to the ductile behaviour shown by vertebral bones (Dall'Ara et al., 2010). This aspect stresses the difference on mechanical behaviour under loading of the different bones, which will therefore influence their failure criterion.

The aim of this study was to generate a methodology to estimate the effect of lytic lesions on the mechanical properties and stability of subject-specific human vertebrae. The present methodological approach differs from similar protocols used for the generation of subject-specific QCT-based FE models of bones due to the presence of lytic lesions (Fig 5.1).

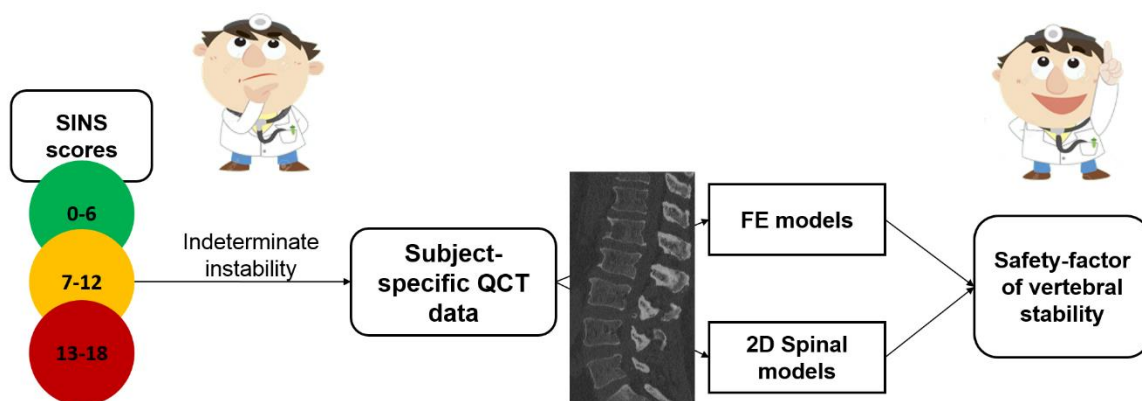


Figure 5.1- Workflow used for the assessment of the mechanical properties and stability of human vertebrae using subject-specific FE models, generated from the QCT images of patients with spinal metastases, and 2D spinal models used to estimate physiological vertebral loads.

The methodology developed in the present chapter will be applied to the clinical data presented in Chapter VI using QCT images of the spine of patients with lytic lesions provided by the National Centre for Spinal Disorders, from Budapest, Hungary. Briefly, from the QCT images of each patient, vertebrae with lytic lesions and the two most adjacent vertebrae without lesions (i.e. controls) will be modelled to analyse the effect of lytic lesion on bone mechanical properties with respect to adjacent vertebrae without lesions (Fig 5.1). Moreover, the proposed modelling approach will provide a quantitative estimation of the stability of the vertebrae with lytic lesions and controls under specific physiological conditions. Such biomechanical analysis could support the clinical decision making in cases where qualitative methods such as the SINS do not provide a clear guidance (Fig 5.1).

The models generated in this work rely on two main assumptions. First, it is assumed that lytic lesions affect only local bone density (Lenherr et al., 2018; Nazarian et al., 2008). Therefore, lytic lesions are considered as low-density bone tissue and modelled as an isotropic and heterogeneous material based on subject-specific density to elasticity relationship. Moreover, the mechanical properties estimated from vertebral models with and without lytic lesions are only assessed for compression loads applied homogeneously over the cranial endplates.

The main challenges in the definition of the modelling method were:

1. To define the densitometric calibration laws to be use in the patient-specific mapping of heterogeneous material properties from the QCT images;
2. To choose the size of the mesh in the FE models;
3. To define the failure criterion and the type of boundary conditions to be applied to the models;
4. To estimate loads applied to each vertebral body in order to compute the compressive loading safety-factor for each vertebra.

In order to make the reading of the chapter easier, each one of the challenges mentioned above will be presented individually with the corresponding material and methods, results, and discussion.

## 5.1. Definition of densitometry calibrations

The aim of this subchapter was to estimate the densitometric calibration laws, which are used in the mapping of the heterogeneous material properties of the QCT-based FE models used in Chapter VI to study the effect of lytic lesions on the strength and stability of patient-specific vertebrae.

### 5.1.1. Materials and methods

Eight QCT datasets from patients with vertebrae with lytic lesions (three males and five females,  $60\pm 12$  years old,  $70\pm 16$  kg, and  $168\pm 12$  cm of height) were provided by the National Center for Spinal Disorders of Budapest, Hungary. The QCT images were obtained from a Hitachi Presto CT machine using a protocol previously set up on the MySpine project (ICT-2009.5.3 VPH) (Rijsbergen et al., 2018) with voltage of 120kV and intensity of 225mA. The images were reconstructed with an in-plane pixel size and a slice thickness of approximately  $0.6\times 0.6\times 0.6$  mm<sup>3</sup>.

The subject-specific FE models were defined under the assumption that the lytic lesions affect only local bone mineral density (BMD) (Nazarian et al., 2008). Therefore, both healthy and lytic tissues were similarly modelled as heterogeneous materials based on the local BMD. The definition of heterogeneous material properties relied on the initial calibration of the QCT Hounsfield unit (HU) values to equivalent BMD, named densitometric calibration law.

The QCT scanning protocol used in this study included an in-line calibration phantom produced by the same manufacturer of the CT machine (Hitachi Presto, Hitachi Medical Corporation, Tokyo, Japan). This calibration phantom is composed by 5 cylindrical insertion rods with diameter equal to 15 mm. Each insertion rod has a known mean equivalent BMD value of 0, 0.5, 0.1, 0.15, and 0.2 g/cm<sup>3</sup> (Fig 5.2). The densitometry calibration was computed using a standard approach, which assumes a linear relationship between the average Hounsfield units (HU) and the known equivalent mean values of BMD of each rod. One region of interest (ROI) was defined manually within each insertion of the phantom using ImageJ software (Schneider et al., 2012) (Fig 5.2). The ROIs were defined as prismatic regions with square section centred within the insertions with a side length equivalent to half of the diameter of the insertions (7.5 mm) (Fig 5.2). The mean and standard deviation of the HU values obtained within each ROI were computed for the complete stack of images, which included the

calibration phantom of each patient. To evaluate the stability of the signal, the mean HU values for each slice of the ROI set for each insertion rod were compared to the overall mean HU values estimated for the whole stack of images set per insertion rod of each image. Moreover, the distribution of the mean and standard deviation of the HU values per slice and per insertion rod in the QCT images that showed highest overall variability (i.e. standard deviation in the HU values) were analysed.

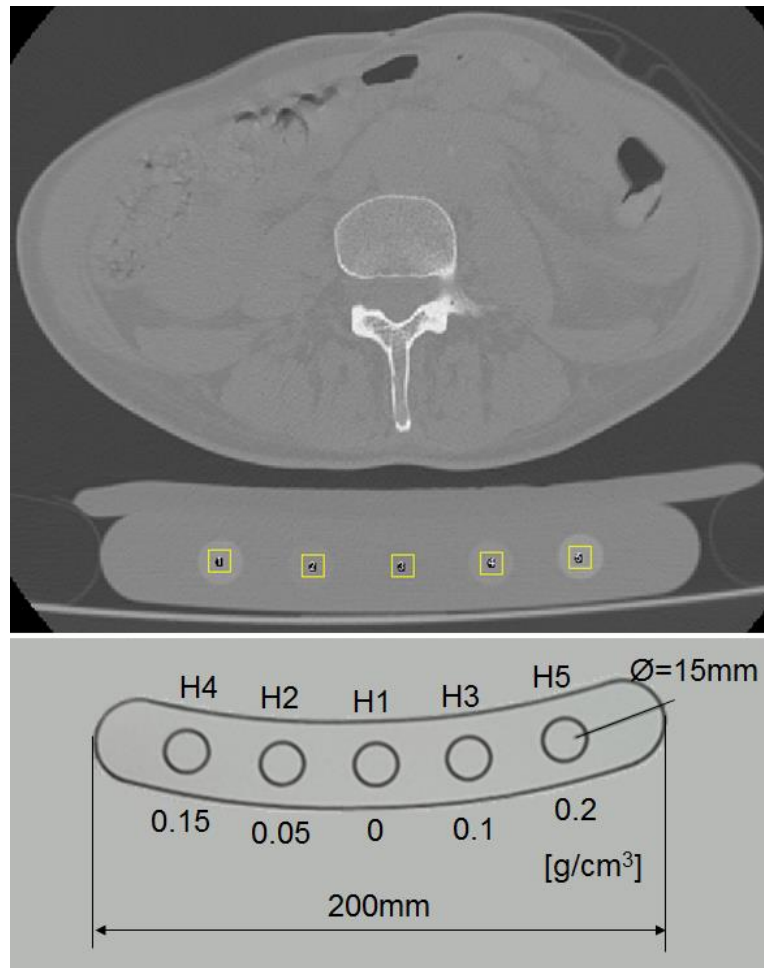


Figure 5.2- Top: Mid-section slice from patient P4 with definition of the five ROIs within each insertion rod of the calibration phantom. Bottom: Length, size and equivalent BMD of each insertion rod of the calibration phantom.

### 5.1.2. Results

The mean values of X-Ray attenuation within each rod were stable across the QCT images (Fig 5.3). Differences between the mean HU values for each insertion rod found per slice of each one of the subject-specific QCT images and the overall mean of HU values estimated per insertion rod for the whole imaging dataset of each subject were smaller than 8% for all the QCT images (Fig 5.3).

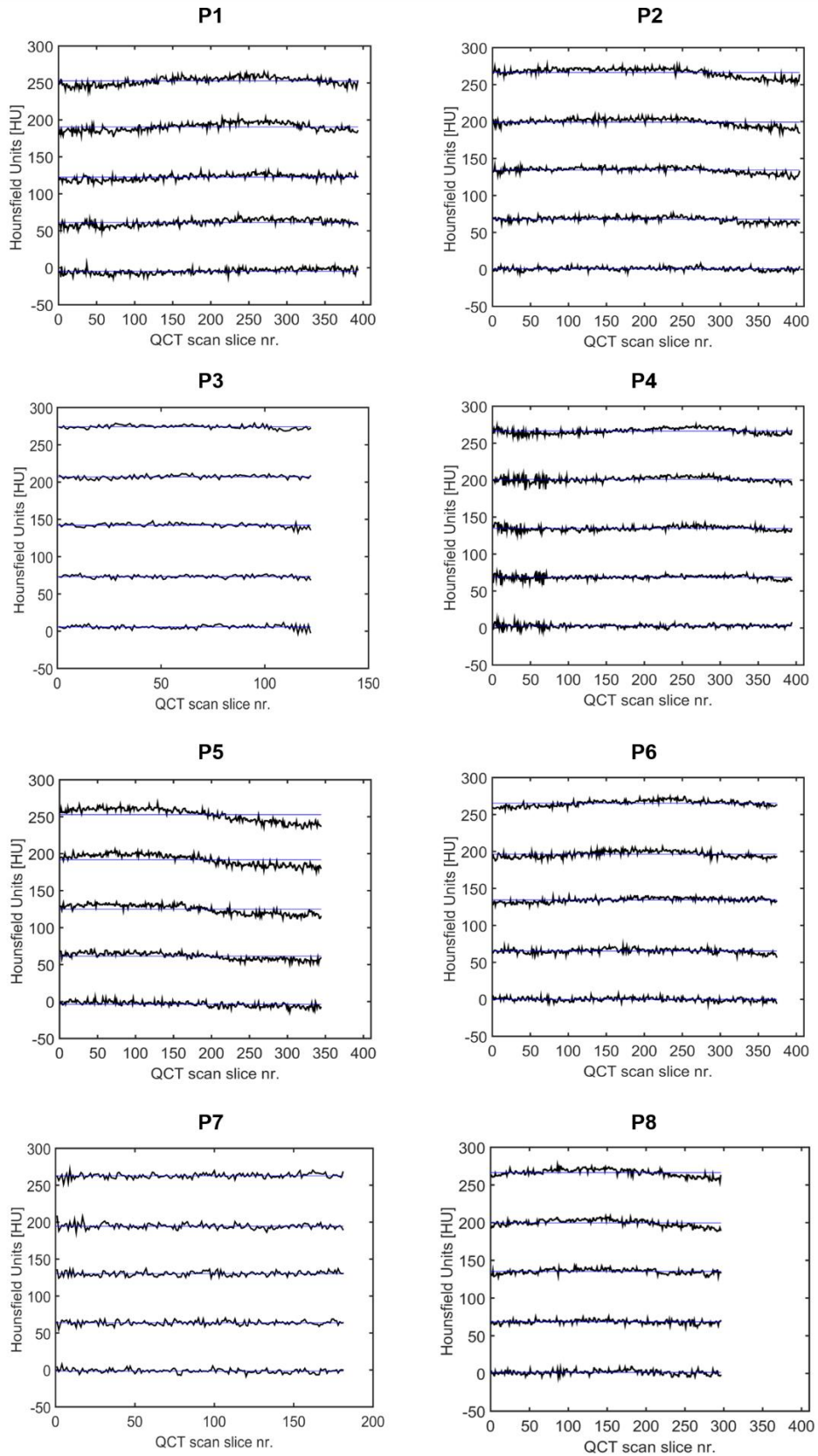


Figure 5.3- Distribution of the mean HU values within each one of the insertion rods of the calibration phantom, computed for each slice of the subject-specific QCT scans (black lines). Blue lines represent the total mean of the HU values computed per insertion and per subject-specific QCT image.

Small differences were observed among the densitometric calibration equations obtained for each subject (Fig 5.4). As expected, linear regression analysis between the mean Hounsfield Units of the insertions of the calibration phantom and their equivalent BMD showed very strong linear correlations (coefficients of determination  $R^2 > 0.99$ ; slopes between 0.0007 and 0.0008; and intercepts between 0.0009 and 0.0047).

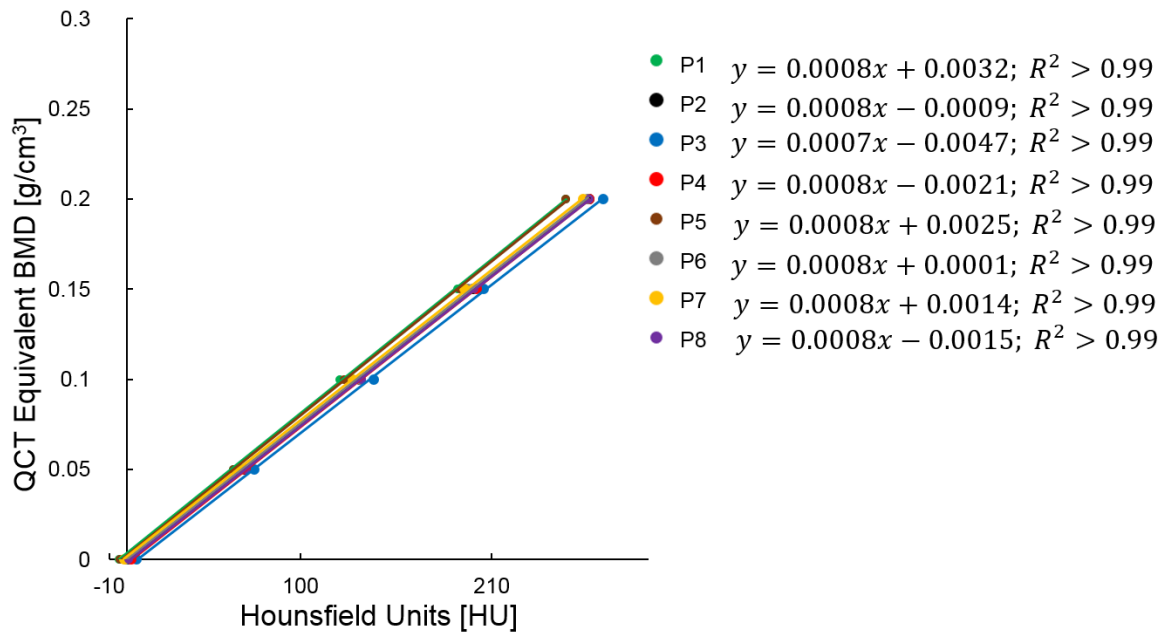


Figure 5.4- Linear regression analyses between the mean Hounsfield Units (HU) values and the equivalent bone mineral density (BMD) within the five insertions rods of the calibration phantom used for the QCT scanning of patients P1 to P8.

High variability (standard deviation) was found among the X-ray attenuation levels of the insertion rods of the calibration phantom, with higher values found for the water equivalent insertion rod (i.e. H1) (Table 5.1). The coefficients of variation (CV) estimated among the hydroxyapatite-equivalent insertion rods (i.e. H2 to H5) of each patient varied from 11% to 93%.

Table 5.1- Mean and standard deviation of the Hounsfield Unit (HU) values within the ROIs set for each insertion rod (H1 to H5 sorted according to their position in the calibration phantom, see Fig 5.2).

Patient ID	Dataset ID	Calibration phantom insertion rods				
		H4 [HU]	H2 [HU]	H1 [HU]	H3 [HU]	H5 [HU]
P1	MV00	191±60	61±57	-4±56	123±57	253±61
P2	MV04	199±47	68±45	1±45	134±47	266±53
P3	MV05	205±31	73±30	6±29	142±29	274±30
P4	MV06	201±34	69±34	3±34	135±34	266±35
P5	MV08	192±58	61±55	-4±53	125±54	253±60
P6	MV09	196±45	65±43	0±42	135±42	265±45
P7	MV10	195±56	64±54	-1±55	130±56	263±60
P8	MV12	200±44	68±41	1±41	135±41	266±44

The QCT dataset that showed higher variability in the HU values of the hydroxyapatite-equivalent insertion rods belonged to patient P1 (i.e. CV up to 93% for H2), whereas the lowest variability was observed for patient P3 (i.e. CV up to 40% for H2) (Table 5.1). However, it was observed that the variability in the HU values found for the dataset that showed higher standard deviations was consistent across the calibration phantom of the QCT dataset (Fig 5.5).

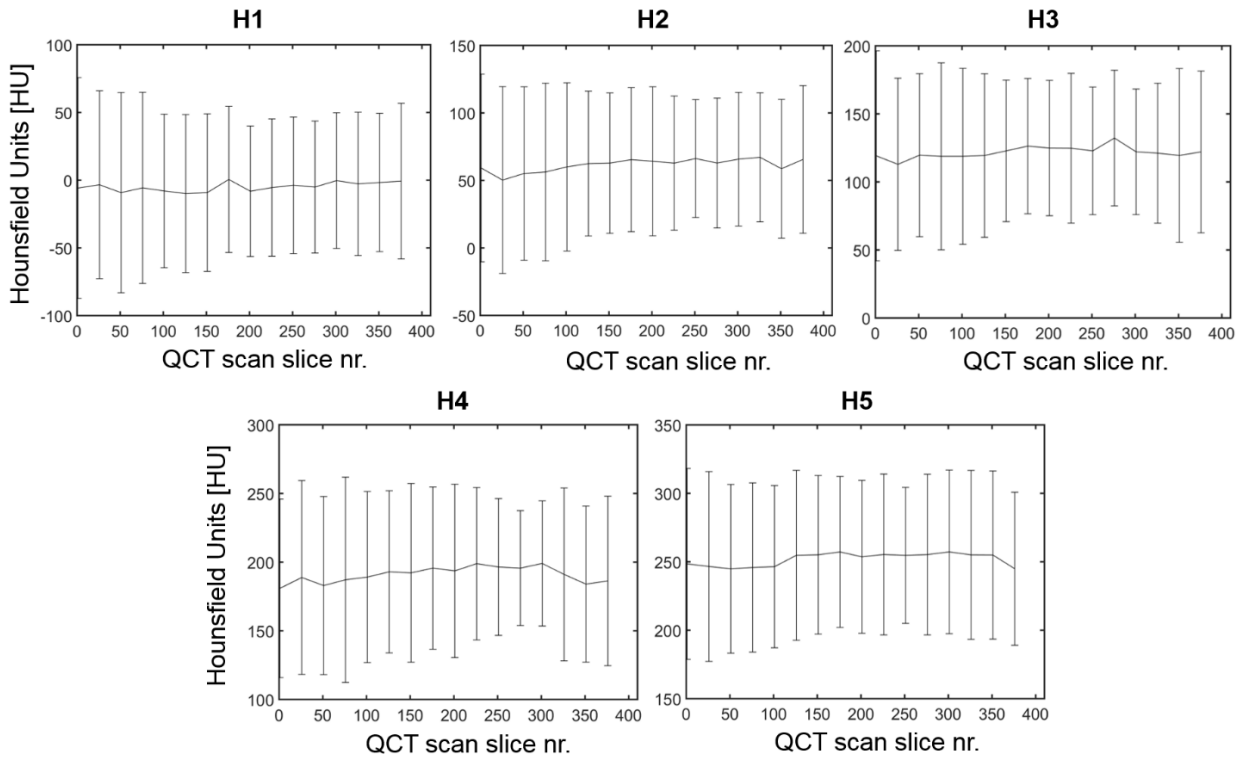


Figure 5.5- Distribution of the mean and variability of the HU values within each insertion rod (H1 to H5) of the QCT images of the patient that showed highest variability, P1. Distribution of the HU values for every 25 slices of the dataset.

### 5.1.3. Discussion

The aim of this sub-study was to define the procedure for the densitometric calibration of the subject-specific QCT datasets to allow for the heterogeneous mapping of material properties of the vertebral models to be generated.

The densitometric calibrations obtained from the QCT images of each subject showed similar but not identical X-ray attenuation levels. A higher attenuation of the X-ray energy was found for patient P1 while the lowest was found for P3. This differences could be explained by the fact that P1 was the patient with highest body mass (i.e. 92 kg), while on the contrary P3 had one of the lowest body masses of the cohort (i.e. 56 kg) and was the only patient that had the upper thoracic spinal levels scanned (i.e. T3-T7, regions with less fat, whereas all the other patients got the thoracolumbar and lumbar segments scanned).

This work has one main limitation: the denser insertion rod of the calibration phantom used in this study was  $0.2 \text{ g/cm}^3$  while the BMD of vertebral bone could range from  $0.1 \text{ g/cm}^3$  to  $0.35 \text{ g/cm}^3$  (Morgan et al., 2003). Nonetheless, previous studies show that similar calibration

phantoms (i.e. with a limit of equivalent BMD equal to  $0.2 \text{ g/cm}^3$ ) are able to capture ranges of higher bone density using the same linear relationship between HU values and equivalent BMD (Dall'Ara et al., 2011; Schileo, Dall'Ara, et al., 2008).

The stability of the mean and standard deviations of the HU values found across the QCT images of each patient showed that there is no need for a vertebral-specific calibration law. However, it is fundamental to account for the different X-ray attenuation levels promoted by the different subjects. Therefore, patient-specific calibration laws were applied to convert the QCT image HU values to equivalent BMD values for each dataset of clinical images of the study.

## 5.2. Choice of the size of the mesh in the FE models

The mesh size analysis performed over the QCT-based models is presented in this section. The heterogeneous nature of these models implies a dependency between the mesh size and the material properties assignment. Therefore, it is impossible to perform a standard mesh-refinement test as refining the mesh also affects the material properties. Nevertheless, it is important to evaluate the effect of changes in geometry and material properties caused by different mesh refinements on the predictions of both local and structural properties. The goal of this sub-study was to choose the optimal mesh size based on the compromise between the accuracy and the computational time of the models.

### 5.2.1. Materials and methods

Data relative to one patient was used in this preliminary analysis towards the definition of the FE modelling methodology. The chosen dataset (MV05) was representative of a critical lytic vertebra present within the study's cohort (see Chapter VI Table 6.1). From this dataset, three vertebrae were modelled: one with a lytic lesion (T5) and two adjacent controls without lesions (T4 and T6) (Fig 5.6). Each vertebra was reconstructed using semi-automatic tools of segmentation and the marching cube algorithm (Amira v6.0.1, Thermo Fisher Scientific, Oregon, USA).

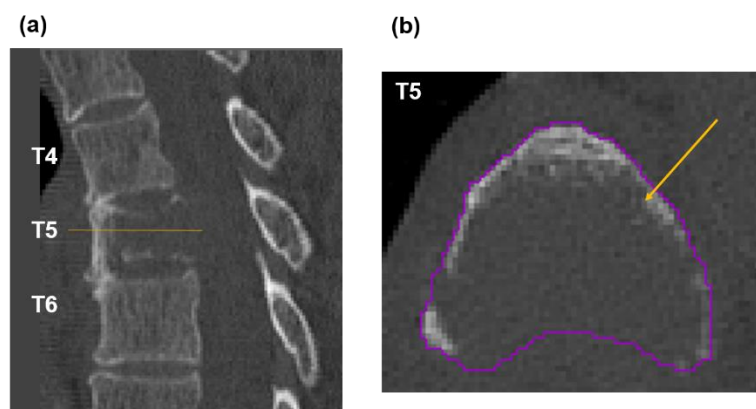
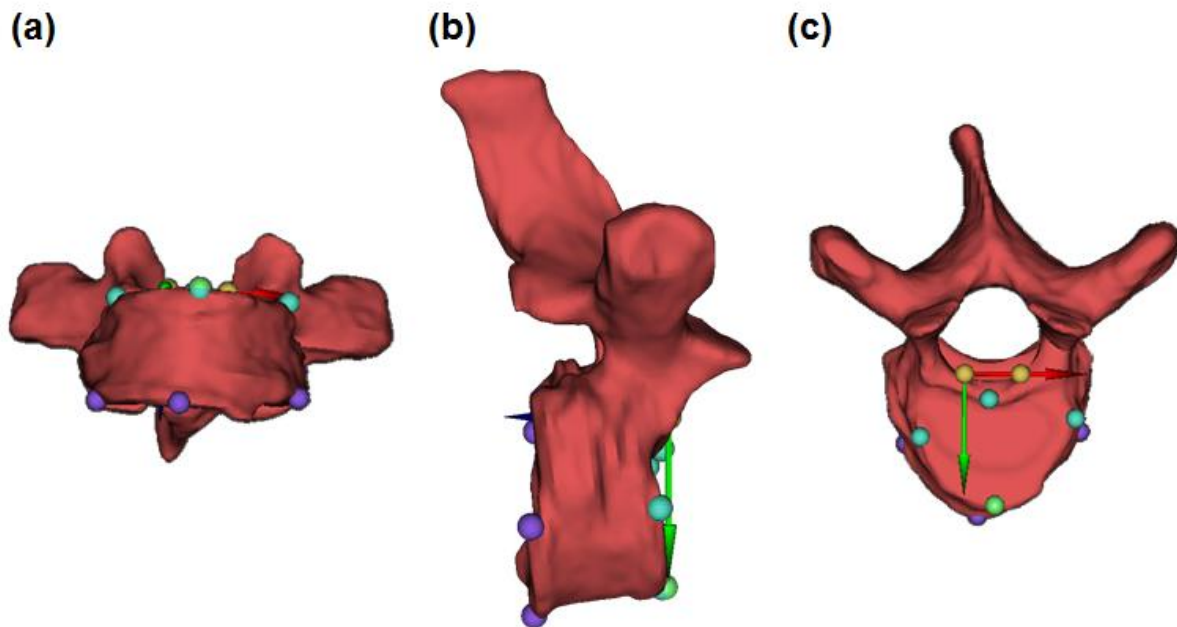


Figure 5.6- (a) Sagittal mid-section view of the QCT dataset MV05 showing the vertebrae with a lytic lesion (T5) and without (T4 and T6). (b) Mid cross-section image of the vertebra with a lytic lesion (pointed with a yellow arrow) T5, with the contour used for segmentation.

Each vertebra was then aligned based on the *in silico* reference framework (Danesi et al., 2014). Briefly, the vertebrae were aligned with respect to pre-defined anatomical planes, by the selection of 10 virtually palpated landmarks, placed over the most anterior-posterior and medio-lateral regions of the top and bottom surfaces of the endplates, and on the right (LR) and left (LL) corners of the posterior wall of the top endplate (Fig 5.7). As the top and bottom endplates of the vertebrae were not parallel to each other, the alignment over the sagittal and frontal planes was performed based on the orientation of the respective bisector planes. A local reference coordinate system set with origin in the LR landmark, the x-direction pointing towards the LL landmark, and the xy-plane with the same orientation as the transverse bisector plane found between endplates was used to help in the alignment (Fig 5.7).



*Figure 5.7- The alignment of the reconstructed surface of the vertebra with a lytic lesion T5 along the (a) frontal plane, (b) sagittal plane, and (c) the transverse plane is shown. Virtually palpated landmarks are differentiated by colours between the cranial (in blue) and caudal (in purple) endplates. Landmarks defined over the right-most and left-most points of the posterior wall of the cranial endplate are displayed in yellow (LR and LL). The xy -plane of the local reference system was defined with the help of a landmark point (in green) set in the anterior region of the cranial endplane with the same orientation of the bisector plane defined between the endplates.*

Quadratic (10 nodes) tetrahedral elements were used to discretize each vertebral volume (ICEM-CFD v15.0, Ansys®, Pennsylvania, USA). Through a meshing sub-step, the surface mesh of the endplates was isolated from the discretized vertebral volume. In this step, the surface of the endplates was split from the overall vertebral surface object through the manual

definition of a cloud of points contouring the endplates. The 3D mesh attached to the surfaces of the endplates was then extracted. After storing the surface mesh information (i.e. nodal number and location), the 2D mesh was deleted preserving only the volumetric mesh (Fig 5.8). These steps were important for the application of boundary conditions directly over the surface of the endplates.

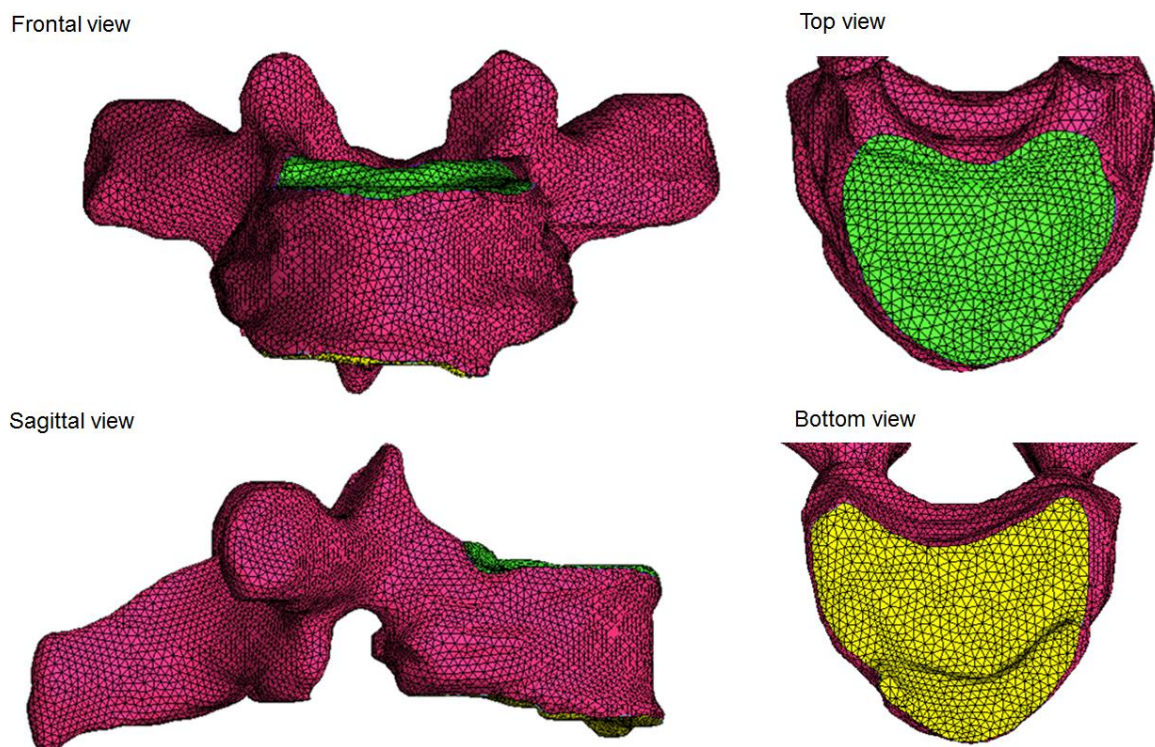


*Figure 5.8 - Discretized vertebral volume represented by pink tetrahedral elements with cranial and caudal endplate surface meshes shown in green and yellow, respectively.*

The minimum edge size of the quadratic tetrahedron elements used to discretize the vertebral models was set to 0.607 mm ( $esize = 0.607\text{mm}$ ) equal to the in plane image resolution of the dataset. Three different coarser meshes were generated from elements with maximum edge sizes increased by 1.65 of the size used in the refined model (i.e.  $esize = 1.00\text{ mm}$ ,  $1.65\text{ mm}$  and  $2.73\text{ mm}$ ). Under the assumption that lytic lesions affect only local bone density (Nazarian et al., 2008) both bone and lytic tissues were modelled similarly as heterogeneous, isotropic, and elastic-plastic materials. Heterogeneous material properties were assigned based on a patient-specific densitometry calibration (see section 5.1) and phenomenological relationships. In

particular elastic properties of the tissue were estimated using a set of density to elasticity relationships [Eq.5.1 to 5.3] and assigned to each element based on the QCT-based HU units averaged over the volume of each element (Bonemat software, Bologna, Italy). Bone plasticity was modelled using an isotropic and symmetric maximum and minimum principal yield stress criterion described based on a density-strength relationship [Eq.5.4], and a 95% reduction in the post-yield modulus of bone [Eq.5.5] (Fig 5.9). Moreover, geometrical nonlinearities were modelled.

$$\rho_{QCT} = 0.0007HU - 0.0047 \text{ [g/cm}^3\text{]}; \quad [\text{Eq.5.1}]$$

Where  $\rho_{QCT}$  represents the QCT equivalent BMD and  $HU$  the Hounsfield unit values of the densitometric calibration law defined in the previous section 5.1 for patient P3 (dataset ID MV05). This calibration law is specific of the QCT images of each patient.

$$\rho_{QCT} = \rho_{ash} = \rho_{app} \times 0.6 \text{ [g/cm}^3\text{]}; \text{ (Les et al., 1994; Schileo et al., 2008)} \quad [\text{Eq.5.2}]$$

Where  $\rho_{QCT}$  represents the QCT equivalent BMD;  $\rho_{ash}$  the ash-density considered as the ratio between the ash weight and the bulk volume; and  $\rho_{app}$  the apparent density estimated from the Archimedes' Principle as the ratio between the wet weight and the bulk volume.

$$E = 4730\rho_{app}^{1.56} \text{ [MPa]}; \text{ (Morgan et al., 2003)} \quad [\text{Eq.5.3}]$$

Where  $E$  represent the elastic modulus, obtained from uniaxial compression and tensile experiments, as a function of the apparent density,  $\rho_{app}$ .

$$\sigma_{y1} = 21.70\rho_{app}^{1.52} \text{ [g/cm}^3\text{]}; \text{ (Morgan \& Keaveny. 2001)} \quad [\text{Eq.5.4}]$$

Where  $\sigma_{y1}$  represents the yield stress for tension (i.e. the lower limit of axial yield properties of bone) as a function of the apparent density,  $\rho_{app}$ .

$$E_{py} = 0.05 \times 4730\rho_{app}^{1.56} \text{ [MPa]}; \text{ (Bayraktar et al., 2004; Morgan et al., 2003)} \quad [\text{Eq.5.5}]$$

Where  $E_{py}$  represents the post-yield elastic modulus as a function of the apparent density,  $\rho_{app}$ .

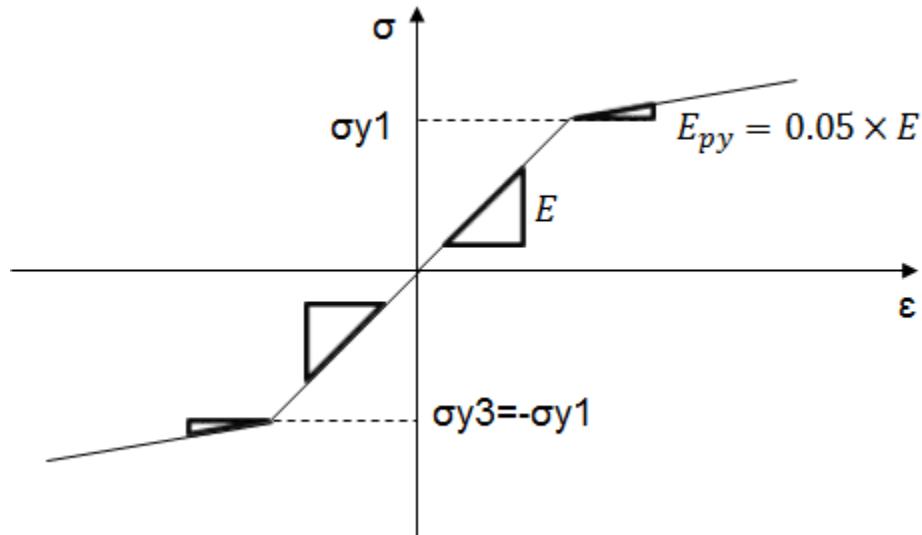


Figure 5.9 - Representation of the bilinear, isotropic, and symmetric yield stress criterion used to model the elastic-plastic behaviour of each vertebral model.

Models were loaded in compression by applying a displacement of 1.9% of the minimum vertebral height ( $H_m$ ), measured between the most concave points of the endplates, to the surface nodes of the most cranial endplate of each vertebra (Fig 5.10). Nodes from the caudal endplates were fixed in all directions.

The sensitivity of the models to the mesh size was evaluated based on the predicted nodal axial displacements ( $UZ$ ), the third principal strains ( $EPEL3$ ), the apparent normalised stiffness ( $E$ ), and the apparent normalised strength ( $\sigma_U$ ), calculated as described in the following paragraphs. The local properties were analysed at the location of the node with highest  $EPEL3$  found in each one of the most refined models. Distributions of third principal strains were analysed for each vertebral model to check uniformity in the strain gradients among the different refined models of each vertebra. To reduce the influence of the boundary effects, local properties were analysed for a sub-region of interest of the vertebral models, which included the middle 50% of minimum height ( $H_m$ ) of the vertebral body excluding all the posterior elements that were 15% away from the furthestmost posterior point of the bottom endplates (Fig 5.10). From each of the most refined vertebral models, the location of the node with the peak value of  $EPEL3$  was taken from the 3D volume of the models (i.e exclusion of surface mesh) for interpolation of results at the same spatial location in the coarser models. As changes in the mesh refinement can generate differences in the geometry of the models, for the different refined models of the same vertebra it was made sure that the interpolation node fell in the space of the coarser models. Local axial displacements and compressive strains were

interpolated using the element shape functions and the nodal information of the element containing the interpolation point.

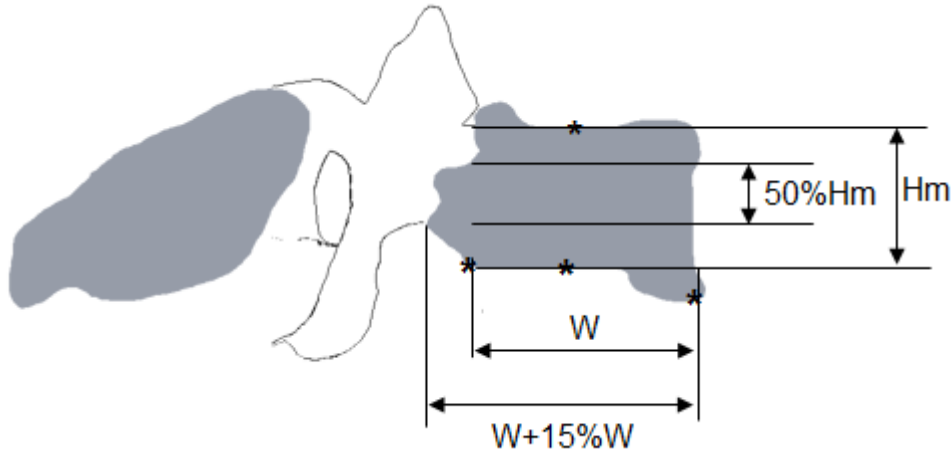


Figure 5.10 - Schematic representation of the portion of the vertebral bodies considered for analysis.

For each vertebral model, the resultant loads were computed as the sum of the axial forces estimated from the bottom endplate nodes of each vertebral model, while displacements ( $\Delta l$ ) were computed in the axial direction for the node closest to the centroid of the top endplate. Such measurements were taken for each iteration of the nonlinear models. Spring stiffness ( $K$ ) was estimated as the slope of the linear range of the force-displacement curves and ultimate load ( $F_U$ ) was estimated as the resultant axial loads generated at 1.9% apparent strain (Buckley et al., 2007; Crawford et al., 2003). The cross-section area ( $CSA$ ) was calculated as the mean value of the portion the masked QCT images of each vertebra which referred only to the vertebral body (i.e. exclusion of the endplates and posterior elements). This was defined by the manual truncation of a bounding box at the most anterior and posterior points of each vertebral body. The normalised stiffness ( $E$ ) and strength ( $\sigma_U$ ) were computed as following:

$$E = \frac{F_U \times Hm}{\Delta l \times CSA} = K \times \frac{Hm}{CSA} \quad [\text{Eq.5.6}]$$

Where  $E$  represents the apparent elastic modulus computed as the ratio between the ultimate force ( $F_U$ ) and the displacements ( $\Delta l$ ) (which is equal to the spring stiffness,  $K$ ), times the ratio between the minimum vertebral height ( $Hm$ ) and the cross-section area ( $CSA$ ) of each vertebra.

$$\sigma_U = \frac{F_U}{CSA} \quad [\text{Eq.5.7}]$$

Where  $\sigma_U$  represents the normalized ultimate force ( $F_U$ ) per vertebral cross section area ( $CSA$ ).

The percentage difference (%diff) was computed between the properties estimated from the models at different refinements with respect to those estimated from the most refined model (i.e. reference model). Convergence was assumed for percentage differences of predicted local and structural properties inferior than 10% (Chen et al., 2014). Stress-strain curves were also computed for each model.

The change in the distribution of material properties within the different refined models of each vertebra was analysed within the sub-region of interest of each model (Fig 5.10). Moreover, the tissue elastic modulus and the equivalent BMD were calculated as the mean values found among the elements connected to the reference node found in the most refined model, or as the values found for the element which contained the coordinates of the reference node in the courser models. Distributions of third principal strains within the vertebra were plotted for each model to check uniformity in the strain gradients among the different refined models.

### **5.2.2. Results**

Changes in material properties of the vertebra with a lytic lesion (T5) and the controls (T4 and T6) caused by changes in the size of the maximum edge length of the different mesh refinement models were on average smaller than 2.7% for equivalent density and elasticity (Fig 5.11). As expected, the increase in the size of the elements resulted in a decreased variability of the material properties within the models.

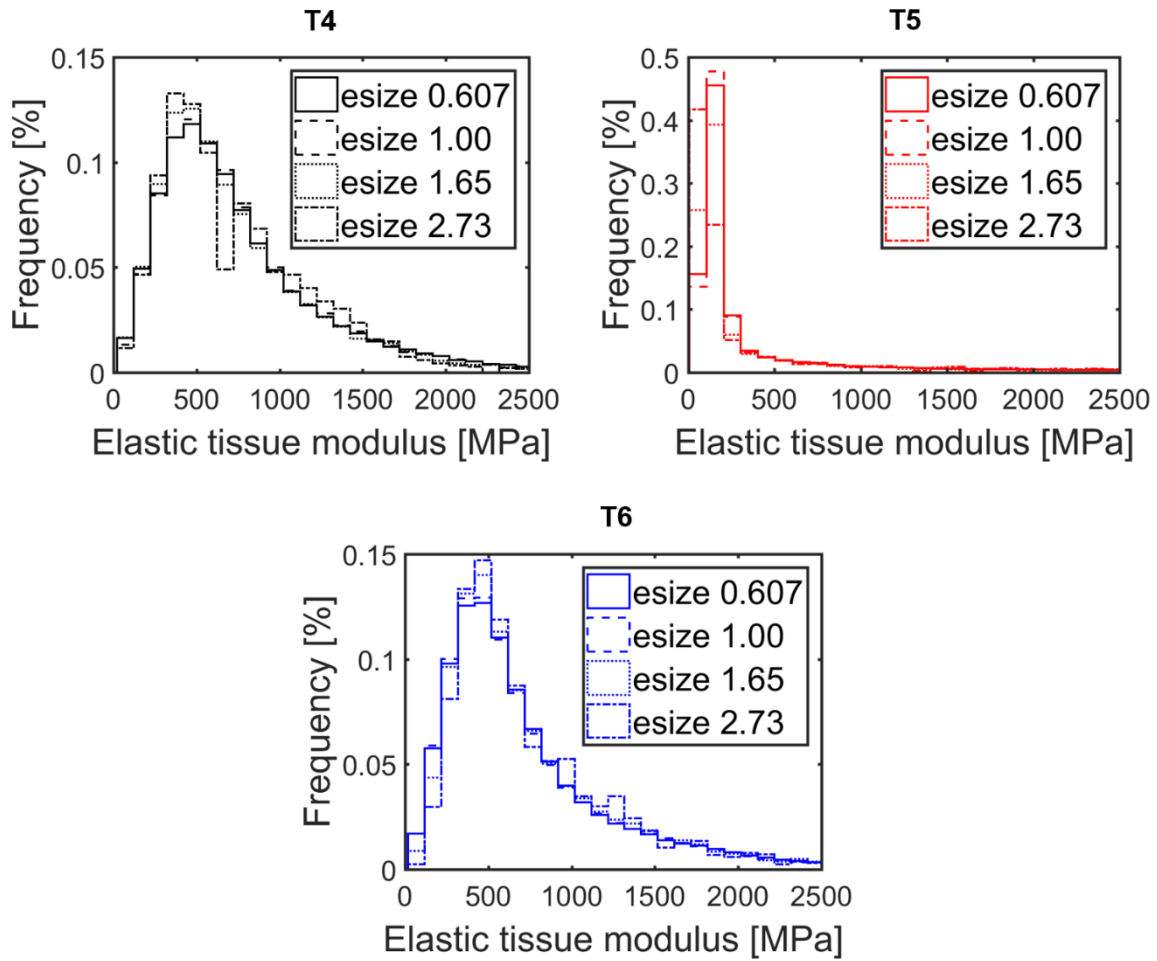


Figure 5.11 - Distribution of the elastic tissue modulus in each one of the different mesh refinement models generated from the control vertebrae (T4 and T6) and from the vertebra with the lytic lesion (T5).

Percentage differences of local displacements and compressive strains found between the second most refined models (esize = 1.00 mm) and the other models were smaller than 10% for both control vertebrae T4 and T6 (Table 5.2). However, for the vertebra with lytic lesion a percentage difference of 17% was observed for the interpolated displacements and a percentage difference of 5% was found for interpolated third principal strains (Table 5.2). For the second coarser models (esize = 1.65 mm) the interpolated axial displacements and the third principal strains increased up to 17% with respect to the reference models of the control vertebrae and up to 62% for the vertebrae with lytic lesion (Table 5.2).

Table 5.2- Report of the size of the models (element size and number of DOF, NDOF), computational costs (elapsed time), local elastic tissue modulus ( $E_t$ ), and percentage difference of local and normalised structural properties (UZ, EPEL3,  $\sigma_u$  and E).

Level	Condition	Element size [mm]	NDOFs [millions]	Elapsed time* [min]	$E_t^{**}$ [MPa]	UZ [mm] (%diff to ref model)	EPEL3 [ $\epsilon$ ] (%diff to ref model)	$\sigma_u$ [MPa] (%diff to ref model)	E [MPa] (%diff to ref model)
T4	Control	2.73	0.3	7.7	69	-0.109 (1%)	-0.012 (-30%)	3.7 (3%)	599 (2%)
		1.65	1.5	8.3	50	-0.104 (-4%)	-0.015 (-15%)	3.6 (1%)	590 (<1%)
		1.00	6.7	17.0	21	-0.099 (-8%)	-0.017 (-1%)	3.6 (1%)	591 (<1%)
		<b>0.607</b>	<b>30.1</b>	<b>61.0</b>	<b>36±23</b>	<b>-0.108</b>	<b>-0.017</b>	<b>3.6</b>	<b>590</b>
T5	Lytic	2.73	0.3	6.9	97	-0.146 (-15%)	-0.010 (-73%)	3.1 (7%)	458 (3%)
		1.65	1.6	19.5	27	-0.142 (-17%)	-0.014 (-62%)	3.0 (3%)	448 (<1%)
		1.00	7.2	18.3	3	-0.142 (-17%)	-0.039 (5%)	2.9 (1%)	442 (-1%)
		<b>0.607</b>	<b>32.2</b>	<b>67.9</b>	<b>16±21</b>	<b>-0.171</b>	<b>-0.036</b>	<b>2.9</b>	<b>446</b>
T6	Control	2.73	0.4	7.2	66	-0.099 (<1%)	-0.011 (-29%)	3.9 (3%)	659 (2%)
		1.65	1.6	8.4	19	-0.103 (4%)	-0.018 (17%)	3.9 (2%)	653 (1%)
		1.00	7.3	18.8	30	-0.104 (5%)	-0.014 (-8%)	3.8 (1%)	647 (<1%)
		<b>0.607</b>	<b>32.7</b>	<b>68.9</b>	<b>20±7e-15</b>	<b>-0.099</b>	<b>-0.015</b>	<b>3.8</b>	<b>648</b>

\*Elapsed time computed for models running in Iceberg taking 32processors shared among 4 nodes.

\*\*Report of the mean  $\pm$  std for the elastic tissue modulus found, in the most refined models, within the elements containing the peak node of EPEL3. For the coarser models, it is reported the elastic tissue modulus of the element which includes the peak node, found in the most refined models.

Predictions of vertebral strength, vertebral stiffness and nodal displacements (%diff lower than 17%) showed in general to be less sensitive than predictions of strains (%diff ranging from 1% to 73% for EPEL3) to the different mesh refinements (Table 5.2). The percentage differences observed between predictions of stiffness and strength of the second most refined models and the reference models were less or equal than 1% for the vertebra with lytic lesion and the vertebrae without lesions (Table 5.2). Small differences were also observed among the stress-strain curves of the different models, with slightly larger difference for the vertebrae with a lytic lesion, T5 (Fig 5.12).

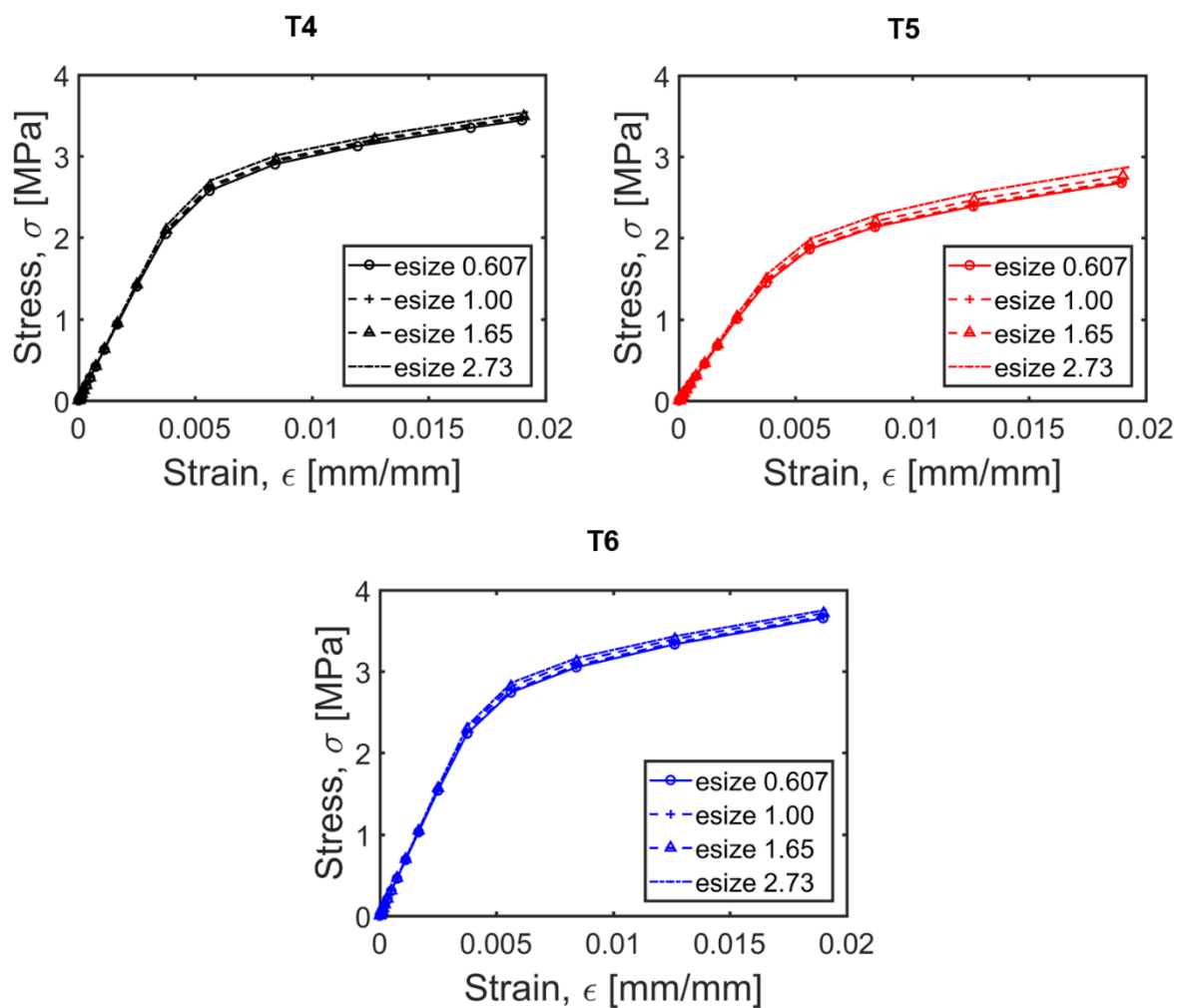


Figure 5.12- Stress-strain curves obtained for each refined model of each control (T4 in black and T6 in blue) and lytic vertebrae (T5 in red).

### 5.2.3. Discussion

The aim of this sub-study was to choose the mesh size for the homogenised subject-specific QCT-based heterogeneous models.

A small variation was observed for predictions of structural properties (i.e. the normalised apparent stiffness and strength) obtained between the refined and the reference models of each vertebra (i.e. %diff < 10%) (Table 5.2). On the other hand, the differences found for predictions of local properties between the different refined modes and the reference models were higher (maximum %diff of 73%) (Table 5.2).

From the analysis of local stiffness, found within the elements containing the interpolation point of the coarser models, it was observed that in the vertebra with lytic lesion the peak location of third principal strains fell in a softer and low density region compared to T4 and T6 (Table 5.2). This explains the local deformation observed for the peak node in T5 of approximately 4%, higher when compared to T4 and T6 with peak EPEL3 of around 2% (Table 5.2). Moreover, it was observed a higher variability within the local elasticity for the elements containing the peak node in the most refined model of T5 compared to the controls (CV = 1.3 against ~ 0 - 0.6 for T6 and T4, respectively). This finding highlights the high gradient in the material properties within T5 close to the lesion, which can explain the higher variability observed in the local properties of this model compared to the controls.

The distribution of the third principal strain was analysed for each vertebra to make sure the interpolation points were located in regions of high gradients of strain (Fig 5.13). For control vertebrae high compressive strains were found in the central portion of the posterior compartment of the vertebral body (Fig 5.13). This region is one of the main regions of vascular entry (Pointillart et al., 2002) thus suggesting the presence of very low density tissues which would justify the presence of high strains. For the vertebra with the lytic lesion, the peak

compressive strain was located in the left region of the central compartment of the vertebral body, region composed by low density tissues associated to the lytic lesion (Fig 5.13).

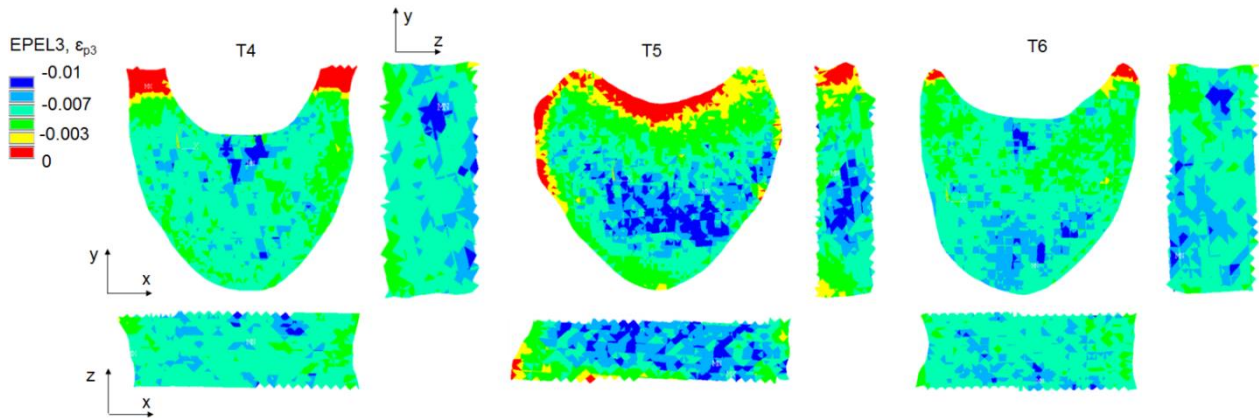


Figure 5.13 - Distribution of the third principal strains over the mid cross-sections of the modelled lytic (T5) and control (T4 and T6) of dataset MV05. Deformation obtained for 1 mm element size.

In general, the estimated displacements decreased with the increase of the element size. This could be explained by the superimposed effect of the mesh refinement on the heterogeneous mapping of material properties of the models. For element sizes smaller or equal to the in-plane pixel resolution, there is a smoother reconstruction of bone geometry. However, the same is not necessarily true with respect to the characterization of the material properties as smaller the element size, higher is the effect of the image noise on the generation of high gradients of material properties within the vertebral models (Dall'Ara et al., 2011).

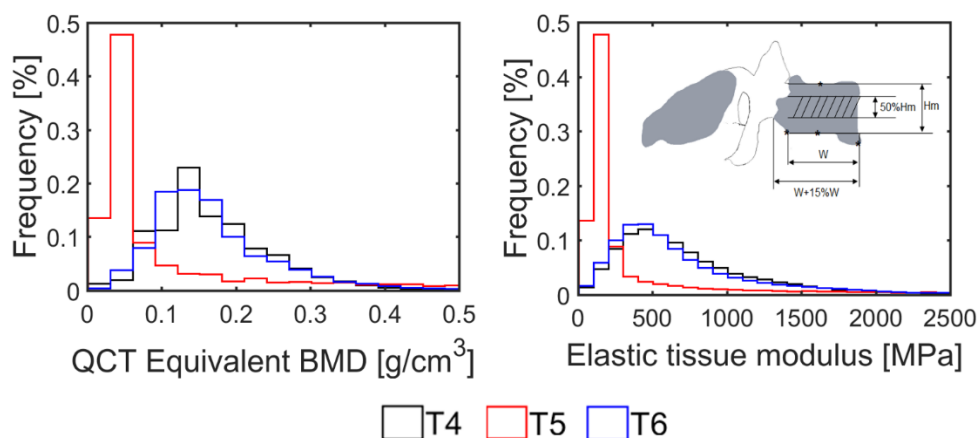
In a standard mesh refinement study the displacements tend to converge faster than the strains, which are computed from the differentiation of the displacements. However, in this case standard conditions do not hold as there is a dependency between the discretization of the models and their local material properties. The faster convergence observed in the second most refined model of T5 for strains compared to displacements (%diff = 5% for EPEL3 against %diff = -17% for UZ) (Table 5.2) could be explained by the heterogeneity in material properties in the region of interpolation of T5, which induced higher deformations possibly causing local interpolation issues. Nevertheless, it was observed that a difference of 17% in predictions of local displacements in the second most refined model of T5 did not affect the predictive ability in terms of structural properties (differences lower or equal to 1% for both controls and lytic models, Table 5.2). Thus, considering that the modelling from clinical data will be focused on the analysis of structural properties, we considered that the models using 1.0 mm element size provided reliable predictions of structural properties for 73% less computational time than the most refined models (Table 5.2). These models shall be therefore used in the generation of future clinical-based homogenised models.

### 5.3. Definition of boundary conditions and failure criterion

The goals of the analyses described in this section were: 1) to choose the failure criteria to be used for the QCT-based FE models, based on available literature, and 2) to choose the type of boundary conditions (i.e. displacement versus load control) to use in the models.

#### 5.3.1. Materials and methods

Similarly to the previous mesh refinement analysis, only the vertebra with lytic lesion (T5) and the two adjacent control vertebrae (T4 and T6) from the MV05 dataset were considered in this study. The methods used for the reconstruction and alignment, mesh and map of the material properties of each vertebra are described in the previous section 5.2.1. For these analyses the vertebrae were meshed using quadratic tetrahedral elements with maximum edge size of 1.00 mm (see section 5.2.1). The distribution of the material properties of these models is reported in (Fig 5.14).



Dataset ID	Level	Condition	$\rho_{\text{QCT}}[\text{g}/\text{cm}^3]$ (range)	E [MPa] (range)
MV05	T4	Control	$0.17 \pm 0.076$ (0.008-0.59)	$741 \pm 511$ (21-4727)
	T5	Lytic	$0.12 \pm 0.14$ (0.021-0.88)	$594 \pm 1078$ (50-8685)
	T6	Control	$0.17 \pm 0.087$ (0.0002-0.74)	$751 \pm 617$ (1-6621)

Figure 5.14- Distribution of equivalent bone mineral density (QCT equivalent BMD) and the elasticity of the bone tissues (Et) computed within the sub-region of interest (defined in section 5.2, Fig. 5.10) of the FE models of lytic (T5) and control vertebrae (T4 and T6).

### *Failure criterion*

For the definition of the failure criterion, it was important to take into account the fact the lytic lesions are filled by less stiff materials which may not necessarily yield at low strains as in bone tissues (Whyne et al., 2000). However in this study, lytic lesions were modelled using the same density to elasticity relationship used for bone tissues. Therefore, to evaluate vertebral failure a structural yield criterion was used. In the literature, there are two main structural failure criterion which were validated and used for healthy human vertebrae under compression. It has been assumed that vertebral failure occurs at 3.0% apparent deformation (Buckley et al., 2007), or at 1.9% apparent deformation (Keaveny et al., 2014; Wang et al., 2012). Thus, structural failure was simulated in each vertebra by applying both 3.0% apparent strain and 1.9% apparent strain, computed with respect to the minimum height ( $H_m$ ) of each vertebra (Fig 5.14). Due to the geometric differences among vertebrae, the minimum vertebral height ( $H_m$ ) was defined as the height measured between the most concave nodes found within the middle quarter of the top and bottom surface nodes of the endplates (Fig 5.14). Both analyses were conducted to compute the strain distribution obtained at the applied apparent strains.

### *Boundary conditions*

The above-mentioned 1.9% apparent strain analysis was compared to an equivalent uniaxial load-control analysis. Thus, the axial reaction forces (i.e. ultimate force) estimated for the 1.9% apparent strain analysis was applied for each vertebra in force-control. Such load was balanced over medio-lateral and anterior-posterior vertebral directions (i.e.  $xx$  and  $yy$  axis) in order to simulate a pure axial compression loading (Fig 5.15). The balance of loads was performed within small bands used to subdivide the top surface along the  $y$ -direction (Fig 5.15). For each vertebra, the band size required to neutralize the bending effect of the axial load was computed. This operation was vertebra-specific due to the heterogeneity and asymmetry of the mesh distribution found for each vertebra (as it conforms to the geometric features present within each specific vertebra) (Fig 5.15). The following equations were used to estimate the nodal axial loads.

$$F_{R,zz} = \sum_{i=1}^{N_{nodes}} F_{zi} \quad [\text{Eq. 5.8}]$$

Where  $F_{zi}$  represents the axial nodal loads which were computed to be equal to the reaction loads estimated from the 1.9% apparent strain analysis,  $F_{R,zz}$ .

$$M_{R,xx} = \sum_{i=1}^{N_{nodes}} F_{zi} \times dy_i \approx 0 \quad [\text{Eq. 5.9}]$$

Where  $M_{R,xx}$  represents the moment along the x-axis, computed as the sum of the nodal axial forces ( $F_{zi}$ ) times the distance in the y-axis between the nodes and the centroid of the endplate ( $dy_i$ ).

$$M_{R,yy} = \sum_{i=1}^{N_{nodes}} F_{zi} \times dx_i \approx 0 \quad [\text{Eq. 5.10}]$$

Where  $M_{R,yy}$  represents the reaction moment along the y-axis, computed as the sum of the nodal axial forces ( $F_{zi}$ ) times the distance in the x-axis between the nodes and the centroid of the endplates ( $dx_i$ ).

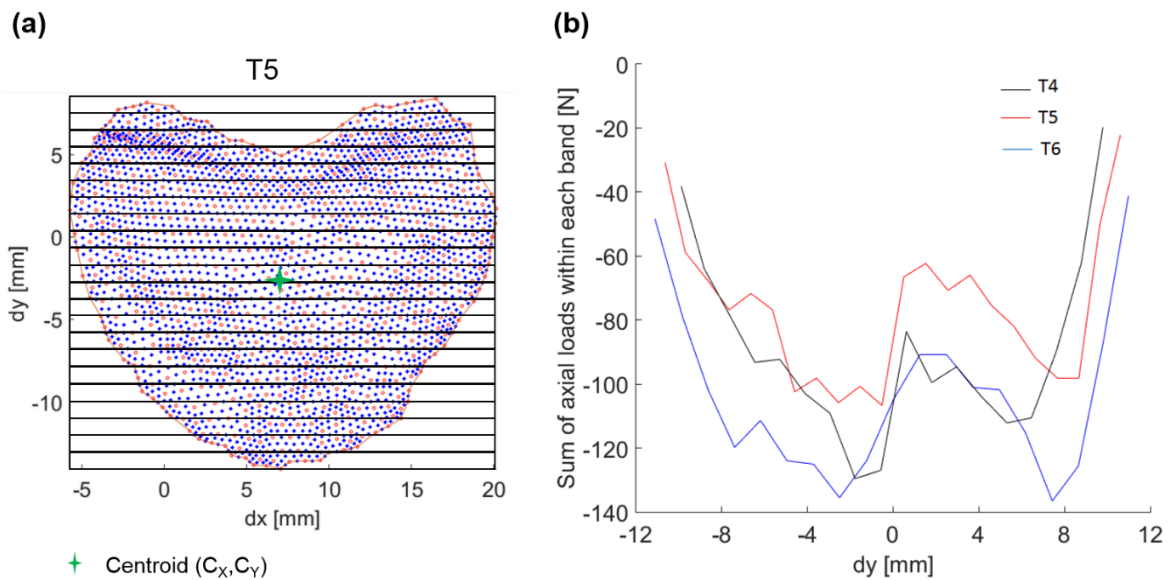


Figure 5.15- (a) Schematic of the partitioning over the top endplate of the vertebra T5 in small bands used to distribute the nodal axial loads in order to neutralize bending moments. (b) Distribution of the sum of the nodal loads generated for each band of the vertebral endplates of T4, T5, and T6.

For each iteration of the nonlinear models, resultant loads were computed as the sum of the axial forces estimated from the bottom surface nodes of the endplates, while displacements were estimated in the axial direction for the node closest to the centroid of the top surface of the endplates. Ultimate loads ( $F_U$ ) were estimated as the axial reaction forces generated at the imposed 3.0% apparent strain ( $3.0\% \epsilon_{app}$ ) or 1.9% apparent strain ( $1.9\% \epsilon_{app}$ ). Spring stiffness ( $K$ ) was computed as the slope of the linear range of the load-displacement curves of each vertebra. Geometrical and normalised structural properties, and apparent stiffness ( $E$ ) and strength ( $\sigma_U$ ), were computed using [Eq. 5.6 and 5.7] reported in section 5.2.1. Principal strains were estimated from the sub-region of interest (described in section 5.2, Fig. 5.10) of each model (Fig 5.14).

### 5.3.2. Results

#### *Failure criterion*

Predicted failure loads were between 1.7 kN and 2.2 kN whereas estimated strength ranged from 2.7 MPa to 4.2 MPa, among the different failure criteria and vertebrae (Table 5.3). A maximum difference of 13% was observed between failure loads and strength estimated from different failure criteria (Table 5.3). As expected, negligible differences were observed for estimated spring and normalised stiffness (i.e. %diff<0.004%) (Table 5.3).

*Table 5.3- Predicted structural ( $K$ ,  $F_U$ ,) and normalised properties ( $E$ ,  $\sigma_U$ ) of vertebral models loaded under two different compressive failure criteria applied in displacement-control.*

Dataset ID	Level	Condition	Failure criterion	$F_U$ [kN]	$\sigma_U$ [MPa]	%diff	$K$ [kN/mm]	$E$ [MPa]	%diff
MV05	T4	Control	1.9% $\epsilon_{app}$	1.7	3.5	11%	18.6	568	0.004%
			3.0% $\epsilon_{app}$	1.9	3.9		18.6	568	
	T5	Lytic	1.9% $\epsilon_{app}$	1.7	2.7	13%	22.0	409	0.002%
			3.0% $\epsilon_{app}$	1.9	3.1		22.0	409	
	T6	Control	1.9% $\epsilon_{app}$	2.0	3.7	12%	20.5	621	0.004%
			3.0% $\epsilon_{app}$	2.2	4.2		20.5	621	

The vertebra with lytic lesion, T5, showed the lowest strength, followed by T4 and T6 respectively (Fig 5.16). Reduction in strength of T5 compared to the mean values of the control vertebrae was up to 25% between the two failure criteria (Table 5.3).

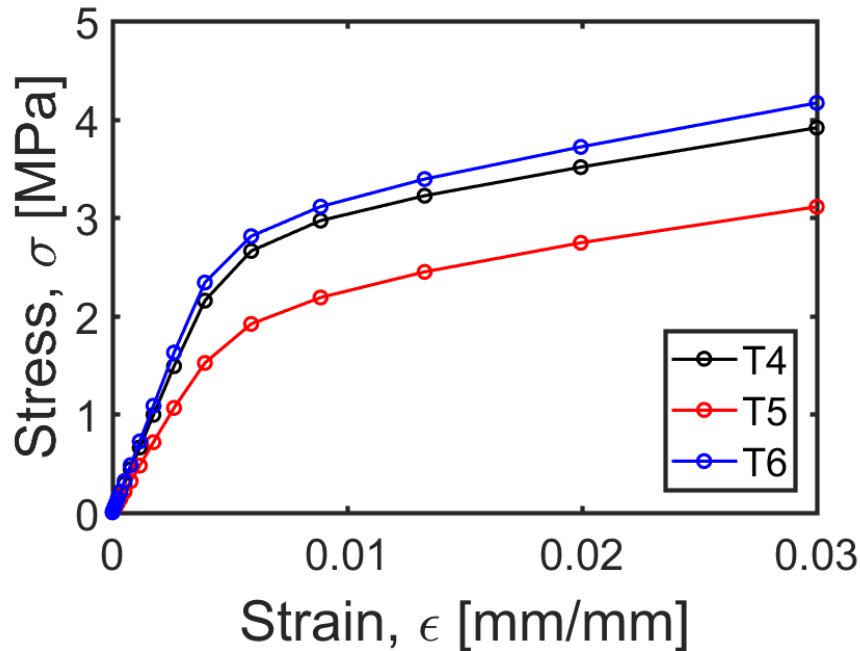


Figure 5.16 - Force-strain curves obtained for each iteration of the vertebral models loaded in compression of 3.0% of the minimum height of each model.

The difference between the mean values of first and third principal strain (i.e. EPEL1 and EPEL3 respectively) distributions estimated from the 3.0% and 1.9% apparent strain analyses were small (percentage difference between mean EPEL3, obtained from both failure criteria were less than 14% for all the models). The lytic lesion showed higher heterogeneity in the strain profiles, with a higher percentage of elements under higher compressive deformations (Fig 5.17). Negative values of EPEL1 show that the vertebrae are, in this case, mostly loaded under compression (Fig 5.17).

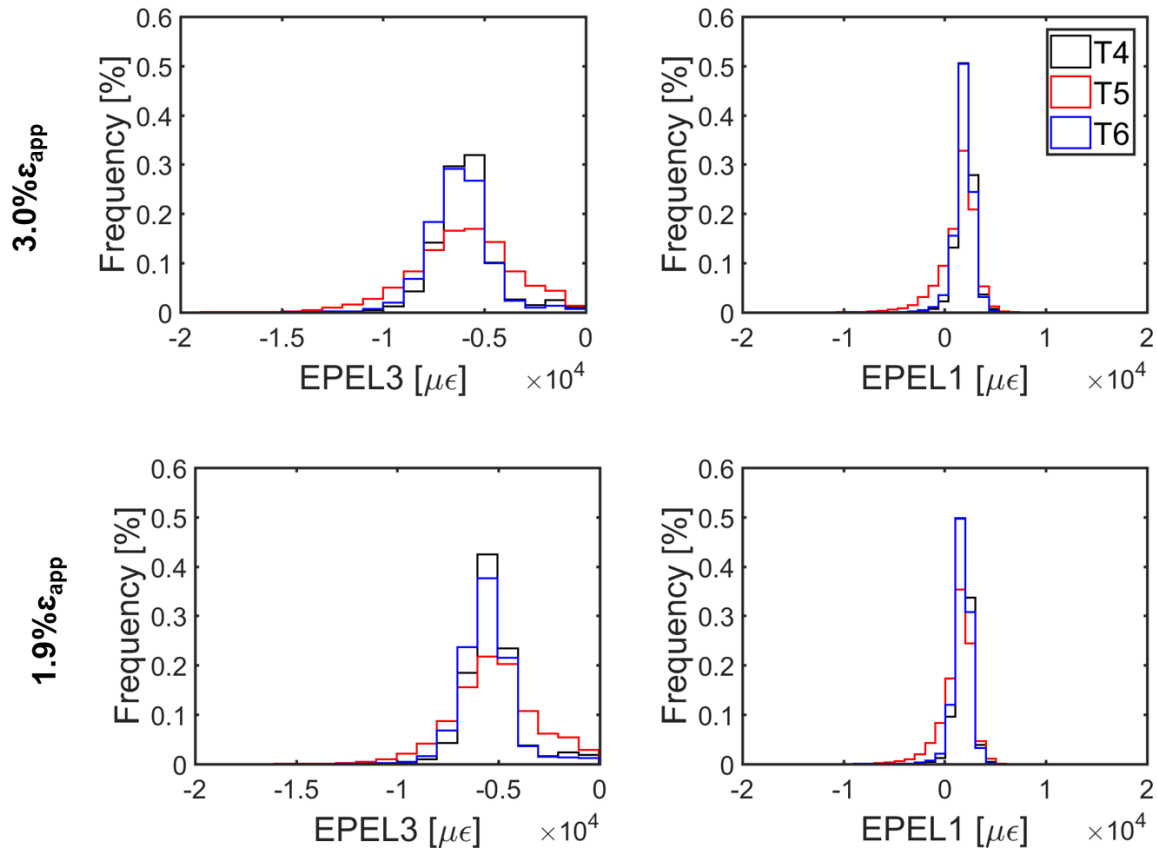


Figure 5.17 - Distribution of the third and first principal strain (EPEL3 and EPEL1) normalised by the total number of elements of each vertebral model analysed at 3.0% and at 1.9% apparent strain failure criteria.

### Boundary conditions

In the force-control analysis, prediction of vertebral strength decreased by 49% for the lytic vertebra and less than 20% for the controls (Table 5.4). The same trend was observed for stiffness (Table 5.4).

Table 5.4 - Predictions of structural and material properties obtained from force-control FE analysis.

Dataset ID	Level	Condition	$F_u$ [kN]	$\sigma_u$ [MPa]	%diff to ref model	K [kN/mm]	E [MPa]	%diff to ref model
MV05	T4	Control	1.4	2.9	-15%	16.1	492	-13%
	T5	Lytic	0.9	1.4	-49%	9.7	180	-56%
	T6	Control	1.6	3.1	-17%	17.5	530	-15%

When the vertebrae were loaded up to compressive failure (i.e. defined at 1.9% apparent strain) in force-control, high deformations were observed (9.0% for T5 against up to 3.0% observed between controls T4 and T6) (Fig 5.18). Reductions in strength for force-control analysis were greater for the lytic vertebra, which underwent plasticity at very low loads (Fig 5.18).

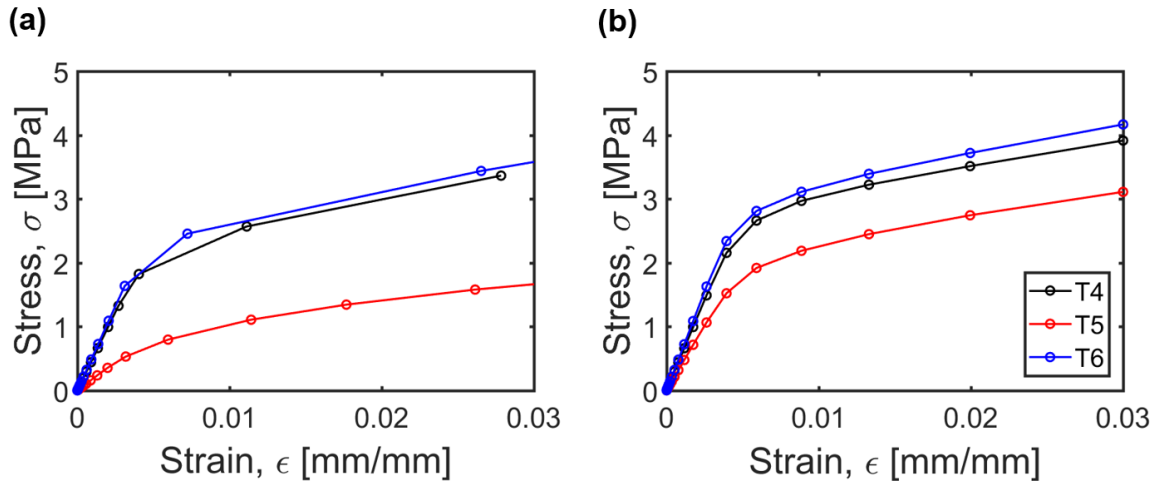


Figure 5.18 - Stress-strain curves of (a) force-control and (b) displacement-control analyses of each vertebrae from patient dataset MV05.

The results obtained from the force-control analysis, showed a higher heterogeneity in the distribution of principal strains compared to the equivalent displacement-control analyses (i.e. displacement of 1.9% apparent strain) (Fig 5.19). The lytic vertebrae T5 showed the highest gradient of compressive (EPEL3) and tensile (EPEL1) strains when compared to the controls under the same conditions, but also when compared to the strain gradients observed for the equivalent loading condition applied in displacement-control (Fig 5.19).

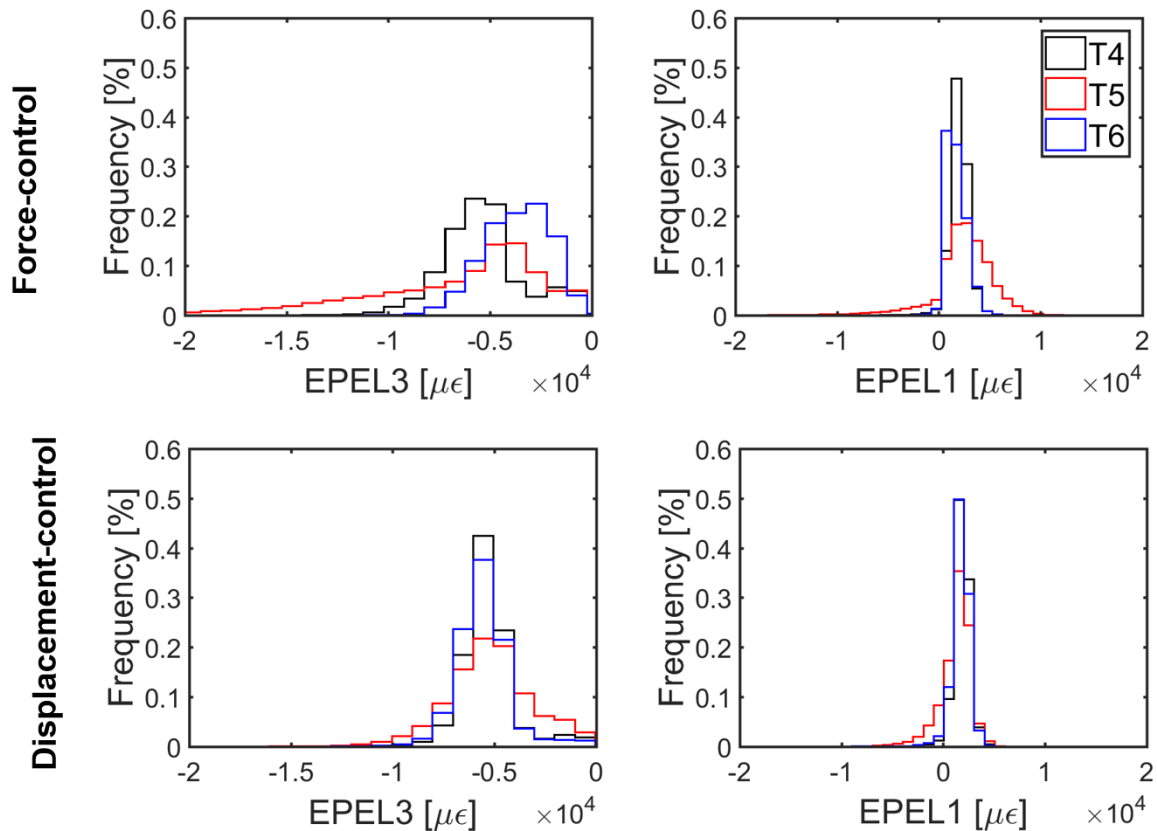


Figure 5.19 - Frequency plots of the third (EPEL3) and first (EPEL1) principal strains obtained from equivalent force-control and displacement-control analyses of the lytic (T5) and control vertebrae (T4 and T6) from patient dataset MV05.

### 5.3.3. Discussion

The purpose of this section was to evaluate the feasibility of the subject-specific models to estimate the vertebral strength, for both vertebrae with and without lytic lesions, based on the current literature data of validated FE models of healthy human vertebrae. Therefore, the effect of different literature-based failure criteria and types of boundary conditions on the FE models predictions of vertebral elastic and yield properties was analysed.

#### *Failure criterion*

Estimated failure loads were between 1.7 kN and 2.0 kN for 1.9% apparent yield strain criterion and between 1.9 kN and 2.2 kN for the 3% apparent yield strain criterion, for control and lytic vertebrae with a mean equivalent BMD of  $0.152 \pm 0.029 \text{ g/cm}^3$  (Table 5.3 and Fig 5.14). Compared to the literature of validated models of human vertebrae used for assessment

of compressive strength, predictions of ultimate force were of the same order of magnitude but smaller. In Melton et al. (2010), estimated vertebral strength of L1-L3 vertebrae (n=90, mean equivalent BMD equal to  $0.185 \pm 0.038 \text{ g/cm}^3$ ) of postmenopausal women was  $5.5 \pm 1.9 \text{ kN}$ . More recently, in Dall'Ara et al. (2012), the compressive strength of vertebral body sections varied between 3.0 kN and 10.6 kN (mean equal to  $6.6 \pm 2.2 \text{ kN}$ ) for a cohort of healthy human vertebrae, dissected from T12-L5 (n=37, equivalent BMD equal to  $0.162 \pm 0.039 \text{ g/cm}^3$ , ranging between  $0.096 \text{ g/cm}^3$  and  $0.237 \text{ g/cm}^3$ ). In Wang et al. (2012), predicted vertebral strengths were equal to  $6.9 \pm 2.3 \text{ kN}$  for a cohort of osteoporotic men (L1-L2, n=243 and a mean equivalent BMD of  $0.199 \pm 0.044 \text{ g/cm}^3$ ). In this study, the predicted mean failure loads were up to 74% smaller than the mean values found in the aforementioned literature. Such differences were probably due to differences in the studied cohorts of patients (gender, vertebral levels, equivalent BMD), and the condition of the tested vertebrae (i.e. lytic vertebrae may induce development of osteophytes that can spread to the adjacent controls), which are known to affect the geometry, size, and material properties of the vertebrae, and therefore its strength (Ebbesen et al., 1999; Singer et al., 1995).

The material properties of the vertebra with lytic lesion were within the range of low bone mass (i.e.  $0.12 \text{ g/cm}^3$  of BMD (Kopperdahl et al., 2014)). As expected, the lytic vertebra T5 showed smaller mean material properties compared to the controls but higher variability (Fig 5.14). In fact, T5 showed a slightly higher presence of high-density tissues, located from the mid to caudal portion of the anterior vertebral compartment, compared to the controls (Fig 5.20), which could explain the slightly higher predicted ultimate force of T5 compared to T4.

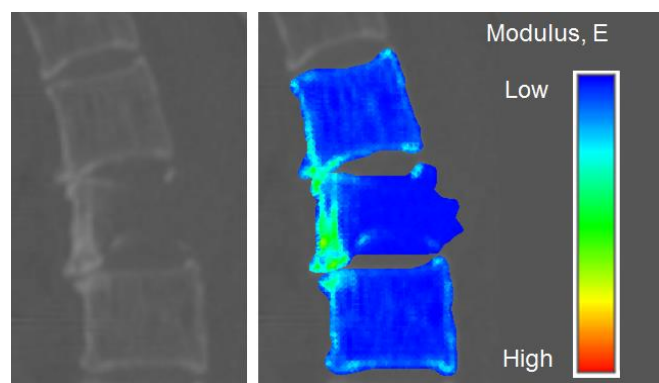


*Figure 5.20 - Sagittal mid-section view of the triplet vertebrae modelled.*

Small differences, of up to 13%, were observed between predicted failure loads and strength estimated from the different yield strain failure criteria used (Table 5.3). These differences were in part induced by the simplified material model used in this study, which caused a systematic increase in strength lead by an increase in deformation (Fig 5.16). Differences in predicted stiffness were negligible as, for both failure criteria, the models shared the same linear elastic material properties. Between analyses, strain distributions were very similar with a slight increase of the percentage of elements under compression and tension for the 3.0% apparent yield strain analysis, as expected. The location of peak compressive strains in both analyses matched those previously found and described in the mesh refinement study (see Fig 5.13 of section 5.2).

The yield strain criteria used in this study have been used to assess the strength of the human vertebrae in two different conditions. In particular, the 3.0% apparent yield strain criterion was used and validated to predict the strength of healthy human vertebrae (Jenni M. Buckley et al., 2007; Crawford, Cann, et al., 2003). On the other hand, the 1.9% apparent yield criteria was also validated for healthy human vertebrae and used to assess the strength and load-to-strength ratios (i.e. the vertebral fracture risk) of old osteoporotic women and men (Keaveny et al., 2014; Wang et al., 2012). As the present study includes the modelling of vertebrae with lytic lesions, which are modelled as low bone density tissues, it seems more appropriate to use a more conservative criterion that would provide an extra safety measure in the assessment of vertebra strength and that has already been proven to work for bony conditions modelled in a similar way. Thus the 1.9% apparent strain criterion was preferred.

### *Boundary conditions*

When the displacement-control analyses were compared with the force-control analyses, large differences in stiffness and strength were found, especially for the vertebra with the lytic lesion (Table 5.4). Control vertebrae showed a reduction in stiffness and strength ranging from 13% to 17% between equivalent force-control and displacement-control analyses (Table 5.4). For the lytic vertebra, a reduction of approximately 50% in stiffness and strength was observed for the force-control analyses compared to the value obtained from the equivalent displacement-control analyses (Table 5.4).

The differences found between predictions obtained from force-control analyses and displacement-control analyses were probably due to local distributions of loads. In fact, in the

force-control analyses, local deformations are dependent on the local stiffness of the tissues at the boundary. As observed in Fig 5.21, there was a large deformation from the centre to the posterior compartment of the lytic vertebra, which covered the region of softer tissues and the node closest to the centroid of the cranial endplate and which was used to measure the axial displacements considered for the computation of the vertebral stiffness and strength.

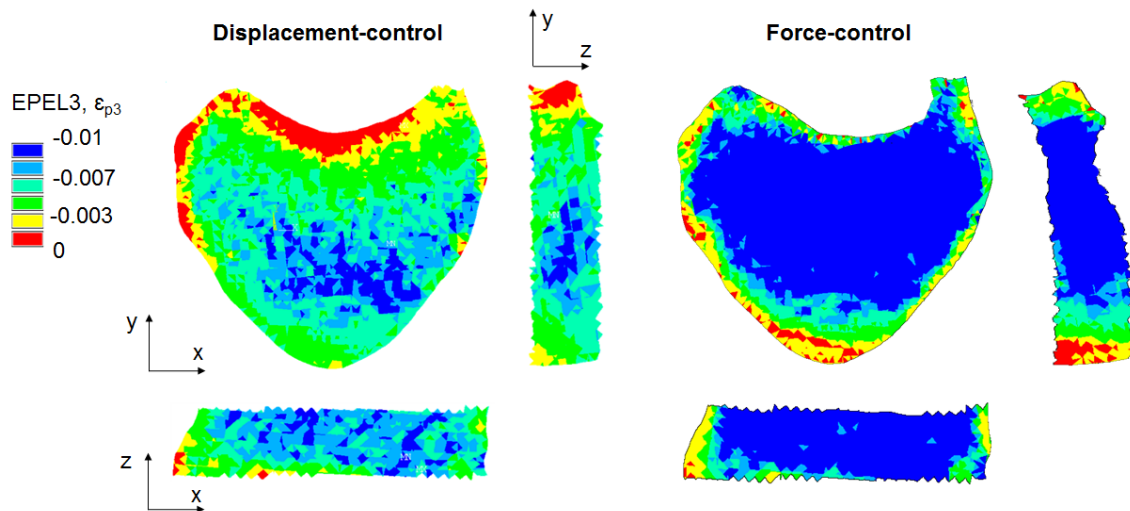


Figure 5.21 - Distribution of the third principal strains (EPEL3) over the vertebra with the lytic lesion, T5, for displacement-control analysis of 1.9% apparent strain (on the left), and for the equivalent force-control analysis (on the right). Plots obtained at approximately the same extent of apparent failure deformation (i.e. 1.9% apparent strain).

From a modelling point of view, the displacement-control analyses were easier to control and less computationally expensive (i.e. force-control analyses took approximately 2.3 times longer to run than equivalent displacement-control analyses).

As the aim of this study was to create efficient subject-specific models of vertebrae with lytic lesions, which may have critical locations and sizes as found for T5, displacement-control boundary conditions were preferred.

## 5.4. Estimation of physiological vertebral loads

This section covers the development of a geometric 2D model of the sagittal alignment of the spine used for the estimation of the physiological external loads applied to the vertebrae of the thoracic and lumbar spine of each subject. This simple model will allow the comparison of the outputs obtained between the vertebrae with lytic lesions and the closest controls.

To date, little is known about vertebral loading conditions in daily living activities due to the limitations of *in vivo* measurements (i.e. intervertebral disk pressure, IDP, and instrumented vertebral implants) (Rohlmann et al., 2008, 2014; Takahashi et al., 2006; Polga et al., 2004; Wilke et al., 2001; Sato et al., 1999; Schultz et al., 1982). Musculoskeletal (MSK) models can provide *in silico* predictions of spinal loads, accounting for body dynamics and the effect of muscles, ligaments, and other anatomical parts (e.g. ribcage), that are otherwise not possible to obtain. The validation of MSK models has been limited to axial loading conditions and is affected by the scarcity of experimental data, which is mostly obtained from IDP and instrumented measurements performed only at a few thoracic and lumbar vertebral levels (Alexander et al., 2017; Ignasiak et al., 2016). Moreover, MSK models have been developed mainly to gain a better understanding of the spine biomechanics and spinal disorders. Thus, MSK models have mostly been applied to study the thoracolumbar and lumbar spinal segments of specific populations (Ignasiak et al., 2016; Han et al., 2012, 2013; Schultz et al., 1982). The aim of this study was to generate a simplified static 2D geometric model of the sagittal alignment of the spine in order to obtain reasonable estimates of the resultant loads acting on each thoracic and lumbar vertebral body of the spine taking into account some of the factors that mostly affect the vertebral loading, namely the subject's weight, height, spinal curvature, spinal balance, spinal range of motion, and external loads (Alexander et al., 2017; Han et al., 2013; Alexander et al., 2012; Christiansen & Bouxsein, 2010). This model was used in the study performed on Chapter VI to compare the structural stability of the vertebrae with and without lytic lesions under representative physiological loading conditions.

### 5.4.1. Materials and methods

A 2D model of the sagittal alignment of the spine (from the second cervical level, C2, to the sacrum S1), was built in Matlab to estimate the loads and moments acting over the centroid of the vertebrae of a subject's spine. Vertebral loads were estimated by accounting for some of the factors that mostly affect the vertebral loading, namely the subject's weight, height, spinal curvature, spinal balance, spinal range of motion, internal and external loads. Estimates of compressive loads, shear loads, and axial bending moments were obtained by this model. However, due to the lack of literature data on shear and bending vertebral loads, this study emphasized on the estimates of compressive vertebral loads. Estimated shear and bending moments can be found in the Supplementary material S2.

#### *Definition of the geometry and sagittal alignment of the model*

The position and orientation of the vertebral bodies' (VB) centroids of the baseline model were defined from the measurements reported by Keller et al. (2005) and Bernhardt & Bridwell (1989). Inter-segmental vertebral orientations were used to define the thoracic kyphosis (TK) and lumbar lordosis (LL) angles, defined as the angles between T1-L1 and L1-L5 respectively, to account for the differences in the vertebral orientations according to the spinal levels. The scaling of the height of a subject's spine (i.e. distance between C2-S1) was performed based on a scaling factor computed for every vertebral segment and adjusted for the body height of the subject to be modelled. The position of the VB centroids was updated based on their normal angle. The scaling of the spinal curvature was applied homogeneously along the thoracic and lumbar segments according to the TK angle defined between T1-L1, and the LL angle defined between L1-L5 (Chen, 1999) (difference of 1° for a TK defined between T1-T12 as it is usually defined based on the Cobb's method). Vertebral loading also depends on the sagittal spinal balance, considered as the horizontal distance between the centroids of C7 and S1 and known as the sagittal vertical axis (SVA) or plumb line, and on the position of the centre of mass of the body weight (LOG). In the literature, the SVA is known to vary in the range of 0±24 mm (Kuntz et al., 2007) for normal spines, whereas the LOG was reported to be at 20 mm anterior to the L1 and L2 (Pearsall et al., 1996). Based on such uncertainties, the definition of this geometric parameters relied on a tuning procedure where the values that generated the best match of vertebral loads predicted between the 2D model and a reference 3D MSK model were used (Alexander et al., 2017) (Supplementary material S1). Thus, the SVA was defined as equal

to 24 mm, by changing the orientation of the sacrum (i.e.  $R_y$ ) in  $10^\circ$ , and the LOG was defined at 7 mm anterior from L2 (i.e. reduction of 35% of the baseline position of the LOG defined with respect to L2) (see Supplementary material S1 for details about the tuning procedure).

### *Estimation of vertebral loads and moments*

The spine was modelled as a series of rigidly linked segments (Fig 5.22). The static equilibrium was computed based on equations [Eq. 5.8-5.12] presented below, assuming that the spinal balance is achieved between the body weight and an internal forces modelled implicitly.

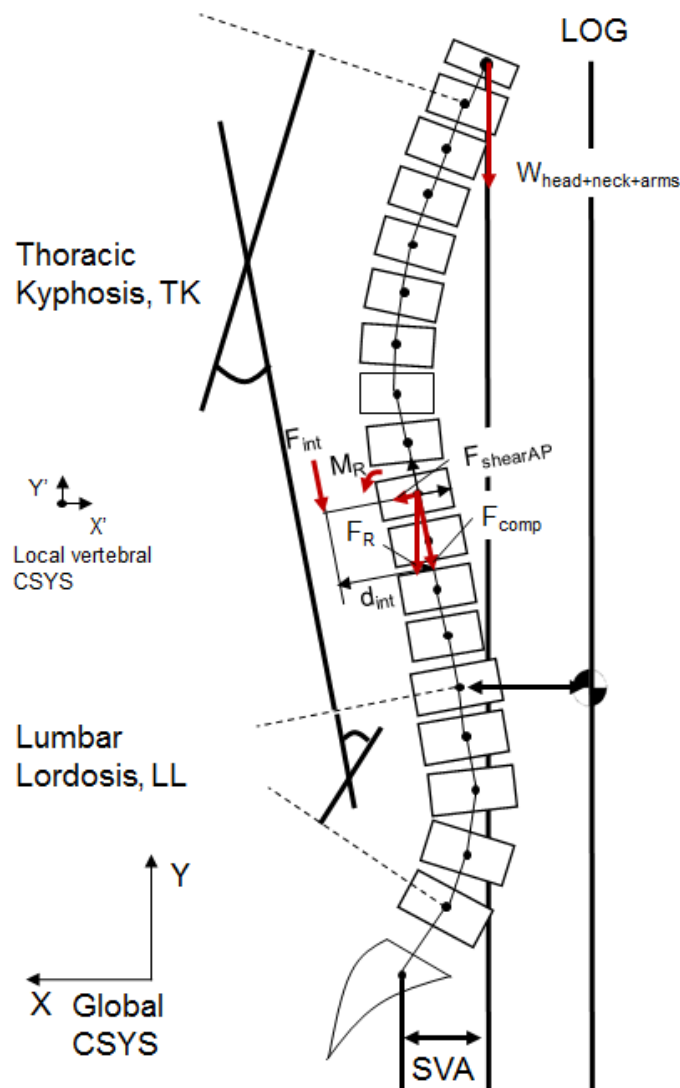


Figure 5.22 - Scheme of the 2D geometric model of the sagittal alignment of the spine under a neutral standing posture. Free body diagram of the static equilibrium computed for the thoracic vertebra T9 balanced by a resultant load which accounted for the body weight at that spinal level plus the internal joint reaction force.

The equivalent internal force required to balance the joint moments and maintain the static equilibrium was computed for each vertebra [Eq. 5.13]. This equivalent internal force was representative of the symmetric actions of the thoracolumbar muscles and ligaments, which were assumed to act along the longitudinal axis of the spine, contributing only for the computation of the axial loads. Based on CT and MRI anatomical measurements taken from the muscle groups known to have a great contribution to the extension of the thoracolumbar spinal (i.e. *erector spinae*, *rectus abdominus*, *multifidus*, *latissimus dorsi*), the average value of the moment arms of the muscles can vary between 50 mm and 60 mm (Christophy et al., 2012; Jorgensen et al., 2001; McGill et al., 1993). Considering that the muscles moment arms can vary of 17.5% between genders (Jorgensen et al., 2001), in this simplified 2D spinal model a constant equivalent moment arm equal to 50 mm or 60 mm was used for female and male subjects respectively. The following equations were used to balance the loads at each vertebra:

$$M_R = M_{BW} = BW \times d_{LOG}; \quad [\text{Eq. 5.11}]$$

Where  $M_R$  represents the resultant moment computed as the moment generated by the body weight ( $M_{BW}$ ), which was estimated as the load generated by the body weight ( $BW$ ) multiplied by the distance between the centroid of the vertebra and the centre of mass of the body weight ( $d_{LOG}$ ).

$$F_R = BW + F_{int}; \quad [\text{Eq. 5.12}]$$

$$F_{int} = \frac{M_R}{d_{int}}; \quad [\text{Eq. 5.13}]$$

Where  $F_R$  represents the reaction loads estimated for each vertebra based on the load generated by body weight ( $BW$ ) and an internal load ( $F_{int}$ ).  $F_{int}$  represents the resultant loads used to balance the joint-reaction moments, which were computed as the ratio between the vertebral reaction moment ( $M_R$ ) and the equivalent lever arm of the muscles ( $d_{int}$ ).

$$F_{comp} = \frac{BW}{\cos \theta_{yy}} + F_{int}; \quad [\text{Eq. 5.14}]$$

Where  $F_{comp}$  represents the axial component of the resultant loads estimated for each vertebra, and  $\theta_{yy}$  represents the angle between the vector of the body weight and the axial direction of the local coordinate system of each vertebra.

$$F_{shearAP} = \frac{BW \times \tan \theta_{y/y}}{\cos \alpha_{x/x}}; \quad [\text{Eq. 5.15}]$$

Where  $F_{shearAP}$  represents the shear load acting over the anterior-posterior axis of each vertebra, and  $\alpha_{x/x}$  represents the angle between the x-axis of the global and local coordinate systems.

The body weight (BW) was distributed along the body segments in the following way: head and neck (8.1%BW), arms and hands (2\*5.6%BW), upper trunk (defined from T1-T12 and equal to 21.6%BW), and lower trunk (defined from L1-L5 and equal to 13.9%BW), based on anthropometric data (Winter, 2009). The masses of each body segment were distributed among the vertebral bodies. In particular, the weights of the head and neck, arms and hands were lumped and applied on the first thoracic vertebra T1, while the body weight of the trunk was homogenously distributed among the thoracolumbar vertebrae (Fig 5.22). The position of the centre of mass of the body weight (line of gravity, LOG) was defined by a reduction of 35% to the 20 mm anterior distance to the L1 reported by Pearsall et al. (1996) (Supplementary material S1 section Combined effect SVA and LOG) (Fig 5.22).

Compressive loads acting along the axial axis, shear loads acting along the anterior-posterior axis, and the resultant moment acting upon the centroid of each vertebral body were, estimated based on a local coordinate system defined for each vertebral body in static equilibrium (Fig 5.22). Two different spinal configurations were modelled with the aim to simulate different physiological activities, namely a relaxed upright standing (Fig 5.22) and a 30° trunk flexion with external forces being applied in front of the body (Fig 5.23).

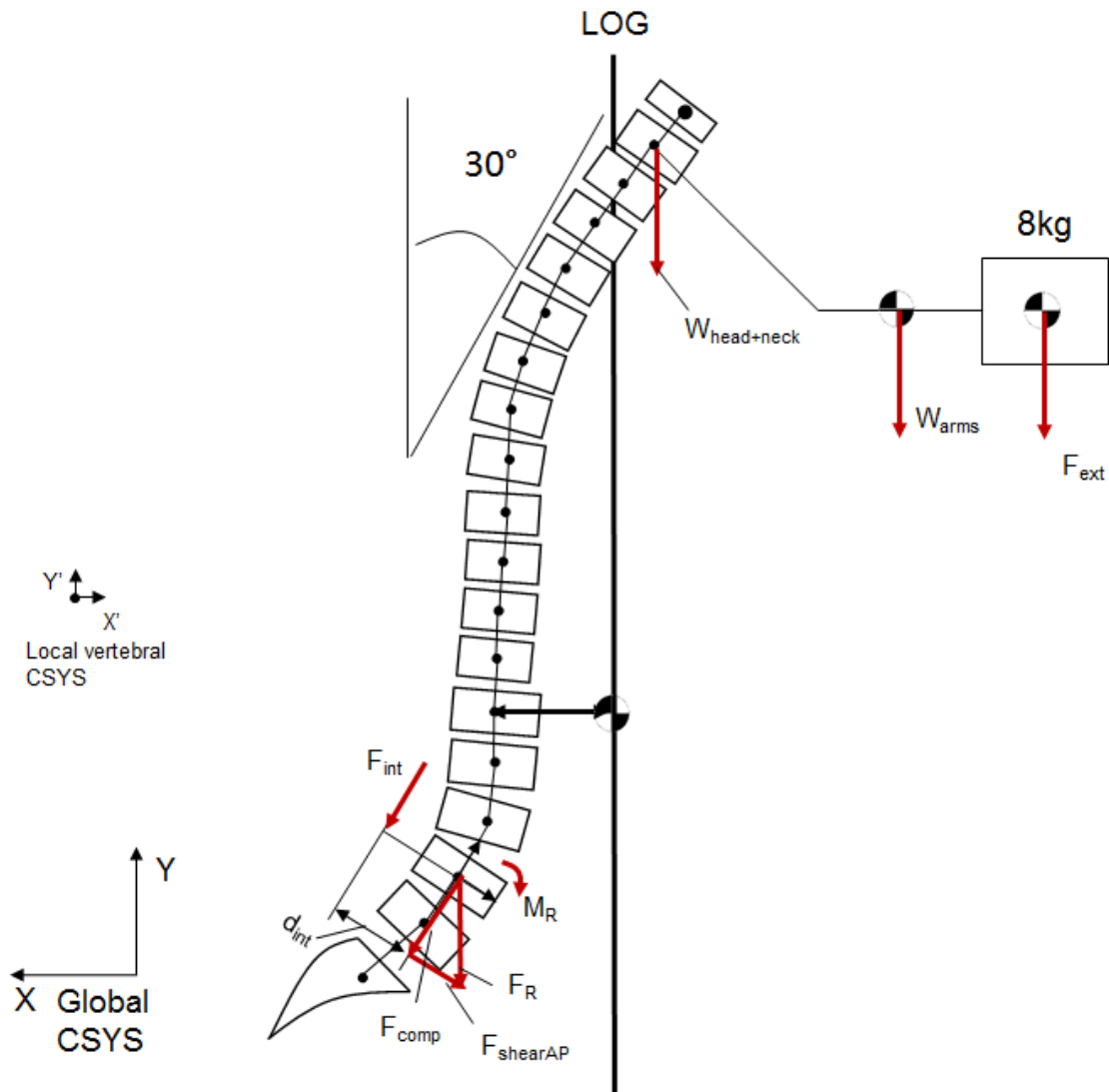


Figure 5.23 – Scheme of a 30° trunk flexion posture with 8kg in front of the body modelled by the 2D spinal model. Free body diagram of the static equilibrium computed at L4 balanced by the resultant load which account for both the body weight at that specific level plus the internal reaction force required to balance the joint moment generated by the body weight, arms and external load.

In the trunk flexion condition, it was assumed that the both thoracic and lumbar segments had similar contributions to the overall trunk flexion (52% contribution of the lumbar spine and 48% contribution of the thoracic spine). A 30° trunk flexion condition was modelled using the baseline ranges of motion between intervertebral thoracolumbar segments (Alexander et al., 2017). The trunk flexion was assumed to occur over the sacrum, S1, which was fixed, limiting the lumbar flexion of the model. The condition simulated by the model represented a 30° trunk flexion holding 8kg in hands with the arms flexed (in particular the shoulders flexed at 45° and the elbows at 135°) (Fig 5.23). The moments generated by the body weight, arms,

and the external load, carried in front of the body, were applied to all the thoracic and lumbar vertebrae [Eq. 5.16] (Fig 5.23). The moment arm related to the carried load was computed for the distance between the centroid of T1 and the total length of extension of the arms (taking the upper arm length as 18.8% of the subject's height (H), the forearm length as 14.5% of H, and the length of the hands as 10.8% of H (Winter, 2009)), assuming a sagittal alignment between the centre of the shoulder and the centroid of T1. For the computation of the lever arm generated by the arms, a centre of mass of 53% of the arm's length (i.e. upper and forearm length) was assumed (Winter, 2009). The static equilibrium computed for the flexed posture with weights was computed based on the following equations:

$$M_R = M_{BW} + M_{Arms} + M_{ext} ; \quad [\text{Eq. 5.16}]$$

Where  $M_R$  represents the reaction moment computed as the sum of the moment generated by the body weight ( $M_{BW}$ ), the arms ( $M_{Arms}$ ), and the external force ( $M_{ext}$ ).

$$F_R = BW + F_{int} + F_{ext} : F_{int} = \frac{M_R}{d_{int}} ; \quad [\text{Eq. 5.17}]$$

Where  $F_R$  represents the resultant load acting on each vertebra, estimated as the sum of the load generated by the body weight ( $BW$ ), the single equivalent action of the spinal muscles ( $F_{int}$ ) used to equilibrate the joint-reaction moment, and the external weight ( $F_{ext}$ ). The equivalent moment arm of the spinal muscles,  $d_{int}$ , is used for the estimation of  $F_{int}$ .

$$F_{comp} = \frac{BW + F_{ext}}{\cos \theta_{y'y}} + F_{int} ; \quad [\text{Eq. 5.18}]$$

Where  $F_{comp}$  represents the axial component of the vertebral reaction loads estimated based on the body weight ( $BW$ ), external and internal loads ( $F_{ext}$  and  $F_{int}$ ). The  $\cos \theta_{y'y}$  represents the cosine of the angle estimated between the body and external weight vector with the axial axis of the local coordinate system of each vertebra.

$$F_{shearAP} = \frac{(BW + F_{ext}) \times \tan \theta_{y'y}}{\cos \alpha_{x'x}} ; \quad [\text{Eq. 5.19}]$$

Where  $F_{shearAP}$  represents the shear component of the resultant loads, generated by the body weight ( $BW$ ) and the external weight ( $F_{ext}$ ), which act over the anterior-posterior axis of the

local vertebral coordinate system. The angles  $\theta_{y/y}$  and  $\alpha_{y/y}$  are estimated between the local and global coordinate systems along the respective yy and xx directions.

### *Comparison with in vivo measurements and a validated MSK model*

The accuracy of the model estimates of compressive loads were compared to experimental measurements of intradiscal pressure (IDP) from the literature. This comparison was performed by a standard procedure used to convert the compressive forces estimated from the 2D spinal model to an equivalent IDP, using the mean correction factor ( $C_{corr}$ ) of 0.66 proposed by Nachemson (1960).

$$IDP_{model} = \frac{F_{comp}}{CSA_{IVD} \times C_{corr}} \quad [Eq 5.20]$$

An average cross section area of the thoracic and lumbar intervertebral disks ( $CSA_{IVD}$ ) was used based on the studies of Panjabi et al. (1991) and Brinckmann & Grootenboer (1991) respectively. Estimated average IDP was computed and compared to the experimental values at a number of thoracic and lumbar levels for a range of standing and trunk flexion activities with or without weights on hands, modelled to match the experimental conditions reported in the literature (Table 5.5). The model was scaled to the average weight and height of the population of each one of the studies used for the validation. The spinal curvature is known to have an effect on vertebral loading (Alkalay et al., 2018; Alexander et al., 2017). However, as no information was available about the spinal curvatures of the patients studied in the mentioned publications, the estimates of vertebral loads were performed for a range of spinal curvatures including one standard deviation from the considered mean normal spinal curvature (TK=50° and LL=43°) (Kuntz et al., 2007; Bernhardt & Bridwell, 1989). The variability included in the spinal curvature was of 12° over the TK and 4.32° in LL (i.e. low kyphosis spine: TK=38°, LL= 38.7°, average kyphosis spine: TK=50°, LL=43° and high kyphosis spine: TK=62°, LL=47.3°) to favour a congruent spinal posture (Alexander et al., 2012).

Table 5.5- Experimental studies used for the comparison of IDP estimates computed from the 2D spinal model, scaled to the average weight and height and physical activities used to measure IDP from a number of lumbar and thoracic levels.

References	Sample size	Weight [kg] (ranges)	Height [cm] (ranges)	Vertebral level	Activities
<b>Schultz et al. (1982)</b>	N=4	63 (56-66)	174 (165-187)	L3-4	-Standing with and without holding 8 kg with arms in* -30° trunk flexion holding or not 8kg with arms out*
<b>Wilke et al. (2001)</b>	N=1	72	1740	L4-5	-Standing with and without holding 20 kg in hands -Flexed forward
<b>Sato et al. (1999)</b>	N=8	73±11 (60-96)	173±6 (166-181)	L4-5	-Standing -30° trunk flexion
<b>Takahashi et al. (2006)</b>	N=3	72±4 (70-77)	176±5 (170-180)	L4-5	-Standing with and without 10kg in hands -30° trunk flexion with and without holding 10kg in hands
<b>Polga et al. (2004)</b>	N=6	73 (54-81)	178 (163-191)	T6-8 and T9-11	-Standing with and without holding 20kg in hands -30° trunk flexion with or without holding 20kg in hands

\*arms in means the arms were close to the body and arms out means that the arms were extended

Moreover, based on the limitations of the experimental data available from direct measurements of vertebral loading, the accuracy of models estimates of vertebral reaction loads and moments was compared to the equivalent vertebral loads predicted by a validated 3D MSK model, which will be referred to as “reference MSK model” (Alexander et al., 2017). This comparison was performed for two matching spinal configurations of, upright standing, and 30° trunk flexion with 8kg in front of the body with arms flexed. The 2D model was scaled in

weight, height, and spinal curvature to match the population modelled in the reference study. The components of the resultant vertebral loading in the sagittal plane, namely compression, shear (Supplementary material S2, Fig S5.1) and axial bending moments (Supplementary material S2, Fig S5.2) were computed for each modelled spinal posture, and compared to predictions of the reference MSK model obtained under similar conditions.

## **5.4.2. Results**

### *Comparison with in vivo measurements and a validated MSK model*

The intradiscal pressures (IDP) estimated from the 2D models estimations of vertebral compression loads showed reasonable correspondence with experimental measurements for stable symmetric activities of neutral standing with and without weights (Fig 5.24 black and yellow points against green and grey points). For flexed spinal postures, the relationship between estimated and measured IDP was more scattered. In general, it was observed an underestimation of lumbar IDP, apart from two scatter points obtained for both standing and flexion postures with weights (Fig 5.24 plot on the right). On the other hand, the thoracic IDP was overestimated, especially for the flexed postures with weights (Fig 5.24 plot on the left). The variation in the model's estimates of IDP was caused by differences in the spinal curvature, which were higher for the lumbar levels. Variability in the experimental measures of IDP was smaller than the variability of the estimated IDP, however experimentally such variability only captured the differences in the experimental methods applied to the studies' cohort, (i.e. variability between 0.04-0.27MPa for the model estimates of IDP against 0.001-0.180MPa for experimental measurements) (Fig 5.24).

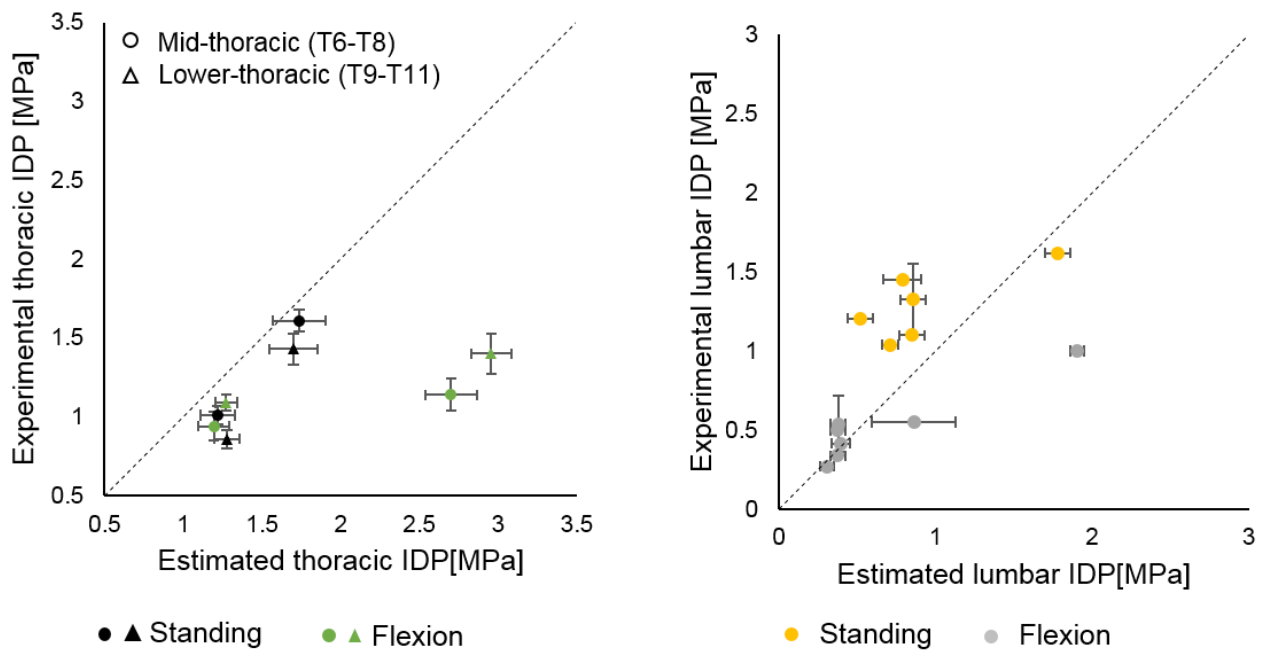


Figure 5.24 - Relationship between estimated intervertebral intradiscal pressure estimated from the 2D spinal model and experimental measurements collected from (a) the thoracic levels (Polga et al., 2004) and (b) the lumbar levels (Takahashi et al., 2006; Wilke et al., 2001; Sato et al., 1999; Schultz et al., 1982) for both standing and flexed spinal postures. Dashed line represents the 1:1 relationship.

Compared to the reference 3D MSK model, the simplified 2D model overestimated the vertebral compressive loads between T6 and T9 up to 36% (i.e. up to 18% of the body mass) for neutral standing posture. For the same levels and a 30° trunk flexion posture with weights, the compressive loads were overestimated by 25%-138% (i.e. between 64% and 185% of the body mass). Between T10 and L5, the vertebral compression loads were underestimated by 10% (i.e. 6% of the body mass) for standing and 8% (i.e. 30% of the body mass) for the flexed postures with respect to the reference model (Alexander et al., 2017) (Fig 5.25).

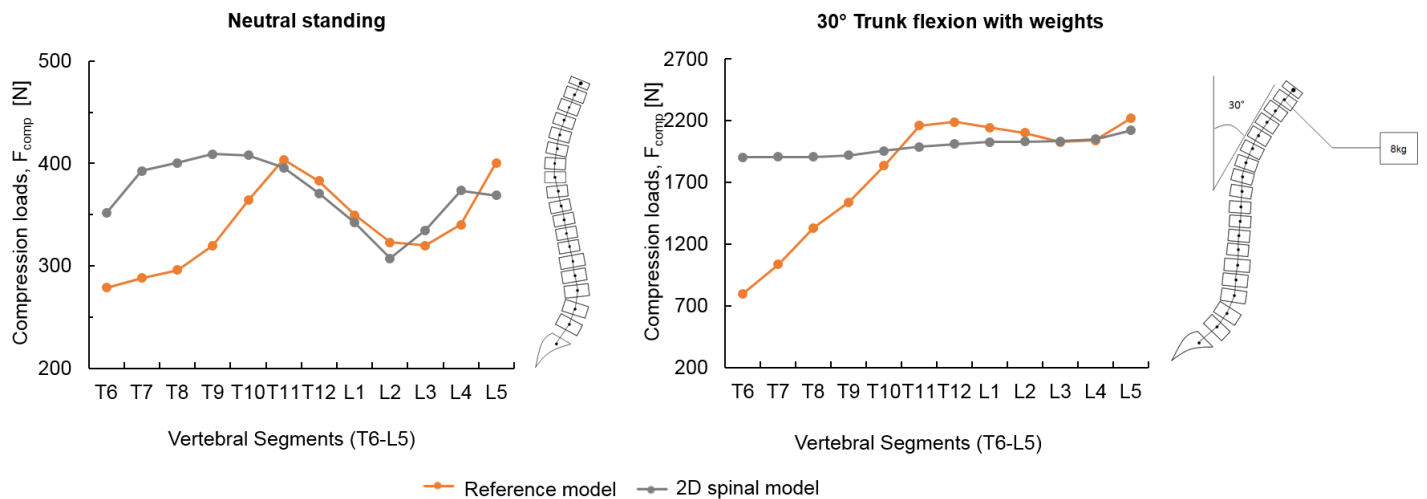


Figure 5.25 - Difference between the distribution of vertebral compressive loads estimated from the 2D spinal model (in gray) and the reference MSK model (Alexander et al., 2017) (in orange) for vertebral levels from T6 to L5 exposed to two different physiological spinal postures. Left: neutral standing posture. Right: 30° trunk flexion posture holding 8kg in front of the body.

### 5.4.3. Discussion

The aim of this study was to develop a simplified 2D model of the spine, to obtain reasonable estimates of vertebral loads as a function of a subject's weight, height, spinal curvature, sagittal vertical balance, and external loads. In the context of the clinical study, described in Chapter VI, it is important to normalise subject-specific vertebral strength to the applied vertebral loading under physiological conditions for different vertebra levels. The model was developed to simulate two static physiological spinal postures, namely standing and a 30° trunk flexion.

A reasonably good correspondence was observed between estimated and measured IDP (Fig 5.24). The model estimates of IDP were better related to the IDP measurements for standing postures than for flexed postures. In general, the IDP values were overestimated for the lower (T6 to T8) and mid-thoracic (T9 to T11) levels and were underestimated for the lumbar levels L3 to L5 (Fig 5.24). These results underline some of the limitations of the 2D model, which does not account for structures as the ribcage, sternum, and intra-abdominal pressure. These structures are known to influence muscle activity, and vertebral compressive forces which are decreased by up to 33% at the thoracic level for flexed spinal postures (Ignasiak et al., 2016; Han et al., 2012; Iyer et al., 2010). For neutral standing postures, the influence of the aforementioned structures is minimal as they act to support a system already in equilibrium (Iyer et al., 2010). A few estimates of the IDP from both the thoracic and lumbar levels showed

higher differences compared to the experimental measurements (Fig 5.24). Such estimates correspond to asymmetric spinal postures involving the support of external weights, which are affected by the simplified representation of the spinal structure of the present model. However, the experimental measurements obtained from those conditions are also influenced by the position of the insertion of the pressure-sensing needle, which due to the expected asymmetric distribution in IDP can move from the centre of the intervertebral disks, as usually targeted, thus failing in the capture of the mean IDP.

The comparison between estimations and measurements of IDP values was focused on the extreme static physiological postures modelled by the 2D spinal model used in this study (i.e. neutral standing and 30° degree trunk flexion, with or without weights). Therefore, the model was scaled for the mean weight and height of the studies' cohort. The variability in spinal curvature was not included in the experimental measurements. However, such variability was shown to reduce the mean vertebral loading between 10% and 40% for standing and trunk flexion posture with weights (Alexander et al., 2017). In the present model, changes of 1 standard deviation in the spinal curvature (i.e. TK=50°±12° and LL=43°±4.32°) affected between 2% to 31% estimates of IDP.

The results of the 2D model were also compared to a reference 3D MSK model from the literature (Alexander et al., 2017) that was validated against *in vivo* measurements. As expected, there was a higher percentage difference between predictions of vertebral loads of the 2D model and of the reference model for the flexed posture compared to the standing posture. Moreover, for both standing and flexed postures, vertebral compressive loads were overestimated for the mid to lower thoracic levels (i.e. T6 to T9), while they were slightly underestimated for the lumbar levels (Fig 5.25) (%diff computed with respect to the reference model higher than 20% from T6-T9 for both standing and flexion and lower than 12% from T10-L5). This higher difference for the thoracic spine is probably due to the lack of detail in the spinal anatomy and the absence of dynamic effects in the 2D model. For instance, the action of muscles and ligaments on the stabilisation of spinal loads is only accounted for in a simplistic way through the use of an internal force factor to represent the resultant effect of the muscle and ligament forces. This approach has been used to account for the interaction between bone and soft tissue structures used by the spine to balance and stabilise spinal loading and avoid underestimation of bone-on-bone loads (Reeves & Cholewicki, 2003). However, muscle and ligaments are known to be grouped in different line-of-actions and more than one muscle can contract to produce equilibrium (Han et al., 2012). By accounting only for a single internal

force acting parallel to the spinal axis, the model becomes unable to capture load peaks, which are generated by high activation of specific muscle groups used to equilibrate the spine under a certain posture, as captured by the reference model (e.g. observed for the thoracolumbar segments T11 to L1 for the standing posture. Fig 5.25). Moreover, compressive loads estimated by the model were sensitive to the equivalent muscle moment arm which is known to vary with population, anatomy, age, gender and spinal position (Christophy et al., 2012; Jorgensen et al., 2001). However, in the 2D model, only constant gender related changes of the lever arm were considered. Another limitation of the 2D spinal model is the lumping of the body weight of segments as head, neck, arms and hands over T1. Similar approaches have been used among MSK models which typically lump both head and neck weights to the first thoracic vertebra (Alexander et al., 2017; Ignasiak et al., 2016). However, the arms and hands are known to have an important effect on the balance of the trunk under asymmetric postures such as flexion. This limitation affected the estimated bending moment, which in contrast to the other estimates of vertebral loading, showed higher differences against the reference model for the standing posture rather than for the flexed posture with weights (i.e. %diff of up to 69% for standing and 15% for flexion. See Supplementary material S2, Fig S5.2).

Compared to the reported mean vertebral compressive loads obtained from a similar 2D static postural model developed by Keller et al. (2005), an average difference of up to 8% of the BW was observed in estimations of compressive load obtained from the full thoracic and lumbar spine (i.e. from T1-L5). Such difference may be explained by differences in the definition of the geometric models. In fact, in both the literature 2D model (Keller et al., 2005), and the reference 3D MSK model (Alexander et al., 2017) predictions of vertebral loads were computed with respect to the centroid of the IVD (also called as the instantaneous axis of rotation), instead of the centroid of the vertebral bodies, as used by the present model. However, changing the local coordinate systems of the vertebral bodies to the centroids of the IVD (Keller et al., 2005), caused negligible differences in the vertebral loads estimated from the different local coordinate systems (mean percentage difference of compressive and shear loads and bending moments were lower than  $2\% \pm 0.5\%$ ).

The present model assumes a normal sagittal alignment and does not account for any change caused by aging or overweight, which have been demonstrated to play an important role in vertebral loading, by causing an increase in TK and an anterior shift in the centre of mass (Alexander et al., 2012). However, changes in the sagittal alignment could be accounted for in the present model by changing the spinal curvature (i.e. TK and LL angles) and the SVA input

parameters. Deformities in the frontal plane, caused by spinal pathologies as scoliosis, were not considered by the model as well.

Considering the above-mentioned limitations of the presented 2D model, it should be stressed that its use will be limited to estimate the physiological load in adjacent vertebrae of the same subject (Chapter VI). In this sense, the 2D spinal model is considered to be able to provide reasonable estimates of vertebral compressive loads between T10 and L5 for standing and flexed posture (i.e. %diff lower than 30% of the body mass computed with respect to the reference model (Alexander et al., 2017)). However, for upper thoracic levels, from T6 to T9, vertebral compressive loads were overestimated by over 30% of the body mass with respect to the reference model for the flexion and up to 18% for standing. Thus, for vertebral levels up to T9, the use of a correction factor equal to the mean difference computed between vertebral loads estimated from the 2D model and the reference model is proposed. Thus, for standing, a correction factor of 0.24 shall be used to correct the vertebral loads estimated by the present 2D spinal model from levels up to T9, whereas for flexion, a factor of 0.38 is more appropriate.

## 5.5. References

- Alexander, B. G., Anderson, D. E., Agostino, J. D. & Bouxsein, M. L. (2012). The Effect of Thoracic Kyphosis and Sagittal Plane Alignment on Vertebral Compressive Loading. *Journal of Bone and Mineral Research*, 27(10), 2144–2151.
- Alexander, B. G., Bouxsein, M. L. & Anderson, D. E. (2017). Development and Validation of a Musculoskeletal Model of the Fully Articulated Thoracolumbar Spine and Rib Cage. *Journal of Biomechanical Engineering*, 137, 1–10.
- Alexander, B. G., Burkhart, A. K., Allaire, A. B., Anderson, D. E. & Bouxsein, M. L. (2017). Spinal Loading Patterns From Biomechanical Modeling Explain the High Incidence of Vertebral Fractures in the Thoracolumbar Region. *Journal of Bone and Mineral Research*, 1–9.
- Alkalay, R., Adamson, R., Miropolsky, A. & Hackney, D. (2018). Female Human Spines with Simulated Osteolytic Defects: CT-Based Structural Analysis of Vertebral Body Strength. *Radiology*, 288(2), 436–444.
- Bernhardt, M. & Bridwell, K. (1989). Segmental Analysis of the Sagittal Plane Alignment of the Normal Thoracic and Lumbar Spines and Thoracolumbar Junction. *Spine*, 14, 717–721.
- Brinckmann, P. & Grootenboer, H. (1991). Change of Disc Height, Radial Disc Bulge and Intradiscal Pressure from Discectomy. An in Vitro Investigation on Human Lumbar Disks. *Spine*, 16(6), 641–646.
- Buckley, J. M., Loo, K. & Motherway, J. (2007). Comparison of Quantitative Computed Tomography-Based Measures in Predicting Vertebral Compressive Strength. *Bone*, 40(3), 767–774.
- Campbell, G. M., Peña, J. A., Giravent, S., Thomsen, F., Damm, T., Glüer, C. C., et al. (2017). Assessment of Bone Fragility in Patients With Multiple Myeloma Using QCT-Based Finite Element Modeling. *Journal of Bone and Mineral Research*, 32(1), 151–156.
- Chen, Y.-L. (1999). Vertebral Centroid Measurement of Lumbar Lordosis Compared with the Cobb Technique. *Spine*, 24(17), 1786–1790.
- Christiansen, B. A. & Bouxsein, M. L. (2010). Biomechanics of Vertebral Fractures and the Vertebral Fracture Cascade. *Current Osteoporosis Reports*, 9, 198–204.
- Christophy, M., Adila, N., Senan, F., Lotz, J. C. & Reilly, O. M. O. (2012). A Musculoskeletal Model for the Lumbar Spine. *Biomech Model Mechanobiol*, (11), 19–34.
- Crawford, R. P., Cann, C. E. & Keaveny, T. M. (2003). Finite Element Models Predict in Vitro Vertebral Body Compressive Strength Better than Quantitative Computed Tomography. *Bone*, 33, 744–750.
- Dall'Ara, E., Pahr, D., Varga, P., Kainberger, F. & Zysset, P. (2012). QCT-Based Finite Element Models Predict Human Vertebral Strength in Vitro Significantly Better than Simulated DEXA. *Osteoporosis International*, 23, 563–572.
- Dall'Ara, E., Schmidt, R., Pahr, D., Varga, P., Chevalier, Y., Patsch, J., et al. (2010). A Nonlinear Finite Element Model Validation Study Based on a Novel Experimental Technique for Inducing Anterior Wedge-Shape Fractures in Human Vertebral Bodies in Vitro. *Journal of Biomechanics*, 43, 2374–2380.
- Dall'Ara, E., Varga, P., Pahr, D. & Zysset, P. (2011). A Calibration Methodology of QCT BMD for Human Vertebral Body with Registered Micro-CT Images. *Medical Physics*, 38(5), 2602–8.

- Derikx, L. C., van Aken, J. B., Janssen, D., Snyers, A., van der Linden, Y. M., Verdonshot, N., et al. (2012). The Assessment of the Risk of Fracture in Femora with Metastatic Lesions: Comparing Case-Specific Finite Element Analysis with Predictions by Clinical Experts. *The Journal of Bone and Joint Surgery*, 94(8), 1135–1142.
- Derikx, L. C., Verdonshot, N. & Tanck, E. (2015). Towards Clinical Application of Biomechanical Tools for the Prediction of Fracture Risk in Metastatic Bone Disease. *Journal of Biomechanics*, 48(5), 761–766.
- Ebbesen, E. N., Thomsen, J. S., Beck-nielsen, H., Nepper-rasmussen, H. J. & Mosekilde, L. I. S. (1999). Age- and Gender-Related Differences in Vertebral Bone Mass, Density, and Strength. *Journal of Bone and Mineral Research*, 14(8), 1394–1403.
- Fisher, C. G., Schouten, R., Versteeg, A. L., Boriani, S., Varga, P. P., Rhines, L. D., et al. (2014). Reliability of the Spinal Instability Neoplastic Score ( SINS ) among Radiation Oncologists : An Assessment of Instability Secondary to Spinal Metastases. *Radiation Oncology*, 9(1), 1–7.
- Fourney, D. R., Frangou, E. M., Ryken, T. C., Dipaola, C. P., Shaffrey, C. I., Berven, S. H., et al. (2011). Spinal Instability Neoplastic Score : An Analysis of Reliability and Validity From the Spine Oncology Study Group. *Journal of Clinical Oncology*, 29(22), 3072–3077.
- Han, K., Rohlmann, A., Zander, T. & Taylor, W. R. (2013). Lumbar Spinal Loads Vary with Body Height and Weight. *Medical Engineering and Physics*, 35(7), 969–977.
- Han, K., Zander, T., Taylor, W. R. & Rohlmann, A. (2012). An Enhanced and Validated Generic Thoraco-Lumbar Spine Model for Prediction of Muscle Forces. *Medical Engineering & Physics*, 34, 709–716.
- Ignasiak, D., Dendorfer, S. & Ferguson, S. J. (2016). Thoracolumbar Spine Model with Articulated Ribcage for the Prediction of Dynamic Spinal Loading. *Journal of Biomechanics*, 49(6), 959–966.
- Imai, K., Ohnishi, I. & Bessho, M. (2006). Nonlinear Finite Element Model Predicts Vertebral Bone Strength and Fracture Site. *Spine*, 31(16), 1789–1794.
- Iyer, S., Christiansen, B. A., Roberts, B. J., Valentine, M. J., Manoharan, R. K. & Bouxsein, M. L. (2010). A Biomechanical Model for Estimating Loads on Thoracic and Lumbar Vertebrae. *Clinical Biomechanics*, 25, 853–858.
- Jorgensen, M. J., Marras, W. S., Granata, K. P. & Wiand, J. W. (2001). MRI-Derived Moment-Arms of the Female and Male Spine Loading Muscles. *Clinical Biomechanics*, 16, 182–193.
- Keller, T. S., Colloca, C. J., Harrison, D. E., Harrison, D. D. & Janik, T. J. (2005). Influence of Spine Morphology on Intervertebral Disc Loads and Stresses in Asymptomatic Adults : Implications for the Ideal Spine. *The Spine Journal*, 5, 297–309.
- Kopperdahl, D. L., Aspelund, T., Hoffmann, P. F., Sigurdsson, S., Siggeirsdottir, K., Harris, T. B., et al. (2014). Assessment of Incident Spine and Hip Fractures in Women and Men Using Finite Element Analysis of CT Scans. *Journal of Bone and Mineral Research*, 29(3), 570–580.
- Kuntz, C. I., Levin, L. S., Ondra, S. L., Shaffrey, C. I. & Morgan, C. J. (2007). Neutral Upright Sagittal Spinal Alignment from the Occiput to the Pelvis in Asymptomatic Adults: A Review and Resynthesis of the Literature. *Journal of Neurosurgery Spine*, 6, 104–112.
- Lenherr, C., Voumard, B., Stadelmann, M., Buck, F., Haschtmann, D., Hoppe, S., et al. (2018). *Indentation Properties of Metastatic Vertebral Trabecular Bone*. 8<sup>th</sup> World Congress of Biomechanics, Dublin, Ireland, 8-12<sup>th</sup> July 2018.

- Matsuura, Y., Giambini, H., Ogawa, Y., Fang, Z., Thoreson, A. R., Yaszemski, M. J., et al. (2014). Specimen-Specific Nonlinear Finite Element Modelling to Predict Vertebral Fracture Loads after Vertebroplasty. *Spine*, 39(22), E1291–E1296.
- McGill, S. M., Santaguida, L. & Stevens, J. (1993). Measurement of the Trunk Musculature from T5 to L5 Using MRI Scans of 15 Young Males Corrected for Muscle Fibre Orientation. *Clinical Biomechanics*, 8, 171–178.
- Melton, L. J., Riggs, B. L., Keaveny, T. M., Achenbach, S. J., Kopperdahl, D., Camp, J. J., et al. (2010). Relation of Vertebral Deformities to Bone Density, Structure, and Strength. *Journal of Bone and Mineral Research*, 25(9), 1922–1930.
- Nachemson, A. (1960). Lumbar Intradiscal Pressure: Experimental Studies on Post-Mortem Material. *Acta Orthopaedica Scandinavica*, 43, 1–104.
- Nazarian, A., Von Stechow, D., Zurakowski, D., Müller, R. & Snyder, B. D. (2008). Bone Volume Fraction Explains the Variation in Strength and Stiffness of Cancellous Bone Affected by Metastatic Cancer and Osteoporosis. *Calcified Tissue International*, 83, 368–379.
- Pahr, D. H., Schwiedrzik, J., Dall, E. & Zysset, P. K. (2014). Clinical versus Pre-Clinical FE Models for Vertebral Body Strength Predictions. *Journal of the Mechanical Behavior of Biomedical Materials*, 33, 76–83.
- Panjabi, M., Takata, K., Goel, V., Federico, D., Oxland, T., Duranceau, J., et al. (1991). Thoracic Human Vertebrae. Quantitative Three-Dimensional Anatomy. *Spine*, 16(8), 888–901.
- Pearsall, D., Reid, J. & Livingston, L. (1996). Segmental Inertial Parameters of the Human Trunk as Determined from Computed Tomography. *Annals of Biomedical Engineering*, 24, 198–210.
- Pointillart, V., Ravaut, A. & Palussière, J. (2002). *Vertebral Metastasis*. France: Springer-Verlag France.
- Polga, D. J., Beaubien, B. P., Kallemeier, P. M., Schellhas, K. P., Lew, W. D., Buttermann, G. R., et al. (2004). Measurement of In Vivo Intradiscal Pressure in Healthy Thoracic Intervertebral Discs. *Spine*, 29(12), 1320–1324.
- Reeves, N. P. & Cholewicki, J. (2003). Modeling of the Human Lumbar Spine for Estimating Spinal Loads, Stability, and Risk of Injury. *Critical Reviews in Biomedical Engineering*, 31, 73–139.
- Rijsbergen, M. van, van Rietbergen, B., Barthelemy, V., Eltes, P., Lazáry, Á., Lacroix, D., et al. (2018). Comparison of Patient-Specific Computational Models vs. Clinical Follow-up, for Adjacent Segment Disc Degeneration and Bone Remodelling after Spinal Fusion. *Plos One*, 13(8), e0200899.
- Rohlmann, A., Graichen, F., Kayser, R., Bender, A., Nat, R. & Bergmann, G. (2008). Loads on a Telemeterized Vertebral Body Replacement Measured in Two Patients. *Spine*, 33(11), 1170–1179.
- Rohlmann, A., Pohl, D., Bender, A., Graichen, F., Dymke, J., Schmidt, H., et al. (2014). Activities of Everyday Life with High Spinal Loads. *PLOS ONE*, 9(5), 1–9.
- Sato, K., Kikuchi, S. & Yonezawa, T. (1999). In Vivo Intradiscal Pressure Measurement in Healthy Individuals and in Patients With Ongoing Back Problems. *Spine*, 24(23), 2468–2474.
- Schileo, E., Dall'Ara, E., Taddei, F., Malandrino, A., Schotkamp, T., Ñ, M. B., et al. (2008). An Accurate Estimation of Bone Density Improves the Accuracy of Subject-Specific Finite Element Models. *Journal of Biomechanics*, 41, 2483–2491.

- Schileo, E., Taddei, F., Cristofolini, L. & Viceconti, M. (2008). Subject-Specific Finite Element Models Implementing a Maximum Principal Strain Criterion Are Able to Estimate Failure Risk and Fracture Location on Human Femurs Tested in Vitro. *Journal of Biomechanics*, 41, 356–367.
- Schneider, C. A., Rasband, W. S. & Eliceiri, K. W. (2012). NIH Image to ImageJ: 25 Years of Image Analysis. *Nature Methods*, 9(7), 671–5.
- Schultz, A., Andersson, G., Ortengren, R., Haderspeck, K. & Nachemson, A. (1982). Loads on the Lumbar Spine. Validation of a Biomechanical Analysis by Measurements of Intradiscal Pressures and Myoelectric Signals. *Journal of Bone and Joint Surgery*, 64(5), 713–720.
- Singer, K., Day, R., Breidahl, P. & Price, R. (1995). Prediction of Thoracic and Lumbar Vertebral Body Compressive Strength: Correlations with Bone Mineral Density and Vertebral Region. *Bone*, 17(2), 167–174.
- Stadelmann, M., Alkalay, R., Maquer, G., Buck, F., Hoppe, S., Theumann, N., et al. (2018). *Can Micro and Homogenized Finite Element Analysis Estimate the Strength of Human Metastatic Vertebrae?* 8<sup>th</sup> World Congress of Biomechanics, Dublin, Ireland, 8-12<sup>th</sup> July 2018.
- Sternheim, A., Giladi, O., Gortzak, Y., Drexler, M., Salai, M., Trabelsi, N., et al. (2018). Pathological Fracture Risk Assessment in Patients with Femoral Metastases Using CT-Based Finite Element Methods. A Retrospective Clinical Study. *Bone*, 110, 215–220.
- Takahashi, I., Kikuchi, S. & Sato, K. (2006). Mechanical Load of the Lumbar Spine During Forward Bending Motion of the Trunk – A Biomechanical Study. *Spine*, 31(1), 18–23.
- Wang, X., Sanyal, A., Cawthon, P. M., Palermo, L., Jekir, M., Christensen, J., et al. (2012). Prediction of New Clinical Vertebral Fractures in Elderly Men Using Finite Element Analysis of CT Scans. *Journal of Bone and Mineral Research*, 27(4), 808–816.
- Whyne, C. M., Hu, S. S., Worman, K. L. & Lotz, J. C. (2000). Biphase Material Properties of Lytic Bone Metastases. *Annals of Biomedical Engineering*, 28, 1154–1158.
- Wilke, H., Neef, P., Hinz, B., Seidel, H. & Claes, L. (2001). Intradiscal Pressure Together with Anthropometric Data - a Data Set for the Validation of Models. *Clinical Biomechanics*, 16(S1), S111–S126.
- Winter, D. A. (2009). *Biomechanics and motor control*, 4<sup>th</sup> Edition, John Wiley & Sons, Inc., New Jersey.
- Yosibash, Z., Plitman, R., Dahan, G., Trabelsi, N., Amir, G. & Milgrom, C. (2014). Predicting the Stiffness and Strength of Human Femurs with Real Metastatic Tumors. *Bone*, 69, 180–190.

## Supplementary materials

### S1. 2D Spinal model: tuning procedure

The tuning procedure aimed to adjust some of the geometrical input parameters of the 2D model to find the best match between vertebral loads predicted from the 2D model and the reference validated 3D MSK model (Alexander et al., 2017). Due to their uncertainty and effect on vertebral loading, the parameters covered in this analysis were the sagittal vertical alignment of the spine (SVA) and the position of the line of gravity (LOG). The effect of each parameter was first evaluated separately and then, as they were not independent from each other, the best values obtained from the independent analyses were crossed to find the values that would provide the best match between models estimates of vertebral loads.

To allow the comparison between models, the 2D models were scaled to the weight, height, and spinal curvature of the population modelled in the reference study (W=61kg, H=163cm, TK=50° and LL=43°) (Alexander et al., 2017). These analyses were performed only for a static upright spinal condition. The mean and standard deviation of the percentage differences of the model estimates of vertebral compression, shear, and moment loads were computed with respect to the reference model.

#### *Effect of the sagittal vertical alignment*

In this analysis, the effect of changes in the sagittal vertical alignment of the spine (SVA) was evaluated through rotations within the sagittal axis of the sacrum (i.e. Ry). The SVA was varied between the normal average values reported for asymptomatic subjects of 0±24mm (Kuntz et al., 2007), by changing the orientation of the sacrum from 2.5° to 12.5° in increments of 2.5°. These models were then compared to the baseline model defined for Ry=0°, SVA=-55mm and a centre of gravity, LOG, defined 20mm anterior from L2.

The effect of the variations in the SVA parameter was higher for estimated shear loads (mean absolute changes to the baseline model ranging from 21%-100%) followed by bending moment, and compressive loads (mean absolute changes to the baseline model ranging from 17%-54% for bending and 4%-17% for compression). Changes from a backward balanced spine (i.e. SVA<0) towards a forward sagittal balance (SVA>0) led to a decrease in the mean

%diff of the estimates of compressive forces and moments of up to 24% and 39%, respectively, computed with respect to the baseline model (Table S5.1). Such decrease was higher for the thoracic and thoracolumbar vertebral levels (i.e. from T6 to L2), which also overestimated both the compression and bending vertebral loads with respect to the reference model (i.e. %diff ranging from 23%-69% between T6-L2 for compression loads and %diff between 58% and 118% for bending moments estimated from the same vertebral levels for the most neutral spinal balance configuration obtained for  $R_y=7.5^\circ$ ). On average, the percentage difference of estimated shear loads also decreased by 74% for a rotation of the sacrum of  $2.5^\circ$  and  $12.5^\circ$  respectively (Table S5.1).

Sagittal rotations of the sacrum between  $5^\circ$  and  $10^\circ$  implied a change in the SVA for values approximately between -16 mm (sagittal balance bent backwards) and 24 mm (sagittal balance bent forward), which were within the range of variability observed for asymptomatic subjects (Kuntz et al.,2007). Within this range, a higher rotation of the sacrum led to a decrease in the average %diff of predictions of vertebral loads and moments (i.e. reduction of 99% on the mean %diff of shear loads computed between the baseline model where  $R_y=0^\circ$  against  $R_y=10^\circ$ , reduction of 32% on the mean %diff of bending moments and 20% for compression loads) (Table S5.1). Therefore, a forward sagittal balance seemed more appropriate than a backwards balance as it generated smaller average errors for predictions of vertebral loads and moments (Table S5.1).

*Table S5.1- Average and standard deviation of the percentage differences computed between vertebral loads (compression,  $F_{comp}$ ; shear,  $F_{shear}$ ; and bending moment,  $M$ ) estimated from the 2D model and the reference model (Alexander et al., 2017) for changes in the sagittal vertical alignment (SVA) generated by rotations of the sacrum ( $R_y$ ).*

<b>Sacrum Rotation, <math>R_y</math> [°]</b>	<b>SVA [mm]</b>	<b>%diff <math>F_{comp}</math> [N] Avg±std</b>	<b>%diff <math>F_{shear}</math> [N] Avg±std</b>	<b>%diff <math>M</math> [N.m] Avg±std</b>
0°	-55.16	50%±36%	279%±224%	92%±37%
2.5°	-35.56	45%±31%	247%±204%	90%±22%
5.0°	-15.90	41%±27%	219%±202%	84%±16%
7.5°	3.80	35%±24%	195%±216%	71%±20%

10.0°	23.49	30%±20%	180%±241%	59%±33%
12.5°	43.92	26%±15%	173%±276%	53%±40%

---

### *Effect of the position of the line of gravity*

Relative changes in the position of the line of gravity (LOG) with respect to the centroid of the vertebral bodies affected mainly the resultant bending moment computed from the static equilibrium of the spinal model, which as a result affected the estimations of the compressive forces required to balance such bending moment. The LOG was varied between 15% and 55%, in increments of 10%, with respect to the reference value defined 20 mm anterior from L1 and L2 (Pearsall et al., 1996). The baseline model assumed no rotation of the sacrum ( $R_y=0^\circ$ ) and a sagittal balance bent backwards ( $SV=-55$  mm).

As expected, a decrease in the relative position of the LOG, defined at 20 mm from L2 (i.e. LOG1) decreased the average percentage difference of estimated vertebral moments with respect to the reference model (Table S5.2). However, when defining the LOG at 20 mm from L1 (i.e. LOG2), the relative decrease of the lever arms increased the average errors of the estimated bending moments (increase of 12% in the %diff obtained between mean bending loads estimated from the 2D model and the reference model for relative changes of 15% and 55% in the position of the LOG2).

A decrease of 45% and 55% in the relative position of LOG1 decreased the average errors of models predictions of bending moments by 25% and 33% respectively (Table S5.2). This decrease in bending moments consequently led to a, lower, decrease in the percentage difference of the estimated mean compressive loads (i.e. decrease in the %diff of the mean estimates of compression loads of up to 9%) (Table S5.2). Small mean %diff in vertebral compressive loads and moments estimated from the 2D model and the reference model were also observed for a LOG defined at 20 mm from L1 (Table S5.2). Therefore, centre of gravities defined at 20 mm anterior from L1 (i.e. LOG2) or at 9 mm and 11 mm anteriorly from L2 (Table S5.2 -45%LOG1 and -55%LOG1) showed to be potentially good parameters and were considered in the next analysis where the combined effects of the SVA and LOG parameters were considered.

Table S5.2-Effect of relative changes in the position of the line of gravity (LOG) of the 2D spinal model on the estimation of vertebral compressive loads and bending moments. Report of the mean percentage difference of vertebral loads and moments computed with respect to the reference model (Alexander et al., 2017).

LOG	%diff Fcomp [N]	%diff_M [N.m]
	Avg±std	Avg±std
LOG1 <sup>1</sup>	50%±36%	92%±37%
-15%LOG1	47%±35%	82%±34%
-25%LOG1	45%±34%	80%±28%
-35%LOG1	43%±33%	74%±26%
-45%LOG1	42%±31%	67%±29%
-55%LOG1	41%±30%	59%±38%
LOG2 <sup>2</sup>	38%±27%	66%±39%

<sup>1</sup>LOG1=20mm from L2; <sup>2</sup>LOG2=20mmL1

### *Combined effect of SVA and LOG*

As the position of the centre of gravity (i.e. LOG) will change with the spinal posture (i.e. SVA), the effect of the LOG for well-balanced configurations of the spine obtained using a sagittal rotation of the sacrum of 7.5° (i.e. SVA~4 mm) and 10° (i.e. SVA~24 mm) were analysed below (Table S5.1).

The results were better for a balanced spine which was slightly bent forward (Ry=10°, SVA=23 mm) compared to a slightly more neutral balanced spine (Ry=7.5°) (Table S5.3). Moreover, varying the position of the centre of gravity using as reference the vertebral level L1 (i.e. LOG2) instead of L2 (i.e. LOG1) was more effective in reducing the differences between estimated and reference vertebral loads and moments (i.e. maximum drop of 36% in the mean %diff of bending moments and 12% for compressive loads computed for LOG2 with respect to LOG1 for Ry=7.5°) (Table S5.3).

Table S5.3- Effect of the position of the LOG and SVA on the percentage difference of the 2D model estimations of compressive loads and moments compared to the reference 3D MSK model.

Sacrum			%diff Fcomp [N]	%diff M [N.m]
Rotation, Ry [°]	SVA[mm]	LOG	avg±std	avg±std
7.5	3.80	LOG1 <sup>1</sup>	35%±24%	71%±20%
7.5	3.80	-45%LOG1	25%±21%	45%±20%
7.5	3.80	-55%LOG1	23%±20%	37%±24%
7.5	3.80	LOG2 <sup>2</sup>	23%±20%	35%±22%
7.5	3.80	-15%LOG2	20%±19%	27%±15%
7.5	3.80	-25%LOG2	19%±18%	28%±19%
7.5	3.80	-35%LOG2	18%±17%	34%±27%
10	23.49	LOG1 <sup>1</sup>	30%±20%	59%±33%
10	23.49	-45%LOG1	20%±17%	37%±24%
10	23.49	-55%LOG1	19%±17%	33±31%
10	23.49	LOG2 <sup>2</sup>	19%±17%	36%±28%
10	23.49	-15%LOG2	16%±16%	26%±27%
10	23.49	-25%LOG2	14%±15%	20%±23%
10	23.49	-35%LOG2	14%±15%	20%±24%

<sup>1</sup>LOG1=20mm from L2; <sup>2</sup>LOG2=20mmL1

The model that provided the smaller mean %diff between estimated and reference loads and moments was the model defined for a rotation of the sacrum Ry=10°, and a reduction of 25% and 35% in LOG2 (Table S5.3). For these models the mean %diff for compression loads and moments was the same and equal to 14% and 20% respectively (Table S5.3). However, the range of %diff computed per vertebra was slightly smaller for a 35% reduction of LOG2 (i.e. %diff of up to 79% for bending moments computed from T6 to L5 for LOG=-25%LOG2, and %diff of up to 69% for LOG=-35%LOG2). Although not reported, it was also observed that a higher reduction in LOG2 would increase the mean %diff of estimated compression loads and bending moments. Estimated vertebral compression loads showed higher %diff compared to the reference model between the thoracic levels T6 and T9 (i.e. %diff of up to 36% between T6-T9 against %diff of up to 12% from T10-L5 computed for LOG=-35%LOG2). In terms of

bending moments, percentage differences higher than 20% were only observed for L2, L4 and L5.

The combined effect of a sagittal spinal balance slightly bent forward (i.e. SVA=24 mm for  $Ry=10^\circ$ ) and the location of the centre of gravity at 7 mm anterior to L2 (i.e. LOG=-35%LOG2) resulted in a reduction of the mean %diff of vertebral loads, estimated between the 2D model and the reference model, compared to the baseline 2D model (i.e. set for LOG2, SVA=-55 mm and  $Ry=0^\circ$ ). Such reduction was of up to 24% for estimated compressive loads, 99% for shear loads, and 46% for bending moments (Table S5.1, S5.2 and S5.3). Thus the input parameters used in the 2D models to define the sagittal alignment and the centre of mass were  $Ry=10^\circ$  (i.e. SVA=24 mm) and LOG defined at 7mm anterior from L2.

## **S2. 2D Spinal model: Shear loads and bending moments**

The anterior-posterior shear loads and bending moments estimated by the 2D spinal model were computed for the range of physiological postures considered in this study, namely standing posture and  $30^\circ$  trunk flexion posture holding 8kg in front of the body. The same conditions were considered by the reference model used for the assessment of the accuracy of the 2D model estimates of vertebral loads and moments.

Anterior-posterior shear loads were majorly underestimated for the standing posture up to a maximum of 9% of the body mass with respect to the reference model (Fig S5.1). For the levels T6, T7 and L1, shear loads were overestimated by up to 12% of the body mass (Fig S5.1). For the flexed posture, differences between the shear loads estimated from the 2D model and the reference model were higher, as there was an underestimation of loads of up to 39% of the body mass at T10. For the thoracolumbar levels T12 to L3 shear loads were overestimated by up to 29% of the body mass (Fig S5.1). Overall, the 2D model was able to capture the pattern of shear loading distribution predicted from the reference 3D MSK model, except for the peak shear loads in T10 and between L1 and L3 (Fig S5.1).

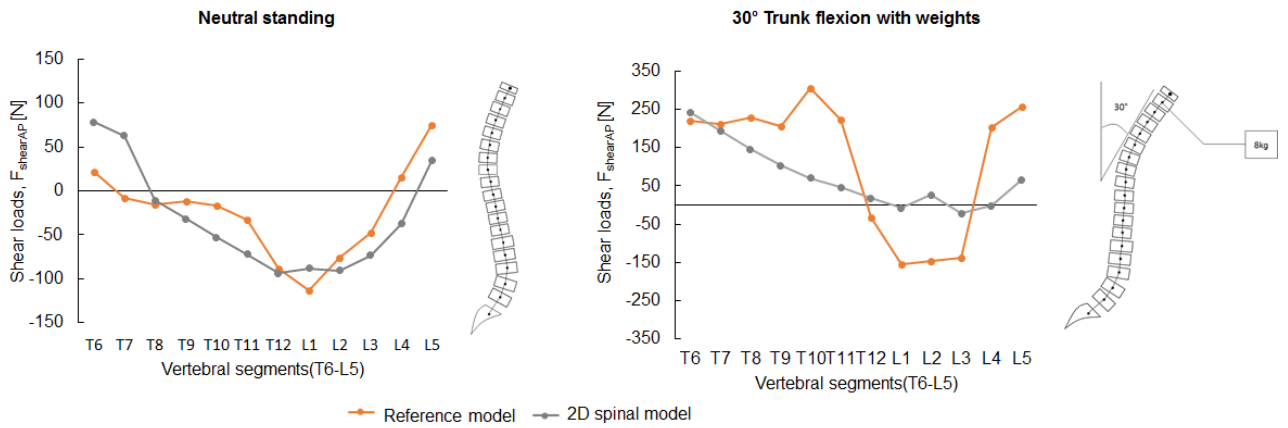


Figure S5.1- Distributions of shear loads estimated by the 2D spinal model (in gray) and the reference MSK model (in orange) (Alexander et al., 2017) from vertebral segments T6 to L5 simulated for a standing (left) and a 30° trunk flexion (right) postures.

The estimated reaction bending moments showed low differences compared to the values predicted from the 3D MSK reference model. For both standing and flexed postures, differences between the 2D model and the reference model were negligible (i.e. equal or lower than 2% of the body mass) (Fig S5.2).

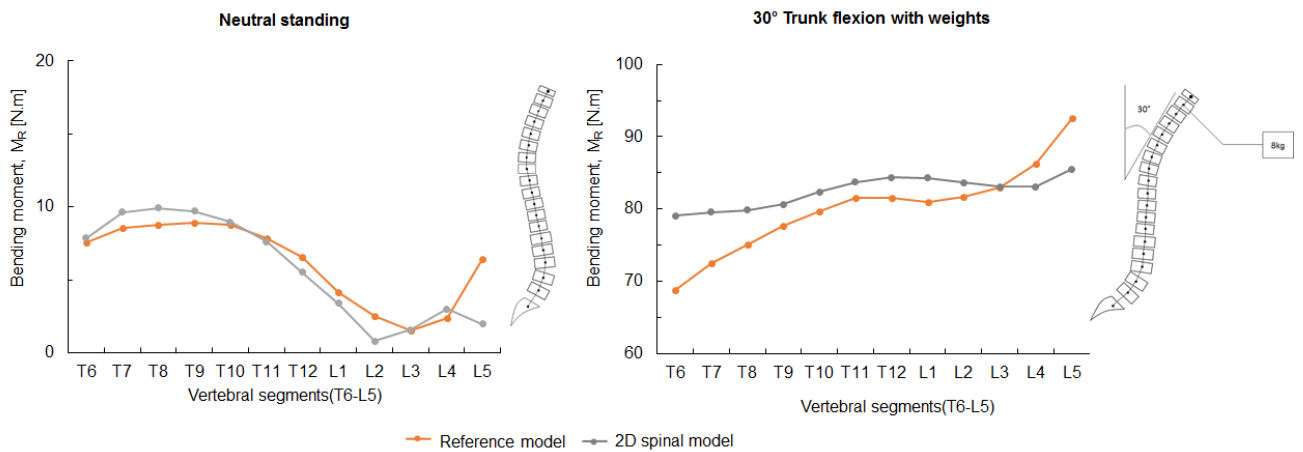


Figure S5.2- Distribution of the resultant bending moment estimated by the 2D spinal model (in gray) and the reference MSK model (in orange) (Alexander et al., 2017) from vertebral segments T6 to L5 simulated for a standing (left) and a 30° trunk flexion (right) postures.



## **Chapter VI. Clinical subject-specific finite element models for prediction of the effect of lytic lesions on vertebral mechanical properties**

### **Acknowledgments**

This study was performed in collaboration with Dr. Peter Endre Eltes and Dr. Áron Lazáry from the National Centre for Spinal Disorders in Budapest, Hungary who provided the anonymized CT datasets of patients with vertebrae with lytic lesions used in the following chapter. The clinical partners have also provided the SINS score for each vertebra with lytic lesions. Moreover, part of the study described in this chapter was submitted for publication in the Journal of Orthopaedic Research (MC Costa, P. Eltes, A. Lazáry, M. Viceconti, E. Dall'Ara Effect of lytic metastases on the vertebral strength estimated with subject-specific finite element models, *Submitted* to the Journal of Orthopaedic Research on November 2018).

## Abstract

The assessment of risk of vertebral fracture in patients with lytic metastases is currently based on the Spinal Instability Neoplastic Score (SINS), which however in many cases does not provide clear guidelines. The aim of this study was to develop a computational approach to evaluate the effect of lytic lesions on the structural properties and stability of patients with spinal metastases.

Eight patients with vertebrae with lytic lesions, with SINS between 7 and 12 (indeterminate unstable), were considered. For each patient, subject-specific computed tomography (QCT)-based, heterogeneous finite element (FE) models of vertebrae with and without lytic lesions were generated to estimate the mechanical properties. From a static 2D spinal model, patient-specific applied vertebral compressive loads were estimated for a physiologic loading condition. A safety factor for each vertebra was calculated as the ratio between the yield stress and the normalised applied load. Three to six vertebrae were modelled (at least one vertebrae with a lesion and the two closest controls) for each patient, for a total of 30 models (12 vertebrae with lytic lesions).

The subject-specific analyses showed that not all the lytic lesions had a detrimental effect on the mechanical properties of the vertebral bodies, due to an increase in the local bone mineral density (equivalent BMD) around the lesion. Predicted compressive vertebral strength was well correlated with equivalent BMD ( $R^2 = 0.84$  for pooled data). Moreover, the models allowed for discrimination between the vertebrae with lytic lesions at risk of fracture ( $n=8$ ) from those that were mechanically stable ( $n=4$ ).

This study shows that there is heterogeneity in the effect of lytic lesions on the structural integrity and stability of vertebrae, which vary from patient-to-patient. Furthermore, in this study it is presented a subject-specific quantitative approach that can be used together with the SINS for a better classification of patients with lytic spinal metastases. However, in order to generalize these finding a larger cohort of patients should be studied.

## 6.1. Introduction

Vertebral metastatic lesions are the most common bone metastases with over 70% of metastases located in the spine (Sutcliffe et al., 2013). Breast, lung, prostate, renal cancers, among others, are the common malignant conditions that lead to the development of lytic lesions on bone (Vialle et al., 2015). Typically, the lytic lesions generated by these types of cancers appear in the radiological images as focal regions with very low bone mineral density (BMD) (Sánchez & Sistol, 2014). Other cancers such as multiple myeloma and spinal haemangiomas cause a widespread of lytic lesions in bone (Sánchez & Sistol, 2014). The lytic lesions were found to decrease bone strength and increase the risk of fracture (Burke et al., 2018; Hardisty et al., 2012; Ebihara et al., 2004). Scoring systems as the SINS have been developed to identify patients who need surgical intervention due to the high fracture risk of vertebrae with metastases. Even though the SINS is considered as the most advanced method currently available to assess spinal metastases, it fails to identify true negative cases (i.e. specificity equal to 79.5%) (Fisher et al., 2014), leading to the overtreatment of patients already weakened due to the radio- and/or chemo-therapies they need to face against the primary cancer. Moreover, for SINS between 7 and 12 no clear guidelines are reported, making the decision of the clinicians more difficult and based on their experience.

Subject-specific FE models, applied to clinical QCT scans were found to be accurate in estimating the structural properties of human vertebrae measured *ex vivo* ( $0.28 \leq R^2 \leq 0.82$  for stiffness and  $0.78 \leq R^2 \leq 0.86$  for ultimate load) (Dall'Ara, 2012; Wang et al., 2012; Buckley et al., 2007; Crawford et al., 2003). This approach was also applied to study the structural response of a functional spinal unit (FSU) composed by two vertebrae, one of which included a mechanically induced lytic lesion (Alkalay & Harrigan, 2016). In that study the QCT-based model of the FSU was able to predict the global deformation of the vertebra with the lesion ( $R^2 = 0.91$ ). Moreover, they also showed that the lesion affected the loading transfer between vertebrae, with significant asymmetric changes in the strain distribution measured among the vertebrae with and without lesion of the FSU ( $p < 0.01$ ) (Alkalay & Harrigan, 2016). More recently, subject-specific FE models of cadaveric vertebrae with real lytic lesions resampled to clinical CT resolution (i.e. from 0.025 mm to 1 mm voxel size) showed to be accurate in predicting vertebral strength ( $R^2 = 0.73$ ) (Stadelmann et al., 2018). Previously, bilinear elastic-plastic clinical-based models of human vertebral bodies with and without mechanically induced lytic lesions were validated for predictions of compressive ultimate forces ( $R^2 = 0.76$ ) (Matsuura

et al., 2014). Despite the clear, local microstructural changes induced by the metastases on bone tissues, it was observed by Nazarian et al. (2008) that the relationship between structural axial compressive loading and BMD of trabecular bone with lytic lesions is similar to that observed for healthy tissues. Therefore, that study suggests that tissues with lytic lesions could be modelled as low-BMD bone tissue, having similar material properties as healthy bone. Recently, Lenherr et al. (2018) have confirmed this assumption by showing that there is no significant differences between the material properties of normal and lytic trabecular tissue extracted from human vertebrae and subjected to micro-indentation experiments (n=14).

The FE model predictions of strength are not sufficient to estimate the fracture risk of bones subjected to a certain loading scenario. Instead, the fracture risk can be estimated as the ratio between the applied load and the bone strength (load-to-strength ratio, the inverse of a safety factor). The applied load under relevant physiological activities can be estimated from biomechanical musculoskeletal models (Wang et al., 2012; Melton et al., 2007; Bouxsein et al., 2006; Myers & Wilson, 1997; Schultz et al., 1982). This approach has been used to better understand the relationship among vertebral fragility, loading, and the risk of fracture for osteoporotic vertebrae (Wang et al., 2012; Melton et al., 2007; Bouxsein et al., 2006). In particular, Wang et al. (2012) showed that predicted vertebral strength, volumetric BMD, and load-to-strength ratios improved the assessment of fracture risk compared to areal BMD measurements (i.e. area under the curve, AUC, between 0.82 and 0.83 versus an AUC equal to 0.76 for areal BMD). Recently, subject-specific heterogeneous QCT-based FE models, showed to improve the assessment of vertebral fracture of patients with multiple myeloma, condition which creates lytic lesions in the vertebral body (Campbell et al., 2017). In that study, predicted structural properties obtained from the subject-specific FE models, loaded in compression, better classified patients who had experienced a vertebral fracture compared to densitometric or microstructural parameters (i.e. Odds Ratios, ORs, between 1.7 and 2.3 found for predicted stiffness, yield force, and work-to-yield, against ORs between 1.4 and 1.7 for trabecular and cortical volumetric BMD and BV/TV) (Campbell et al., 2017). Nevertheless, the potential of the subject-specific FE models in predicting the mechanical stability of vertebrae with lytic lesions remains to be investigated.

The aim of this study was to use the subject-specific QCT-based FE models developed in Chapter V, to assess the effect of lytic lesions on the mechanical properties and stability of the vertebrae of patients with lytic metastases, thus providing a computational approach to support the decision-making of clinicians when the SINS does not provide clear guidelines.

## 6.2. Materials and methods

Twelve QCT scans collected from patients with vertebrae with lytic lesions, were provided by the National Center for Spinal Disorders of Budapest, Hungary in compliance with the ethical committee (10848-5/2018/EKU). Only vertebrae with lytic lesions classified as indeterminate unstable by the SINS (i.e. scores between 7-12) (Fourney et al., 2011), were included in this study. Four QCT scans were excluded due to SINS scores larger than 12 or with lesions affecting only the posterior elements. None of the patients were subjected to any radiotherapy session in the 6 months prior to the QCT scanning. From the eight QCT datasets of the considered patients (three males and five females,  $60\pm 12$  years old,  $70\pm 16$ kg weight, and  $168\pm 12$ cm height), vertebrae with lytic lesions were identified with the help of an experienced orthopaedic surgeon, who assessed the vertebral stability based on the SINS (Table 6.1).

*Table 6.1- Details of the cohort including patient's ID, dataset ID, age, gender (M for male and F for female), weight, height, vertebral levels modelled, their condition, and the SINS for the vertebrae with lytic lesions.*

Patient ID	Dataset ID	Age [yrs]	Gender	Weight [kg]	Height [cm]	Vertebral Level	Condition	SINS score
P1	MV00	59	M	92	192	T12	Control	-
						L1	Lytic	9
						L2	Control	-
						L3	Control	-
						L4	Lytic	7
						L5	Control	-
P2	MV04	63	F	69	164	L3	Control	-
						L4	Control	-
						L5	Lytic	7
P3	MV05	68	F	56	153	T4	Control	-
						T5	Lytic	10
						T6	Control	-
P4	MV06	39	F	44	166	L1	Control	-
						L2	Lytic	10
						L3	Lytic	8
						L4	Control	-

<b>P5</b>	MV08	70	F	82	163	L1	Control	-
						L2	Lytic	11
						L3	Control	-
<b>P6</b>	MV09	74	M	63	175	L2	Control	-
						L3	Lytic	12
						L4	Lytic	9
<b>P7</b>	MV10	63	F	80	162	L5	Control	-
						T11	Control	-
						T12	Lytic	8
<b>P8</b>	MV12	44	M	75	172	L1	Lytic	11
						L2	Control	-
						L3	Control	-
<b>P8</b>	MV12	44	M	75	172	L4	Lytic	7
						L5	Control	-

The QCT scans were acquired with a Hitachi Presto CT machine using an in-line calibration phantom, and a protocol previously defined in the MySpine project (ICT-2009.5.3 VPH) (Rijsbergen et al., 2018) with a voltage of 120 kV and an intensity of 225 mA. Images were reconstructed with a voxel size of  $0.6 \times 0.6 \times 0.6 \text{ mm}^3$ . For each patient, at least one vertebra with a lytic lesion and the two most adjacent control vertebrae (i.e. without lesions) were reconstructed and modelled.

For the patients P1, P4, P6, and P7 two vertebrae with lytic lesions were modelled (Table 6.1), whereas for the remaining patients only one vertebra with lytic lesions was modelled (Table 6.1). The QCT dataset of patient P5 was affected by local image artifacts, which affected the greylevels of some voxels in some of the cross-sections of the reconstructed image. Such artifacts were smoothed in a pre-processing operation to avoid potential issues in the mapping of material properties of the vertebrae (details in the Supplementary material S1).

The methods, described in Chapter V, were used to model each selected vertebra. In brief, each vertebra was reconstructed in Amira (v6.0.1, Thermo Fisher Scientific, Oregon, USA), using semi-automatic tools of segmentation and the marching cube algorithm. Each vertebra was then aligned based on an *in silico* reference framework (Danesi et al., 2014), and meshed using quadratic tetrahedral elements with a maximum edge size of 1.0 mm. Under the assumption that lytic lesions only affect local bone density (Nazarian et al., 2008), bone and

lytic tissue were modelled similarly as heterogeneous, isotropic, and elastic-plastic materials (details in Chapter V, section 5.2.1). The elastic properties of the tissues were estimated based on the subject-specific densitometric calibrations used to convert the HU values of the QCT images into BMD equivalent values at each element (see Chapter V, section 5.1.2, Fig 5.4), then converted to apparent density and elastic modulus (Chapter V, section 5.2.1, Eq 5.2 and 5.3) (Schileo, Dall'Ara, et al., 2008; Morgan et al., 2003; Les et al., 1994) (Bonemat software, Bologna, Italy). Bone plasticity was modelled using an isotropic yield criterion based on the density-strength relationship proposed by Morgan & Keaveny (2001), and a 95% reduction in the post-yield elastic modulus (Bayraktar et al., 2004; Morgan et al., 2003) (see Chapter V, section 5.2.1, Eq 5.4 and 5.5).

Each model was loaded up compressive failure by applying a 1.9% apparent deformation (Keaveny et al., 2014; Wang et al., 2012) to the surface nodes of the most cranial endplate. Vertebral models had on average 3 million of degrees of freedom and took approximately 2 hours to solve in the finite element software Mechanical APDL (ANSYS® Academic Research, Release 15.0) using parallel distributed memory over a maximum of 32 cores on Iceberg, the High-Performance Computing cluster of the University of Sheffield (3440 cores, 31.8TB of RAM).

For each vertebra model, axial resultant loads were computed as the sum of the nodal loads obtained from the bottom endplate. The displacements along the axial direction were computed for the node which was closest to the centroid of the cranial endplate. Such measurements were taken for each iteration of the nonlinear models. Spring stiffness ( $K$ ) was estimated as the slope of the linear range of the force-displacement curves and ultimate force ( $F_U$ ) was estimated as the resultant axial reaction force at 1.9% apparent strain (Keaveny et al., 2014; Wang et al., 2012). Work-to-failure ( $W$ ) was calculated as the area under the load-displacement curve until 1.9% global deformation. The cross section area (CSA) of each vertebra was calculated from the portion of the binary CT images which only included the vertebral body section, defined by a bounding box truncated manually at the most anterior and posterior points of the vertebral body excluding the endplates. The minimum height ( $H_m$ ) of each vertebra was computed as the axial distance between the most concave points of the vertebral endplates (details in Chapter V, section 5.2). Based on this geometrical parameters, normalised structural properties as apparent stiffness ( $E$ ), strength ( $\sigma_U$ ), and energy-to-failure ( $U$ ) were calculated. From the stress-strain curves of each vertebral model, yield stresses were estimated based on the 0.2% offset method (Morgan et al., 2001). Moreover, the equivalent BMD was estimated for a sub-region

of interest of each QCT image, which included the cortical and trabeculae bone tissues, in the middle portion of each vertebral body (50% of Hm), excluding the posterior elements (more details in Chapter V, section 5.2, Fig. 5.10). Bone mineral content (BMC) was then estimated as the equivalent BMD times the volume (V) of each considered sub-region of interest.

The effect of lytic lesions was evaluated as percentage differences between densitometric and mechanical properties of the vertebrae with the lesions, with respect to those computed for the control vertebrae, for each patient. A safety-factor (SF) was computed for the most critical loading case simulated from the 2D spinal model, presented in Chapter V, section 5.4 (i.e. 30° trunk flexion holding 8kg in hands). Based on the limitation of the FE models predictions of post-yield properties, the SF was defined as the ratio between the yield stress and the applied critical physiological stress estimated for each vertebra. The percentage difference between the SF of the vertebra with lytic lesion and the mean SF obtained for the control vertebrae was also computed for each patient. A warning system was implemented to identify vertebrae at risk of fracture due to a decrease in strength with respect to the controls (Warning FE), or due to a low safety-factor (Warning SF). Bearing in mind the limitations in the estimation of vertebral compressive loads, in this study, the warning SF was triggered for SFs lower or equal to 2.5. The risk of fracture of the vertebrae with lytic lesions was then classified based on the warning system in the following way: if a vertebra had no warnings it was considered safe (colour-coded by green), if it had one warning it was considered at risk of fracture (colour-coded by yellow), and if it had both warnings it was considered at very high risk of fracture (colour-coded by red).

Differences in densitometric and structural properties (normalised and non-normalised) predicted between the groups of vertebrae with and without lytic lesions were tested with an unpaired two-tails t-test also known as the Welch's test computed for a significance level of 0.05. Linear regressions were used to analyse the relationships between mechanical (normalised and non-normalised) and densitometric properties or between normalised stiffness and strength. Slope, intercept and coefficient of determination ( $R^2$ ) were reported.

### 6.3. Results

The mean equivalent BMD found for all vertebrae (pooled data) ranged from 0.10 g/cm<sup>3</sup> to 0.33 g/cm<sup>3</sup> (0.20±0.05 g/cm<sup>3</sup>) (Table 6.2). No significant difference was found between the BMD values obtained for vertebrae with or without lesions (p=0.57, 0.20±0.06 g/cm<sup>3</sup> against 0.21±0.05 g/cm<sup>3</sup> for controls) (Table 6.2 and 6.3). A similar trend was observed for the BMC (p=0.90, with 3.23±1.57 g for pooled data, 3.28±1.57 g for vertebrae with lytic lesions, and 3.20±1.61 g for controls).

*Table 6.2-Geometrica (i.e. minimum vertebral height, Hm, and cross-section area, CSA) and densitometric (mean equivalent bone mineral density, BMD, and bone mineral content, BMC) properties of each vertebral model.*

Patient ID	Dataset ID	Level	Condition	Hm [mm]	CSA [cm <sup>2</sup> ]	QCT Equivalent BMD [g/cm <sup>3</sup> ]	BMC [g]
P1	MV00	T12	Control	25.3	14.2	0.23	3.86
		L1	Lytic	22.2	16.6	0.22	3.85
		L2	Control	23.7	17.2	0.25	4.57
		L3	Control	24.1	17.0	0.27	5.09
		L4	Lytic	25.4	16.0	0.25	4.75
		L5	Control	23.6	15.6	0.33	6.24
P2	MV04	L3	Control	27.3	12.4	0.14	2.17
		L4	Control	25.1	13.4	0.15	2.42
		L5	Lytic	23.5	16.5	0.24	5.37
P3	MV05	T4	Control	14.6	4.79	0.17	0.55
		T5	Lytic	11.6	6.24	0.12	0.43
		T6	Control	16.1	5.32	0.17	0.66
P4	MV06	L1	Control	23.5	10.8	0.21	2.54
		L2	Lytic	21.0	11.8	0.25	2.92
		L3	Lytic	23.2	11.3	0.23	2.75
		L4	Control	27.7	10.7	0.22	3.03
P5	MV08	L1	Control	22.1	12.0	0.18	2.27
		L2	Lytic	23.2	15.2	0.18	2.91
		L3	Control	25.1	13.1	0.17	2.59
P6	MV09	L2	Control	23.4	14.5	0.25	3.84
		L3	Lytic	19.1	21.9	0.10	2.12
		L4	Lytic	24.4	16.3	0.21	4.32
		L5	Control	24.3	15.1	0.29	5.93
P7	MV10	T11	Control	19.8	11.8	0.16	1.72
		T12	Lytic	21.2	13.0	0.14	1.68
		L1	Lytic	22.7	14.2	0.17	2.52
		L2	Control	23.7	13.2	0.16	2.31
P8	MV12	L3	Control	26.1	15.3	0.19	3.60
		L4	Lytic	27.5	16.0	0.27	5.72
		L5	Control	23.5	15.9	0.21	5.95

There was also no significant difference among the mechanical properties (normalised and non-normalised) predicted between the groups of vertebrae with and without lytic lesions ( $0.61 \leq p \leq 0.98$ ) (Table 6.3).

*Table 6.3- Differences in densitometric (mean BMC and equivalent BMD) and estimated mechanical properties (K, F<sub>Y</sub>, F<sub>U</sub>, W, E,  $\sigma_Y$ ,  $\sigma_U$ , and U) computed for the vertebrae with or without lytic lesions. Percentage differences (%diff) computed with respect to the controls and p-values was also reported.*

	Controls		Lytic lesions		diff	%diff	p-value
	Avg±	Std	Avg±	Std			
<b>BMC [g]</b>	3.20±	1.61	3.28±	1.57	0.08	2%	0.90
<b>QCT Eq. BMD [g/cm<sup>3</sup>]</b>	0.21±	0.05	0.20±	0.06	-0.01	-6%	0.57
<b>K [kN/mm]</b>	41.40±	18.34	43.74±	15.25	2.35	6%	0.71
<b>F<sub>Y</sub> [kN]</b>	4.58±	2.17	4.56±	2.03	-0.02	-0.4%	0.98
<b>F<sub>U</sub> [kN]</b>	6.21±	3.02	6.23±	2.67	0.03	0.4%	0.98
<b>W [kN.mm]</b>	2.07±	1.05	2.02±	1.06	-0.05	-2%	0.90
<b>E [MPa]</b>	733±	206	692±	267	-41.74	-6%	0.65
<b><math>\sigma_Y</math> [MPa]</b>	3.43±	0.96	3.17±	1.26	-0.26	-7%	0.56
<b><math>\sigma_U</math> [MPa]</b>	4.62±	1.34	4.32±	1.63	-0.30	-6%	0.61
<b>U [MPa]</b>	0.065±	0.019	0.060±	0.023	-0.0044	-7%	0.59

The load-displacement and stress-strain curves predicted for the vertebrae with or without lesions showed a wide range of properties (Fig 6.1). Predicted ultimate load varied between 1.7 kN and 12.3 kN (6.2±2.8 kN for pooled data, 6.2±2.7 kN for vertebrae with lytic lesions, and 6.2±3.0 kN for control vertebrae) for all the vertebrae modelled with and without lytic lesions. Vertebral strength ranged from 1.4 MPa to 7.2 MPa (4.5±1.4 MPa for pooled data, 4.5±1.6 MPa for vertebrae with lytic lesions, and 4.6±1.3 MPa for control vertebrae) (Fig 6.1).

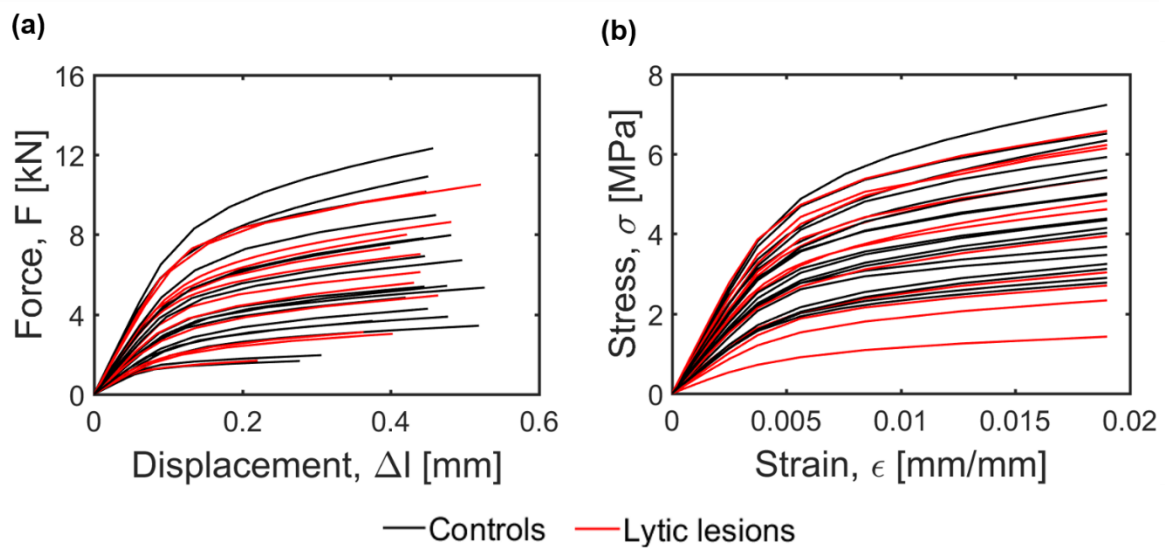


Figure 6.1-(a) Force-Displacement and (b) Stress-strain curves of all the vertebrae analysed in this study with lytic lesions (in red) and without lesions (controls, in black).

Predicted spring stiffness, yield force and ultimate force correlated well with the mean BMC measured within the vertebral body for pooled data ( $R^2=0.75$  for structural stiffness,  $R^2=0.84$  for yield force and  $R^2=0.82$  for ultimate force) (Fig 6.2). Slightly better correlations were found between normalised structural properties and BMD for pooled data ( $0.82 \leq R^2 \leq 0.85$  for normalised stiffness, strength and yield stress, against  $0.73 \leq R^2 \leq 0.78$  for structural properties) (Fig. 6.2). In most cases similar or better correlations between mechanical and densitometric properties were found for vertebrae with metastases (Fig 6.2).

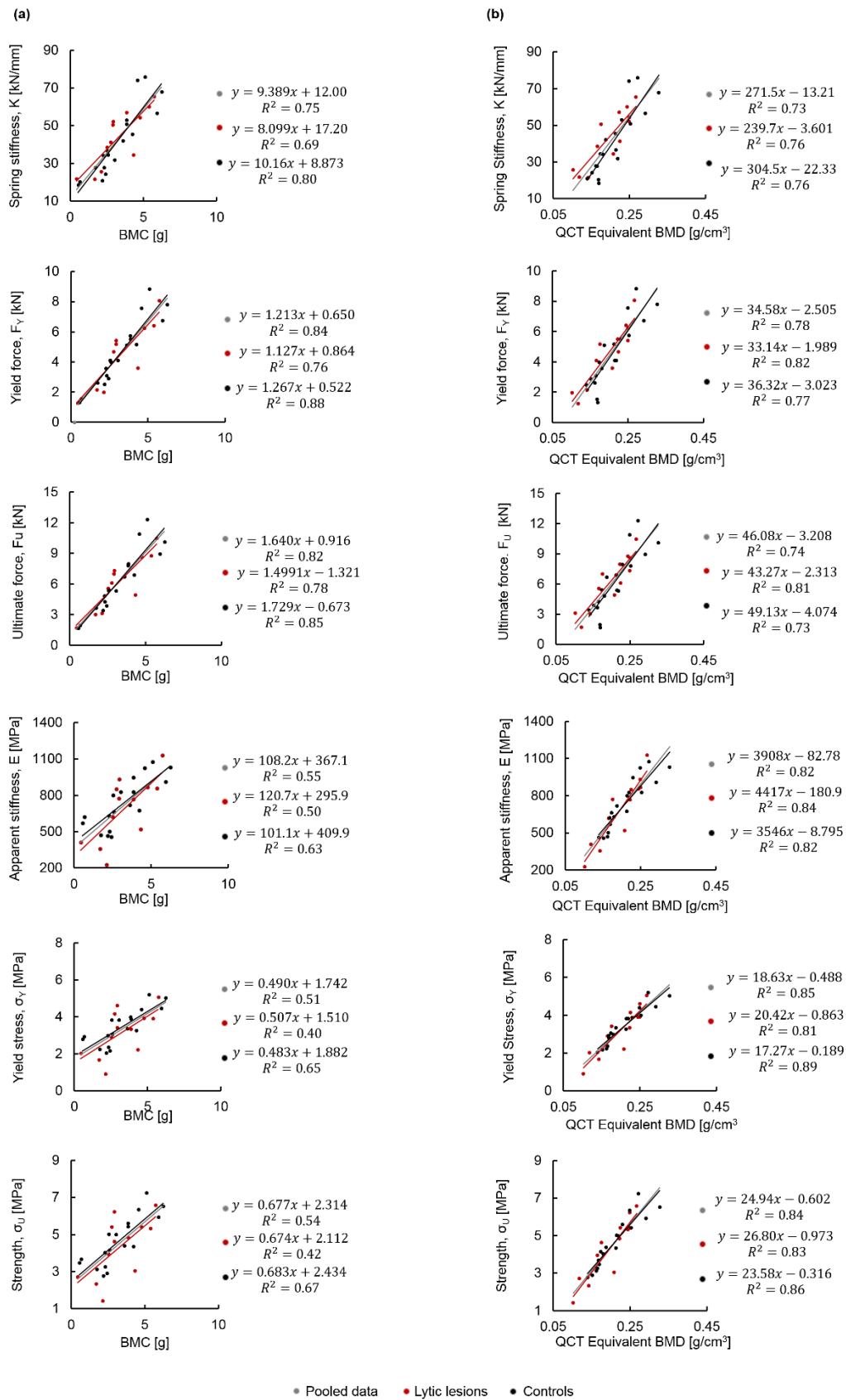


Figure 6.2- Linear regressions between (a) BMC or (b) BMD and structural and normalised structural mechanical parameters. Regression equations are reported for vertebrae with lesions (red), control vertebrae (black) or pooled data (grey).

As expected, predicted normalised structural properties as apparent stiffness and strength were highly correlated ( $R^2 \geq 0.98$ ) (Fig 6.3).

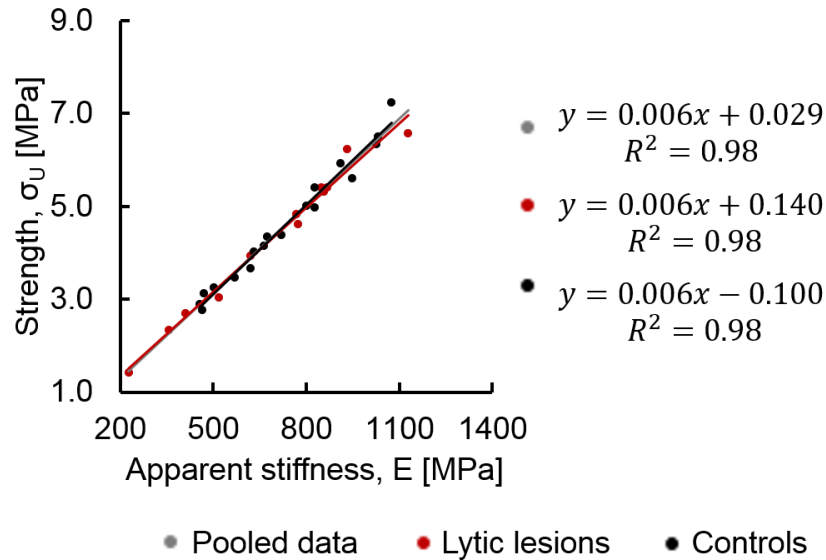


Figure 6.3- Linear regression analysis between predicted normalised stiffness and strength for vertebrae with lytic lesions (red circles), and vertebrae without lesions (controls, black circles). The equation for the pooled data was also reported in gray.

A wide range of mechanical properties was observed among vertebrae of different patients, with and without lesions (Fig 6.1 and 6.2). In some cases the vertebrae with the lesions were found to be stiffer and stronger than the vertebrae without lesions of the same patient (Table 6.4). This observation suggests that subject-specific analyses are required for a better understanding of the effect of lytic lesions on the mechanical stability of vertebrae with lesions.

Table 6.4- Predicted normalised structural properties ( $E$ ,  $\sigma_U$ ,  $U$ ) and safety factors ( $SF$ ) estimated for a patient set of vertebrae with and without lytic lesions. The %diff computed between the values estimated between the vertebrae with lytic lesions and the controls are also reported.

Patient ID	Level	Condition	E [MPa] Avg (ranges)	%diff to controls	$\sigma_U$ [MPa] Avg (ranges)	%diff to controls	U [MPa] Avg (ranges)	%diff to controls	SF	%diff to controls
P1	T12+L2	Controls	985 (947-1024)	-22%	6.0 (5.6-6.3)	-19%	0.08 (0.08-0.09)	-20%	2.8 (2.3-3.2)	-16%
	L1	Lytic lesions	767		4.8		0.07		2.3	
	L3+L5	Controls	1052 (1030-1074)	-18%	6.9 (6.5-7.2)	-21%	0.10 (0.09-0.10)	-22%	3.4 (3.7-3.1)	-24%
	L4	Lytic lesions	866		5.4		0.08		2.6	
P2	L3+L4	Controls	460 (457-464)	86%	2.8 (2.8-2.9)	88%	0.04 (0.04)	86%	1.3 (1.2-1.3)	128%
	L5	Lytic lesions	856		5.3		0.07		2.9	
P3	T4+T6	Controls	594 (568-621)	-31%	3.6 (3.5-3.7)	-24%	0.05 (0.05)	-27%	1.3 (1.2-1.4)	-13%
	T5	Lytic lesions	409		2.7		0.04		1.2	
P4	L1+L4	Controls	813 (800-826)	15%	5.0 (5.0)	25%	0.07 (0.07)	22%	2.2 (2.2)	33%
	L2	Lytic lesions	931		6.2		0.09		3.0	
	L1+L4	Controls	813 (800-826)	4%	5.0 (5.0)	8%	0.07 (0.07)	8%	2.2 (2.2)	14%
	L3	Lytic lesions	849		5.4		0.08		2.6	
P5	L1+L3	Controls	646 (630-662)	19%	4.1 (4.0-4.2)	13%	0.06 (0.06)	15%	1.6 (1.6-1.7)	37%
	L2	Lytic lesions	772		4.6		0.07		2.3	
P6	L2+L5	Controls	868 (826-909)	-74%	5.7 (5.4-5.9)	-75%	0.08 (0.07-0.08)	-76%	3.3 (3.1-3.4)	-68%
	L3	Lytic lesions	226		1.4		0.02		1.1	
	L2+L5	Controls	868 (826-909)	-40%	5.7 (5.4-5.9)	-46%	0.08 (0.07-0.08)	-47%	3.3 (3.1-3.4)	-42%
	L4	Lytic lesions	518		3.0		0.04		1.9	
P7	T11+L2	Controls	485 (470-501)	-27%	3.2 (3.1-3.3)	-27%	0.04 (0.04)	-27%	1.3 (1.2-1.4)	-24%
	T12	Lytic	356		2.3		0.03		1.0	
	T11+L2	Controls	485 (470-501)	28%	3.2 (3.1-3.3)	24%	0.04 (0.04)	25%	1.3 (1.2-1.4)	42%
	L1	Lytic lesions	620		3.9		0.05		1.8	
P8	L3+L5	Controls	696 (673-719)	62%	4.4 (4.4)	51%	0.06 (0.06)	53%	2.5 (2.5-2.6)	59%
	L4	Lytic lesions	1129		6.6		0.09		4.0	

As expected, for some patients, as P1, P3, and P6, vertebrae with lytic lesions showed lower normalised structural properties compared to the adjacent controls (ranging from 19% to 75% for vertebral strength) (Table 6.4). However, for other patients (P2, P4, P5, and P8) vertebrae with lytic lesions were stiffer (4% to 86%) and stronger (8% to 88%) compared to the controls (Table 6.4). Patient P7 in particular had two vertebrae with lytic lesions, T12 and L1. The T12 was less stiff and strong (difference of 27% in for both properties) than the controls, whereas L1 was stiffer and stronger (difference of 28% in stiffness and 24% in strength) (Table 6.4). Furthermore, not all the vertebrae with lytic lesions were considered at risk of fracture (Table 6.5).

*Table 6.5-Classification of each vertebra with lytic lesions based on the SINS, and the warning system used in this study to identify vertebrae at risk due to a decrease in strength (Warning FE) or due to physiological overloading based on vertebral yield properties (Warning SF). Colour-code: Green colour used for safe vertebrae, yellow vertebrae at risk of fracture, and red for vertebrae at a very high risk of fracture.*

Patient ID	Level	SINS scores	Warning FE	Warning SF	Notes
P1	L1	9	1	1	Warning SF for control T12
	L4	7	1	0	-
P2	L5	7	0	0	Warning SF for controls
P3	T5	10	1	1	Warning SF for controls
P4	L2	10	0	0	Warning SF for controls
	L3	8	0	0	
P5	L2	11	0	1	Warning SF for controls
P6	L3	12	1	1	-
	L4	9	1	1	
P7	T12	8	1	1	Warning SF for controls
	L1	11	0	1	
P8	L4	7	0	0	Warning SF for control L5

For every patient a report was prepared for providing a mechanical evaluation for each vertebra with lesions (Fig. 6.4 to 6.6 and Supplementary material S2, Figs S6.2 to S6.6). The report included: a sagittal mid-section view of the QCT images, a cross section highlighting the

vertebra(e) with lytic lesions, the distribution of BMD within the sub-region of interest of vertebrae with and without lesions, the stress-strain curves predicted with subject-specific FE models of vertebrae with and without lesions, including the applied vertebral stresses estimated from the 2D spinal model for 30° trunk flexion holding 8kg posture, and a table with the percentage differences of the normalised structural properties and safety-factors (SF) found between the vertebrae with lytic lesions and the controls.

The computational models suggested, that for patients P3 and P6 lytic lesions have a critical effect on both normalised structural properties and safety factors (Table 6.4 and 6.5). In both cases, the lesions decreased the normalised structural properties of the vertebrae compared to the adjacent subject-specific controls (Table 6.4). In particular for P6, which had two contiguous vertebrae with lytic lesions (L3 and L4), there was a reduction of up to 74% in apparent stiffness, 75% in strength, and 76% in energy to failure for the vertebrae with lytic lesions with respect to the controls (Fig. 6.4). The effect of the lytic lesion observed in the L3 over the vertebral structure, was greater than the effect of the lytic lesion observed in the L4, but for a considered critical physiological loading condition (30° trunk flexion holding 8kg in hands), both vertebrae were considered at very high risk of fracture (reduction in strength of the vertebrae with lytic lesions compared to the controls and  $SF \leq 2.5$ ) (Fig. 6.4).

**Patient P6**  
Cancer type: Small cell lung carcinoma

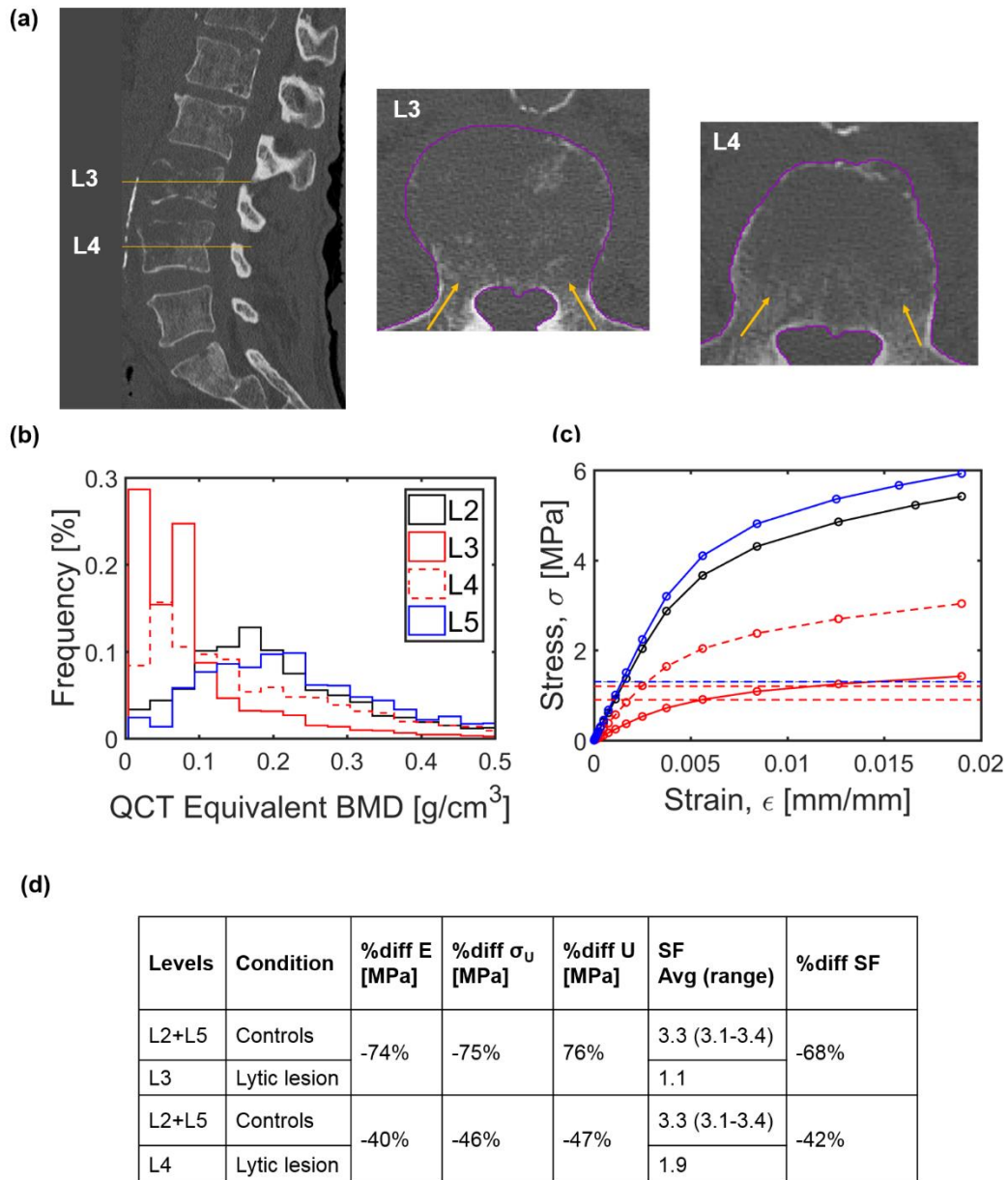


Figure 6.4- Report for patient P6. (a) Sagittal mid-section view of the QCT images of the patient, highlighting both vertebrae with lytic lesions shown in a mid-cross section. (b) Distribution of BMD within the sub-region of interest of the vertebrae with lesions (solid and dashed red lines) and without lesions (solid black and blue lines). (c) Stress-strain curves computed from the subject-specific FE models of vertebrae with lesions (solid and dashed red lines) and without lesions (solid black and blue lines). Horizontal dashed lines represent the applied vertebral stresses estimated from the 2D model simulating a 30° trunk flexion holding 8kg in hands. Bottom and top horizontal dashed red lines correspond to the applied vertebral stresses computed for L3 and L4, respectively. Applied stresses computed for the control vertebrae L2 and L5 are represented as an horizontal blue line (overlapp). (d) Percentage differences observed in predicted normalised structural properties (E,  $\sigma_U$ , and U) and safety-factor (SF) computed between the vertebrae with lytic lesions and the controls.

In other cases (e.g. patient P5) the vertebra with the lytic lesion showed higher normalised structural properties compared to the controls (Table 6.4) (Fig 6.5). For example, the vertebra with lytic lesions L4 of patient P5 had higher apparent stiffness (19%), strength (13%), and energy-to-failure (15%) than the controls (Fig 6.5). However, L4 was considered at a critical stage of deformation ( $SF \leq 2.5$ ) and, therefore, at risk of fracture. Moreover, in this case, the adjacent control vertebrae, L1 and L3, were also considered at a critical stage of deformation ( $SF \leq 2.5$ ) (Fig 6.5).

Similar conditions, where vertebrae without lytic lesions showed lower structural properties compared to those estimated for the vertebra with lesions and were at a critical stage of deformation ( $SF \leq 2.5$ ), were observed for other four patients: P2, P4, P7, and P8 (Table 6.4 and 6.5). In particular, for patient P7 two vertebrae with lesions were identified (T12 and L1). The lumbar vertebra with lytic lesions showed higher stiffness (28%) and strength (24%) compared to the adjacent controls. On the other hand, the other vertebra with lesions, T12, was 27% less stiff and strong than the controls (Table 6.4). Nonetheless, all vertebrae with or without lesions were considered at a critical stage of deformation ( $SFs \leq 2.5$ ) with T12 showing the most critical fracture risk conditions (decrease in strength and  $SF \leq 2.5$ ) (Fig 6.6).

**Patient P5**  
Cancer type: Aggressive spinal hemangioma

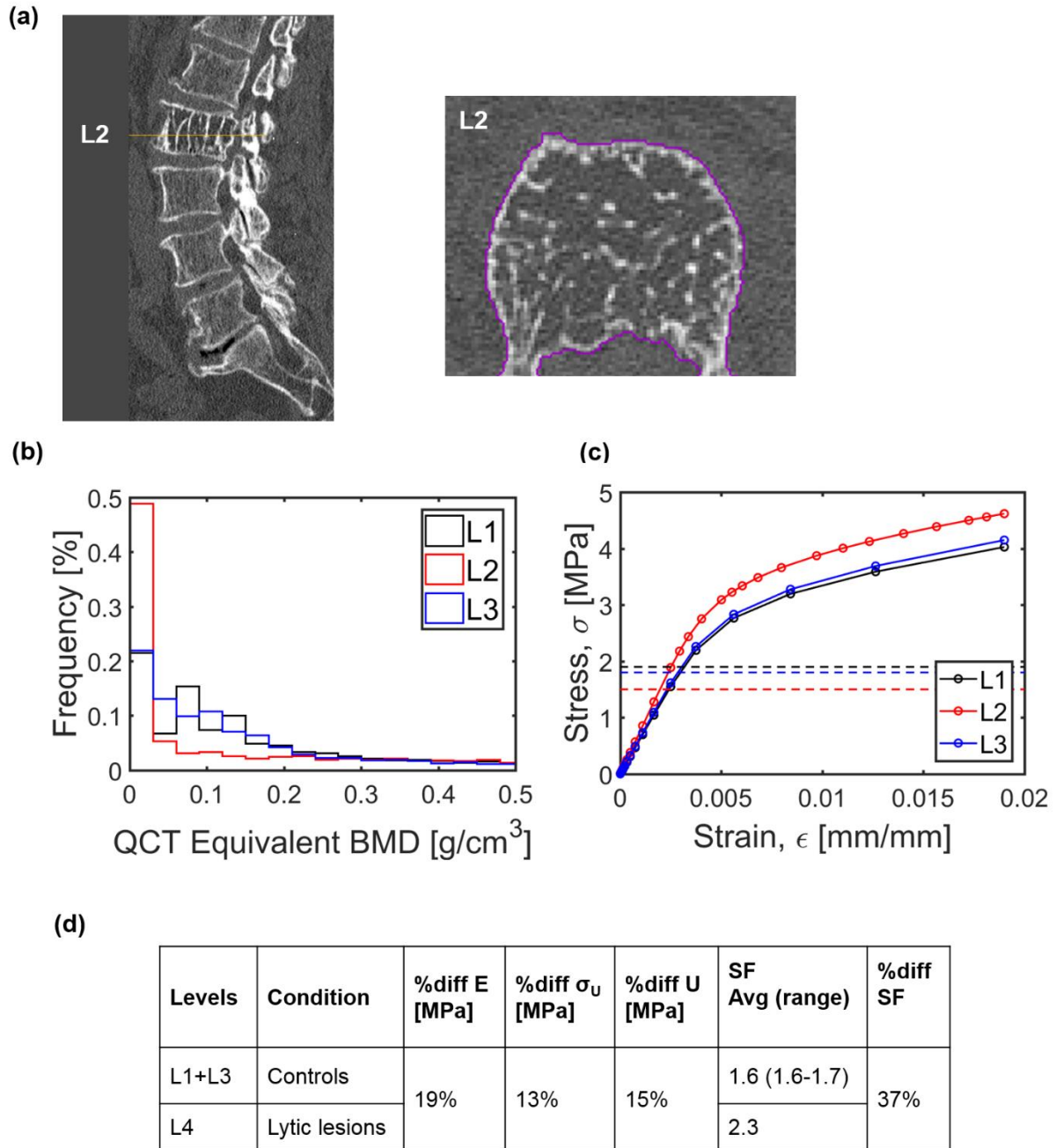


Figure 6.5- Report for patient P5. (a) Shows a sagittal mid-section view of the QCT images of the patient, highlighting the vertebra with lytic lesions shown in a mid-cross section. (b) Distribution of BMD within the sub-region of interest of the vertebra with lesions (solid red line) and without lesions (solid black and blue lines). (c) Stress-strain curves computed from the subject-specific FE models of vertebrae with lesions (solid red line) and without lesions (solid black and blue lines). Horizontal dashed lines represent the applied vertebral stresses estimated from the 2D model simulating a 30° trunk flexion holding 8kg in hands. (d) Percentage differences observed in predicted normalised structural properties (E,  $\sigma_U$ , and U) and safety-factor (SF) computed between the vertebrae with lytic lesions and the controls.

**Patient P7**  
Cancer type: Aggressive spinal hemangioma

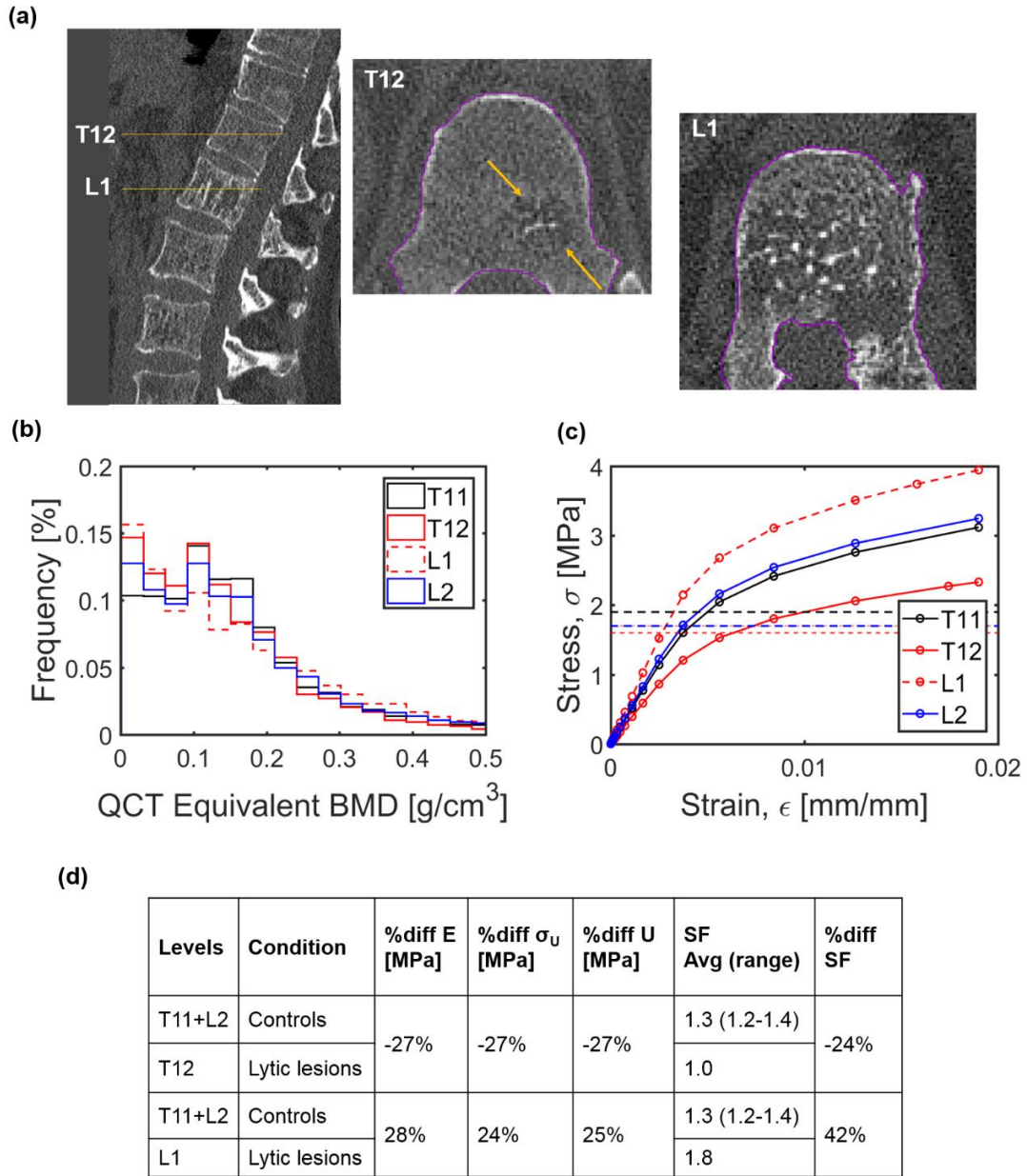


Figure 6.6- Report for patient P7. (a) Shows a sagittal mid-section view of the QCT images of the patient, highlighting the vertebrae with lytic lesions shown in a mid-cross section. (b) Distribution of BMD within the sub-region of interest of the vertebrae with lesions (solid and dashed red lines) and without lesions (solid black and blue lines). (c) Stress-strain curves computed from the subject-specific FE models of vertebrae with lesions (solid and dashed red lines) and without lesions (solid black and blue lines). Horizontal dashed lines represent the applied vertebral stresses estimated from the 2D model simulating a 30° trunk flexion holding 8kg in hands. Applied stresses computed for the lytic vertebra T12 and the control L2 are overlapped (horizontal blue line). (d) Percentage differences observed in predicted normalised structural properties ( $E$ ,  $\sigma_U$ , and  $U$ ) and safety-factor (SF) computed between the vertebrae with lytic lesions and the controls.

## 6.4. Discussion

The aim of this study was to evaluate the effect of lytic lesions on the mechanical properties and integrity of the vertebrae of patients with spinal metastases under physiological conditions.

None of the vertebrae evaluated in this study had BMD values below the osteoporotic threshold (BMD lower than  $0.08 \text{ g/cm}^3$ ), and only two of the vertebrae with lesions (T5 of P3 and L3 of P6) were classified as osteopenic (equivalent BMD between  $0.08 \text{ g/cm}^3$  and  $0.12 \text{ g/cm}^3$ ) (Fig 6.7 (b)) (Zysset, Qin, et al., 2015). These estimations were performed from volumetric BMD values computed from QCT images as Dual Energy X-Ray Absorptiometry (DXA) based measurements, the gold standard for classifying osteoporotic and osteopenic patients (Cummings et al., 2002), were not available.

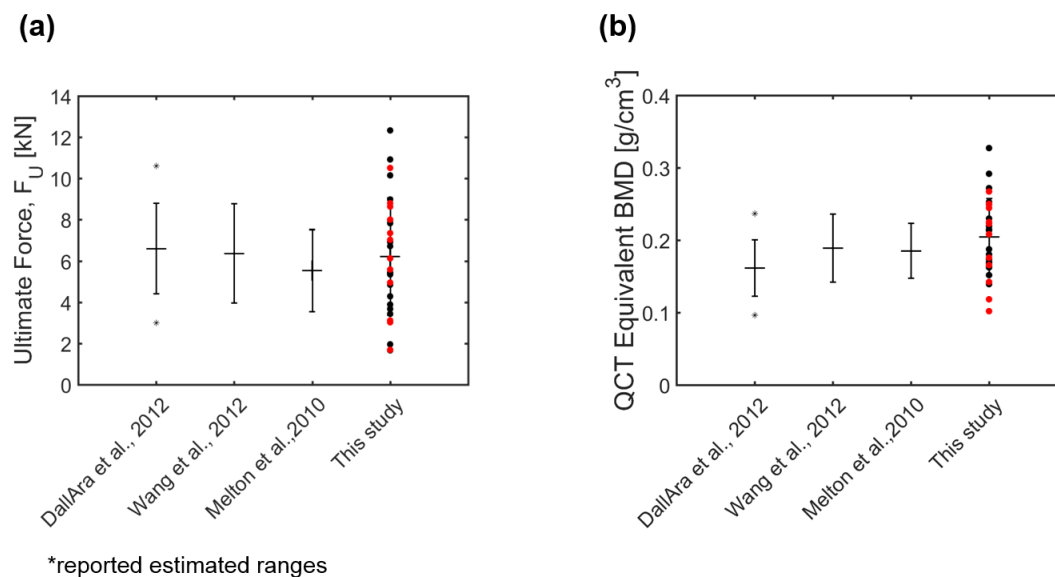


Figure 6.7- Figure 6- Values of ultimate force predicted from the FE models (left) and of measured BMD (right) for this study and some relevant literature (data extracted from Dall'Ara et al. (2012); Wang et al. (2012); and Melton et al. (2010)). Data from this study are reported in red for vertebrae with lytic lesions and in black for controls.

In this study, values of ultimate force obtained from the pooled data were slightly higher than those reported in the literature for human vertebrae without metastatic lesions (Dall'Ara et al., 2012; Wang et al., 2012; Melton et al., 2010) (Fig 6.7 (a)). Higher variability among the predicted ultimate forces was found compared to the values reported in the literature (i.e. coefficient of variation, CV of 45% found for ultimate forces versus a CV of up to 38% found in Wang et al., 2012) (Fig 6.7 (a)). The higher variability is most likely due to the fact that in

this study, vertebrae with and without lytic lesions were included in the analysis and levels from T4 to L5 were considered. Conversely, in the literature only healthy, osteopenic or osteoporotic vertebrae (Dall'Ara, 2012; Wang et al., 2012; Melton et al., 2010) from thoracolumbar levels were analysed (i.e. T12-L5 in Dall'Ara et al., 2012; L1-L2 in Wang et al., 2012; and L1-L3 in Melton et al., 2010). Moreover, the small cohort size of this study and the fact that for most vertebrae with lytic lesions, higher BMD was found around the lesion, may explain why it was not also observed, as expected, a high variability in the equivalent BMD for the pooled data. Compared to the validated QCT-based vertebral body models with and without induced lytic lesions, generated from cadaveric fresh-frozen vertebrae by Matsuura et al. (2014), a similarly high variability in  $F_U$  was found for the vertebrae with simulated lytic lesions compared to the intact vertebrae (i.e. CV of 54% for ultimate forces of vertebrae with induced lesions against 40% for the intact vertebrae). Moreover, as observed by Matsuura et al. (2014), there were also no significant differences between the predicted ultimate forces of vertebrae with and without lytic lesions ( $p=0.98$  in this study and  $p=0.91$  in Matsuura et al. (2014)).

In line with the literature on vertebral mechanics, structural properties were well correlated with the mean BMC of the vertebral bodies with and without lytic lesions ( $R^2=0.82$  for pooled ultimate forces against  $R^2=0.70$  in Dall'Ara et al. (2012);  $R^2=0.75$  for pooled stiffness against  $R^2=0.62$  in Dall'Ara et al. (2012)). As expected, the equivalent BMD correlated better with normalised structural properties ( $R^2=0.84$  for the estimated pooled strength against  $R^2=0.74$  in Dall'Ara et al. (2012);  $R^2=0.82$  for the estimated pooled normalised stiffness against  $R^2=0.71$  in Dall'Ara et al. (2012)). The similar correlation between BMD and vertebral strength estimated from the FE models for vertebrae with lytic lesions of controls, suggests that the vertebral mechanical properties are driven by the geometrical and densitometric properties of the bone. Therefore, it seems reasonable to use approaches developed to estimate the vertebral strength in osteoporotic subjects for estimating the mechanical properties of vertebrae with lesions. Nevertheless, this is not necessarily true for modelling bones with blastic lesions or primary tumours (e.g. osteosarcoma), for which a similar assessment is required and further experimental analyses to characterize the properties of the tumoral tissue are needed. The optimal correlation between predicted vertebral strength and normalised stiffness ( $R^2=0.98$ ) was probably due to the simple material model used to describe the post-yield behaviour of bone. Similar strong correlations between normalised structural stiffness and strength have been reported in the literature for human vertebrae without lesions by analysing experimental

measurements ( $R^2=0.90$ ) (Pahr et al., 2011), or predictions from FE models ( $R^2=0.92$ ) (Pahr et al., 2011). To the author's knowledge, there is only one study in the literature that investigated the effect of lytic lesions on the structural failure of vertebrae under axial compression with anterior bending, which showed a weak correlation between axial stiffness and ultimate force of vertebrae with defects induced by drilling holes (Ron N. Alkalay, 2015). Nonetheless, more studies are needed to better understand the effect of lytic lesion of the failure process of human vertebrae.

From the results of this study it is clear that detailed subject-specific analyses should be performed in order to better predict the risk of fracture of vertebrae with lytic lesions. In fact, for the cases studied for which the SINS was inconclusive, the results showed that the vertebrae with metastases were in some cases even stronger than the adjacent control vertebrae. Therefore, every patient should be treated as a case on its own.

For three patients (P1, P3, and P6) the lytic lesions had a detrimental effect on the normalised structural properties of the vertebrae compared to the corresponding controls (Table 6.4). For example, patient P1 had two vertebrae affected by lytic lesions, L1 and L4, both with slightly higher low BMD compared to the controls (Fig S6.2 (b) at Supplementary materials). The lytic lesion in L1 was larger than that in L4 and it was located in the anterior left region of the vertebral body causing a disruption of the cortical shell (Fig S6.2 (a)). Both vertebrae showed a lower normalised stiffness and strength compared to the adjacent controls (i.e. reduction of approximately 20%) and, therefore, both were classified as being at risk of fracture based on the warning system (Fig S6.2 (c) and (d)). The SINS for L1 and L4 were 9 and 7 respectively, suggesting that L1 was more critical than L4. In fact, this was confirmed from the quantitative analysis performed in this study for which L1 was considered at a critical stage plastic deformation ( $SF=2.3$ ) for the physiological condition considered in this study, while L4 was not ( $SF=2.6$ ). On the other hand, for patient P3, all vertebrae with and without lesions showed low equivalent BMD compared to the values of the cohort (equivalent BMD ranged from  $1.2 \text{ g/cm}^3$  to  $1.7 \text{ g/cm}^3$  for P3 vertebrae against  $0.20 \pm 0.05 \text{ g/cm}^3$  for the pooled data) (Table 6.2). The vertebra with lytic lesion (T5) had 24-31% reduction in normalised structural properties compared to the controls and was shown to be at high risk of fracture (low strength compared to the controls and  $SF \leq 2.5$ ) (Fig S6.4 (c) and (d)). In this case, however, one should also pay attention to the critical stage of deformation observed for the adjacent control vertebrae ( $SF \leq 2.5$ ). Nevertheless, it should be noted that P3 is the only patient of the cohort that had a lytic lesion on the thoracic level and for this specific case, a correction factor of 0.38 was used

to compute the applied load due to the errors of the 2D model in estimating the loads for thoracic levels up to T9 (details in Chapter V, section 5.4, Fig 5.25). Patient P6 had two contiguous vertebrae with lytic lesions, L3 and L4, scored by the SINS with a 12 and 9 respectively (Table 6.5). Consistently, L3 had a reduction of 75% in strength and higher risk of fracture compared to the controls ( $SF=1.1$  and %diff SF of 68% computed with respect to the controls) (Fig 6.4 (d)). The lytic lesion in L4 had a lower effect on its strength (reduction of approximately 50% compared to the controls) but it was also at a critical stage of deformation ( $SF \leq 2.5$ ), and therefore it was at very high risk of fracture based on the present analysis (Fig 6.4 (d)).

For patients P2, P4, P5, and P8, vertebrae with lytic lesions showed increased normalised structural properties compared to the control vertebrae (Table 6.4). Patient P7 was the only patient with two vertebrae with lytic lesions, T12 and L1, that had opposite effects on the normalised structural properties of the vertebrae compared to the controls (i.e. decrease of stiffness and strength for T12 and increase for L1) (Fig 6.6). Patient P7 suffered from an aggressive spinal hemangioma. In this case the lytic lesions, in particular in L1, were widely spread within the vertebral body, which was composed of trabeculae thicker than those observed in other vertebrae, whereas for T12 the lesion was less developed (Fig. 6.6 (a)). The SINS of T12 and L1 were 8 and 11 respectively, suggesting that L1 was more critical than T12. However, from the computational analysis, it was observed that both vertebrae with lesions were at a critical stage of deformation ( $SF \leq 2.5$ ) with T12 having a higher risk of fracture (lower strength than the controls and  $SF \leq 2.5$ ) than L1 (Fig 6.6 (d)). A similar type of lesions was observed in patient P5. In this case the analyses performed for the vertebra with lytic lesions (L5, SINS equal to 11) suggested that it was at a critical stage of plastic deformation ( $SF=2.3$ ). Even though, the strength of L5 was higher than that of the controls it was classified at risk of fracture due to the critical loading stage shown for the physiological condition considered in this study (Fig. 6.5 (d)). For patients P5 and P7, all the vertebrae, with or without lesions, reached the yield under the critical loading condition considered in this study ( $1.2 \leq SF \leq 2.3$ ) (Figs. 6.5 and 6.6). For patient P2, the vertebra with lytic lesion showed much higher safety factor (2.9) compared to the controls ( $SF < 1.3$ ) (Fig. S6.3). In this case, the patient suffered from a breast cancer, and the 86%-88% increase in normalised structural properties observed in L5 compared to the control vertebrae were probably due to high BMD tissue surrounding the lesion (Fig. S6.3 (a) and (b)). Lastly, for patients P4 and P8 vertebrae with lytic lesions showed higher structural properties compared to the controls (i.e. increase of up to 25% for P4

and 51% for P8) and they were considered safe for the loading condition considered in this study ( $2.6 \leq SF \leq 4.0$ ) (Figs. S6.5 and S6.6) (Table 6.4). These results highlight that with this computational approach, further information about the biomechanical status of the vertebrae can be estimated, something that is not possible with the current scoring systems.

There are some limitations in this study. Firstly, lytic lesions were modelled as low density bone tissues instead of being modelled as a poro- and visco-elastic material used in previous studies to model the solid and fluid phases of the tumour tissues (Tschirhart et al., 2004; Whyne et al., 2000). Currently, little is known about the materials properties of lytic tissues. To the author's knowledge there is only one study that has characterized the poro-elastic material properties of metastatic lytic tumours derived from 7 different primary cancers ( $n=24$ ) (Whyne et al., 2000). Moreover, the composition of the lytic tumour tissues can vary greatly according to the type of primary cancer (Vialle et al., 2015), which is very likely to affect the mechanical properties of the lesions, making it even harder to characterize the best constitutive model for this tissues. Nevertheless, the assumption that the lytic lesions can be approximated to low density bone tissues under axial compression is supported by a number of studies (Lenherr et al., 2018; Stadelmann et al., 2018; Nazarian et al., 2008). In addition, it has also been shown that there is no significant difference among the material properties of bones affected by lytic lesions originating from different primary cancer types, which supports the previous findings of Whyne et al. (2000). Secondly, the QCT images did not allow identification of lytic lesions that protrude from the endplates to the posterior wall of the vertebral bodies. Thus, only the volume of the lytic lesion that fell within the vertebrae, and which were possible to identify, were reconstructed and modelled and in some cases the contour of the vertebral body had to be guessed. This step of the procedure could be improved by registering CT and magnetic resonance images for each vertebra, which however, was not available for the cohort of patients. Thirdly, the prediction of vertebral strength was performed only for compressive loads. In order to account for the possible physiological loading scenarios, torsion, bending, and multi-axial loading should be simulated. Nonetheless, compression is one of the most important loading conditions of the spine which often relates to vertebral fractures, making it one of the most studied and used conditions for assessment of vertebral strength (Jackman et al., 2015; Wang et al., 2012; Buckley et al., 2007; Crawford, Rosenberg, et al., 2003). Moreover, in this study loading is applied to single vertebral body, not considering structures as intervertebral discs and articular contacts between facet-joints, that contribute to the physiologic loading transfer and distribution to the vertebrae (Groenen, 2018; Hussein et al.,

2012). This simplification also did not consider the important effect of lytic lesions on the rearrangement of the loading conditions over the vertebrae and consequently on vertebral failure (Alkalay & Harrigan, 2016; Hardisty et al., 2012; Whyne et al., 2003). This aspect could be relevant for cases as patient P6, who has two contiguous lytic vertebrae, L3 and L4, with L3 having a biconcave fracture, which may cause changes in the spinal loading. Finally, for the computation of vertebral loads a simple 2D spinal model was used under static equilibrium conditions (Chapter V, section 5.4). Such model was normalised to each patient's weight and height. However, it did not take into account the patient-specific, sagittal spinal alignment or spinal curvature, which are known to affect estimations of vertebral loading (Alexander et al., 2017; Alexander et al., 2012). Instead, mean population values were used to define such parameters in the 2D spinal model (details in Chapter V, section 5.4).

In conclusion, in this study it is presented a biomechanical approach used to estimate the mechanical properties and stability of patients with lytic spinal metastases. Such approach can be used together with the SINS to provide a more objective classification of vertebrae with lytic lesions, which stability is uncertain. However, future work is needed in order to validate the predictions of the modelling framework in retrospective or prospective clinical studies.

## 6.5. References

- Alexander, B. G., Anderson, D. E., Agostino, J. D. & Bouxsein, M. L. (2012). The Effect of Thoracic Kyphosis and Sagittal Plane Alignment on Vertebral Compressive Loading. *Journal of Bone and Mineral Research*, 27(10), 2144–2151.
- Alexander, B. G., Mokhtarzadeh, H., Allaire, B. T., Velie, K. R., Kaluza, M. C. D. P., Anderson, D. E., et al. (2017). Incorporation of CT-Based Measurements of Trunk Anatomy Into Subject-Specific Musculoskeletal Models of the Spine Influences Vertebral Loading Predictions. *Journal of Orthopaedic Research*, 1–10.
- Alkalay, R. N. (2015). Effect of the Metastatic Defect on the Structural Response and Failure Process of Human Vertebrae: An Experimental Study. *Clinical Biomechanics*, 30(2), 121–128.
- Alkalay, R. N. & Harrigan, T. P. (2016). Mechanical Assessment of the Effects of Metastatic Lytic Defect on the Structural Response of Human Thoracolumbar Spine. *Journal of Orthopaedic Research*, 34(10), 1808–1819.
- Bouxsein, M. L., Melton, L. J., Riggs, B. L., Muller, J., Atkinson, E. J., Oberg, A. L., et al. (2006). Age- and Sex-Specific Differences in the Factor of Risk for Vertebral Fracture: A Population-Based Study Using QCT. *Journal of Bone and Mineral Research*, 21(9), 1475–1482.
- Buckley, J. M., Cheng, L., Loo, K. & Slyfield, C. (2007). Quantitative Computed Tomography-Based Predictions of Vertebral Strength in Anterior Bending. *Spine*, 32(9), 1019–1027.
- Buckley, J. M., Loo, K. & Motherway, J. (2007). Comparison of Quantitative Computed Tomography-Based Measures in Predicting Vertebral Compressive Strength. *Bone*, 40(3), 767–774.
- Burke, M., Akens, M., Kiss, A., Willett, T. & Whyne, C. (2018). Mechanical Behavior of Metastatic Vertebrae Are Influenced by Tissue Architecture, Mineral Content, and Organic Feature Alterations. *Journal of Orthopaedic Research*, 1–10.
- Campbell, G. M., Peña, J. A., Giravent, S., Thomsen, F., Damm, T., Glüer, C. C., et al. (2017). Assessment of Bone Fragility in Patients With Multiple Myeloma Using QCT-Based Finite Element Modeling. *Journal of Bone and Mineral Research*, 32(1), 151–156.
- Crawford, R. P., Cann, C. E. & Keaveny, T. M. (2003). Finite Element Models Predict in Vitro Vertebral Body Compressive Strength Better than Quantitative Computed Tomography. *Bone*, 33, 744–750.
- Crawford, R. P., Rosenberg, W. S. & Keaveny, T. M. (2003). Quantitative Computed Tomography-Based Finite Element Models of the Human Lumbar Vertebral Body : Effect of Element Size on Stiffness , Damage , and Fracture Strength. *Journal of Biomechanical Engineering*, 125, 434–438.
- Cummings, S. R., Bates, D. & Black, D. M. (2002). Clinical Use of Bone Densitometry Scientific Review. *JAMA*, 288(15), 1889–1897.
- Dall'Ara, E., Pahr, D., Varga, P., Kainberger, F. & Zysset, P. (2012). QCT-Based Finite Element Models Predict Human Vertebral Strength in Vitro Significantly Better than Simulated DEXA. *Osteoporosis International*, 23, 563–572.
- Ebihara, H., Ito, M., Abumi, K., Taneichi, H., Kotani, Y., Minami, A., et al. (2004). A Biomechanical Analysis of Metastatic Vertebral Collapse of the Thoracic Spine: A Sheep Model Study. *Spine*, 29(9), 994–999.
- Fisher, C. G., Schouten, R., Versteeg, A. L., Boriani, S., Varga, P. P., Rhines, L. D., et al. (2014). Reliability of the Spinal Instability Neoplastic Score ( SINS ) among Radiation

- Oncologists : An Assessment of Instability Secondary to Spinal Metastases. *Radiation Oncology*, 9(1), 1–7.
- Fourney, D. R., Frangou, E. M., Ryken, T. C., Dipaola, C. P., Shaffrey, C. I., Berven, S. H., et al. (2011). Spinal Instability Neoplastic Score : An Analysis of Reliability and Validity From the Spine Oncology Study Group. *Journal of Clinical Oncology*, 29(22), 3072–3077.
- Groenen, K. (2018). Spinal (in)Stability in Metastatic Bone Disease. Experimental, Computational, and Clinical Perspectives. *PhD Thesis*. Radboud University Medical Center, Nijmegen.
- Hardisty, M. R., Akens, M. K., Hojjat, S. P., Yee, A. & Whyne, C. M. (2012). Quantification of the Effect of Osteolytic Metastases on Bone Strain within Whole Vertebrae Using Image Registration. *Journal of Orthopaedic Research*, 30, 1032–1039.
- Hussein, A., Barbone, P. E. & Morgan, E. F. (2012). Digital Volume Correlation for Study of the Mechanism of Whole Bones. *Procedia IUTAM*, 4, 116–125.
- Jackman, T. M., Hussein, A. I., Curtiss, C., Fein, P. M., Camp, A., De, L., et al. (2015). Quantitative, 3-D Visualization of the Initiation and Progression of Vertebral Fractures under Compression and Anterior Flexion. *Journal of Bone and Mineral Research*, 31(4) 1–37.
- Keaveny, T. M., McClung, M. R., Genant, H. K., Zanchetta, J. R., Kendler, D., Brown, J. P., et al. (2014). Femoral and Vertebral Strength Improvements in Postmenopausal Women With Osteoporosis Treated With Denosumab. *Journal of Bone and Mineral Research*, 29(1), 158–165.
- Lenherr, C., Voumard, B., Stadelmann, M., Buck, F., Haschtmann, D., Hoppe, S., et al. (2018). *Indentation Properties of Metastatic Vertebral Trabecular Bone*. 8<sup>th</sup> World Congress of Biomechanics, Dublin, Ireland, 8-12<sup>th</sup> July 2018.
- Les, C. M., Keyak, J., Stover, S. M., Taylor, K. T. & Kaneps, A. J. (1994). Estimation of Material Properties in the Equine Metacarpus with Use of Quantitative Computed Tomography. *Journal of Orthopaedic Research*, 12, 822–833.
- Matsuura, Y., Giambini, H., Ogawa, Y., Fang, Z., Thoreson, A. R., Yaszemski, M. J., et al. (2014). Specimen-Specific Nonlinear Finite Element Modelling to Predict Vertebrae Fracture Loads after Vertebroplasty. *Spine*, 39(22), E1291–E1296.
- Melton, L. J., Riggs, B. L., Keaveny, T. M., Achenbach, S. J., Hoffmann, P. F., Camp, J. J., et al. (2007). Structural Determinants of Vertebral Fracture Risk. *Journal of Bone and Mineral Research*, 22(12), 1885–1892.
- Melton, L. J., Riggs, B. L., Keaveny, T. M., Achenbach, S. J., Kopperdahl, D., Camp, J. J., et al. (2010). Relation of Vertebral Deformities to Bone Density, Structure, and Strength. *Journal of Bone and Mineral Research*, 25(9), 1922–1930.
- Morgan, E. F., Bayraktar, H. H. & Keaveny, T. M. (2003). Trabecular Bone Modulus-Density Relationships Depend on Anatomic Site. *Journal of Biomechanics*, 36(7), 897–904.
- Morgan, E. F., Yeh, O. C., Chang, W. C. & Keaveny, T. M. (2001). Nonlinear Behavior of Trabecular Bone at Small Strains. *Journal of Biomechanical Engineering*, 123, 1–9.
- Myers, E. R. & Wilson, S. E. (1997). Biomechanics of Osteoporosis and Vertebral Fracture. *Spine*, 22, 25S–31S.
- Nazarian, A., Von Stechow, D., Zurakowski, D., Müller, R. & Snyder, B. D. (2008). Bone Volume Fraction Explains the Variation in Strength and Stiffness of Cancellous Bone Affected by Metastatic Cancer and Osteoporosis. *Calcified Tissue International*, 83, 368–379.

- Pahr, D. H., Dall'Ara, E., Varga, P. & Zysset, P. K. (2011). HR-PQCT-Based Homogenised Finite Element Models Provide Quantitative Predictions of Experimental Vertebral Body Stiffness and Strength with the Same Accuracy as MFE Models. *Computer Methods in Biomechanics and Biomedical Engineering*, 15, 711–20.
- Rijsbergen, M. van, van Rietbergen, B., Barthelemy, V., Eltes, P., Lazáry, Á., Lacroix, D., et al. (2018). Comparison of Patient-Specific Computational Models vs. Clinical Follow-up, for Adjacent Segment Disc Degeneration and Bone Remodelling after Spinal Fusion. *Plos One*, 13(8), e0200899.
- Sánchez, A. B. & Sistol, A. G. (2014). A Quantitative Method for the Characterization of Lytic Metastases of the Bone from Radiographic Images. *Scientific World Journal*, 2014.
- Schileo, E., Dall'Ara, E., Taddei, F., Malandrino, A., Schotkamp, T., Ñ, M. B., et al. (2008). An Accurate Estimation of Bone Density Improves the Accuracy of Subject-Specific Finite Element Models. *Journal of Biomechanics*, 41, 2483–2491.
- Schultz, A., Andersson, G., Ortengren, R., Haderspeck, K. & Nachemson, A. (1982). Loads on the Lumbar Spine. Validation of a Biomechanical Analysis by Measurements of Intradiscal Pressures and Myoelectric Signals. *Journal of Bone and Joint Surgery*, 64(5), 713–720.
- Stadelmann, M., Alkalay, R., Maquer, G., Buck, F., Hoppe, S., Theumann, N., et al. (2018). *Can Micro and Homogenized Finite Element Analysis Estimate the Strength of Human Metastatic Vertebrae?* 8<sup>th</sup> World Congress of Biomechanics, Dublin, Ireland, 8-12<sup>th</sup> July 2018.
- Sutcliffe, P., Connock, M., Shyangdan, D., Court, R., Kandala, N. B. & Clarke, A. (2013). A Systematic Review of Evidence on Malignant Spinal Metastases: Natural History and Technologies for Identifying Patients at High Risk of Vertebral Fracture and Spinal Cord Compression. *Health technology assessment (Winchester, England)*, 17, 1–274.
- Tschirhart, C. E., Nagpurkar, A. & Whyne, C. M. (2004). Effects of Tumor Location, Shape and Surface Serration on Burst Fracture Risk in the Metastatic Spine. *Journal of Biomechanics*, 37(5), 653–660.
- Vialle, L. R., Gokaslan, Z. L., Fisher, C. G. & Boriani, S. (2015). *AOSpine Master Series. Volume 1. Metastatic S* (L. R. Vialle, Ed.). New York, NY: Thieme Medical Publishers, Inc.
- Wang, X., Sanyal, A., Cawthon, P. M., Palermo, L., Jekir, M., Christensen, J., et al. (2012). Prediction of New Clinical Vertebral Fractures in Elderly Men Using Finite Element Analysis of CT Scans. *Journal of Bone and Mineral Research*, 27(4), 808–816.
- Whyne, C. M., Hu, S. S. & Lotz, J. C. (2003). Burst Fracture in the Metastatically Involved Spine: Development, Validation, and Parametric Analysis of a Three-Dimensional Poroelastic Finite-Element Model. *Spine*, 28(7), 652–660.
- Whyne, C. M., Hu, S. S., Worman, K. L. & Lotz, J. C. (2000). Biphase Material Properties of Lytic Bone Metastases. *Annals of Biomedical Engineering*, 28, 1154–1158.
- Zysset, P., Qin, L., Lang, T., Khosla, S., Leslies, W. D., Shepherd, J. A., et al. (2015). Clinical Use of Quantitative Computed Tomography-Based Finite Element Analysis of the Hip and Spine in the Management of Osteoporosis in Adults: The 2015 ISCD Official Positions - Part II. *Journal of Clinical Densitometry*, 18(3).

## Supplementary materials

### S1. Image pre-processing

An image pre-processing smoothing operation was done in order to control the effect of an artifact, possibly caused by the presence of dead pixels in the CT detector, observed in a few image section of the QCT dataset of patient P5 (Fig S6.1).

As the artifact was only present in some image sections, a few 2D region of interest (ROIs) were defined within the areas affected by the artifact, and in surrounding areas not affected by the artifact. Thus, for each section affected by the artifact, it was computed the mean HU found within the ROIs defined in the surrounding area free of the artifact. The mean HU value found within those areas was then used to replace the HU values found within the ROI defined by the artifact, for a certain image section. This operation was performed only over the image sections which correspond to the set of vertebrae with and without lytic lesions to be models (i.e. L1 to L3). For the image section that defined L1 and L3 only one slice was affected by the artifact, whereas for L2 four sections were affected.

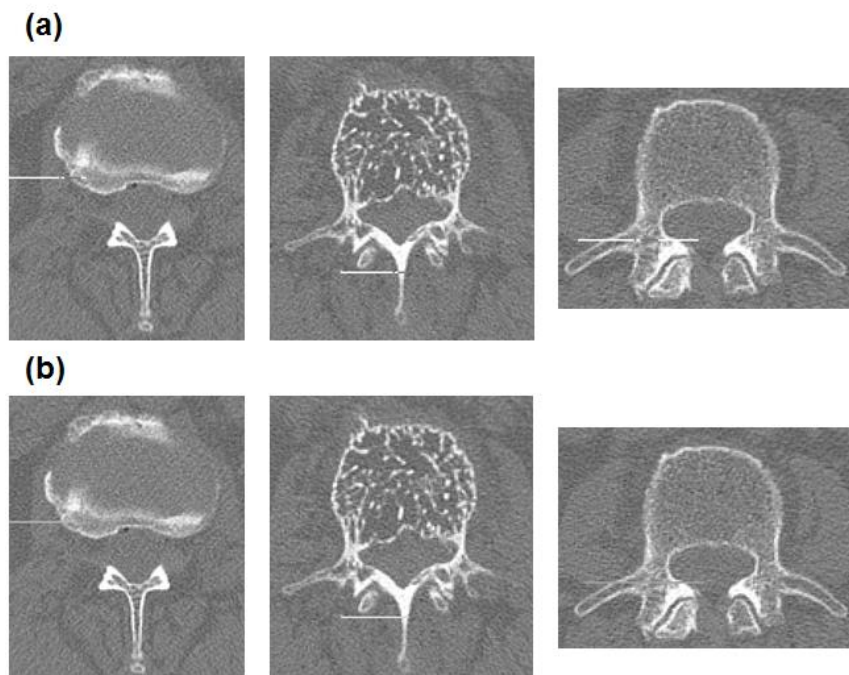
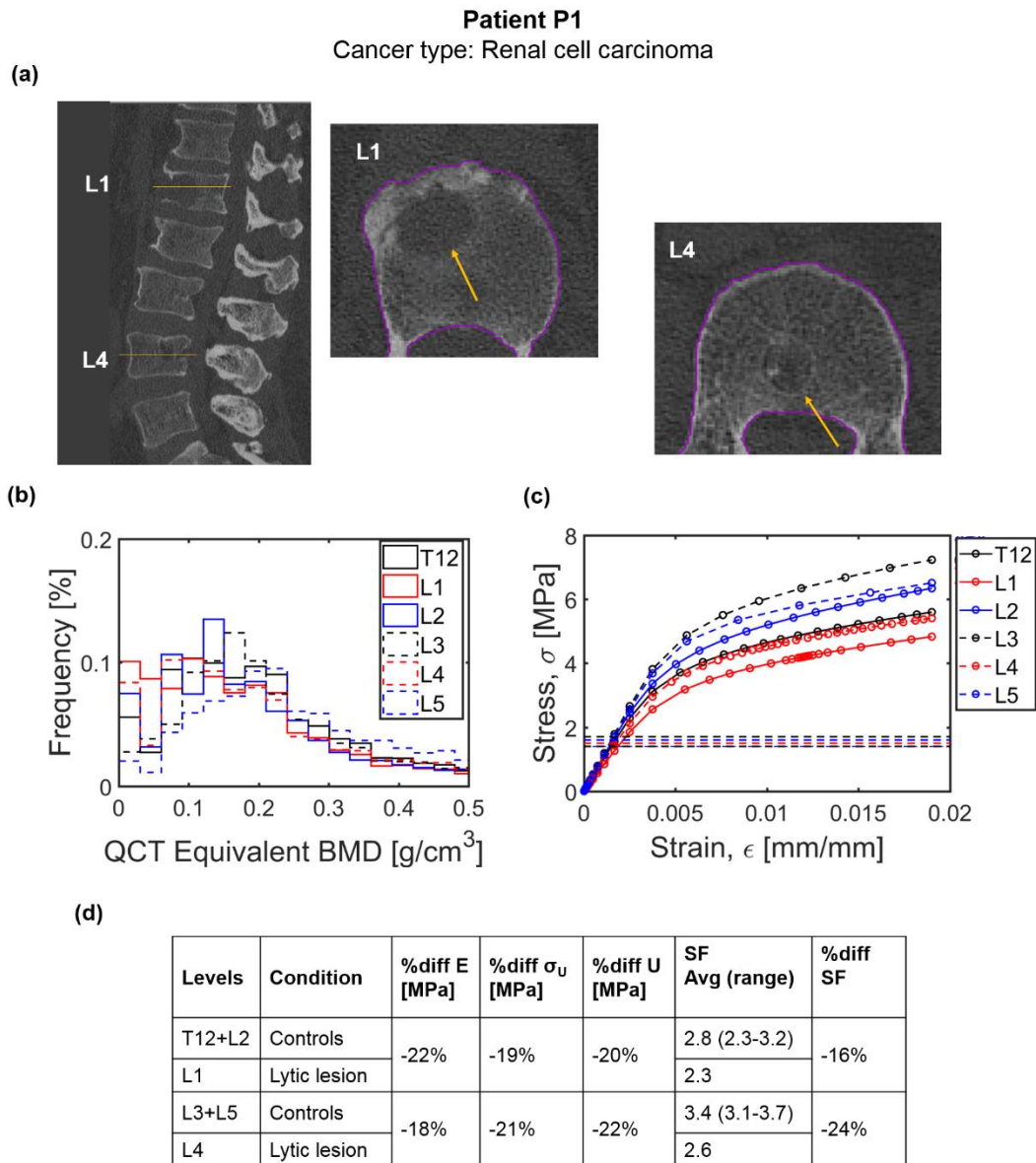


*Figure S6.1– Patient P5 image sections (a) before and (b) after the smoothing operations performed over the regions affected by dead pixel's artifact.*

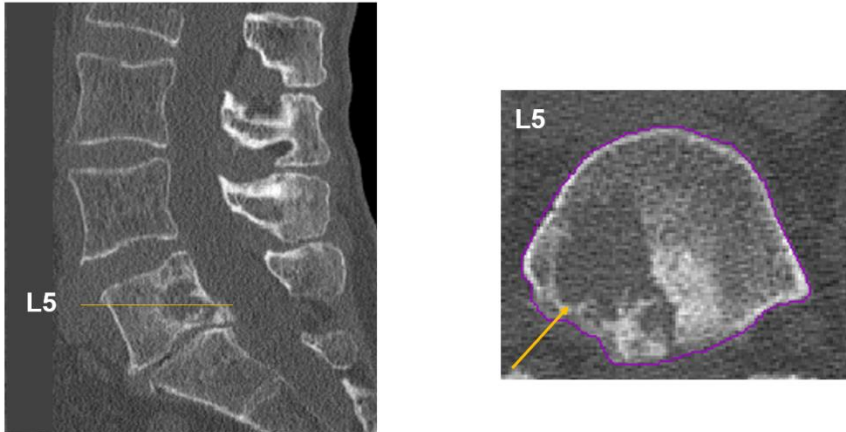
## S2. Reports for the remaining patients



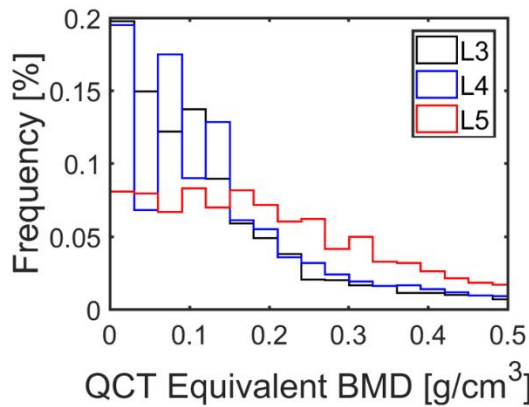
S6.2 Figure- Report for patient P1. (a) Shows a sagittal mid-section view of the QCT images of the patient, highlighting both vertebrae with lytic lesions shown in a mid-cross section. (b) Distribution of BMD within the sub-region of interest of the vertebrae with lesions (solid and dashed red lines) and without lesions (solid and dashed black and blue lines). (c) Stress-strain curves computed from the subject-specific FE models of vertebrae with lesions (solid and dashed red lines) and without lesions (solid and dashed black and blue lines). Horizontal dashed lines represent the applied vertebral stresses estimated from the 2D model simulating a 30° trunk flexion holding 8kg in hands. Applied stresses computed for vertebrae L1, L2, and L3 are overlapped (horizontal black line). (d) Percentage differences observed in predicted normalised structural properties (E,  $\sigma_U$ , and U) and safety-factor (SF) computed between the vertebrae with lytic lesions and the controls.

**Patient P2**  
Cancer type: Breast cancer

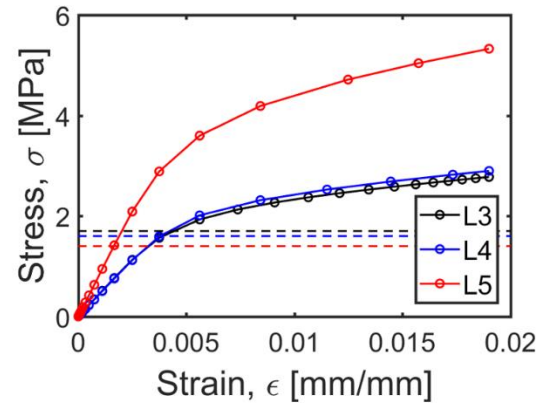
(a)



(b)



(c)



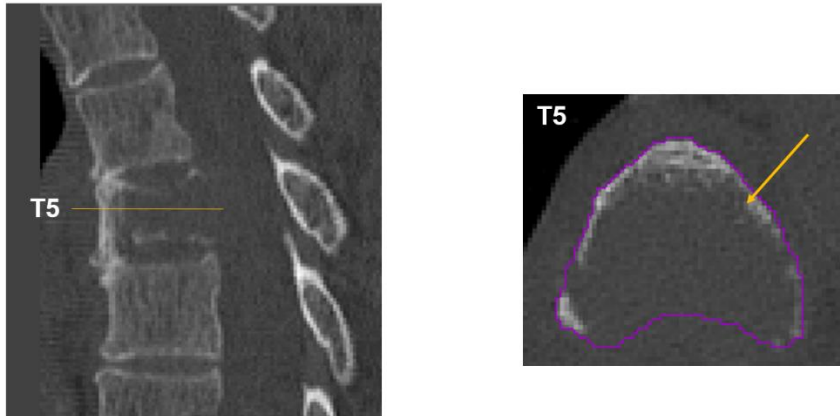
(d)

Levels	Condition	%diff E [MPa]	%diff $\sigma_u$ [MPa]	%diff U [MPa]	SF Avg (range)	%diff SF
L3+L4	Controls	86%	88%	86%	1.3 (1.2-1.3)	128%
L5	Lytic lesion				2.9	

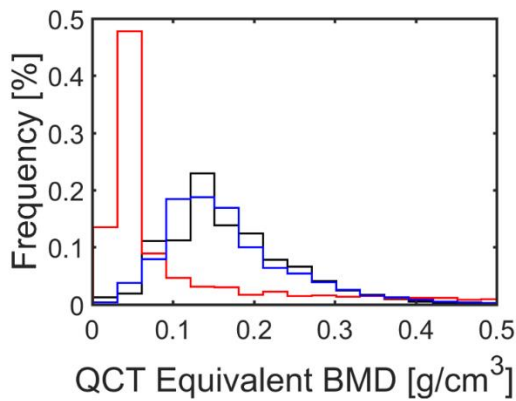
S6.3 Figure- Report for patient P2. (a) Shows a sagittal mid-section view of the QCT images of the patient, highlighting the vertebra with lytic lesions shown in a mid-cross section. (b) Distribution of BMD within the sub-region of interest of the vertebrae with lesions (solid red line) and without lesions (solid black and blue lines). (c) Stress-strain curves computed from the subject-specific FE models of vertebrae with lesions (solid red line) and without lesions (solid black and blue lines). Horizontal dashed lines represent the applied vertebral stresses estimated from the 2D model simulating a 30° trunk flexion holding 8kg in hands. (d) Percentage differences observed in predicted normalised structural properties (E,  $\sigma_u$ , and U) and safety-factors (SF) computed between the vertebrae with lytic lesions and the controls.

**Patient P3**  
Cancer type: Breast cancer

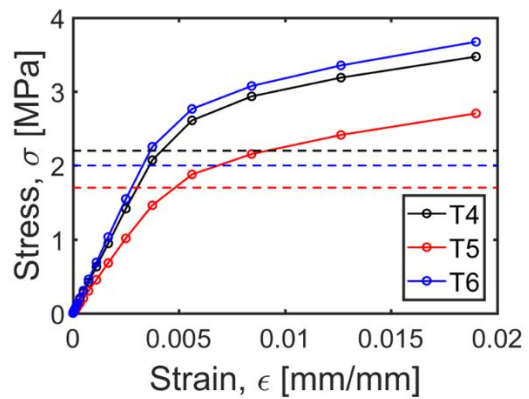
(a)



(b)



(c)

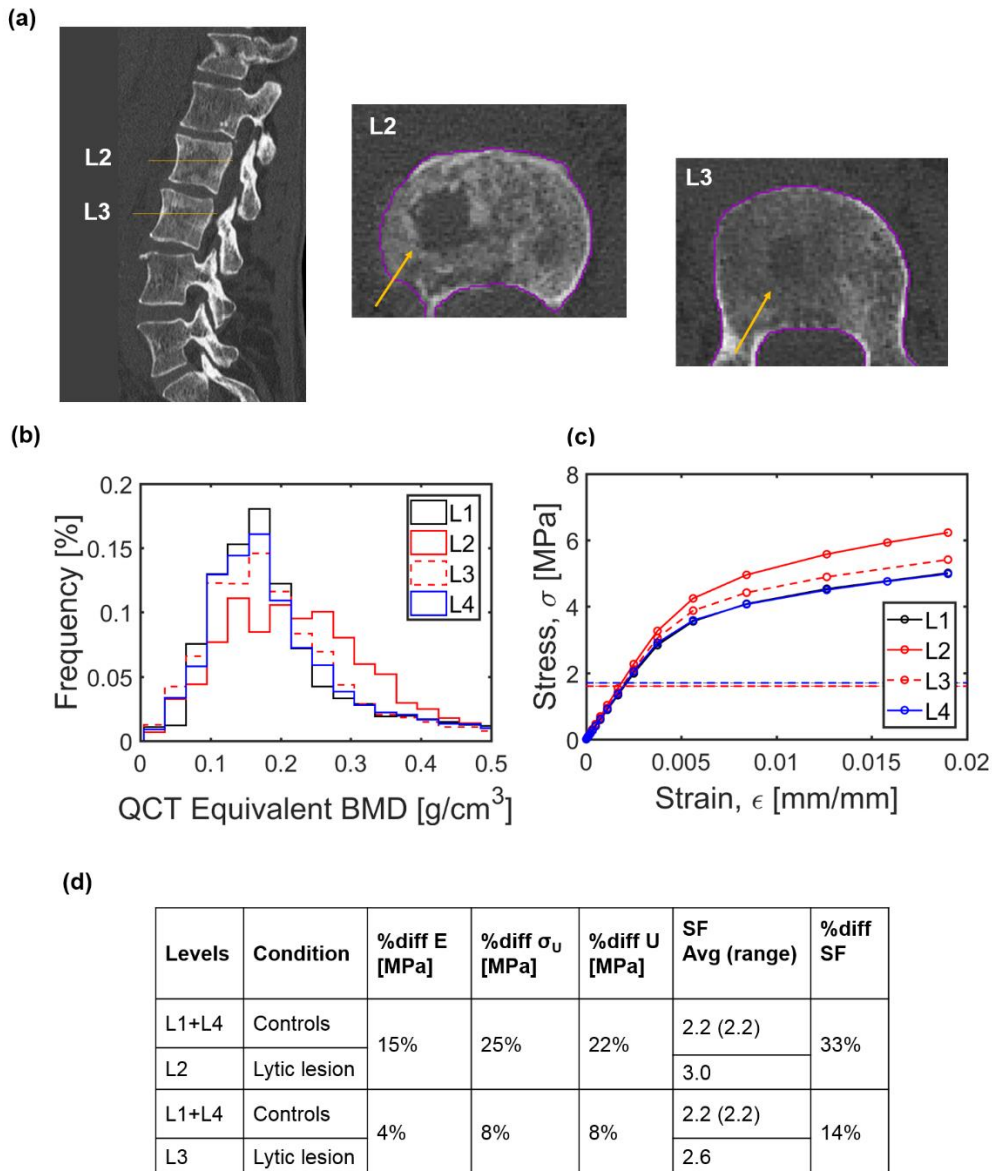


(d)

Levels	Condition	%diff E [MPa]	%diff $\sigma_U$ [MPa]	%diff U [MPa]	SF Avg (range)	%diff SF
T4+T6	Controls	-31%	-24%	-27%	1.3 (1.2-1.4)	-13%
T5	Lytic lesion				1.2	

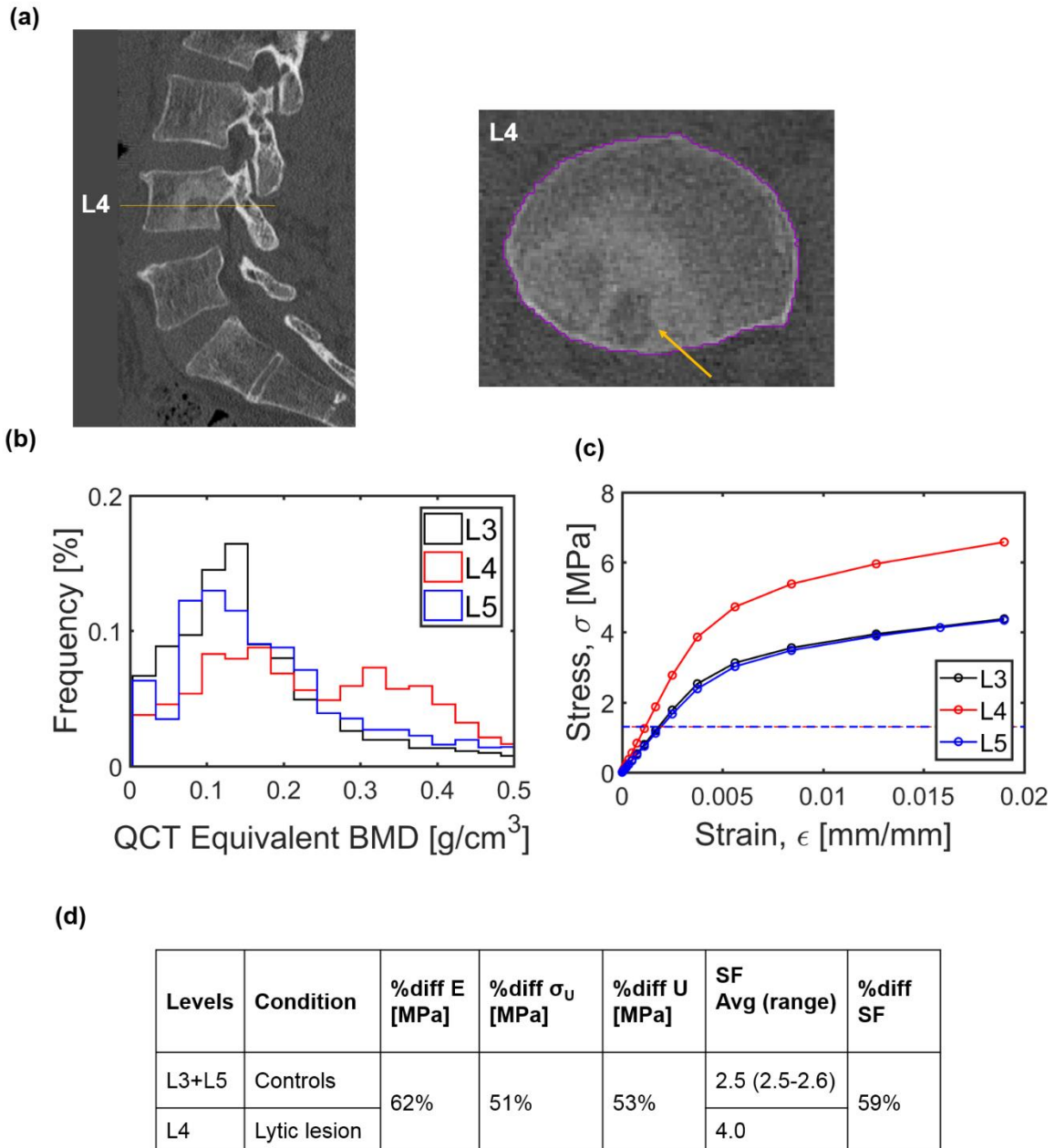
S6.4 Figure- Report for patient P3. (a) Shows a sagittal mid-section view of the QCT images of the patient, highlighting the vertebra with lytic lesions shown in a mid-cross section. (b) Distribution of BMD within the sub-region of interest of the vertebrae with lesions (solid red line) and without lesions (solid black and blue lines). (c) Stress-strain curves computed from the subject-specific FE models of vertebrae with lesions (solid red line) and without lesions (solid black and blue lines). Horizontal dashed lines represent the applied vertebral stresses estimated from the 2D model simulating a 30° trunk flexion holding 8kg in hands. (d) Percentage differences observed in predicted normalised structural properties (E,  $\sigma_U$ , and U) and safety-factors (SF) computed between the vertebrae with lytic lesions and the controls.

**Patient P4**  
Cancer type: Colorectal cancer



S6.5 Figure- Report for patient P4. (a) Shows a sagittal mid-section view of the QCT images of the patient, highlighting both vertebrae with lytic lesions shown in a mid-cross section. (b) Distribution of BMD within the sub-region of interest of the vertebrae with lesions (solid and dashed red lines) and without lesions (solid black and blue lines). (c) Stress-strain curves computed from the subject-specific FE models of vertebrae with lesions (solid and dashed red lines) and without lesions (solid black and blue lines). Horizontal dashed lines represent the applied vertebral stresses estimated from the 2D model simulating a 30° trunk flexion holding 8kg in hands. Applied stresses computed for vertebrae with lytic lesions are overlapped with the applied stresses of the control vertebra L1 (horizontal red line). (d) Percentage differences observed in predicted normalised structural properties (E,  $\sigma_U$ , and U) and safety-factors (SF) computed between the vertebrae with lytic lesions and the controls.

**Patient P8**  
Cancer type: Gr I chondrosarcoma



S6.6 Figure- Report for patient P8. (a) Shows a sagittal mid-section view of the QCT images of the patient, highlighting the vertebra with lytic lesions shown in a mid-cross section. (b) Distribution of BMD within the sub-region of interest of the vertebrae with lesions (solid red line) and without lesions (solid black and blue lines). (c) Stress-strain curves computed from the subject-specific FE models of vertebrae with lesions (solid red line) and without lesions (solid black and blue lines). Horizontal dashed lines represent the applied vertebral stresses estimated from the 2D model simulating a 30° trunk flexion holding 8kg in hands. Applied stresses computed for vertebrae with and without lytic lesions overlapped (horizontal blue line). (d) Percentage differences observed in predicted normalised structural properties (E,  $\sigma_U$ , and U) and safety-factors (SF) computed between the vertebrae with lytic lesions and the controls.

### S3. Supplementary results

S6.2 Table-Report of supplementary results used to build the subject-specific biomechanical reports. It included the applied compressive vertebral loads and stresses estimated from the 2D spinal model for a 30° trunk flexion holding 8kg configuration, the FE models predictions of yield loads ( $F_Y$ ) ultimate loads ( $F_U$ ) and the respective normalised values of yield stress ( $\sigma_Y$ ) and strength ( $\sigma_U$ ).

Patient ID	Level	Condition	$F_{comp}$ [kN]	$\sigma_{comp}$ [MPa]	$F_Y$ [kN]	$F_U$ [kN]	$\sigma_Y$ [MPa]	$\sigma_U$ [MPa]
P1	T12	Control	2.35	1.7	5.52	7.97	3.9	5.6
	L1	Lytic	2.38	1.4	5.52	8.01	3.3	4.8
	L2	Control	2.39	1.4	7.57	10.92	4.4	6.3
	L3	Control	2.39	1.4	8.85	12.33	5.2	7.2
	L4	Lytic	2.42	1.5	6.25	8.64	3.9	5.4
	L5	Control	2.52	1.6	7.83	10.15	5.0	6.5
P2	L3	Control	2.15	1.7	2.51	3.43	2.03	2.8
	L4	Control	2.17	1.6	2.90	3.89	2.16	2.9
	L5	Lytic	2.25	1.4	6.43	8.80	3.89	5.3
P3	T4	Control	1.07	2.2	1.33	1.66	2.8	3.5
	T5	Lytic	1.08	1.7	1.26	1.69	2.0	2.7
	T6	Control	1.09	2.0	1.55	1.95	2.9	3.7
P4	L1	Control	1.84	1.7	4.11	5.40	3.8	5.0
	L2	Lytic	1.84	1.6	5.43	7.35	4.6	6.2
	L3	Lytic	1.84	1.6	4.69	6.12	4.1	5.4
	L4	Control	1.85	1.7	4.10	5.34	3.8	5.0
P5	L1	Control	2.30	1.9	3.59	4.85	3.0	4.03
	L2	Lytic	2.30	1.5	5.19	7.03	3.4	4.62
	L3	Control	2.31	1.8	4.00	5.44	3.1	4.15
P6	L2	Control	1.88	1.3	5.76	7.83	4.0	5.42
	L3	Lytic	1.88	0.9	1.98	3.11	0.9	1.42
	L4	Lytic	1.90	1.2	3.60	4.95	2.2	3.04
	L5	Control	1.96	1.3	6.75	8.98	4.5	5.93
P7	T11	Control	2.21	1.9	2.63	3.67	2.2	3.12
	T12	Lytic	2.24	1.7	2.16	3.03	1.7	2.33
	L1	Lytic	2.26	1.6	4.10	5.59	2.9	3.95
	L2	Control	2.27	1.7	3.10	4.28	2.4	3.25
P8	L3	Control	2.00	1.3	5.12	6.72	3.3	4.39
	L4	Lytic	2.02	1.3	8.07	10.51	5.1	6.58
	L5	Control	2.10	1.3	5.18	6.92	3.3	4.35

## Chapter VII. Conclusions

### 7.1. Original contributions

The aim of this thesis was to develop subject-specific Finite Element (FE) models to better understand the effect of lytic lesions on the structural properties and stability of human vertebrae. These methods can be used to provide a more objective way of classifying patients with vertebral lytic metastases at high risk of fracture. This goal was accomplished by the use of two different FE modelling methods described in Chapters III, IV, and Chapters V, VI.

In Chapter III, FE models based on subject-specific micro Computed Tomography (microCT) images of porcine vertebrae were validated against Digital Volume Correlation (DVC) measurements for prediction of local properties. This study was the first evidencing the accuracy of microFE models predictions of local displacements ( $R^2=0.86-0.99$ ,  $RMSE\%=1\%-5\%$ ) for both the trabecular and cortical bone compartments of vertebral bodies scanned at high resolution. Predictions of local strain values were only validated qualitatively due to the limited spatial resolution of the experimental strain measurement. Reasonable predictions of structural properties were only possible for back-calculated tissue modulus (differences between predicted and measured reaction forces in the range of 10%-31%). This study showed that the simplest, most efficient, and commonly used homogeneous and linear elastic subject-specific microFE modelling approach can predict accurately the local properties of the bone tissues of vertebral bodies.

In Chapter IV, the effect of the size and location of virtually simulated lytic lesions on the local and structural properties of human vertebral bodies was studied using an imaging and modelling method similar to that validated in Chapter III. This study showed that the size of the simulated lytic lesions was linearly related to the decrease in structural properties of the vertebrae under compression ( $R^2\geq 0.99$  and intercept ranging from -0.004% to -0.049%). For the tested cases, no major changes were observed in the redistribution of local principal strains and stresses comparing to the values obtained for the control model. This approach can be used to improve the assessment of spinal instability from clinical scoring systems by adding details about the properties of the lesions (i.e. size and location) that can be measured from the clinical CT images. Nevertheless, in order to generalise the findings, this approach should be applied to a large number of human vertebrae with different microstructures and densities (see below). At the present time the sample size of this study was limited due to the high computational

demand of the models. Therefore, the second part of this PhD project focused on the development of subject-specific FE models based on clinical images.

In Chapter V, a methodology was developed to compare the mechanical properties and structural stability of vertebrae with lesions and adjacent control vertebrae by means of subject-specific Quantitative Computed Tomography (QCT) based FE models. The development of these models involved the definition of densitometric calibrations used to map the heterogeneous material properties of bone, a mesh refinement analysis to choose the optimal mesh size, and the definition of a failure criterion and the boundary conditions used to evaluate vertebral strength. Tetrahedral elements with maximum edge length of 1 mm, with heterogeneous, isotropic, and elastic-plastic material properties were found to provide a good compromise between computational time and differences in predictions of mechanical properties with respect to the outputs of the models with the most refined mesh. Moreover, a geometric 2D model of the spine was developed to estimate ranges of compressive loads applied to different vertebrae simulating a standing or a 30° flexion spinal posture. These models were used to normalise the outputs of the FE models for control vertebrae and for vertebrae with lesions in function of different vertebral levels for each patient. Thus, this study established a methodology for the evaluation of structural strength and stability of vertebrae with lytic lesions compared to those of the adjacent control vertebrae through the use of subject-specific clinical data.

In Chapter VI, it was evaluated the feasibility of the method developed in the previous chapter. Subject specific FE models were generated from eight QCT images of the thoracolumbar spine of patients with clinically identified vertebrae with lytic lesions. For each patient at least one vertebra with a lytic lesion and the two most adjacent control vertebrae were modelled. No significant differences were found among the densitometric and structural properties estimated between the groups of vertebrae with and without lytic lesions modelled ( $p \geq 0.57$ ). The percentage differences found between predicted mechanical properties of vertebrae with lytic lesions with respect to the control vertebrae ranged from -74% to 88%, showing that not all the lytic lesions had a detrimental effect on the mechanical properties of the vertebrae. For the 12 vertebrae with lytic lesions modelled in this study, and classified by the SINS with a possibly impending fracture risk, 4 were found to be mechanically stable. The remaining 8 vertebrae with lesions showed to be at higher risk of fracture compared to the adjacent controls or to be not strong enough to resist the load induced by a physiological trunk flexion posture. The results were included in biomechanical reports created for each patient

that can be used by clinicians together with the qualitative results of the SINS during the decision making process.

## **7.2. Limitations**

While the objectives of this thesis have been achieved, there are a few limitations that shall be addressed in future work.

In particular, the material properties used to generate the microFE models of the vertebrae were tuned to best fit the experimental results. This aspect limits the generalization of the method for the study of the mechanical properties of bones. Moreover, the use of microFE models to study the effect of virtually simulated lytic lesions on vertebral strength was limited due to the high computational demand of the models (between 5hours and 28hours of running time with the currently available computational resources of the High-Performance Computing cluster Beagle - 2.70GHz, 104 cores, and 1.7TB of RAM). Considering that this study aimed to test the feasibility of this approach, only one healthy sample was used and a small parametric analysis of simulated lytic lesions of 4 different sizes placed in 5 different locations within the vertebral body was performed. Nevertheless, in order to create a clinical tool, a large number of specimens should be tested to take into account the inter subject variability of densitometric and morphometric properties.

For the clinical based computational framework developed to predict the structural properties and stability of vertebrae with lytic lesions with respect to the adjacent control vertebrae, the main limitation was the lack of validation. Nevertheless, this approach is similar to other approaches found in the literature that showed to predict between 80% and 95% of the variability of vertebral strength for healthy subjects (Wang et al., 2012; Buckley et al., 2007; Imai et al., 2006). The main assumption in this study was that the tissue of the lytic lesions was considered as being bone tissue with low BMD. Therefore the relationship between BMD and bone strength was similar for both healthy vertebrae and vertebrae with lesions. This assumption is well supported by the literature (Lenherr et al., 2018; Stadelmann et al., 2018; Nazarian et al., 2008). Furthermore, only compressive loads were applied to a single vertebral unit, without accounting for more realistic and physiological loading scenarios. Considering the potential instability that occurs in vertebrae with lytic lesions, further loading scenarios may be more critical and should be modelled as well in order to have a comprehensive assessment of the vertebral stability.

### 7.3. Future work

This thesis established novel approaches to study the effect of lytic lesions on the strength and fracture risk of human vertebrae. However such approaches can be further improved taking into account some of the following aspects:

- The improvement of microFE models in order to increase their applicability and generalization for predictions of structural properties. Such improvements may include the use of more objective and automated segmentation methods and the use of tetrahedral meshes for a more accurate recovery of the boundary of bone structures.
- The extension of the parametric analysis performed with the subject-specific microFE models of human vertebrae to a larger sample size and number of parameters in order to have a meaningful representation of a population of patients affected by spinal metastases. This would allow a more extensive analysis of the effect of the size and location of simulated lytic lesions on the reduction of mechanical properties. Moreover, and based on the improvements of fracture risk assessment obtained by the use of a cortical disruption parameter in the assessment of femoral metastasis (Van der Linden et al., 2004), this analysis can also explore the effect of lesions occupying different bone types and their different impacts on the mechanical properties of the vertebrae.
- The application of the QCT based subject-specific FE models should be extended to at least 100 patients, typical number of patients involved in a phase II clinical trial.
- Other loading scenarios (torsion, bending, eccentric compression, etc.) shall also be modelled in order to study the effect of lytic lesions on vertebral stability for the other critical loading conditions.

## 7.4. References

- Buckley, J. M., Loo, K. & Motherway, J. (2007). Comparison of Quantitative Computed Tomography-Based Measures in Predicting Vertebral Compressive Strength. *Bone*, 40(3), 767–774.
- Imai, K., Ohnishi, I. & Bessho, M. (2006). Nonlinear Finite Element Model Predicts Vertebral Bone Strength and Fracture Site. *Spine*, 31(16), 1789–1794.
- Lenherr, C., Voumard, B., Stadelmann, M., Buck, F., Haschtmann, D., Hoppe, S., et al. (2018). *Indentation Properties of Metastatic Vertebral Trabecular Bone*. 8<sup>th</sup> World Congress of Biomechanics, Dublin, Ireland, 8-12<sup>th</sup> July 2018.
- Van der Linden, Y. M., Dijkstra, P. D. S., Kroon, H. M., Lok, J. J., Noordijk, E. M., Leer, J. W. H., et al. (2004). Comparative Analysis of Risk Factors for Pathological Fracture with Femoral Metastases. *The Journal of bone and joint surgery. British volume*, 86(4), 566–573.
- Nazarian, A., Von Stechow, D., Zurakowski, D., Müller, R. & Snyder, B. D. (2008). Bone Volume Fraction Explains the Variation in Strength and Stiffness of Cancellous Bone Affected by Metastatic Cancer and Osteoporosis. *Calcified Tissue International*, 83, 368–379.
- Stadelmann, M., Alkalay, R., Maquer, G., Buck, F., Hoppe, S., Theumann, N., et al. (2018). *Can Micro and Homogenized Finite Element Analysis Estimate the Strength of Human Metastatic Vertebrae?* 8<sup>th</sup> World Congress of Biomechanics, Dublin, Ireland, 8-12<sup>th</sup> July 2018.
- Wang, X., Sanyal, A., Cawthon, P. M., Palermo, L., Jekir, M., Christensen, J., et al. (2012). Prediction of New Clinical Vertebral Fractures in Elderly Men Using Finite Element Analysis of CT Scans. *Journal of Bone and Mineral Research*, 27(4), 808–816.